



T.C.  
MANİSA CELAL BAYAR ÜNİVERSİTESİ  
FEN BİLİMLERİ ENSTİTÜSÜ

MANİSA CELAL BAYAR UNIVERSITY  
INSTITUTE OF NATURAL&APPLIED  
SCIENCE

CİLT:19 SAYI:3 YIL:2023  
VOLUME:19 ISSUE:3 YEAR:2023

ISSN: 1305-130X  
e-ISSN: 1305-1385

**CELAL BAYAR ÜNİVERSİTESİ  
FEN BİLİMLERİ DERGİSİ**

**CELAL BAYAR UNIVERSITY  
JOURNAL OF SCIENCE**

**CELAL BAYAR  
ÜNİVERSİTESİ**



# Journal of Science

Volume: 19, Issue: 3, Year: 2023

## Contact

Manisa Celal Bayar University  
Institute of Natural and Applied Sciences  
Campus of Şehit Prof Dr İlhan Varank 45140 Yunusemre – MANİSA, TÜRKİYE  
Tel: (00 90) 236 201 27 05  
Fax: (00 90) 236 241 21 49  
e-mail: cbujos@gmail.com  
Web: <https://dergipark.org.tr/tr/pub/cbayarfbe>

“CBU Journal of Science is indexed by ULAKBIM-TUBITAK TR-DIZIN”



ISSN 1305-130X

E-ISSN 1305-1385

CBUJOS is published quarterly at Manisa Celal Bayar University Printing House

“CBU Journal of Science is a refereed scientific journal”



## Celal Bayar University Journal of Science

### Owner

Manisa Celal Bayar University,

**Editors :** Prof. Dr. Kamil ŞİRİN

**Assistant Editor:** Assoc. Prof. Dr. Mustafa AKYOL

### Layout Editor & Secretary

Assoc. Prof. Dr. İlker Çetin KESKİN

### Subject Editors

Prof. Dr. Abdullah AKDOĞAN, Pamukkale University, Chemical Engineering  
Prof. Dr. Ayhan ORAL, Çanakkale Onsekiz Mart University, Chemistry  
Prof. Dr. Ali DEMİR, Manisa Celal Bayar University, Civil Engineering  
Prof. Dr. Ali KONURALP, Manisa Celal Bayar University, Mathematics  
Prof. Dr. Fatih KALYONCU, Manisa Celal Bayar University, Biology  
Prof. Dr. Halil BABACAN, Manisa Celal Bayar University, Physics  
Prof. Dr. Mehmet ÇEVİK, Katip Çelebi University, Mechanical Engineering  
Prof. Dr. Mustafa CAN, Katip Çelebi University, Bioengineering  
Prof. Dr. Oğuz GÜRSOY; Mehmet Akif Ersoy University, Food Engineering  
Prof. Dr. Sezai TAŞKIN, Manisa Celal Bayar University, Electrical and Electronic Engineering  
Prof. Dr. Şerafettin DEMİÇ, Katip Çelebi University, Materials Engineering  
Assoc. Prof. Dr. İbrahim Fadıl SOYKÖK, Manisa Celal Bayar University, Mechatronics Engineering  
Assoc. Prof. Dr. İzzet YÜKSEK, Manisa Celal Bayar University, Architecture  
Assoc. Prof. Dr. Mehmet Ali ILGIN, Manisa Celal Bayar University, Industrial Engineering  
Assoc. Prof. Dr. Tuğba ÖZACAR ÖZTÜRK, Manisa Celal Bayar University, Computer Engineering

### International Scientific Advisory Board

Prof. Dr. Arianit REKA; State University of Tetova, Macedonia  
Prof. Dr. Tomasz NIEMIEC; Warsaw University of Life Sciences, Poland  
Prof. Dr. Alyani ISMAIL; Universiti Putra, Malaysia  
Prof. Dr. Iuliana APRODU; Dunarea de Jos University, Romania  
Assoc. Prof. Can BAYRAM; University of Illinois, USA  
Assoc. Prof. Dr. Johanan Christian PRASANNA; Madras Christian College, South India  
Assoc. Prof. Dr. Noureddine ISSAOUI; Université de Monastir, Tunisie.  
Assoc. Dr. Edward Albert UECKERMANN; North-West University, South Africa  
Assoc. Dr. Zhi-Qiang ZHANG; The University of Auckland, Holland  
Assist. Prof. Dr. Young Ki KIM; Pohang University of Science and Technology, South Korea  
Assist. Prof. Dr. Mona MIRHEYDARI; Rutgers University, USA  
Assist. Prof. Dr. Donatella ALBANESE; Università Degli Studi Di Salerno, Italy  
Assist. Prof. Dr. Jinghua JIANG; The University of Memphis, USA  
Assist. Prof. Dr. Jens OLDELAND; University of Hamburg, Germany  
Dr. Cheng CHENG; Apple Inc., USA  
Dr. Sajedah AFGHAH; Microsoft Corporation, USA  
Dr. Jinghua JIANG; The University of Memphis

### National Scientific Advisory Board

Prof. Dr. Mustafa Ersöz; Selçuk University  
Prof. Dr. Oğuz Gürsoy; Mehmet Akif University  
Prof. Dr. Mehmet Çevik; İzmir Katip Çelebi University  
Prof. Dr. Sezgin Çelik; Yıldız Teknik University  
Prof. Dr. Osman Dayan; Çanakkale Onsekiz Mart University  
Prof. Dr. Serdar İplikçi; Pamukkale University  
Prof. Dr. Yasin Üst; Yıldız Teknik University  
Prof. Dr. Mahmut Kuş; Konya Teknik University  
Prof. Dr. Ertunç Gündüz; Hacettepe University  
Prof. Dr. Tülin Aydemir; Manisa Celal Bayar University  
Prof. Dr. Sezai Taşkın; Manisa Celal Bayar University  
Prof. Dr. Fatma Şaşmaz Ören; Manisa Celal Bayar University  
Prof. Dr. Fatih Selimefendigil; Manisa Celal Bayar University  
Prof. Dr. Osman Çulha; Manisa Celal Bayar University  
Prof. Dr. Ali Konuralp; Manisa Celal Bayar University  
Prof. Dr. Erol Akpınar; Abant İzzet Baysal University  
Prof. Dr. Ali Demir; Manisa Celal Bayar University  
Prof. Dr. Serap Derman; Yıldız Teknik University  
Assoc. Prof. Dr. Fatih Doğan; Çanakkale Onsekiz Mart University  
Assoc. Prof. Dr. Yeliz Yıldırım; Ege University  
Assoc. Prof. Dr. Hayati Mamur; Manisa Celal Bayar University  
Assoc. Prof. Dr. Özlem Çağındı; Manisa Celal Bayar University  
Assoc. Prof. Dr. Mehmet Söylemez, Adıyaman University  
Assoc. Prof. Dr. Nil Mansuroğlu; Ahi Evran University  
Assist. Prof. Dr. Zeynep Çipiloğlu Yıldız; Manisa Celal Bayar University



## **CBU Journal of Science**

Celal Bayar University Journal of Science (CBUJOS) covers scientific studies in the fields of Engineering and Science and publishes accounts of original research articles concerned with all aspects of experimental and theoretical studies. CBU Journal of Science is a refereed scientific journal published four times annually (March, June, September and December) by Institute of Natural and Applied Sciences of Manisa Celal Bayar University. CBU Journal of Science considers the original research articles written in English for evaluation.

CBU Journal of Science is indexed by TUBİTAK ULAKBİM TR-DİZİN, and also is included in DOAJ, Cite Factor, Journal TOCS, Advanced Science Index and OAJI databases. Digital Object Identifier (DOI) number will be assigned for all the articles being published in CBU Journal of Science.

Instructions for Authors and Article Template can be found on the main page of MCBU Institute of Natural and Applied Sciences (<http://fbe.cbu.edu.tr>)





**Vol: 19, Issue: 3, Year: 2023**

**Contents**

**Research Article**

**Pages**

- A Neural Network Model for Estimation of Maximum Next Day Energy Generation Capacity of a Hydropower Station: A Case Study from Turkey  
DOI: 10.18466/cbayarfbe.1218381  
Serkan İnal, Sibel Akkaya Oy, Ali Ekber Özdemir  
197-204
- Modeling of the Cooling of the Batteries of Electric Vehicles Using the Cabin Air Conditioning System  
DOI: 10.18466/cbayarfbe1247445  
Haluk Güneş  
205-210
- Palladium/1,3-bis(ferrocenylmethyl)imidazolinium Chloride Catalyst for Suzuki Cross-Coupling Reactions  
DOI: 10.18466/cbayarfbe.1261392  
Mehmet Günaltay, Hülya Avcı Özbek , Funda Demirhan  
211-218
- A Study on the Solutions of (3+1) Conformal Time Derivative Generalized q-deformed Sinh-Gordon Equation  
DOI: 10.18466/cbayarfbe.1264314  
Yeşim Sağlam Özkan  
219-229
- LC-MS/MS Analysis and Biological Activities of Methanol Extract from *Sagina apetala* Ard.  
DOI: 10.18466/cbayarfbe.1264511  
Rabia Nur Ün  
231-235
- Preparation of ECH-PCCB for the Pre-concentration and Determination of Cadmium (II) Ions Prior to FAAS by FIA  
DOI: 10.18466/cbayarfbe.1280291  
Vedia Nüket Tirtom, Fatma Özkafalı  
237-242
- Evaluation of Various Flexibility Resources in Power Systems  
DOI: 10.18466/cbayarfbe.1280545  
Emir Kaan Tutuş, Nevzat Onat  
243-252
- Enhanced Microfluidics Mixing Performance in a Grooved Serpentine Microchannel at Different Flow Rates  
DOI: 10.18466/cbayarfbe.1293522  
Faruk Aksoy, Gürkan Yeşilöz  
253-260
- Use of Pyrolysed Almond and Walnut Shells (PAS and PWS) for the Adsorption of Cationic Dye: Reusing Agro-Waste for Sustainable Development  
DOI: 10.18466/cbayarfbe.1310461  
Gül Kaykioğlu, Nesli Aydın  
261-269



- Experimental and DFT-Based Investigation of Structural, Spectroscopic, and Electronic Features of 6-Chloroquinoline 271-281  
DOI: 10.18466/cbayarfbe.1313229  
Etem Köse, Fehmi Bardak
- Preparation and Characterization of Polylactic Acid Based Nanofiber Loaded with Tangerine Peel (Citrus Unshiu) Essential Oil 283-287  
DOI: 10.18466/cbayarfbe.1333674  
Tuğba Güngör Ertuğral, Sevim Akçura
- Chemical Composition and Antibacterial Activities of *Corylus avellana* L. Bioproducts Grown in Giresun-Türkiye 289-299  
DOI: 10.18466/cbayarfbe.1346393  
Mehmet Emin Şeker, Ayşegül Erdoğan, Emriye Ay, Derya Efe, Rena Hüseyinoğlu

# A Neural Network Model for Estimation of Maximum Next Day Energy Generation Capacity of a Hydropower Station: A Case Study from Turkey

Serkan İnal<sup>1</sup> , Sibel Akkaya Oy<sup>2\*</sup> , Ali Ekber Özdemir<sup>2</sup> 

<sup>1</sup> Darıca-2 Hydroelectric Power Plant, Kabadüz, Ordu, Türkiye  
<sup>2</sup> Fatsa Faculty of Marine Sciences, Ordu University, Ordu, Türkiye  
[\\*sibelakkaya@odu.edu.tr](mailto:sibelakkaya@odu.edu.tr)  
\*Orcid No: 0000-0002-1209-920X

Received: 13 December 2022  
Accepted: 16 August 2023  
DOI: 10.18466/cbayarfbe.1218381

## Abstract

Energy planning in a hydro power station (HPS) is essential for reservoir management, and to ensure efficient operation and financial usage. For robust energy planning, operators should estimate next day energy generation capacity correctly. This paper investigates use of a robust neural network model to estimate maximum next day energy generation capacity by using reservoir inflow rates for the previous four days, the current level of water in the reservoir, and the weather forecast for the Darıca-2 HPS in Ordu Province, Turkey. The generated energy in an HPS is directly dependent on the level of stored water in the reservoir, which depends on reservoir inflow. As the level of water in a reservoir varies during the year depending on climatic conditions, it is important to be able to estimate energy generation in an HPS to operate the HPS most effectively. This paper uses reservoir inflow data that has been collected daily during 2020 for the training phase of a neural network. The neural network is tested using a data set that has been collected daily during the first four months of 2021. Used neural network structure is called as LWNRBF (Linear Weighted Normalized Radial Basis Function) network, which is developed form of RBF network. In order to be able to be created valid model, LWNRBF network is trained with a two-pass hybrid training algorithm. After the training and testing stages, average training and testing error percentages have been obtained as 0.0012% and -0.0044% respectively

**Keywords:** Hydro-electric power generation, hydropower generation, neural network, reservoir inflow, renewable energy sources

## 1. Introduction

Although electrical energy is a clean form of energy, some electrical energy generation methods such as nuclear and thermoelectric plants have negative environmental effects. The most important negative effect in electrical energy generation is global warming due to the use of fossil fuels that cause unwanted CO<sub>2</sub> emission, especially in thermoelectric plants. Annual CO<sub>2</sub> emission due to use of fossil fuels is about 32.8 billion tons [1,2]. In order to reduce the effects of global warming, the most effective way is to use renewable energy sources such as hydro-electric, with hydropower stations being one of the most commonly used renewable energy sources. Globally, the hydropower industry meets about 17% of the world's electricity demand [3,4].

Today HPSs are among the most cost-effective means of generating electricity [5]. The general structure of an HPS is given in Fig.1 [6].

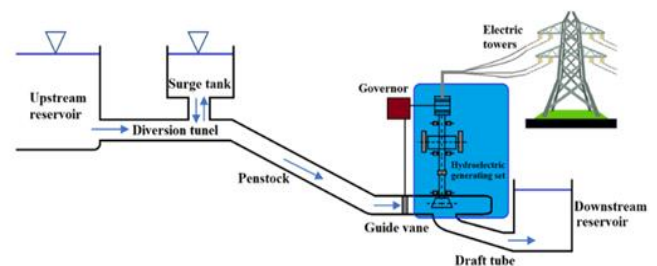


**Figure 1.** General structure of a hydropower station.

Generally, HPSs can be categorized into three groups depending on their function; storage, run-of-the-river, and pumped-storage technologies. HPSs can also be grouped by size; small, medium and large [7]. A small size HPS has a capacity less 10MW. Capacity of a medium size HPS is between 10 and 100MW for run-of-the river type and between 100 and 300MW for reservoir type HPS. A large-scale hydropower station capacity is greater than 300 MW [8].

Optimization of energy generation and planning processes depends on many parameters such as the technology, physical features, environmental features, losses (mechanic, electrical, hydraulic), and load demand. Optimization of several processes in an HPS using neural network structures and regression models have been investigated [9–11]. This includes predicting reservoir inflow and reservoir flow. Models include climatology of historical flow observations and pre-dam storage volumes [12–14].

Most HPSs have been established on rivers, as HPSs need a reliable water supply. This requires planning due to scarcity of water, population, and increasing energy demand [15]. Proper management and planning approaches are essential for efficient utilization of an HPS.

The paper is structured as follows: review of academic literature on studies of optimization of energy generation and planning; introduction of case study; methodology; conclusions and suggestions for further research.

## 2. Literature Review

Optimization of energy generation and planning processes in an HPS is an important and complex problem in terms of technological, economic, physical, and environmental aspects. This study focuses on the energy generation stage in a hydropower station. Most solutions for power optimization can be divided in two groups (i) optimization of reservoir operation and (ii) scheduling the water flow [16]. However, optimization in this field includes many uncertainties such as unpredictable future demand, water flow, climate conditions, and economic factors. However, the generated energy is directly related to the power produced at the turbine shaft by water pressure. This mechanical power,  $P$  can be estimated as (1) [17].

$$P = \eta_t p_w g Q h \quad (2.1)$$

where

$\eta_t$  = hydraulic efficiency of the turbine  
 $p_w$  = density of water  
 $g$  = acceleration due to gravity  
 $Q$  = discharge of water acting on the turbine  
 $h$  = head of water acting on the turbine

As seen in (1), the power produced at the generator shaft depends directly on the flow of the water. As the only energy input to the HPS is water flow, management of the water is essential for optimal operation of the HPS. Ren et al. investigated management of water resources and its impact on optimal hydropower generation [18]. They suggested an algorithm for resolving optimization problems in the management of the reservoir and hydropower generation. Huangpeng et al. used a neural network model to predict future hydropower generation under the influence of climate change [19]. Wang et al. developed a neural network model that includes water storage, water inflow, monthly water inventory, monthly reservoir level, and average water consumption for electricity generation as inputs to predict energy generation of an HPS [20].

Optimization of reservoir operation has been extensively studied in the literature; often referred as operating rules. Jia et al. used a Bayesian based method to determine the operating rules for hydropower reservoirs. They used 129-annual flow records as input to obtain the optimal operation trajectories [9]. Optimization of reservoir operation is also important for efficient use of the water supply. Li et al. redesigned the operating rules of a reservoir to satisfy the demand for lake water in a real-world case by using a form of genetic algorithm [21]. Their method reduced use of lake water by 5% and improved hydropower generation and hydropower reliability by 3.9% and 8.3%, respectively.

When hydropower stations are established on the same river, they act in a cascade, which requires more complex optimization strategies. Feng et al. proposed an adaptive sine cosine algorithm for optimization of multiple hydropower reservoirs [22], applying their proposed method to a hydropower system in China; claiming that their method would be suitable for similar problems in other research fields. Emami et al. used machine learning with a hybrid constrained coral reefs optimization algorithm to optimize operation of multi-reservoir systems [23]. Li et al. proposed a multi-objective tangent algorithm for optimization of the operation rules of cascade reservoirs, with the main objective to maximize hydropower generation, ecology and navigation [24].

Neural networks are a useful tool for optimization in many engineering problems, including extensive use in every stage of HPS optimization. For example, Cai et al. used an artificial neural network to evaluate soil and water resources in power generation at HPSs [25]. Shanga et al. used a back propagation neural network for real-time forecasting of downstream water levels in a case study from China. [26]

Recent studies have shown that, accurate reservoir inflow forecasting is also highly important for multi-purpose reservoir systems to improve on the economy of hydropower production. Olofintoyea et al. used a neural network model for real-time optimal water allocation in an HPS [27].

Yang et al. used a neural network model to predict inflow for real-time reservoir operation [28]. Hadiyan et al. used neural network structures to predict reservoir inflow [29], using several different models of static and dynamic artificial neural network structures in their study. Ahmad et al. used a neural network model that used short-term weather forecasts, historic hydrological data, and reservoir inflow as inputs to maximize hydropower generation [12]. Karunanayake et al. used a neural network with well-known learning algorithms (Levenberg–Marquardt, quasi-Newton, scaled conjugate gradient) to estimate reservoir inflow in a real-world case investigating future climate scenarios [30].

Although reservoir inflow estimation is a popular field in the literature, estimation of reservoir inflow is not an easy task due to the changing climate and human activity. However, these factors do not change rapidly over a period of days or months and robust methods for estimation of reservoir inflow for short time periods can be very useful for hourly or daily energy generation of an HPS. For example, Cheng et al. developed an artificial neural network model to estimate daily reservoir runoff [31]. Xu et al. used an artificial neural network to estimate short term reservoir inflow, achieving estimates of reservoir inflow for the forthcoming 1-7 hours [32]. Dampage et al. used a convolutional neural network to estimate daily reservoir inflow for an HPS [33].

Most studies using neural network models have been applied to real-world applications as each HPS has unique geographic, physical and seasonal properties and uncertainties. Ahmad et al. developed a web-based decision support system for the Detroit dam (Oregon) using weather forecasts to generate the daily optimized release decisions [34]. Liu et al. developed a Bayesian deep learning-based model that considered multiple uncertainties to derive operation rules for the Three Gorges Project on the Yangtze River [35].

Turkey is a developing country. Increasing energy demand and environmental considerations are making renewable energy sources popular in Turkey. Currently, HPSs provide 18.4% of energy generation in Turkey [36]. However, for HPSs to be more efficient, Turkey needs to adopt technological and scientific innovations in HPS operation and water management. Cobaner et al. developed an artificial neural network-based model to evaluate the feasibility of installing a hydropower plant at an existing irrigation dam [37]. Kucukali et al. developed a Fuzzy logic-based model to identify suitable existing irrigation dams where small HPSs could be developed [38]. Koç investigated the problems of the operation of hydropower plants that were integrated with irrigation schemes in Turkey and, by analyzing technical, environmental, social and structural problems occurring during the operation of an HPS, determined solutions for these problems [39].

In this study, we develop a neural network model that is used in energy planning for the Darica-2 HPS established in Ordu Province, Turkey.

### 3. Material and Methods

The Darica-2 HPS (Fig.2 and Fig.3) is on the Melet River in Ordu Province, Turkey.

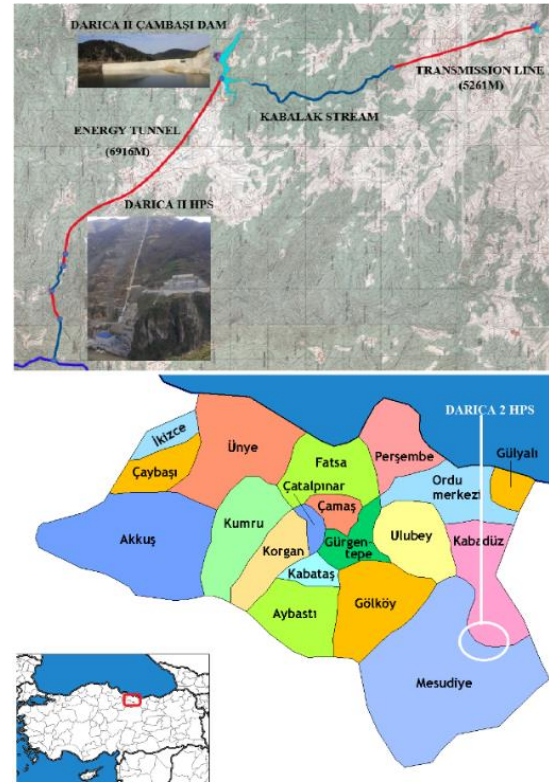


Figure 2. Location of Darica-2 HPS.

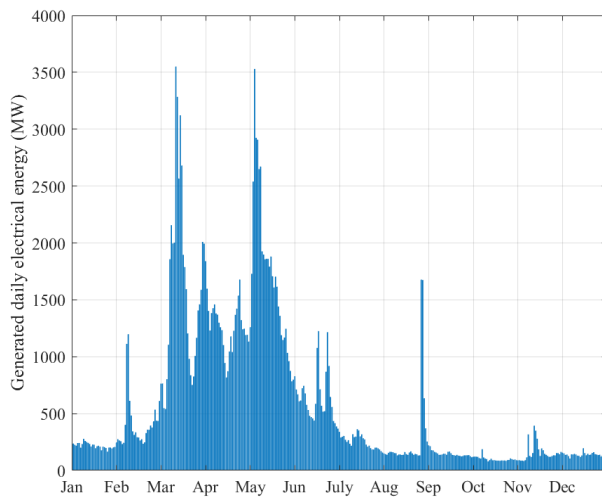


Figure 3. Location Darica-2 hydropower station, Ordu, Turkey.

The HPS is fed by the Çambaşı Dam, which is at an altitude of 1395 m. The Darıca-2 HPS is at 330 m, giving a hydraulic head of 1064 m, the second highest in Turkey. Its reservoir size is 4 million m<sup>3</sup>. The Darıca-2 HPS, with a capacity of 75 MW, is a medium scale HPS, and has an average annual electrical energy generation capacity of 207 GWh.

### 3.1 Data Acquisition

This study uses a neural network structure called LWNRBF to estimate the maximum possible next day energy generation capacity of the HPS. The inputs to the neural network are the reservoir inflow rates from the previous four days, the current level of water in the reservoir, and weather forecast data.



**Figure 4.** Daily generated electrical energy during 2020

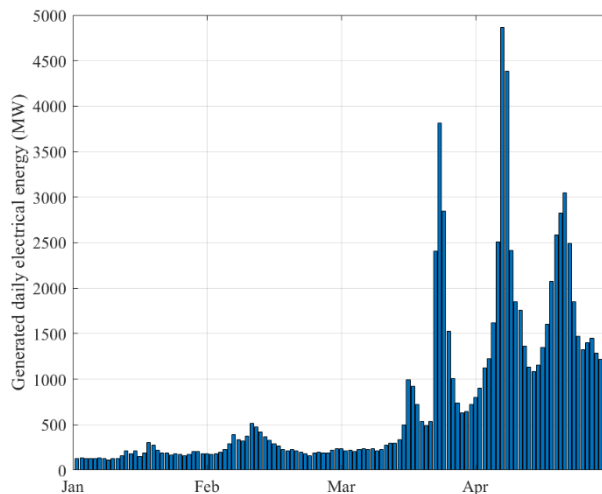


**Figure 5.** Daily generated electrical energy during first four months of 2021.

Data collected daily during 2020 were used in the training and testing stages of neural network and data collected daily from the first four months of 2021 were used for testing. The daily generated energy, shown in Fig.4 and Fig.5, were used in the training and testing stages.

### 2.1. Modelling

Many artificial neural network structures for pattern recognition, classification or modelling are described in the literature. Well-known forms include; multilayer perceptron network [40], radial basis neural network [41] and adaptive neuro fuzzy inference system (ANFIS) [42]. Learning methods include; gradient descent [43], back propagation [44], Levenberg–Marquardt [45], and orthogonal least squares [46]. Hybrid learning algorithms have also been used in the training stage of a neural network [47].

This study uses a new type neural network structure called LWNRBF with a two-pass hybrid learning algorithm which was developed by Özdemir [47], [48]. As known, classic RBF networks use widely in literature. RBF network structure is given with Fig. 6.

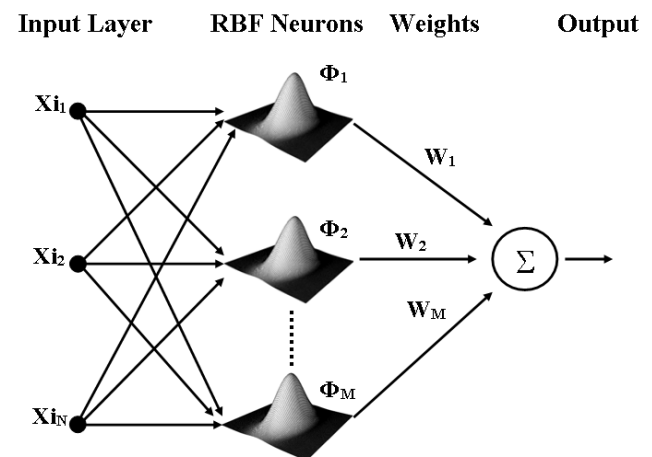


**Figure 6.** RBF Neural network structure.

RBF network structure is very suitable tool in system modelling. Training stage of RBFN needs to find two set of parameters. In the training stage of RBFN needs to find three set of parameters. These are centres, widths and weights of RBF neurons. In this study, an improved version of RBF network called LWNRBF is used with a two-pass hybrid learning algorithm. LWNRBF network structure is given with Fig. 7.

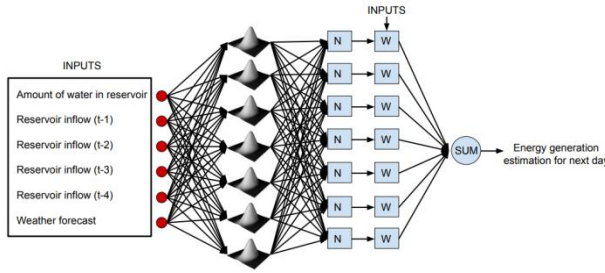


**Figure 7.** LWNRRBF Neural network structure used.

The LWNRRBF network has better modelling performance than the classical RBF network. But its structure is more complex than classic RBF network. Therefore, it needs more sophisticated training algorithm. Used training algorithm is given with Fig. 8.

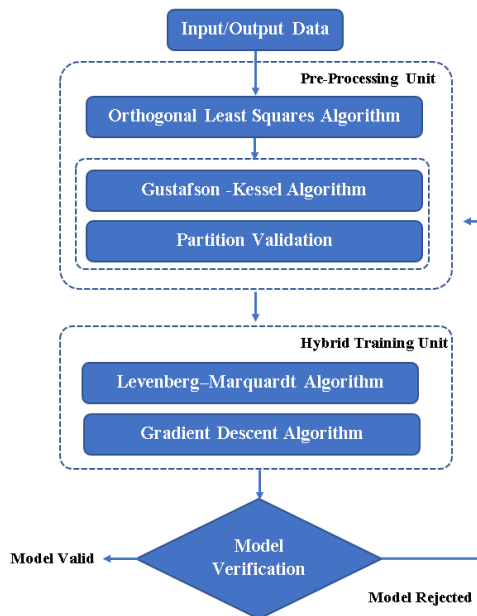


**Figure 8.** General framework of used two two-pass hybrid learning algorithm.

In first step, centres of RBF neurons are selected by OLS Algorithm from input data. However, these centers may not be fully suitable. They need to be optimized by Gustafson – Kessel (GK) algorithm with partition validation. First step is started by selecting an  $\epsilon$ OLS parameter between 0 and 1. A small value of  $\epsilon$ OLS causes finding more centres. Centres found by OLS are optimized by GK Algorithm. After determining of the centres, a two-pass hybrid training algorithm uses to fine tuning of the network parameters. In first pass (Forward computation) RBF weights are calculated by LM algorithm and other parameters is fixed. In second pass (Backward computation) fine tuning of centres and widths of RBF is made by Gradient Descent (GD) algorithm.

**Table 1.** Two-pass hybrid training procedure for LWNRRBF networks.

	Forward computation	Backward computation
RBF weights	LM algorithm	Fixed
RBF centers and widths	Fixed	GD algorithm
Signal	Node outputs	Error rates

Thanks to complex structure of LWNRRBF network can be used for modelling very complex data. However, LWNRRBF network needs more sophisticated training algorithm as mentioned above than classic RBF network.

Another important issue is to select input parameters of the network to create acceptable model. In this study, amount of water in reservoir, past four days reservoir inflow rates and weather forecast are used as inputs of the network. Output of the network is selected as possible energy generation capacity of the HPS for the next day (W).

In experiments, a set of past reservoir inflow rates were used. The best model performance is obtained for past four days reservoir inflow rates.

Training stage starts with selection only three parameters: OLS training parameter ( $\epsilon$ OLS) and learning parameters ( $\mu$ GD and  $\mu$ LM) for GD and LM algorithms. After the training process, if model is rejected user selects new parameter set until a valid model is created.

**Table 2:** Some parameter values used in OLS Algorithm.

Used learning parameter values			Number of Selected Centers by OLS
$\epsilon$ OLS	$\mu$ GD	$\mu$ LM	
0.1	0.005	0.005	1
0.09	0.005	0.005	3
0.04	0.005	0.005	6
0.01	0.005	0.005	8

For the valid model creating, in the training stage  $\epsilon$ OLS parameter was selected as 0.01 and 8 RBF neuron centres were selected by OLS algorithm. These centres were optimized and reduced as 7 by GK algorithm. Learning parameters  $\mu$ GD and  $\mu$ LM were selected as 0.005. It has been observed that in order to be able to reach best training and testing values of error, values of  $\mu$ GD and  $\mu$ LM should be selected as 0.005 experimentally.

Due to structure of OLS algorithm, these two parameters have not any effect on number of calculated values of centers by OLS algorithm.

Data collected daily during 2020 were used in the training and testing stages of neural network and data collected daily from the first four months of 2021 were used for testing. The daily generated energy, shown in Fig.4 and Fig.5, were used in the training and testing stages. Training process with modelling errors is given by Fig.9.

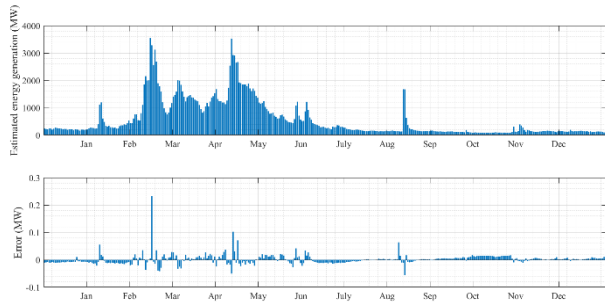


**Figure 9.** Estimated daily electrical energy generation and modelling error for months of 2020.

In the training process, average training error is calculated as 0.0012%. Outcomes of the testing process for first 4 days of 2021 is shown in Fig.10 – Fig.13.

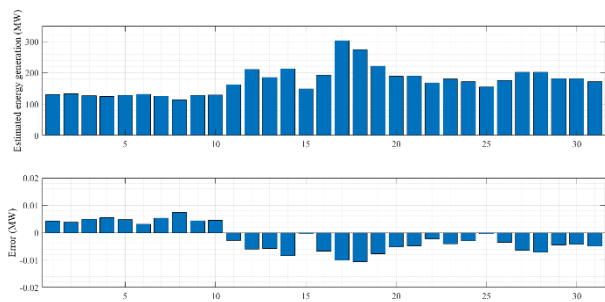


**Figure 10.** Estimated daily electrical energy generation and modelling error for January of 2021.

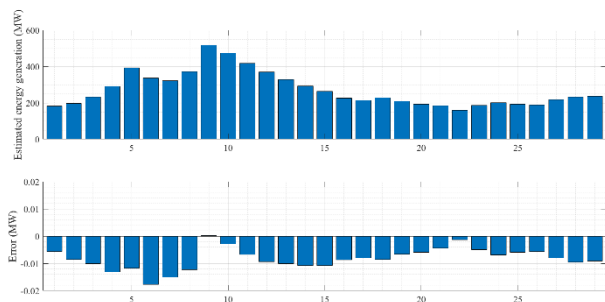


**Figure 11.** Estimated daily electrical energy generation and modelling error for February of 2021.

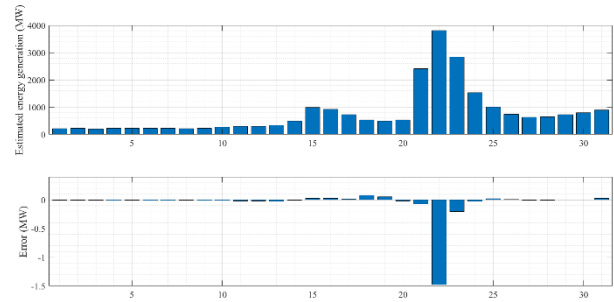


**Figure 12.** Estimated daily electrical energy generation and modelling error for March of 2021.

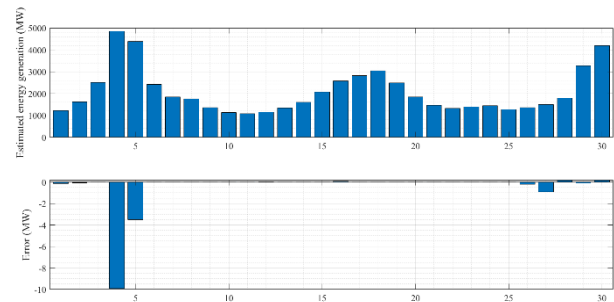


**Figure 13.** Estimated daily electrical energy generation and modelling error for April of 2021.

In the training process, average training error is calculated as -0.044%.

This study has developed a neural network model to be used in planning the daily energy generation of an HPS that has been shown to be accurate and reliable for estimation of daily energy generation. However, sudden rain and unpredictable seasonal change will affect the accuracy of the model. It was seen that when there was a sudden change in reservoir inflow, the model could adapt to the new condition within a few days.

#### 4. Conclusion

The most important and principal criterion for determining the energy generation of an HPS is the water flow into the basin where the plant is located and energy planning in an HPS is generally made according to the expected water level in the reservoir. Efficient operation of an HPS depends on robust planning of its energy generation. Energy planning for an HPS can be summarized in three main points:

1. The energy generation of an HPS to be made on the next day is announced to the authorized body. It is mandatory for the HPS to fulfil its announced energy generation otherwise the HPS will face fines and sanctions.

2. Maximum efficiency of use of the water in the reservoir depends directly on energy planning and estimation. During a flood period, the entire volume of water cannot be used for electrical energy generation because the excess water must be drained. Outside a flood period, most of the water in the reservoir can be used for energy generation through robust estimation of energy generation.

3. Incorrect planning will cause unwanted stop-start operations and this will increase maintenance costs. This study uses a neural network model to estimate next day energy generation of an HPS and has shown that the neural network can provide accurate prediction of next day energy generation.

The study shows that unforeseen weather events will cause errors in the estimations. Although sudden rainfall causes deviations in the output of the model, it was seen that model would adapt to the new situation within a short period.

The model works most accurately with hourly data and for very short-term estimation. However, to be most useful for energy planning, the model needs to provide accurate estimation of next day energy generation. Although the neural network model made some incorrect estimates in the testing stage, with the main reason due to unpredictable conditions such as faults, sudden rain, and incorrect stop-start operations, the overall error was small and, as a result, the presented neural network is considered useful for energy planning.

Our aim in future work is to use a recursive neural network structure that can adapt itself to new conditions and new data coming and can make more reliable estimations for energy planning.

#### Author's Contributions

**Serkan Inal and Ali Ekber Özdemir:** Designed and developed the models and methods, analyzed the data, and drafted the manuscript.

**Sibel Akkaya Oy:** Guided and supervised the whole process.

S. Inal., S. Akkaya Oy and A.E. Ozdemir revised the manuscript; and all authors read and approved the final manuscript.

#### Ethics

There are no ethical issues after the publication of this manuscript.

#### References

- [1]. Saravanan, A, Senthil kumar, P, Vo, DVN, Jeevanantham, S, Bhuvanawari, V, Anantha Narayanan, V, Yaashikaa, PR, Swetha, S, Reshma, B. 2021. A comprehensive review on different approaches for CO<sub>2</sub> utilization and conversion pathways. *Chemical Engineering Science*; 236: 116515
- [2]. IEA (International Energy Agency) 2017. CO<sub>2</sub> emissions from fuel combustion: Highlight. <https://euagenda.eu/upload/publications/untitled-110953-ea.pdf/> (accessed at 12.01.2021).
- [3]. Kuriqi, A, Pinheiro, AN, Sordo-Ward, A, Bejarano, MD, Garrote, L. 2021. Ecological impacts of run-of-river hydropower plants—Current status and future prospects on the brink of energy transition. *Renewable and Sustainable Energy Reviews*; 142: 110833.
- [4]. IHA. Hydropower status report. 7 ed. London United Kingdom: International Hydropower Association (IHA). [https://hydropower-assets.s3.eu-west-2.amazonaws.com/publications-docs/2020\\_hydropower\\_status\\_report.pdf](https://hydropower-assets.s3.eu-west-2.amazonaws.com/publications-docs/2020_hydropower_status_report.pdf) (accessed at 08.12.2020).
- [5]. IRENA (International Renewable Energy Agency). Available online: <https://www.irena.org/hydropower> (accessed at 15.05.2021).
- [6]. Shi, Y, Zhou, J, Lai, X, Xu, Y, Guo, W, Liu, B. 2021. Stability and sensitivity analysis of the bending-torsional coupled vibration with the arcuate whirl of hydro-turbine generator unit. *Mechanical Systems and Signal Processing*; 149: 107306
- [7]. Bilgili, M, Bilirgen, H, Ozbek, A, Ekinci, F, Demirdelen, T. 2018. The role of hydropower installations for sustainable energy development in Turkey and the world. *Renewable Energy*; 126: 755-764.
- [8]. IEA Renewable Energy Essentials: Hydropower Available online: [https://iea.blob.core.windows.net/assets/5b4df552-d99d-4bbb-b41e-c8ab4b6123b5/Hydropower\\_Essentials.pdf](https://iea.blob.core.windows.net/assets/5b4df552-d99d-4bbb-b41e-c8ab4b6123b5/Hydropower_Essentials.pdf) (16.05.2021).
- [9]. Jia, B, Zhou, J, Chen, X, He, Z, Qin, H. 2019. Deriving Operating Rules of Hydropower Reservoirs Using Gaussian Process Regression. *IEEE Access*; 7: 158170-158182.
- [10]. Feng, Z, Liu, S, Niu, W, Liu, Y, Lou, B, Miao, S, Wang, S. 2019. Optimal Operation of Hydropower System by Improved Grey Wolf Optimizer Based on Elite Mutation and Quasi-Oppositional Learning. *IEEE Access*; 7: 155513-155529.
- [11]. Li, B., Li, C., Cui, X., Lai, X., Ren, J., He, Q.: A Disassembly Sequence Planning Method with Team-Based Genetic Algorithm for Equipment Maintenance in Hydropower Station. *IEEE Access*. 8, 47538-47555 (2020).
- [12]. Shahryar Khaliq, A, Hossain, F. 2019. A generic data-driven technique for forecasting of reservoir inflow: Application for hydropower maximization. *Environmental Modelling & Software*; 119: 147-165.
- [13]. Ahmad, A, El-Shafie, A, Razali, SFM. 2014. Reservoir Optimization in Water Resources: A Review. *Water Resour Manage*; 28: 3391-3405.
- [14]. Rahman, I, Mohamad-Saleh, J. 2018. Hybrid bio-Inspired computational intelligence techniques for solving power system optimization problems: A comprehensive survey. *Applied Soft Computing*; 69: 72-130.
- [15]. Chong, K.L., Lai, S.H., Ahmed, A.N., Zurina, W., Jaafar, W., El-Shafie, A.: Optimization of hydropower reservoir operation based on hedging policy using Jaya algorithm. *Applied Soft Computing*; 106, 107325.
- [16]. Azad, A., Rahaman, SA, Watada, J, Vasant, P, Vintaned, JAG. 2020. Optimization of the hydropower energy generation using Meta-Heuristic approaches: A review. *Energy Reports*; 6: 2230-2248.

- [17]. Mishra, S, Singal, SK, Khatod, DK. 2011. Optimal installation of small hydropower plant—A review. *Renewable and Sustainable Energy Reviews*; 15: 3862-3869.
- [18]. Ren, X, Zhao, Y, Hao, D, Sun, Y, Chen, S, Gholinia, F. 2021. Predicting optimal hydropower generation with help optimal management of water resources by Developed Wildebeest Herd Optimization (DWHO). *Energy Reports*; 7: 968-980.
- [19]. Huangpeng, Q, Huang, W, Gholinia, F. 2021. Forecast of the hydropower generation under influence of climate change based on RCPs and Developed Crow Search Optimization Algorithm. *Energy Reports*; 7: 385-397.
- [20]. Wang, Y, Liu, J, Han, Y. 2020. Production capacity prediction of hydropower industries for energy optimization: Evidence based on novel extreme learning machine integrating Monte Carlo. *Journal of Cleaner Production*; 272: 122824.
- [21]. Li, X, Liu, P, Gui, Z, Ming, B, Yang, Z, Xie, K, Zhang, X. 2020. Reducing lake water-level decline by optimizing reservoir operating rule curves: A case study of the Three Gorges Reservoir and the Dongting Lake. *Journal of Cleaner Production*; 264: 121676.
- [22]. Feng, ZK, Niu, WJ, Liu, S, Luo, B, Miao, SM, Liu, K. 2020. Multiple hydropower reservoirs operation optimization by adaptive mutation sine cosine algorithm based on neighborhood search and simplex search strategies. *Journal of Hydrology*; 590: 125223.
- [23]. Emami, M, Nazif, S, Mousavi, SF, Karami, H, Daccache, A. 2021. A hybrid constrained coral reefs optimization algorithm with machine learning for optimizing multi-reservoir systems operation. *Journal of Environmental Management*; 286: 112250.
- [24]. Li, J., Qin, H., Zhang, Z., Yao, L., Gul, E., Jiang, Z, Wang, Y., Mo, L, Pei. S.: Operation Rules Optimization of Cascade Reservoirs Based on Multi-Objective Tangent Algorithm. *IEEE Access*. 7, 161949-161962 (2019).
- [25]. Cai, X, Ye, F, Gholinia, F. 2020. Application of artificial neural network and Soil and Water Assessment Tools in evaluating power generation of small hydropower stations. *Energy Reports*; 6: 2106-2118.
- [26]. Yizi Shang, Yang Xu, Ling Shang, Qixiang Fan, Yongyi Wang, Zhiwu Liu, A method of direct, real-time forecasting of downstream water levels via hydropower station reregulation: A case study from Gezhouba Hydropower Plant, China, *Journal of Hydrology*, Volume 573, 2019, Pages 895-907, ISSN 0022-1694,
- [27]. Olofintoye, O, Otiemo, F, Adeyemo, J. 2016. Real-time optimal water allocation for daily hydropower generation from the Vanderkloof dam South Africa. *Applied Soft Computing*; 47: 119-129.
- [28]. Yang, S, Yang, D, Chen, J, Zhao, B. 2019. Real-time reservoir operation using recurrent neural networks and inflow forecast from a distributed hydrological model. *Journal of Hydrology*; 579: 579124229.
- [29]. Hadiyan, PP, Moeini, R, Ehsanzadeh, E. 2020. Application of static and dynamic artificial neural networks for forecasting inflow discharges case study: Sefidroud Dam reservoir. *Sustainable Computing: Informatics and Systems*; 27: 100401.
- [30]. Karunanayake, C, Gunathilake, MG, Rathnayake, U. 2020. Inflow Forecast of Iranamadu Reservoir Sri Lanka under Projected Climate Scenarios Using Artificial Neural Networks. *Applied Computational Intelligence and Soft Computing*; 1-11.
- [31]. Cheng, CT, Niu, WJ, Feng, ZK, Shen, JJ, Chau, KW. 2015. Daily Reservoir Runoff Forecasting Method Using Artificial Neural Network Based on Quantum-behaved Particle Swarm Optimization. *Water*; 7: 4232-4246.
- [32]. Xu ZX and Li JY. 2002. Short-term inflow forecasting using an artificial neural network model. *Hydrol. Process*; 16:2423-2439.
- [33]. Dampage, U, Gunaratne, Y, Bandara, O, Silva, SD, Waraketiya, V. 2020. Artificial Neural Network for Forecasting of Daily Reservoir Inflow: Case Study of the Kotmale Reservoir in Sri Lanka 2020 5th International Conference on Computational Intelligence and Applications (ICCIA) Beijing China 19-21 June 2020.
- [34]. Ahmad, SK, Hossain, F. 2019. A web-based decision support system for smart dam operations using weather forecasts. *Journal of Hydroinformatics*; 21: 687-707.
- [35]. Liu, Y, Qin, H, Zhang, Z, Yao, L, Wang, Y, Li, J, Liu, G, Zhou, J. 2019. Deriving reservoir operation rule based on Bayesian deep learning method considering multiple uncertainties. *Journal of Hydrology*; 579: 124207.
- [36]. Energy Atlas of Turkey. <https://www.enerjiatlas.com/elektrik-uretimi/> (accessed at 23.05.2021).
- [37]. Cobaner, M, Haktanir, T, Kisi, O. 2008. Prediction of Hydropower Energy Using ANN for the Feasibility of Hydropower Plant Installation to an Existing Irrigation Dam. *Water Resour Manage*; 22: 757-774.
- [38]. Kucukali, S, Bayatı, OA, Maraş, HH. 2021. Finding the most suitable existing irrigation dams for small hydropower development in Turkey: A GIS-Fuzzy logic tool. *Renewable Energy*; 172: 633-650.
- [39]. Koç, C. 2018. A study on operation problems of hydropower plants integrated with irrigation schemes operated in Turkey. *International Journal of Green Energy*; 15: 129-135.
- [40]. Mazroua, AA, Salama, MMA, Bartnikas, R. 1993. PD pattern recognition with neural networks using the multilayer perceptron technique. *IEEE Transactions on Electrical Insulation*; 28: 1082-1089.
- [41]. Lippmann, RP. 1993. Pattern classification using neural networks. *IEEE Communications Magazine*; 27: 47-50.
- [42]. Jang, JR. 1993. ANFIS: adaptive-network-based fuzzy inference system. *IEEE Transactions on Systems Man and Cybernetics*; 23: 665-685.
- [43]. Baldi, P. 1995. Gradient descent learning algorithm overview: a general dynamical systems perspective. *IEEE Transactions on Neural Networks*; 6: 182-195.
- [44]. Karnin, ED. 1990. A simple procedure for pruning back-propagation trained neural networks. *IEEE Transactions on Neural Networks*; 1: 239-242.
- [45]. Hagan, MT, Menhaj, MB. 1994. Training feedforward networks with the Marquardt algorithm. *IEEE Transactions on Neural Networks*; 5: 989-993.
- [46]. Chen, S, Cowan, CFN, Grant, PM. 1991. Orthogonal least squares learning algorithm for radial basis function networks. *IEEE Transactions on Neural Networks*; 2: 302-309.
- [47]. Kayhan, G, Özdemir, AE, Eminoğlu, İ. 2013. Reviewing and designing pre-processing units for RBF networks: initial structure identification and coarse-tuning of free parameters. *Neural Computing and Applications*; 22: 1655-1666.
- [48]. Ozdemir, AE. 2011. Algorithmic signal processing substructure improvement needed for control of multifunctional myoelectric prosthesis hand and arm. PHD thesis, Ondokuz Mayıs University, Samsun Turkey.

# Modeling of the Cooling of the Batteries of Electric Vehicles Using the Cabin Air Conditioning System

Haluk Güneş<sup>1\*</sup> 

<sup>1</sup> Dumlupınar University, Tavşanlı Vocational School, Department of Motor Vehicles and Transportation Technologies / Kütahya-Türkiye

\*[haluk.gunes@dpu.edu.tr](mailto:haluk.gunes@dpu.edu.tr)

\*Orcid No: 0000-0002-0915-0924

Received: 03 February 2023

Accepted: 19 September 2023

DOI: 10.18466/cbayarfbe1247445

## Abstract

In this study, a simulation on management of battery temperature, which is a significant problem for electric vehicles, has been made. Battery temperatures can reach up to 50 °C if not checked during quick charging and discharging processes. Such situation shortens the lifetime of battery and also increases the temperature inside the cabin. More importantly, they can be dangerous. LMS Amesim software and WLTC driving cycle have been used for the simulation. Three battery packages have been used in simulations. Temperature of the battery have been checked at three different ambient temperatures (25 °C, 30 °C, 35 °C). During the test, it has been enhanced to keep the battery temperature below 35 °C under all conditions. Air-conditioner of the vehicle has been used to cool the batteries. When the temperature increased, the air-conditioner automatically checked the operating cycle of the compressor and cooled the batteries by means of constant air flow. In conclusion, the simulation has kept the battery temperature at desired level at ambient temperatures of 25 °C and 30 °C. At ambient temperature of 35°C, battery temperature increased up to 35.2°C.

**Keywords:** Battery temperature management, Electric vehicle, Hybrid electric vehicle, WLTC driving cycle.

## 1. Introduction

Global warming and environment pollution have increased rapidly due to recent development of industry. Especially carbon emission during generation and use of technology and mixing of pollutants into nature have become a major problem of the world. Internal combustion engines used nowadays in vehicles are the most important elements causing environment pollution and global warming [1]. Therefore, their production has started to be restricted throughout the world. Especially, all internal combustion engines, primarily diesel engines, are subjected to heavier driving cycles when compared to past and are forced to be less pollutant [2, 3]. However, it becomes impossible day by day to keep up with such cycles due to physical effects. Manufacturers have intensified their works on hybrid or electric vehicles, which sense such hard conditions less, in order to meet the vehicle requirements of the society [4]. In general terms, hybrid engines include a gasoline internal combustion engine and a small electric motor supporting the former one in certain circumstances [5]. In fact,

hybrid engine makes the traditional vehicle with internal combustion engine much more complicated. Systems, requiring more parts and maintenance, are altogether [6]. The electric motor operates less quietly and more environment-friendly during urban and easy driving, and complies with driving cycles. Here, there is a small lithium battery providing energy to the electric motor. [7]. In the beginning, hybrid vehicles used to be charged only during the driving process while new hybrid vehicles can be charged by charger. Hybrid vehicles are actually a start directing the society to full transition to electric automobiles. In the following years, the roads will be occupied completely by electric vehicles. Electric vehicles have a plainer structure when compared to the hybrid ones. Electric motors included in their structure are the only elements providing power and making the driving wheel. Therefore, they can operate completely environment-friendly and quietly during their use [8]. Moreover, they can easily adapt themselves to driving cycles under the harshest conditions. The electric motor can be on both front wheels or on four wheels in certain brands. In such engines, the power is generally provided

by means of lithium-ion batteries/accumulator placed on the basement of the vehicle. Compared to the batteries found in hybrid vehicles, these batteries in electric vehicles are larger in terms of weight and size and contain more power. [9]. Depending on the size and using purpose of the vehicles, electric engines at various powers and batteries at supportive power are selected [10]. As during the driving process, whole energy is provided by such batteries, their volume and weight are great. This situation increases the weight of the vehicle and shortens the distance to be covered and increases the re-charging duration. Electric vehicles are also subjected to driving cycle just like vehicles with internal combustion engine and hybrid engines [11-12]. This is a driving cycle operating according to theoretical test procedures of New European Driving Cycles (NEDC), which entered into force in 1980 and have become outdated [13]. As theoretical data are used, changes and emission values occurring in real driving cannot be put forward. Today, Worldwide Harmonised Light Vehicles Test Procedure (WLTC), accepted in 2017, is used [14]. In this cycle, real driving conditions are used for vehicles and a more realistic emission and speed/fuel consumption values occur. There are many theoretical and experimental researches in which driving cycles are applied on hybrid and electric vehicles. Some of them have intensified in energy consumption [15]. In such studies, battery consumptions in different driving cycles have been examined. In some of them, battery charging amount of regenerative gains have been put forward [16].

Effects of the heat emerging in battery during use can be considered as a significant research subject. The researches have focused on methods for protection

against negative effects of such heat or prevention of increasing the temperature of battery above critical level. [17-19]. The batteries start to get discharged quickly in power-requiring regions and accordingly their temperature increases. The increase in temperature is an important element shortening the lifetime of battery [20-21]. In a study, ammonium was used to cool lithium-ion batteries [22]. In another study, LiFePO<sub>4</sub> batteries used in electric vehicles were cooled with water-passing plates [23]. In previous studies, comparisons of liquid-cooled, air-cooled conventional battery cooling systems with thermoelectric element-based, phase-change material-based, heat pipe-based battery thermal management systems were made [24]. This study is on modelling of an electric vehicle by means of LMS Amesim simulation programme produced by Siemens Industry Software company. The vehicle used in such model is tested by WLTC cycle. The battery temperature occurring during related time has been cooled by the air-conditioning system of the vehicle.

## 2. Modelling and Simulation conditions

LMS Amesim simulation programme can achieve design and simulation in various parts of heavy-duty type vehicles, automotive, aircraft industry, defence industry, mechanical and production stages. In such kind of programmes, the parts and sections composing the system are selected and a work which is closer to real test procedures can be achieved. In the model, which is subject of this study, it has been tried to prevent temperature increase in the battery and to provide cabin comfort for the passengers during the driving by means of air-conditioning system.

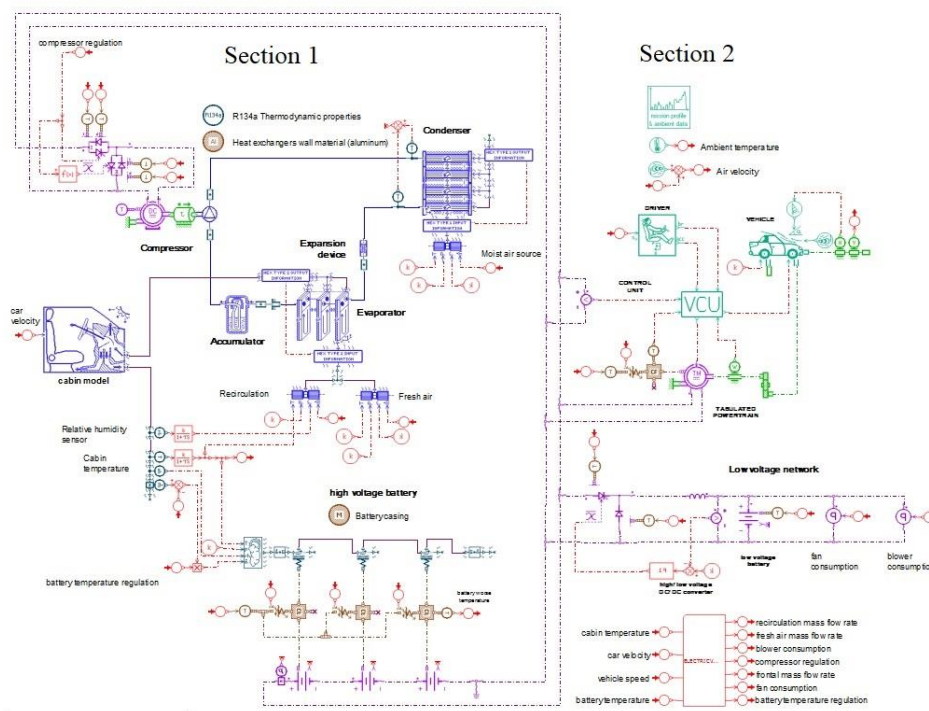


Figure 1. Design screen of the programme.

The system is composed of two parts. In the first part, a scheme required for operation of the air-conditioner is included, and in the second part, the scheme showing the driving cycle of the electric vehicle is included. The battery temperature has been tried to keep under 35°C by a part of the air of the air-conditioner. At the same time, the air-conditioner has been programmed in a manner not disturbing basic comfort of the passengers.

The programme scheme is shown in Figure 1. In the air-conditioning system, R134 coolant gas and a direct current compressor with constant magnet have been used. Air properties inside and outside the vehicle cabin have been given in Table 1. Here, cabin volume has been designed as 3.5 m<sup>3</sup>.

**Table 1.** Properties of the air inside and outside the cabin.

Cabin volume	3.5 m <sup>3</sup>
Wall thermal capacity	15000 J/°C
Internal exchange surface	15 m <sup>2</sup>
Cabin initial relative humidity	% 40
External pressure	1.013 bar
Solar flux	1000 W/m <sup>2</sup>

Vehicle battery is composed of 3 cells, each of which is 160 Volt, connected serially to each other and having a total capacity of 40 KWh. At the beginning of the test, the battery is charged by 80%. Features of the test vehicle have been given in Table 2.

**Table 2.** Features of the Test Vehicle.

Total vehicle mass	1400 kg
Mass distribution	50 %
Wheel inertia	0.75 kgm <sup>2</sup>
Tire width	165 mm
Tire height	65 %
Wheel rim diameter	15 in
rolling resistance coefficient	0.01
Air penetration coefficient (Cx)	0.3
Vehicle active area for aerodynamic drag	2 m <sup>2</sup>
Friction coefficient	1.2

During simulation, desired driving cycle can be selected. In this study, WLTC driving cycle has been used. Features of such driving cycle have been given in Table 3. In this cycle, maximum speed is 131 km/h; average speed is 46.5 km/h; total driving cycle is 1800 s and cycle length is 23.25 km.

**Table 3.** Features of WLTC driving cycle.

Cycle Time	30 min.
Cycle Distance	23.25 km
Driving Phases	52% urban, 48% extra-urban
Average Speed	46.5 km / h
Max Speed	131 km / h
Test Temperatures	23 °C
Total Time (s)	1800
Max. Acceleration (m/s <sup>2</sup> )	1.7
Max. Deceleration (m/s <sup>2</sup> )	-1.5
Fixed Driving Time (s)	66 (3.5%)
Acceleration Time (s)	789 (44%)
Deceleration Time (s)	719 (40%)
Stop Time (s)	226 (12.5%)

The simulation carries out WLTC cycle respectively at ambient temperatures of 25°C, 30 °C and 35 °C. At that moment, while the battery temperature is prevented to exceed 35°C, temperature comfort inside the cabin has been tried to be met. The air-conditioning system has programmed air-conditioner compressor to turn at appropriate cycles in order to fulfil such conditions. The air is let at a constant flow in order to cool the battery when required. The main reason of this is to make the temperature comfort inside the cabin more efficient in all conditions.

## 2. Results and Discussion

In Figure 2, there is a graphic showing the WLTC driving cycle and the compliance of the test vehicle with such cycle. The cycle also includes the speed area. The change in battery temperature at the end of the simulation has been obtained depending on the time. Especially in regions requiring high power, increase in battery temperature is an expected result. At that moment, cycle of air-conditioner compressor is increased and the battery is cooled by producing more coolant.

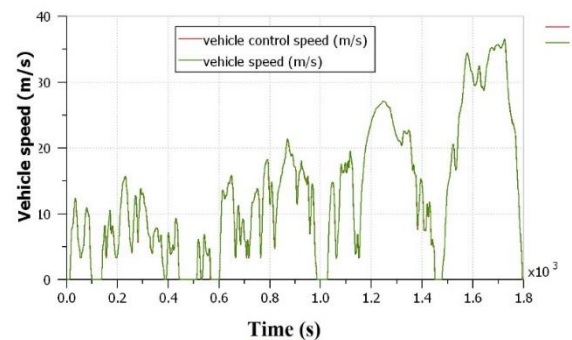


**Figure 2.** Speed-time graphics of test vehicle and WLTC driving cycle.

In Figure 3, the graphic including time-dependent battery temperature while the ambient temperature is 35°C, and mass flow of the air coming from the air-conditioning system. The battery temperature has started the cycle with a temperature of 35 °C which is equal to the ambient temperature. The system sends the coolant air into the battery according to the temperature of the hottest battery package.

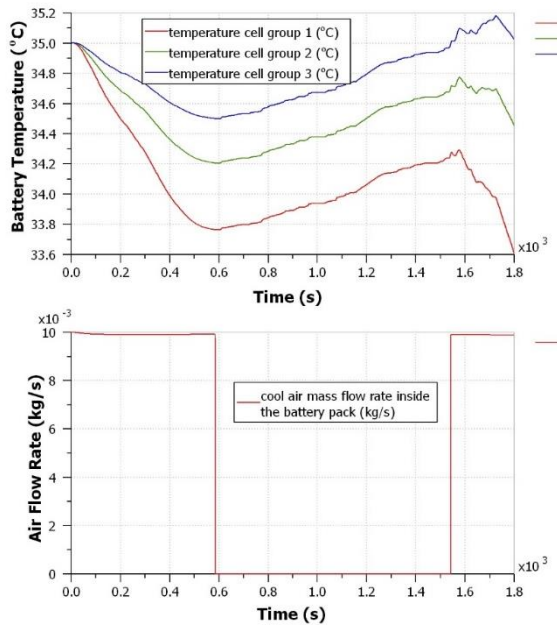


**Figure 3.** Temperature changes and air flow rate in battery packages while the ambient temperature is 35 °C.

At that moment, the air conditioner compressor is active. Hence, the air is sent to 3 battery packages by a flow rate of 0,01 kg/s. It is understood from the graphics that the battery temperatures drop quickly when it is started to send air to the battery packages. The first battery package located in front of the air inlet cools firstly; the other packages located at the back remain warmer. At the last part of the cycle requiring high power, there is an excessive energy consumption, and the battery package located backmost is a bit above 35°C. When whole cycle is examined, all battery packages have remained under 35.2°C.

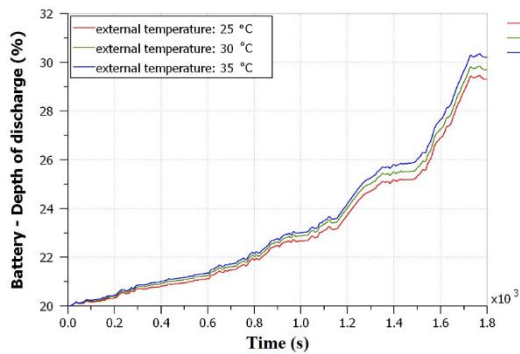


**Figure 4.** Time-dependent change of battery's deep cycle percentage.

In Figure 4, change of battery discharge during the whole cycle is shown. At the beginning of the cycle, the battery is 20% empty. Here, results of driving tests at 3 different ambient temperatures are included. At ambient temperature of 35 °C, deep cycle of the battery has increased above 30%. Ambient temperature of 30 °C has caused less battery consumption. The lowest consumption is observed at 25 °C. As it can be understood that as the ambient temperature decreases, battery consumption decreases too.

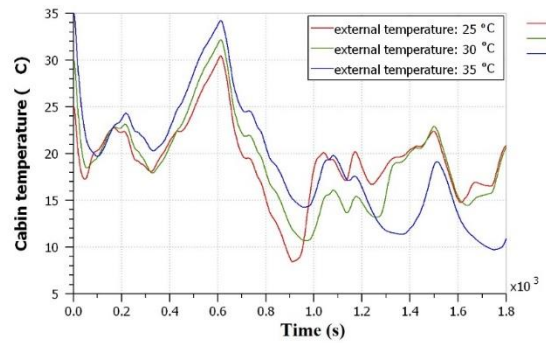


**Figure 5.** Time-dependent change of cabin temperature.

In Figure 5, change of cabin temperature during the cycle is shown. The tests have been made in three different ambient temperatures again. At the beginning of driving, cabin temperature is equal to the ambient temperature. As soon as the driving begins, the air-conditioner compressor starts to operate and cools both the battery and the cabin. In order to make cabin temperature below 25 °C, the coolant air is continued to be sent inside the cabin. At the 600th second of the cycle, the battery temperature drops below the targeted value. The air-conditioning air given to the battery is cut off at that moment and therefore battery temperature increases immediately. Such situation increases the cabin temperature quickly too.

As soon as the battery temperature reaches up to 35 °C, the coolant air is directed again to the battery and accordingly temperatures of both cabin and the battery decrease.

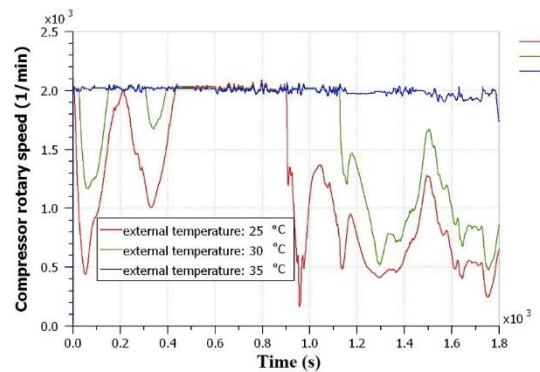


**Figure 6.** Time-dependent change of rotary speed of air-conditioner compressor.

In Figure 6, time-dependent change of rotary speed of air-conditioner compressor has been given. The compressor rotates at a maximum speed of 2100 1/min. When the graphic is examined, it is observed that the compressor rotates at a value close to the highest speed at 35 °C. The main reason of this is the fact that ambient temperature is high and accordingly battery temperature increases constantly. Such two increases result in significant increase in cabin temperature. The speed of the compressor is less at ambient temperature of 30 °C and 25 °C respectively. At those temperatures, the cabin temperature increases especially at the 400th second. The system increases the compressor cycle at the highest level as a reaction to this.

### 3. Conclusion

When simulation findings are examined, it is observed that battery temperature increases depending on the ambient temperature. At the same time, the quick increase in battery consumption in regions requiring high power according to WLTC cycle increases the battery temperature as well. Placement of battery packages at the basement of the vehicle increases the cabin temperature and affects the comfort of the passengers. As both battery temperature and cabin temperature are tried to be decreased by means of air-conditioner, the air-conditioner compressor cuts in more in hot weather and rotates at higher speed. Another conclusion derived from the tests is the higher level of battery's deep cycle in hot weather conditions. It has been observed that as the temperature increases, battery consumption increases too. In electric vehicles, batteries must be cooled. To this end, liquid cooling can be an effective method apart from the one studied here in.

### Author's Contributions

**Haluk Güneş:** Drafted and wrote the manuscript, performed the experiment and result analysis.

### Ethics

There are no ethical issues after the publication of this manuscript.

### References

- [1] Behi, H., Karimi, D., Jaguemont, J., Gandoman, F.H., Kalogiannis, T., Berecibar, M., Mierlo, J.V. (2021). Novel thermal management methods to improve the performance of the Li-ion batteries in high discharge current applications. *Energy*, 224: 1-17. <https://doi.org/10.1016/j.energy.2021.120165>.
- [2] Kunt, M.A. (2022). Analysis of engine and powertrain losses of a passenger type 4-stroke gasoline vehicle in 4 different driving cycles with gt-suite vehicle simulation program. *International Journal of Automotive Science and Technology*, 6(4): 340-346. <https://doi.org/10.30939/ijastech.1152980>.
- [3] Kunt, M.A. (2021). Analysis of The Effect of Different Gearbox/Transmission Types on Driveline Friction Losses by Means of Gt Suite Simulation Programme. *International Journal of Automotive Science and Technology*, 5(3): 271-280.
- [4] Sevim, E., Çetin, E. (2022). The performance comparison of the sic and si mosfets used in the 3-phase brushless DC motor drives for electric vehicles. *International Journal of Automotive Science and Technology*, 6(4): 331-339. <https://doi.org/10.30939/ijastech.1132500>.
- [5] Prajapati, K.C., Patel, R., Sagar, R. (2014). Hybrid vehicle: a study on technology. *International Journal of Engineering Research & Technology*, 3 (12): 1076-1082.
- [6] León, R., Montaleza, C., Maldonado, J.L., Véliz, M.T., Jurado, F. (2021). Hybrid electric vehicles: a review of existing configurations and thermodynamic cycles. *Thermo*, 1 (2): 134-150. <https://doi.org/10.3390/thermo1020010>
- [7] Moawad, A., Rousseau, A. (2012). Effect of Electric Drive Vehicle Technologies on Fuel Efficiency – Final Report. Argonne National Laboratory, Chicago.
- [8] Cheng, K.W.E. (2009). Recent development on electric vehicles. 3rd International conference on power electronics systems and applications.
- [9] Lalith, D.V., Ghatge, G.C., Setloor, K.G. (2021). Electric and hybrid electric vehicles. *International Journal of Research and Analytical Reviews*, 8 (4): 76-82.
- [10] Sanguesa, J.A., Sanz, V.T., Garrido, P., Martinez, F.J., Barja, J.M.M. (2021). A review on electric vehicles: technologies and challenges. *Smart Cities*, 4 (1): 372-404. <https://doi.org/10.3390/smartcities4010022>
- [11] Kiyakli, A.O., Solmaz, H. (2018). Modeling of an electric vehicle with matlab/simulink. *International Journal of Automotive Science and Technology*, 2 (4): 9-15. [10.30939/ijastech.475477](https://doi.org/10.30939/ijastech.475477)
- [12] Wang, Z., Zhang, J., Liu, P., Qu, C., Li, X. (2019). Driving cycle construction for electric vehicle based on markov chain and monte carlo method: a case study in Beijing. *Energy Procedia*, 158: 2494-2499. <https://doi.org/10.1016/j.egypro.2019.01.389>.
- [13] Pfieml, M., Gauterin, F. (2016). Development of real-world driving cycles for battery electric vehicles. *EVS29 International Battery, Hybrid and Fuel Cell Electric Vehicle Symposium*. 1-11.
- [14] Micari, S., Foti, S., Testa, A., De Caro, S., Sergi, F., Andaloro, L., Aloisio, D., Leonardi, S.G., Napoli, G. (2022). Effect of WLTP class 3B driving cycle on lithium-ion battery for electric vehicles. *Energies*, 15 (8): 1-25. <https://doi.org/10.3390/en15186703>.
- [15] Asef, P., Milan, M., Laphorn, A., Padmanaban, S. (2021). Future trends and aging analysis of battery energy storage systems for electric vehicles. *Sustainability*, 13(24): 1-28. <https://doi.org/10.3390/su132413779>.
- [16] Berjoza, D., Pirs, V., Jurgena, I. (2022). Research into the regenerative braking of an electric car in urban driving. *World Electric Vehicle Journal*, 13(11): 1-13. <https://doi.org/10.3390/wevj13110202>.
- [17] Xu1, Z., Jiang, D., Li, M., Ning, P., Wang, F., Liang, Z. (2012). Si IGBT phase-leg module packaging and cooling design for operation at 200 °C in hybrid electrical vehicle applications. 2012 Twenty-Seventh Annual IEEE Applied Power Electronics Conference and Exposition (APEC), 483-490.
- [18] Behi, H., Karimi, D., Youssef, R., Patil, M.S., Mierlo, J.V., Berecibar, M. (2021). Comprehensive passive thermal management systems for electric vehicles. *Energies*, 14 (13): 1-15. <https://doi.org/10.3390/en14133881>.
- [19] Soltani, M., Ronsmans, J., Jaguemont, J., Mierlo, J.V., Bossche, P.V., Omar, N. (2019). A Three-dimensional thermal model for a commercial lithium-ion capacitor battery pack with non-uniform temperature distribution. 2019 IEEE International Conference on

Industrial Technology (ICIT), 1126-1131.  
10.1109/ICIT.2019.8755081.

[20] Behi, H., Karimi, D., Behi, M., Ghanbarpour, M., Jaguemont, J., Sokkeh, M.A., Gandoman, F.H., Berecibar, M., Mierlo, J.V. (2020). A new concept of thermal management system in Li-ion battery using air cooling and heat pipe for electric vehicles. *Applied Thermal Engineering*, 174: 1-14. <https://doi.org/10.1016/j.applthermaleng.2020.115280>.

[21] Behi, H., Behi, M., Karimi, D., Jaguemont, J., Ghanbarpour, M., Behnia, M., Berecibar, M., Mierlo, J.V. (2021). Heat pipe air-cooled thermal management system for lithium-ion batteries: High power applications. *Applied Thermal Engineering*, 183: 1-13. <https://doi.org/10.1016/j.applthermaleng.2020.116240>.

[22] Al-Zareer, M., Dinçer, I., Rosen, M.A. (2017). Electrochemical modeling and performance evaluation of a new ammonia-based battery thermal management system for electric and hybrid electric vehicles. *Electrochimica Acta*, 247: 171-182. <http://dx.doi.org/10.1016/j.electacta.2017.06.162>.

[23] Monika, K., Chakraborty, C., Roy, S., Dinda, S., Singh, S.A., Datta, S.P. (2021). An improved mini-channel based liquid cooling strategy of prismatic LiFePO<sub>4</sub> batteries for electric or hybrid vehicles. *Journal of Energy Storage*, 35: 1-15. <https://doi.org/10.1016/j.est.2021.102301>

[24] Lu, M., Zhang, X., Ji, J., Xu, X., Zhang, Y. (2020). Research progress on power battery cooling technology for electric vehicles. *J. Energy Storage*, 27: <https://doi.org/10.1016/J.EST.2019.101155>.

# Palladium/1,3-bis(ferrocenylmethyl)imidazolium Chloride Catalyst for Suzuki Cross-Coupling Reactions

Mehmet Günaltay<sup>1</sup> , Hülya Avcı Özbek<sup>1</sup> , Funda Demirhan<sup>1\*</sup> 

<sup>1</sup> Manisa Celal Bayar University, Faculty of Sciences and Letters, Department of Chemistry, Muradiye-Manisa, Türkiye  
\*[funda.demirhan@cbu.edu.tr](mailto:funda.demirhan@cbu.edu.tr)  
Orcid No: 0000-0001-9428-9607

Received: 07 March 2023

Accepted: 05 July 2023

DOI: 10.18466/cbayarfbe.1261392

## Abstract

We describe here the first results on the catalytic performance of in-situ prepared  $[\text{Pd}(\text{O}_2\text{CCH}_3)_2]$  / 1,3-bis(ferrocenylmethyl)imidazolium chloride. This saturated imidazole ring was successfully used in Suzuki cross-coupling reactions of various aryl bromides (bromobenzene, 2-bromobenzonitrile, 2-bromotoluene, *p*-bromobenzaldehyde, *p*-bromoacetophenone, *p*-bromoanisole, *p*-bromotoluene, and *p*-bromobenzotrifluoride) with phenylboronic acid under optimal conditions. The optimal conditions were determined to be 24 hours, 80°C,  $\text{K}_2\text{CO}_3$  as a base, dioxane as a solvent, and 1,3-bis(ferrocenylmethyl)imidazolium chloride as an auxiliary ligand. Under these conditions, 2-bromobenzonitrile, *p*-bromoacetophenone, and *p*-bromobenzaldehyde reacted with phenylboronic acid in moderate yields of 57%, 50%, and 46%, respectively. Catalytic experiments showed that the  $[\text{Pd}(\text{O}_2\text{CCH}_3)_2]$  / 1,3-bis(ferrocenylmethyl)imidazolium chloride catalytic system was moderately efficient in the Suzuki cross-coupling reaction of aryl bromides in dioxane.

**Keywords:** Ferrocene, 1,3-bis(ferrocenylmethyl)imidazolium salt, Palladium, Suzuki

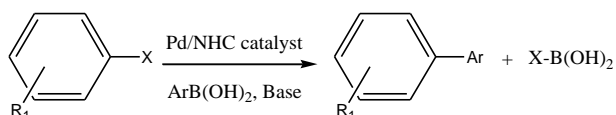
## 1. Introduction

The use of N-heterocyclic carbenes (NHCs) in transition metal catalysis has inspired numerous studies since it was first reported by Hermann et al. in 1995. Different metal complexes of NHCs, such as Pd, Ru, Rh, Pt, and Ir, have been extensively used to catalyze various reactions, including olefin metathesis, polymerization, hydrogenation, and C-N and C-C coupling [1-3]. Pd-NHC systems have been shown to compete with phosphane-bonded systems in reactions such as Kumada, Sonogashira, Heck, and Suzuki [4-6]. Therefore, NHCs are known as potential alternatives to phosphines.

Ferrocenyl-substituted carbenes are interesting compounds in terms of being an electron source, reversible redox chemistry, and the stereoelectronic effect of ferrocenyl groups [7]. The first study on this subject were conducted by Bildstein et al. in the late 1990s, and diferrocenylcarbene and ferrocenyl-substituted NHCs were synthesized [8-9]. After the publication of the work on carbenes containing ferrocene groups by Bildstein in 2001, great progress has been

made in the studies conducted in this field. This period is counted as the "post-Bildstein period" in carbene chemistry containing ferrocene groups [10].

The first study on *N,N'*-diferrocenyl-linked carbenes were also carried out by Bildstein et al. [8-9]. Later, imidazolium salts containing *N,N'*-diferrocenyl-linked phosphine, aryl, or silyl groups were reported [11-15]. These salts have been converted into NHC complexes with various metals (Ru(II), Ir(I), Mo), Pd(II), Rh(I), and some of the obtained complexes have been used in catalytic applications. Especially in recent years, ferrocenyl-substituted Pd-NHCs have wide applications in homogeneous catalysis [16-21]. In addition, in situ catalytic studies of  $[\text{Pd}(\text{O}_2\text{CCH}_3)_2]$  / ferrocenyl NHCs are known but are very scarce in the literature [22-26]. For example, Shi et al. reported an in situ Suzuki-Miyaura coupling reaction of aryl bromides by reacting  $[\text{Pd}(\text{O}_2\text{CCH}_3)_2]$  / ferrocenylimidazolium salts as shown in the general mechanism in Scheme 1 [22-24]. Dallas et al. have also investigated the catalytic properties of the  $[\text{Pd}(\text{O}_2\text{CCH}_3)_2]$  / ferrocenyl azolium salt systems in the Heck reaction [25].



Scheme 1. Suzuki-Miyaura coupling reaction

We have recently reported on the catalytic activity of 1,3-bis(ferrocenylmethyl)imidazolium chloride/bromide salts (Figure 1) in the Heck coupling reaction [26]. This study represents the first example of utilizing 1,3-bis(ferrocenylmethyl)imidazolium salts, featuring a saturated imidazole ring as the auxiliary ligand, with  $[Pd(O_2CCH_3)_2]$  for the Suzuki reaction. These salts performed moderately well as auxiliary ligands in the Suzuki reaction and were active in the Heck coupling reaction.

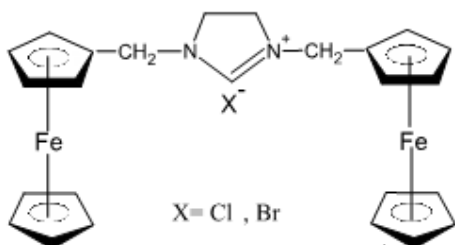


Figure 1. 1,3-bis(ferrocenylmethyl)imidazolium salts

## 2. Materials and Methods

1,3-bis(ferrocenylmethyl)imidazolium chloride/bromide were synthesized using previously reported procedures, and the analytical properties (FT-IR,  $^1H$  NMR, and melting point) of these salts were consistent with those reported in the literature [27]. The  $^1H$  NMR spectra of 1,3-bis(ferrocenylmethyl)imidazolium chloride/bromide and the biaryl product were recorded on a VARIAN ASW-400 spectrometer, while the melting points were measured using an Electrothermal 9200 melting point apparatus.

### 2.1. General procedure for the Suzuki cross-coupling reactions

A 25 mL flask was filled with 1,3-bis(ferrocenylmethyl)imidazolium salt (0.005 mmol),  $[Pd(O_2CCH_3)_2]$  (0.005 mmol),  $C_6H_5B(OH)_2$  (1.5 mmol), aryl bromide (1.0 mmol), solvent (2 mL), and a base (2 mmol) in an air atmosphere. The solution was stirred at the specified temperature for 2-24 hours, and the reactions were monitored using TLC. The mixture was then cooled, diluted with  $Et_2O$ , and purified via column chromatography. The purity of the compounds was confirmed using  $^1H$  NMR, and the yields were based on the amount of aryl bromide used.

## 2.2. Data for biaryl

**2.2.1. 4-Acetylbiphenyl** [28]. Mp: 118 °C.  $^1H$  NMR (400 MHz,  $CDCl_3$ )  $\delta$  (ppm) 8.04 (Ar-H, 2H, d), 7.65 (Ar-H, 2H, m), 7.48 (Ar-H, 2H, d), 7.43 (Ar-H, 3H, m), 2.64 ( $COCH_3$ , 3H, s) (Figure S1).

**2.2.2. Biphenyl** [28]. Mp: 68 °C.  $^1H$  NMR (400 MHz,  $CDCl_3$ )  $\delta$  (ppm) 7.60 (Ar-H, 4H, m), 7.46-7.42 (Ar-H, 4H, t), 7.36-7.33 (Ar-H, 2H, t) (Figure S2).

**2.2.3. 4-Methoxybiphenyl** [28]. Mp: 88 °C.  $^1H$  NMR (400 MHz,  $CDCl_3$ )  $\delta$  (ppm) 7.57-7.54 (Ar-H, 4H, m), 7.41 (Ar-H, 2H, m), 7.30 (Ar-H, 1H, dd), 6.98 (Ar-H, 2H, m.), 3.86 ( $OCH_3$ , 3H, s,) (Figure S3).

**2.2.4. Biphenyl-2-carbonitrile** [29]. Mp: 37 °C.  $^1H$  NMR (400 MHz,  $CDCl_3$ )  $\delta$  (ppm) 7.75 (Ar-H, 2H, dd), 7.66 (Ar-H, 1H, m), 7.58 (Ar-H, 2H, m), 7.52 (Ar-H, 3H, m.), 7.44 (Ar-H, 2H, m) (Figure S4).

**2.2.5. Biphenyl-4-carboxaldehyde** [30]. Mp: 57 °C.  $^1H$  NMR (400 MHz,  $CDCl_3$ )  $\delta$  (ppm) 10.06 ( $O=CH$ , 1H, s), 7.97 (Ar-H, 2H, m), 7.77 (Ar-H, 2H, m), 7.51-7.48 (2H, m), 7.44 (1H, s) (Figure S5).

## 3. Results and Discussion

The reaction processes were optimized using 4-bromoacetophenone and phenylboronic acid as substrates in situ with  $[Pd(O_2CCH_3)_2]$  / 1,3-bis(ferrocenylmethyl)imidazolium as the catalyst. The optimization involved varying the temperature, base, solvent, time, and auxiliary ligand. The results of the optimization are shown in Table 1.

Initially, the reaction was carried out without the auxiliary ligand, and only  $[Pd(O_2CCH_3)_2]$  was used as a catalyst. However, a trace amount of product was formed. The addition of 1,3-bis(ferrocenylmethyl)imidazolium chloride/bromide as an auxiliary ligand produced 50% and 38% yield, respectively (Table 1, entries 1-2, 4). Thus, it was decided to use 1,3-bis(ferrocenylmethyl)imidazolium chloride as the auxiliary ligand.

The effect of varying temperatures was studied, and it was found that the yield was moderate at a higher temperature of 80°C. No product was obtained at room temperature, and the yield did not change at the highest temperature of 110°C (Table 1, entries 4-5). The optimum temperature was determined to be 80°C as it is advantageous to work at lower temperatures.

The effect of different solvents, dioxane, toluene, and DMF- $H_2O$ , on the yield was studied. (Table 1, entries 4, 6-7). Dioxane was chosen as the solvent as it gave the highest yield.

Different bases were investigated to optimize the yield of the transformation.  $K_2CO_3$  gave a 50% yield, while  $Cs_2CO_3$  and NaOH produced 54% and 43% yield, respectively.  $Na_2CO_3$ ,  $Li_2CO_3$ , and  $CH_3COONa$  did not work for the present coupling reaction (Table 1, entries 4, 8-12).  $K_2CO_3$  was preferred as a base due to its effectiveness and lower cost.

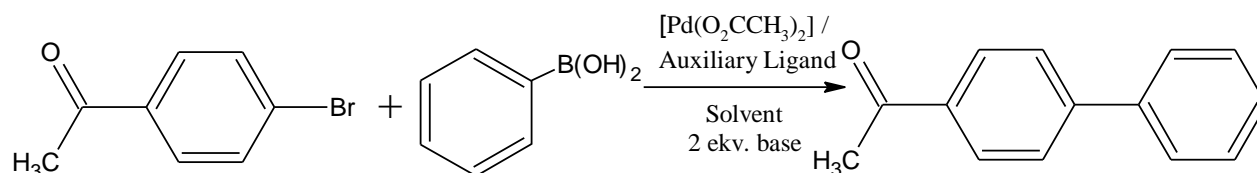
The yield was found to increase with the reaction time, and trace amounts of product were obtained at 2, 4, 6, and 8 hours. The optimum time was determined as 24 hours, as the yield increased with reaction time (Table 1, entries 4, 13-16).

Optimum conditions were determined as 24 hours at  $80^\circ C$ , with  $K_2CO_3$  as the base, dioxane as the solvent, and 1,3-bis(ferrocenylmethyl)imidazolium chloride as the auxiliary ligand. Under these conditions, moderate yields of 57%, 50%, 46%, 13%, and 8% were obtained for the reactions of 2-bromobenzonitrile, *p*-bromoacetophenone,

*p*-bromobenzaldehyde, bromobenzene, and *p*-bromoanisole, respectively, with phenylboronic acid (Table 2, entries 1-5). No product was obtained when using 2-bromotoluene, *p*-bromotoluene, and *p*-bromobenzotrifluoride (Table 2, entries 6-8). Unfortunately, the in situ  $[Pd(O_2CCH_3)_2]$  / 1,3-bis(ferrocenylmethyl)imidazolium catalyst system was not effective in the Suzuki reaction.

The proposed mechanism for the Suzuki coupling reaction of biaryl products using the Pd/NHC catalytic system is outlined in Scheme 2. This reaction follows a sequence of three steps: oxidative addition, transmetalation, and reductive elimination. In the first step, Pd(0) species are oxidized by organic halides to form Pd(II), which is the rate-determining step of the reaction. Next, transmetalation occurs between Pd(II) and the alkyl borate complex. Finally, Pd(0) is regenerated by the reductive cleavage of the C-C sigma bond.

**Table 1.** Optimizations of Suzuki cross-coupling reaction



Entry <sup>a</sup>	Base	Solvent	T (°C)	Time (h)	Yield <sup>b,c</sup> (%)
1 <sup>d</sup>	$K_2CO_3$	1,4-Dioxane	80	24	Trace
2 <sup>e</sup>	$K_2CO_3$	1,4-Dioxane	80	24	38
3	$K_2CO_3$	1,4-Dioxane	RT	24	ND
4	$K_2CO_3$	1,4-Dioxane	80	24	50
5	$K_2CO_3$	1,4-Dioxane	110	24	48
6	$K_2CO_3$	Toluene	80	24	40
7	$K_2CO_3$	DMF-H <sub>2</sub> O	80	24	36
8	$Cs_2CO_3$	1,4-Dioxane	80	24	54
9	NaOH	1,4-Dioxane	80	24	43
10	$Na_2CO_3$	1,4-Dioxane	80	24	Trace
11	$Li_2CO_3$	1,4-Dioxane	80	24	ND
12	$CH_3COONa$	1,4-Dioxane	80	24	Trace
13	$K_2CO_3$	1,4-Dioxane	80	2	Trace
14	$K_2CO_3$	1,4-Dioxane	80	4	Trace
15	$K_2CO_3$	1,4-Dioxane	80	6	Trace
16	$K_2CO_3$	1,4-Dioxane	80	8	Trace

a Reaction conditions:  $[Pd(O_2CCH_3)_2]$  (0.05 mmol), 1,3-bis(ferrocenylmethyl)imidazolium chloride (0.05 mmol), *p*-bromoacetophenone (1.0 mmol),  $C_6H_5B(OH)_2$  (1.5 mmol), base (2 mmol), solvent (2 mL). ND: Not determined.

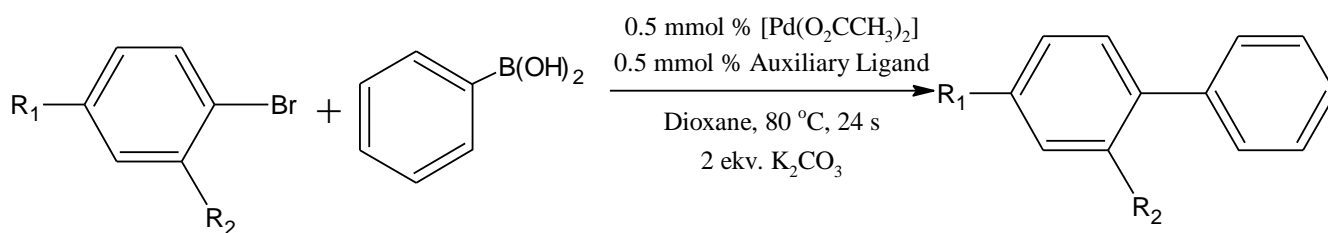
b Isolated yields based on *p*-bromoacetophenone.

c All reactions were monitored by TLC.

d  $[Pd(O_2CCH_3)_2]$  was used as catalyst.

e 1,3-bis(ferrocenylmethyl)imidazolium bromide was used as an auxiliary ligand.

**Table 2.** Suzuki cross-coupling reaction of aryl bromides with  $C_6H_5B(OH)_2$



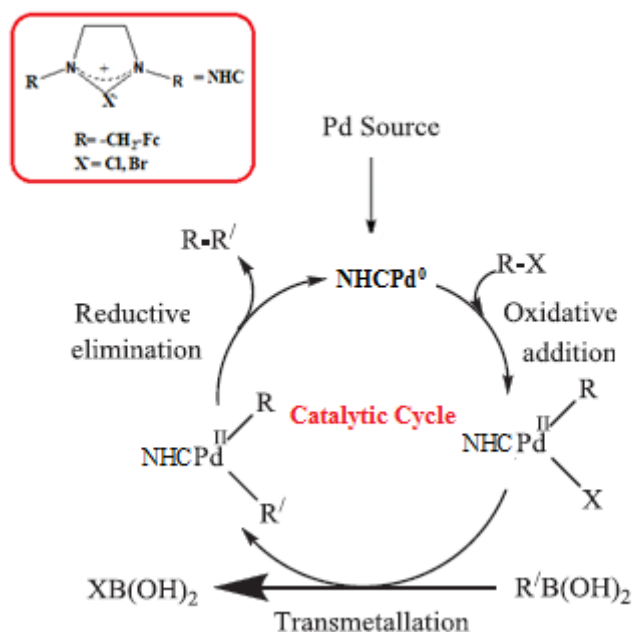
Entry <sup>a</sup>	R <sub>1</sub>	R <sub>2</sub>	Yield <sup>b,c</sup> (%)
1	H	CN	57
2	COCH <sub>3</sub>	H	50
3	CHO	H	46
4	H	H	13
5	OCH <sub>3</sub>	H	8
6	H	CH <sub>3</sub>	ND
7	CH <sub>3</sub>	H	ND
8	CF <sub>3</sub>	H	ND

a Reaction conditions:  $[Pd(O_2CCH_3)_2]$  (0.05 mmol), 1,3-bis(ferrocenylmethyl)imidazolium chloride (0.05 mmol), *p*-bromoacetophenone (1.0 mmol),  $C_6H_5B(OH)_2$  (1.5 mmol),  $K_2CO_3$  (2 mmol), and 1,4-Dioxane (2 mL), 24 h. ND: Not determined.

b Isolated yields based on aryl bromide.

c All reactions were monitored by TLC.

### Suzuki-Miyaura Cross Coupling Reaction Mechanism



**Scheme 2.** General mechanism of Suzuki reaction for Pd/NHC catalytic systems



#### 4. Conclusion

In summary, the in situ  $[Pd(O_2CCH_3)_2]$  / 1,3-bis(ferrocenylmethyl)imidazolium chloride catalyzed Suzuki reaction has been described. Optimum conditions were determined as 24 h, 80 °C,  $K_2CO_3$  as a base, dioxane as a solvent, and 1,3-bis(ferrocenylmethyl)imidazolium chloride as auxiliary ligand. Under these conditions, 2-bromobenzonitrile, *p*-bromoacetophenone, and *p*-bromobenzaldehyde react with phenylboronic acid in moderate yields of 57%, 50%, and 46%, respectively. While this catalytic system performed moderately in the Suzuki reaction, the results provide a good basis for studies targeting efficient catalyst activity.

#### Acknowledgement

This study was supported by Manisa Celal Bayar University Scientific Research Projects Coordination Unit. Project Number: 2015-168

#### Author's Contributions

**Mehmet Günaltay:** Performed the experiment.

**Hülya Avcı Özbek:** Performed the experiment and result analysis; and wrote the manuscript.

**Funda Demirhan:** Supervised the progress of the experiment, the interpretation of the results, drafted the manuscript.

#### Ethics

There are no ethical issues after the publication of this manuscript.

#### References

- [1]. Angoy, M, Jiménez MV, Lahoz FJ, Vispe, E, Pérez-Torrente JJ. 2022. Polymerization of phenylacetylene catalyzed by rhodium(I) complexes with N-functionalized N-heterocyclic carbene ligands. *Polymer Chemistry*; 13:1411-1421.
- [2]. Troiano, R, Costabile, C, Grisi, F. 2022. Alternating Ring-Opening Metathesis Polymerization Promoted by Ruthenium Catalysts Bearing Unsymmetrical NHC Ligands. *Catalysts*; 13: 34.
- [3]. Jayaraj, A, Raveedran, AV, Latha, AT, Priyadarshini, D, Ayya Swamy PC. 2023. Coordination Versatility of NHC-metal Topologies in Asymmetric Catalysis: Synthetic Insights and Recent Trends. *Coordination Chemistry Reviews*. 478:214922.
- [4]. Ye, Y, Liu Z, Wang, Y, Zhang, Y, Yin, F, He Q, Peng J, Tan K, Shen, Y. 2022. N-Indole-substituted N-heterocyclic carbene palladium precatalysts: Synthesis, characterization and catalytic cross-couplings. *Tetrahedron Letters*. 107:154125.
- [5]. Nair, PP, Jayaraj, A, Ayya Swamy PC. 2022. Recent Advances in Benzimidazole Based NHC-Metal Complex Catalyzed Cross-Coupling Reactions. *ChemistrySelect*. 7:e202103517.
- [6]. Anju, PJ, Neetha, M, Anilkumar, G. 2022. Recent Advances on N-Heterocyclic Carbene-Palladium catalyzed Heck Reaction *ChemistrySelect*. 7:e202103564.
- [7]. Bildstein, B, Malaun, M, Kopacka, H, Ongania, K, Wurst, K. 1998. Imidazoline-2-ylidene metal complexes with pendant ferrocenyl substituents. *Journal of Organometallic Chemistry*. 552:45-61.
- [8]. Bildstein, B, Malaun, M, Kopacka, H, Ongania, K, Wurst, K. 1999. N-Heterocyclic carbenes with N-ferrocenyl-N'-methyl-substitution: synthesis, reactivity, structure and electrochemistry. *Journal of Organometallic Chemistry*. 572:177-187.
- [9]. Bildstein, B, Malaun, M, Kopacka, H, Wurst, K, Mitterböck, M, Ongania, KH, Opromolla, G, Zanello, 1999. P. N,N'-Diferrocenyl-N-Heterocyclic carbenes and their derivatives. *Organometallics*.18:4325-4336.
- [10]. Siemeling, U. 2012. Singlet carbenes derived from ferrocene and closely related sandwich complex. *European Journal of Inorganic Chemistry*. 3523- 3536.
- [11]. Brogini, D, Togni, A. 2002. Synthesis and structure of an enantiomerically pure C2 symmetric ferrocenyl carbene. *Helvetica Chimica Acta*. 85: 2518-2522.
- [12]. Seo, H, Kim, BY, Lee, JH, Park, HJ, Son, SU, Chung, YK. 2003. Synthesis of chiral ferrocenyl imidazolium salts and their rhodium(I) and iridium(I) complexes. *Organometallics*. 22: 4783-4791.
- [13]. Gisching, S, Togni, A. 2005. Pd II complexes of tridentate PCP N-heterocyclic carbene ligands: structural aspects and application in asymmetric hydroamination of cyano olefins. *European Journal of Inorganic Chemistry*. 4745-4754.
- [14]. Willms, H, Frank, W, Ganter, C. 2008. Hybrid ligands with N-Heterocyclic carbene and chiral phosphaferrrocene components. *Chemistry-A European Journal*. 14: 2719-2729.
- [15]. Bertogg, A, Camponovo, F, Togni, A. 2004. N-Ferrocenyl-Substituted Planar-Chiral N-Heterocyclic Carbenes and Their Pd II Complexes. *European Journal of Inorganic Chemistry*. 691.
- [16]. Siemeling, U, Färber, C, Bruhn, C, Fürmeier, S, Schulz, T, Kurlemann, M, Tripp, S. 2010. Group 10 Metal Complexes of a Ferrocene-Based N-Heterocyclic Carbene: Syntheses, Structures and Catalytic Applications. *European Journal of Inorganic Chemistry*. 1413-1422.
- [17]. Soni, A, Sharma, C, Negi, L, Joshi, RK. 2023. NHC-Pd (II) full pincer catalyzed Mizoroki-Heck Type Cross-Coupling of Vinyl Chloride and Alkenes: Synthesis of Novel Ferrocenylated Conjugated Dienes. *Journal of Organometallic Chemistry*. 983: 122550.
- [18]. Pore, DM, Gaikwad, DS, Patil, JD. 2013. Ferrocene-tagged N-heterocyclic carbene-Pd complex for Suzuki-Miyaura coupling. *Monatsh Chemie*. 144:1355-1361.
- [19]. Kale, D, Rashinkar, G, Kumbhar, A, Salunkhe, R. 2017. Facile Suzuki-Miyaura cross coupling using ferrocene tethered N-heterocyclic carbene-Pd complex anchored on cellulose. *Reactive and Functional Polymers*. 116:9-16.
- [20]. Gaikwad, V, Kurane, R, Jadhav, J, Salunkhe, R, Rashinkar, G. 2013. A viable synthesis of ferrocene tethered NHC-Pd complex via supported ionic liquid phase catalyst and its Suzuki coupling activity. *Applied Catalysis A: General*. 451:243-250.
- [21]. Khanapure, S, Pore, D, Jagdale, M, Patil, V, Rashinka, G. 2021. Sustainable Synthesis of Biaryls Using Silica Supported Ferrocene Appended N-Heterocyclic Carbene-Palladium Complex. *Catalysis Letters*. 151:2237-2249.
- [22]. Shi, JC, Yang, PY, Tong, Q, Wu, Y, Peng, Y. 2006. Highly efficient and stable palladium/imidazolium salt-phosphine catalysts for Suzuki-Miyaura cross-coupling of aryl bromides. *Journal of Molecular Catalysis A: Chemical* 259:7-10.

[23]. Shi, JC, Yang, PY, Tong, Q, Jia, L. 2008. Palladium-catalyzed aminations of aryl halides with phosphine-functionalized imidazolium ligands *Dalton Transactions*. 938–945.

[24]. Yu, HW, Shi JC, Zhang, H, Yang, PY, Wang, XP, Jin, ZL. 2006. Unsymmetric-1,3-disubstituted imidazolium salt for palladium-catalyzed Suzuki–Miyaura cross-coupling reactions of aryl bromides. *Journal of Molecular Catalysis A: Chemical*. 250:15–19.

[25]. Dallas, A, Kultz, H, Farrell, A, Quilty, B, Nolan, K. 2007. Versatile reagents: ferrocenyl azolium compounds as auxiliary ligands for the Heck reaction and potential antifungal agents. *Tetrahedron Letters*. 48:1017–1021.

[26]. Musaoğlu, D, Avcı Özbek, H, Demirhan, F. 2023. Heck coupling reactions of aryl halides catalyzed by saturated ferrocenylmethylimidazolium salts/palladium. *Journal of the Iranian Chemical Society*. 20:637–643.

[27]. Avcı Özbek, H, Sözen Aktaş, P, Daran JC, Oskay, M, Demirhan, F, Çetinkaya.B. 2014. Synthesis, structure, electrochemical and antimicrobial properties of *N,N'*-bis(ferrocenylmethyl)imidazolium salts. *Inorganica Chimica Acta*. 42:435–442.

[28]. Huang, W, Guo, J, Xiao, Y, Zhu, M, Zou, G, Tang, J. 2005. Palladium–benzimidazolium salt catalyst systems for Suzuki coupling: development of a practical and highly active palladium catalyst system for coupling of aromatic halides with arylboronic acid. *Tetrahedron*. 61:9783–9790.

[29]. Liu, C, Zhang, Y, Liu, N, Qiu, J. 2012. A simple and efficient approach for the palladium-catalyzed ligand-free Suzuki reaction in water. *Green Chemistry*. 14:2999-3003.

[30]. Srinivas, K, Srinivas, P, Prathima, PS, Balaswamy, K, Sridhar, B, Rao, MM. 2012. *Catalysis Science & Technology*. 2:1180–1187.

## Supporting Information

### <sup>1</sup>H NMR Spectra for biaryl compounds

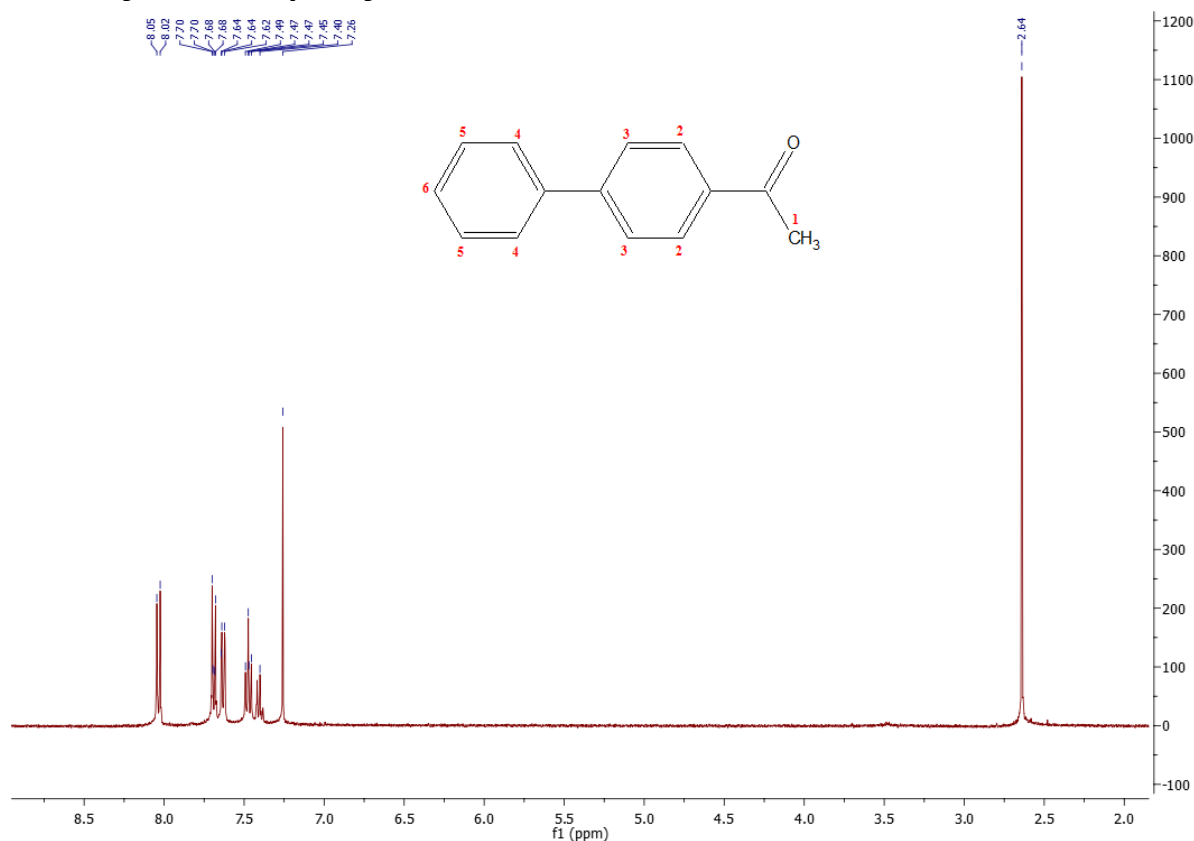


Figure S1. <sup>1</sup>H NMR spectra of 4-acetylbiphenyl

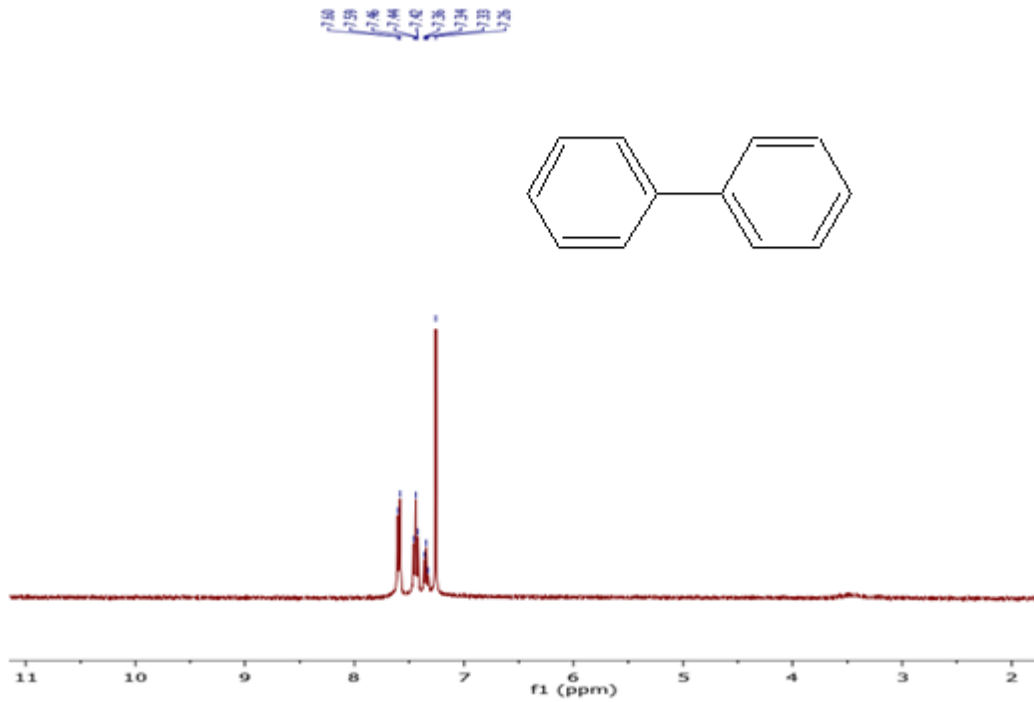


Figure S2. <sup>1</sup>H NMR spectra of biphenyl

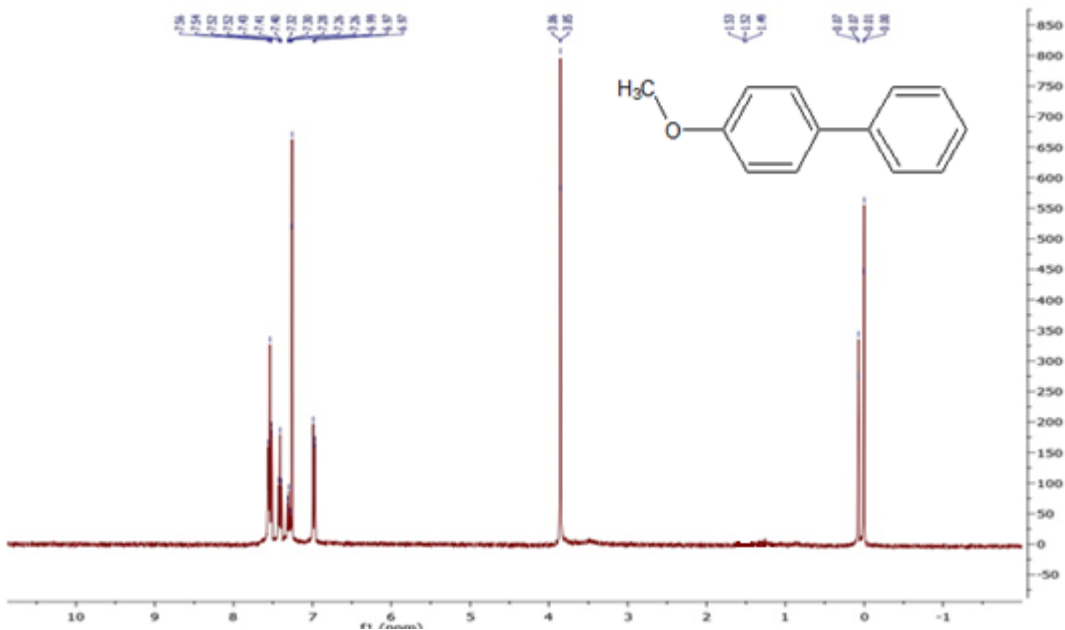


Figure S3. <sup>1</sup>H NMR spectra of 4-methoxybiphenyl

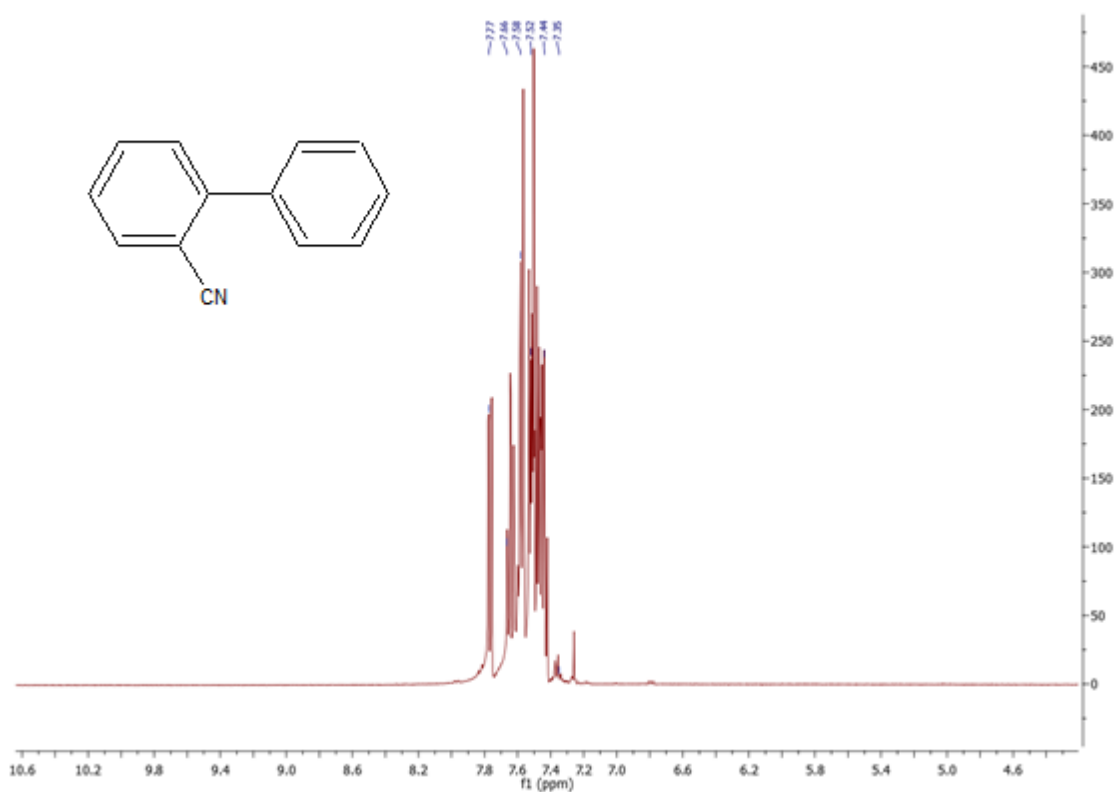


Figure S4. <sup>1</sup>H NMR spectra of biphenyl-2-carbonitrile

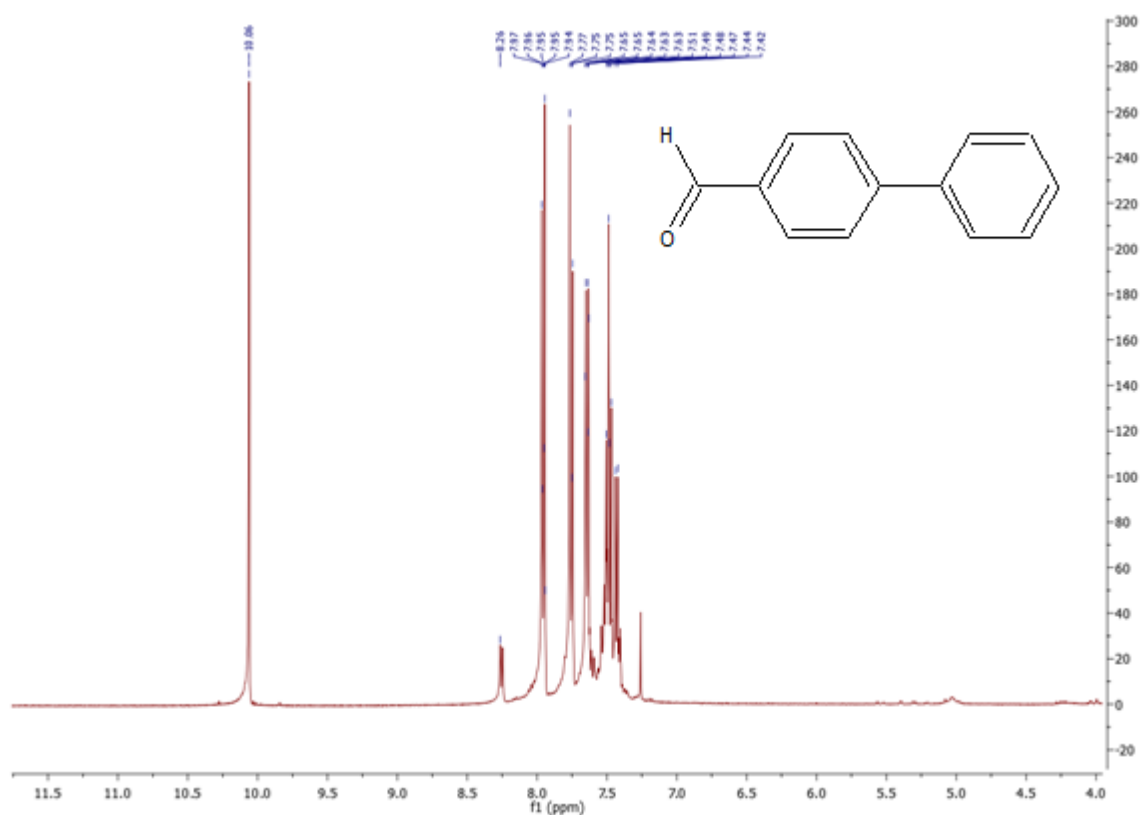


Figure S5. <sup>1</sup>H NMR spectra of biphenyl-4-carboxaldehyde

# A Study on the Solutions of (3 + 1) Conformal Time Derivative Generalized q-deformed Sinh-Gordon Equation

Yeşim Sağlam Özkan<sup>1\*</sup> 

<sup>1</sup> Department of Mathematics, Faculty of Arts and Sciences, Uludag University, Bursa, Türkiye

\*[ysaglam@uludag.edu.tr](mailto:ysaglam@uludag.edu.tr)

\*Orcid No: 0000-0002-1364-5137

Received: 13 March 2023

Accepted: 13 September 2023

DOI: 10.18466/cbayarfbe.1264314

## Abstract

This article is about examining the solutions of the (3 + 1) conformal time derivative generalized q-deformed Sinh-Gordon equation. The integration method used to reach the solutions of the equation is the generalized exponential rational function method. In this article, the process of examining the solutions goes step by step, first the basic steps of the proposed method are given, then the reduction of the equation is examined, and then the solutions are obtained by applying the method. The obtained wave solutions include hyperbolic soliton solutions. In addition, dark and bright solitons have been obtained. To perceive the physical phenomena, 2D and 3D graphical patterns of some of solutions obtained in this study are plotted by using Maple programming. The worked-out solutions ascertained that the suggested method is effectual, simple and direct.

**Keywords:** Conformal time derivative; The generalized exponential rational function method; The generalized q- deformed Sinh–Gordon equation.

## 1. Introduction

Fractional differential equations, which have attracted a lot of attention since they were discovered, have found many applications in fields such as physics, engineering, optics, biology, technology and so on. Theoretical models expressed in fractional analysis are more compatible with experimental data than models expressed in integer orders. When describing physical mechanical problems, the model expressed by fractional analysis has been revealed to have a clearer physical meaning and a simpler expression [1]. Thanks to these advantages, the models obtained using fractional order differentials attract a lot of attention, and researches and studies on this subject are increasing. Therefore, the solutions of these equations and the behavioral interpretations about them gain importance. Therefore, the solutions and behavioral interpretations of these equations gain importance. A soliton solution is a large amplitude, permanent pulse whose shape and velocity do not change due to collisions with other soliton waves, and is the exact solution of a nonlinear equation. The solitary wave was discovered experimentally by John Scott Russell in 1834. Optical solitons are a type of solitary wave that have the ability to propagate waves long distance without scattering, i.e. retain their shape over a long distance, and optical soliton models have

found use in solitary wave-based communication links, amplifiers, optical pulse compressors, fiber optics, and some other mechanisms. Since soliton theory has a wide application area, direct and indirect methods that provide exact solutions of nonlinear differential equations have been brought to the literature by scientists. Some of these methods are the Jacobi elliptic function method [2], the (G'/G) method [3], the Sardar subequation method [4], the exponential rational function method [5,6], the Bernoulli sub-ODE method [7], the Hirota bilinear method [8], the new extended direct algebraic method [9], the Cole-Hopf transformation method [10], the local fractional generalized-exp function method [11], Kudryashov and exponential methods [12, 13], the variational direct method [14] and so on.

The classical sinh-Gordon equation given as

$$u_{tt} - u_{xx} = \sinh u \quad (1.1)$$

is well-known equation and appears in integrable quantum field theory, kink dynamics, fluid dynamics, the propagation of fluxing in Josephson junctions (a junction between two superconductors), the motion of rigid pendulum attached to a stretched wire, and dislocations in crystals and in many other scientific

applications [15-18]. The generalized q-deformed Sinh-Gordon equation [19] described as

$$\frac{\partial^2 u}{\partial x^2} - \frac{\partial^2 u}{\partial t^2} = [\sinh_q(L^\theta)]^l - \omega. \quad (1.2)$$

Definitions and basic properties of q-calculus are reviewed by Victor and Pokman [20]. The q-deformed function which is introduced by Arai [21]. When this function is included in the dynamic system, the symmetry of the system and the solution is broken. Symmetry breaking [22] is a fundamental phenomenon in particle physics. In its most basic form, spontaneous symmetry breaking happens when a dynamical system's symmetry is not visible in its ground state or equilibrium state. Many classical and quantum systems have this property. Alrebdi et al. investigated the (2+1)-dimensional q-deformed Sinh-Gordon model given as [23]

$$\frac{\partial^2 u}{\partial x^2} + \frac{\partial^2 u}{\partial y^2} - \frac{\partial^2 u}{\partial t^2} = [\sinh_q(L^\theta)]^l - \omega \quad (1.3)$$

And the (G'/G, 1/G) expansion and sine-Gordon expansion methods are applied. The Sinh-Gordon equation with conformal time derivative generalized q-deformation has the following form:

$$\frac{\partial^2 u}{\partial x^2} - \frac{\partial^2 u}{\partial t^{2\beta}} = [\sinh_q(L^\theta)]^l - \omega \quad (1.4)$$

where  $\frac{\partial^\beta u}{\partial t^\beta}$  is the conformable derivative operator. The definition of conformable fractional derivative of order  $\beta \in (0, 1)$  [24] defined as

$$\frac{\partial^\beta f(t)}{\partial t^\beta} = \lim_{\epsilon \rightarrow 0} \frac{f(t+\epsilon t^{1-\beta}) - f(t)}{\epsilon}, f: (0, \infty) \rightarrow \mathbb{R} \quad (1.5)$$

Substituting  $\beta = 1$  in Eq. (1.4), Eq. (1.3) is obtained. In this study, we consider the three-dimensional conformal time derivative generalized q-deformed Sinh-Gordon equation [25] given as

$$\frac{\partial^2 L}{\partial x^2} + \frac{\partial^2 L}{\partial y^2} + \frac{\partial^2 L}{\partial z^2} - \frac{\partial^2 L}{\partial t^{2\beta}} = [\sinh_q(L^\theta)]^l - \omega \quad (1.6)$$

The proposed equation has expanded modeling possibilities for complex processes with broken symmetry. To obtain optical soliton solutions of (1.6) we utilized the generalized exponential rational function method which was introduced by Ghanbari and Inc [26] in 2018. This method, which was reduced to the "exponential rational function" method in a special case, has been used many times since then. The following studies can be considered for the efficiency and effectiveness of the method [27-33].

This paper is organized as follows: the second section is devoted to methodology. In the third section, the mathematical model is investigated. The fourth section contains the solutions. We provide several figures for solutions in the fifth section. We conclude in the last section.

## 2. Materials and Methods

### 2.1 The Generalized Exponential Rational Function Method (GERFM)

This section is devoted to explain the basic steps of GERFM. For this, consider the following partial differential equation (PDE)

$$P(u, u_t, u_x, u_{tt}, u_{xt}, \dots) = 0, \quad (2.1)$$

where  $P$  is a polynomial in dependent function  $u$  and its partial derivatives with respect to  $x$  and  $t$ . With the help of the traveling wave transformation  $u = u(\xi)$ ,  $\xi = k(x - ct)$ , where  $c$  is a constant, Eq. (2.1) is transformed to an ordinary differential equation (ODE)

$$Q(v, v', v'', \dots) = 0, \quad (2.2)$$

where  $(\cdot)' = \frac{d}{d\xi}(\cdot)$ .

**Step 1.** Exact solutions of the Eq. (2.2) can be constructed as [26, 34]:

$$v(\xi) = A_0 + \sum_{k=1}^N A_k \phi(\xi)^k + \sum_{k=1}^N B_k \phi(\xi)^{-k}, \quad (2.3)$$

where

$$\phi(\xi) = \frac{p_1 e^{q_1 \xi} + p_2 e^{q_2 \xi}}{p_3 e^{q_3 \xi} + p_4 e^{q_4 \xi}}. \quad (2.4)$$

Here  $p_1, \dots, p_4, q_1, \dots, q_4, A_0, A_k$  and  $B_k$  ( $k = 1, \dots, N$ ) are constants.

**Step 2.** The positive integer  $N$  is determined using the homogeneous balance principle.

**Step 3.** An algebraic equation  $T(\xi, e^{q_1 \xi}, e^{q_2 \xi}, e^{q_3 \xi}, e^{q_4 \xi}) = 0$  is obtained inserting Eq. (2.3) into Eq. (2.2) and arranging all terms.

**Step 4.** Equating coefficients of powers of  $T$  to zero, a system with respect to  $A_0, A_k$  and  $B_k$  and  $p_1, \dots, p_4, q_1, \dots, q_4$  is obtained.

**Step 5.** Using the obtained values with solving the set of equations by use of a computer program, the soliton solutions of Eq. (2.1) is found.

### 2.2 The Mathematical Model

We must reduce Eq. (1.6) to an ODE to examine the soliton solutions of this equation with the proposed method. For this, the following transformation should be used.

$$\begin{cases} L(x, y, z, t) = V(\xi), \\ \xi = \sigma x + \nu y + R z - \frac{\kappa}{\beta} t^\beta. \end{cases} \quad (2.5)$$

Here,  $\sigma, v, R$  constants and  $\kappa$  shows the speed of traveling wave. Using (2.5), Eq. (1.6) can be converted into:

$$(-\kappa^2 + v^2 + \sigma^2 + R^2)V'' + \omega - [\sinh_q(V^\theta)]^l = 0, \quad (2.6)$$

where  $(\cdot)' = \frac{d}{d\xi}$ . There are two cases according to choice of  $l, \theta, \omega$ .

**Case one:**  $l = \theta = 1, \omega = 0$ . Therefore, Eq. (2.6) can be written as:

$$(-\kappa^2 + v^2 + \sigma^2 + R^2)V'' - \sinh_q(V) = 0. \quad (2.7)$$

If both sides of the above equation are multiplied by  $V'$  and integrated with respect to  $\xi$  once, the following equation is obtained.

$$(-\kappa^2 + v^2 + \sigma^2 + R^2)(V'^2 - \cosh_q(V)) - 2M_1 = 0, \quad (2.8)$$

where  $M_1$  is the integration constant. Now, if the transformation  $V = \ln(u)$ ,  $u = u(\xi)$  is used, we get

$$(\kappa^2 - v^2 - \sigma^2 - R^2)u'^2 + 2M_1u' + Qu + u^3 = 0. \quad (2.9)$$

**Case two:**  $l = 2, \theta = 1, \omega = -\frac{Q}{2}$ . Eq. (2.6) can be rewritten as:

$$(-\kappa^2 + v^2 + \sigma^2 + R^2)V'' - (\sinh_q(V))^2 + \frac{Q}{2} = 0. \quad (2.10)$$

After simplifying Eq. (2.10) and using the transformation  $V = \frac{1}{2}\ln(u)$ , we get

$$2(-\kappa^2 + v^2 + \sigma^2 + R^2)u'^2 - 2(-\kappa^2 + v^2 + \sigma^2 + R^2)uu'' + Q^2u + u^3 = 0. \quad (2.11)$$

### 2.3 Application of GERFM to (2.9)

According to the homogeneous balance principle, it is clear to have  $2N + 2 = 3N, N = 2$ . Therefore, the solution can be written as follows:

$$u(\xi) = A_0 + A_1\phi(\xi) + \frac{B_1}{\phi(\xi)} + A_2\phi(\xi)^2 + \frac{B_2}{\phi(\xi)^2}. \quad (2.12)$$

Inserting (2.12) to (2.9), we obtain a system of algebraic equations made up of tedious and rather long equations. Solving this system with computer program, we get the following results:

**Group 1:**  $p_1 = -3, p_2 = -2, p_3 = 1, p_4 = 1$  and  $q_1 = 1, q_2 = 0, q_3 = 1, q_4 = 0$  provides:

$$\phi(\xi) = -\frac{5 + \sinh(\xi) + 5 \cosh(\xi)}{2(\cosh(\xi) + 1)} \quad (2.13)$$

**Set 1.1:**

$$\left\{ \begin{array}{l} A_0 = \frac{25}{4}A_2, A_1 = 5A_2, B_1 = B_2 = 0, \\ M_1 = -\frac{A_2}{4}, Q = \frac{A_2^2}{16}, \\ R = \frac{\sqrt{A_2 - 4\sigma^2 + 4\kappa^2 - 4v^2}}{2}. \end{array} \right\} \quad (2.14)$$

Placing values in Eqs. (2.12) and (2.13), yields the following solution

$$u_{1.1}(\xi) = \frac{(\cosh(\xi) - 1)A_2}{4(\cosh(\xi) + 1)}. \quad (2.15)$$

Then we get the following dark soliton solution of Eq. (1.6):

$$L_{1.1.1}(x, y, z, t) = \ln \left( \frac{(\cosh(\sigma x + v y + R z - \frac{\kappa t^\beta}{\beta}) - 1)A_2}{4(\cosh(\sigma x + v y + R z - \frac{\kappa t^\beta}{\beta}) + 1)} \right). \quad (2.16)$$

**Set 1.2:**

$$\left\{ \begin{array}{l} A_0 = \frac{25B_2}{144}, A_1 = A_2 = 0, B_1 = \frac{5}{6}B_2, \\ M_1 = -\frac{1}{144}B_2, Q = \frac{1}{20736}B_2^2, \\ R = \frac{\sqrt{-144v^2 + B_2 - 144\sigma^2 + 144\kappa^2}}{12}. \end{array} \right\} \quad (2.17)$$

Inserting these values into Eq. (2.12), we have:

$$u_{1.2}(\xi) = \frac{1}{144} \frac{B_2 (5 \sinh(\xi) - 12 + 13 \cosh(\xi))}{5 \sinh(\xi) + 12 + 13 \cosh(\xi)}. \quad (2.18)$$

Consequently, we get

$$L_{1.1.2}(x, y, z, t) = \ln \left( \frac{1}{144} B_2 \frac{5 \sinh(\sigma x + v y + R z - \frac{\kappa t^\beta}{\beta}) - 12 + 13 \cosh(\sigma x + v y + R z - \frac{\kappa t^\beta}{\beta})}{5 \sinh(\sigma x + v y + R z - \frac{\kappa t^\beta}{\beta}) + 12 + 13 \cosh(\sigma x + v y + R z - \frac{\kappa t^\beta}{\beta})} \right). \quad (2.19)$$

**Group 2:**  $p_1 = 2, p_2 = 0, p_3 = 1, p_4 = 1$  and  $q_1 = -1, q_2 = 0, q_3 = 1, q_4 = -1$  provides:

$$\phi = \frac{\cosh(\xi) - \sinh(\xi)}{\cosh(\xi)}. \quad (2.20)$$

**Set 2.1:**

$$\left\{ \begin{array}{l} A_0 = \sqrt{Q}, A_1 = -2\sqrt{Q}, A_2 = \sqrt{Q}, \\ B_1 = B_2 = 0, \\ M_1 = -\sqrt{Q}, R = \frac{\sqrt{\sqrt{Q} + 4\kappa^2 - 4\sigma^2 - 4v^2}}{2} \end{array} \right\} \quad (2.21)$$

The  $u(\xi)$  in (2.12) can be written as following

$$u_{2.1}(\xi) = \frac{\sqrt{Q}(\sinh(\xi))^2}{(\cosh(\xi))^2}. \quad (2.22)$$

Then we get the following solution of Eq. (1.6):

$$L_{12.1}(x, y, z, t) = \ln \left( \sqrt{Q} \frac{\left( \sinh \left( \sigma x + vy + Rz - \frac{\kappa t^\beta}{\beta} \right) \right)^2}{\left( \cosh \left( \sigma x + vy + Rz - \frac{\kappa t^\beta}{\beta} \right) \right)^2} \right). \quad (2.23)$$

**Group 3:**  $p_1 = -3, p_2 = -1, p_3 = 1, p_4 = 1$  and  $q_1 = 1, q_2 = -1, q_3 = 1, q_4 = -1$  provides:

$$\phi(\xi) = -\frac{2 \cosh(\xi) + \sinh(\xi)}{\cosh(\xi)}. \quad (2.24)$$

**Set 3.1:**

$$\left\{ \begin{array}{l} A_0 = \frac{4}{9} B_2, A_1 = 0, A_2 = 0, B_1 = \frac{4}{3} B_2, \\ M_1 = -\frac{1}{9} B_2, Q = \frac{1}{81} B_2^2, \\ R = \frac{\sqrt{-36 \sigma^2 - 36 v^2 + B_2 + 36 \kappa^2}}{6}. \end{array} \right\} \quad (2.25)$$

Inserting these values in Eqs. (2.12) and (2.24), we get

$$u_{3.1}(\xi) = \frac{B_2 (4 \cosh(\xi) \sinh(\xi) + 5 (\cosh(\xi))^2 - 4)}{9 (4 \cosh(\xi) \sinh(\xi) + 5 (\cosh(\xi))^2 - 1)}. \quad (2.26)$$

Then we get the following solution of Eq. (1.6):

$$L_{13.1}(x, y, z, t) = \ln \left( \frac{B_2 (4 \cosh(\xi) \sinh(\xi) + 5 (\cosh(\xi))^2 - 4)}{9 (4 \cosh(\xi) \sinh(\xi) + 5 (\cosh(\xi))^2 - 1)} \right), \quad (2.27)$$

where  $\xi = \sigma x + vy + Rz - \frac{\kappa t^\beta}{\beta}$ .

**Group 4:**  $p_1 = 1, p_2 = 1, p_3 = -1, p_4 = 1$  and  $q_1 = 1, q_2 = -1, q_3 = 1, q_4 = -1$  provides:

$$\phi(\xi) = -\frac{\cosh(\xi)}{\sinh(\xi)}. \quad (2.28)$$

**Set 4.1:**

$$\left\{ \begin{array}{l} A_0 = 8(-\kappa^2 + v^2 + \sigma^2 + R^2), \\ A_1 = 0, B_1 = 0, \\ A_2 = 4(v^2 + \sigma^2 + R^2 - \kappa^2), \\ M_1 = -16(v^2 + \sigma^2 + R^2 - \kappa^2), \\ B_2 = 4(v^2 + \sigma^2 + R^2 - \kappa^2), \\ Q = 512(-R^2 \kappa^2 + R^2 \sigma^2 - v^2 \kappa^2 \\ + v^2 \sigma^2 - \kappa^2 \sigma^2 + R^2 v^2) \\ + 256(\kappa^4 + \sigma^4 + R^4 + v^4). \end{array} \right\} \quad (2.29)$$

Placing values in (2.29) into Eq. (2.12) and using Eq. (2.28), we achieve

$$u_{4.1}(\xi) = \frac{4 (4 (\cosh(\xi))^4 - 4 (\cosh(\xi))^2 + 1) (-\kappa^2 + v^2 + \sigma^2 + R^2)}{\sinh(\xi)^2 \cosh(\xi)^2}. \quad (2.30)$$

Then we get the following solution of Eq. (1.6):

$$L_{14.1}(x, y, z, t) = \ln \left( \frac{4 (-\kappa^2 + v^2 + \sigma^2 + R^2) \left( 2 \cosh \left( \sigma x + vy + Rz - \frac{\kappa t^\beta}{\beta} \right) - 1 \right)^2}{\left( \sinh \left( \sigma x + vy + Rz - \frac{\kappa t^\beta}{\beta} \right) \right)^2 \left( \cosh \left( \sigma x + vy + Rz - \frac{\kappa t^\beta}{\beta} \right) \right)^2} \right). \quad (2.31)$$

where  $\xi = \sigma x + vy + Rz - \frac{\kappa t^\beta}{\beta}$ .

**Group 5:**  $p_1 = -1, p_2 = 3, p_3 = 1, p_4 = -1$  and  $q_1 = 1, q_2 = -1, q_3 = 1, q_4 = -1$  provides:

$$\phi(\xi) = \frac{\cosh(\xi) - 2 \sinh(\xi)}{\sinh(\xi)}. \quad (2.32)$$

**Set 5.1:**

$$\left\{ \begin{array}{l} A_0 = 4 A_2, A_1 = 4 A_2, B_1 = B_2 = 0, \\ M_1 = -A_2, Q = A_2^2, \\ R = \frac{\sqrt{A_2 - 4 \sigma^2 + 4 \kappa^2 - 4 v^2}}{2}. \end{array} \right\} \quad (2.33)$$

Inserting values in Eqs. (2.12) and (2.32), we have

$$u_{5.1}(\xi) = \frac{A_2 \cosh(\xi)^2}{\sinh(\xi)^2}. \quad (2.34)$$

Then we get the following bright soliton solution of Eq. (1.6):

$$L_{15.1}(x, y, z, t) = \ln \left( \frac{A_2 \left( \cosh \left( \sigma x + vy + Rz - \frac{\kappa t^\beta}{\beta} \right) \right)^2}{\left( \sinh \left( \sigma x + vy + Rz - \frac{\kappa t^\beta}{\beta} \right) \right)^2} \right). \quad (2.35)$$

**Set 5.2:**

$$\left\{ \begin{array}{l} A_0 = \frac{4}{9} B_2, A_1 = 0, A_2 = 0, B_1 = \frac{4 B_2}{3}, \\ M_1 = -\frac{1}{9} B_2, Q = \frac{1}{81} B_2^2, \\ R = \frac{\sqrt{-36 v^2 + 36 \kappa^2 + B_2 - 36 \sigma^2}}{6}. \end{array} \right\} \quad (2.36)$$

Placing values in Eq. (2.12) and Eq. (2.32), we obtain

$$u_{5.2}(\xi) = \frac{B_2 (-4 \cosh(\xi) \sinh(\xi) + 5 (\cosh(\xi))^2 - 1)}{9 (-4 \cosh(\xi) \sinh(\xi) + 5 (\cosh(\xi))^2 - 4)}. \quad (2.37)$$

Then we get the following solution of Eq. (1.6):

$$L_{15,2}(x, y, z, t) = \ln \left( \frac{B_2(-4 \cosh(\xi) \sinh(\xi) + 5(\cosh(\xi))^2 - 1)}{9(-4 \cosh(\xi) \sinh(\xi) + 5(\cosh(\xi))^2 - 4)} \right), \quad (2.38)$$

where  $\xi = \sigma x + \nu y + Rz - \frac{\kappa t^\beta}{\beta}$ .

**Group 6:**  $p_1 = 1, p_2 = 2, p_3 = 1, p_4 = 1$  and  $q_1 = -1, q_2 = 1, q_3 = -1, q_4 = 1$  provides:

$$\phi(\xi) = \frac{3 \cosh(\xi) + \sinh(\xi)}{2 \cosh(\xi)}. \quad (2.39)$$

**Set 6.1:**

$$\left\{ \begin{array}{l} A_0 = \frac{9B_2}{16}, A_1 = A_2 = 0, B_1 = -\frac{3B_2}{2}, \\ M_1 = -\frac{1}{16} B_2, Q = \frac{1}{256} B_2^2, \\ R = \frac{\sqrt{-64 \sigma^2 + B_2 + 64 \kappa^2 - 64 \nu^2}}{8}. \end{array} \right\} \quad (2.40)$$

Putting these results in Eqs. (2.12) and (2.39) leads to

$$u_{6,1}(\xi) = \frac{B_2(6 \cosh(\xi) \sinh(\xi) + 10(\cosh(\xi))^2 - 9)}{16(6 \cosh(\xi) \sinh(\xi) + 10(\cosh(\xi))^2 - 1)}. \quad (2.41)$$

Then we get the following solution of Eq. (1.6):

$$L_{16,1}(x, y, z, t) = \ln \left( \frac{B_2(6 \cosh(\xi) \sinh(\xi) + 10(\cosh(\xi))^2 - 9)}{16(6 \cosh(\xi) \sinh(\xi) + 10(\cosh(\xi))^2 - 1)} \right), \quad (2.42)$$

where  $\xi = \sigma x + \nu y + Rz - \frac{\kappa t^\beta}{\beta}$ .

**Group 7:**  $p_1 = -1, p_2 = 0, p_3 = 1, p_4 = 1$  and  $q_1 = 0, q_2 = 0, q_3 = 0, q_4 = 1$  provides:

$$\phi(\xi) = -(1 + \cosh(\xi) + \sinh(\xi))^{-1} \quad (2.43)$$

**Set 7.1:**

$$\left\{ \begin{array}{l} A_0 = -\kappa^2 + \nu^2 + \sigma^2 + R^2, \\ A_1 = 4R^2 - 4\kappa^2 + 4\nu^2 + 4\sigma^2, \\ A_2 = 4R^2 - 4\kappa^2 + 4\nu^2 + 4\sigma^2, \\ B_1 = 0, B_2 = 0, \\ M_1 = \kappa^2 - \nu^2 - \sigma^2 - R^2, \\ Q = R^4 + 2R^2\nu^2 + 2R^2\sigma^2 \\ -2\kappa^2\nu^2 - 2R^2\kappa^2 + 2\nu^2\sigma^2 + \kappa^4 + \\ + \nu^4 - 2\kappa^2\sigma^2 + \sigma^4. \end{array} \right\} \quad (2.44)$$

Substituting these results into Eq. (2.12) and (2.43), we get

$$u_{7,1}(\xi) = \frac{(-1 + \cosh(\xi))(-\kappa^2 + \nu^2 + \sigma^2 + R^2)}{1 + \cosh(\xi)}. \quad (2.45)$$

Then we get the following solution of Eq. (1.6):

$$L_{17,1}(x, y, z, t) = \ln \left( \frac{(-\kappa^2 + \nu^2 + \sigma^2 + R^2) \left( -1 + \cosh \left( \sigma x + \nu y + Rz - \frac{\kappa t^\beta}{\beta} \right) \right)}{1 + \cosh \left( \sigma x + \nu y + Rz - \frac{\kappa t^\beta}{\beta} \right)} \right). \quad (2.46)$$

**Group 8:**  $p_1 = -2, p_2 = -1, p_3 = 1, p_4 = 1$  and  $q_1 = 0, q_2 = 1, q_3 = 0, q_4 = 1$  provides:

$$\phi(\xi) = -\frac{3 - \sinh(\xi) + 3 \cosh(\xi)}{2(1 + \cosh(\xi))}. \quad (2.47)$$

**Set 8.1:**

$$\left\{ \begin{array}{l} A_0 = \frac{9B_2}{16}, A_1 = 0, A_2 = 0, B_1 = \frac{3B_2}{2}, \\ M_1 = -\frac{1}{16} B_2, Q = \frac{1}{256} B_2^2, \\ R = \frac{\sqrt{16 \kappa^2 + B_2 - 16 \nu^2 - 16 \sigma^2}}{4}. \end{array} \right\} \quad (2.48)$$

Substituting these results into Eq. (2.12) and (2.47), we obtain

$$u_{8,1}(\xi) = \frac{B_2(-3 \sinh(\xi) - 4 + 5 \cosh(\xi))}{16(-3 \sinh(\xi) + 5 \cosh(\xi) + 4)}. \quad (2.49)$$

Then we get the following solution of Eq. (1.6):

$$L_{18,1}(x, y, z, t) = \ln \left( \frac{B_2(-3 \sinh(\xi) - 4 + 5 \cosh(\xi))}{16(-3 \sinh(\xi) + 5 \cosh(\xi) + 4)} \right). \quad (2.50)$$

where  $\xi = \sigma x + \nu y + Rz - \frac{\kappa t^\beta}{\beta}$ .

## 2.4 Application of GERFM to (2.11)

According to the homogeneous balance principle, it is clear to have  $2N + 2 = 3N, N = 2$  for (2.11). Therefore, the solution can be written as follows:

$$w(\xi) = A_0 + A_1 \phi(\xi) + \frac{B_1}{\phi(\xi)} + A_2 \phi(\xi)^2 + \frac{B_2}{\phi(\xi)^2}. \quad (2.51)$$

Inserting (2.51) to (2.11), we obtain a system of algebraic equations made up of tedious and rather long equations. Solving this system with computer program, we get the following results:

Using the values in Group 1 and (2.13) for Eq. (2.11), we have

**Set 1.1:**

$$\left\{ \begin{array}{l} A_0 = \frac{25A_2}{4}, A_1 = 5A_2, B_1 = 0, \\ B_2 = 0, Q = \frac{1}{4} i A_2, \\ R = 1/2 \sqrt{4 \kappa^2 - 4 \nu^2 - 4 \sigma^2 + A_2}. \end{array} \right\} \quad (2.52)$$

Placing values in Eqs. (2.51) and (2.13), yields the following solution

$$w_{1.1}(\xi) = \frac{1}{4} \frac{(\cosh(\xi)-1)A_2}{\cosh(\xi)+1}. \quad (2.53)$$

Then we get the following solution of Eq. (1.6):

$$L_{2,1.1}(x, y, z, t) = \frac{1}{2} \ln \left( \frac{\cosh\left(\sigma x + \nu y + Rz - \frac{\kappa t^\beta}{\beta}\right) - 1}{\cosh\left(\sigma x + \nu y + Rz - \frac{\kappa t^\beta}{\beta}\right) + 1} \frac{A_2}{4} \right). \quad (2.54)$$

**Set 1.2:**

$$\left\{ \begin{array}{l} A_0 = \frac{25}{144} B_2, A_1 = 0, A_2 = 0, \\ B_1 = \frac{5}{6} B_2, B_2 = B_2, Q = \frac{1}{144} i B_2, \\ R = \frac{\sqrt{B_2 - 144 v^2 - 144 \sigma^2 + 144 \kappa^2}}{12}. \end{array} \right\} \quad (2.55)$$

Placing values in Eqs. (2.51) and (2.13), yields the following solution

$$w_{1.2}(\xi) = \frac{1}{144} \frac{B_2 (5 \sinh(\xi) - 12 + 13 \cosh(\xi))}{5 \sinh(\xi) + 12 + 13 \cosh(\xi)}. \quad (2.56)$$

Then we get the following solution of Eq. (1.6):

$$L_{2,1.2}(x, y, z, t) = \frac{1}{2} \ln \left( \frac{1}{144} B_2 \frac{(5 \sinh(\xi) - 12 + 13 \cosh(\xi))}{(5 \sinh(\xi) + 12 + 13 \cosh(\xi))} \right) \quad (2.57)$$

where  $\xi = \sigma x + \nu y + Rz - \frac{\kappa t^\beta}{\beta}$ .

Using the values in Group 2 and (2.20) for Eq. (2.11), we have

**Set 2.1:**

$$\left\{ \begin{array}{l} A_0 = iQ, A_1 = -2 iQ, A_2 = iQ, \\ B_1 = 0, B_2 = 0, \\ R = \frac{1}{2} \sqrt{iQ - 4 \sigma^2 - 4 v^2 + 4 \kappa^2} \end{array} \right\} \quad (2.58)$$

Placing values in Eqs. (2.51) and (2.20), yields the following solution

$$w_{2.1}(\xi) = \frac{iQ(\sinh(\xi))^2}{(\cosh(\xi))^2}. \quad (2.59)$$

Then we get the following solution of Eq. (1.6):

$$L_{2,2.1}(x, y, z, t) = \frac{1}{2} \ln \left( \frac{iQ \left( \sinh\left(\sigma x + \nu y + Rz - \frac{\kappa t^\beta}{\beta}\right) \right)^2}{\left( \cosh\left(\sigma x + \nu y + Rz - \frac{\kappa t^\beta}{\beta}\right) \right)^2} \right). \quad (2.60)$$

Using the values in Group 3 and (2.24) for Eq. (2.11), we have

**Set 3.1:**

$$\left\{ \begin{array}{l} A_0 = A_1, A_2 = \frac{1}{4} A_1, B_1 = 0, \\ B_2 = 0, Q = \frac{1}{4} i A_1, \\ R = \frac{\sqrt{16 \kappa^2 + A_1 - 16 v^2 - 16 \sigma^2}}{4}. \end{array} \right\} \quad (2.61)$$

Placing values in Eqs. (2.51) and (2.24), yields the following solution

$$w_{3.1}(\xi) = \frac{A_1 (\sinh(\xi))^2}{4(\cosh(\xi))^2}. \quad (2.62)$$

Then we get the following solution of Eq. (1.6):

$$L_{2,3.1}(x, y, z, t) = \frac{1}{2} \ln \left( \frac{1}{4} A_1 \frac{\left( \sinh\left(\sigma x + \nu y + Rz - \frac{\kappa t^\beta}{\beta}\right) \right)^2}{\left( \cosh\left(\sigma x + \nu y + Rz - \frac{\kappa t^\beta}{\beta}\right) \right)^2} \right). \quad (2.63)$$

Using the values in Group 5 and (2.32) for Eq. (2.11), we have

**Set 5.1:**

$$\left\{ \begin{array}{l} A_0 = A_1, A_2 = \frac{1}{4} A_1, \\ B_1 = 0, B_2 = 0, Q = \frac{1}{4} i A_1, \\ R = \frac{\sqrt{-16 v^2 + A_1 + 16 \kappa^2 - 16 \sigma^2}}{4}. \end{array} \right\} \quad (2.64)$$

Placing values in Eqs. (2.51) and (2.32), yields the following solution

$$w_{5.1}(\xi) = \frac{A_1 (\cosh(\xi))^2}{4(\sinh(\xi))^2}. \quad (2.65)$$

Then we get the following solution of Eq. (1.6):

$$L_{2,5.1}(x, y, z, t) = \frac{1}{2} \ln \left( \frac{A_1}{4} \frac{\cosh\left(\sigma x + \nu y + Rz - \frac{\kappa t^\beta}{\beta}\right)}{\sinh\left(\sigma x + \nu y + Rz - \frac{\kappa t^\beta}{\beta}\right)} \right). \quad (2.66)$$

**Set 5.2:**

$$\left\{ \begin{array}{l} A_0 = \frac{4}{9} B_2, A_1 = 0, A_2 = 0, \\ B_1 = \frac{4}{3} B_2, Q = \frac{1}{9} i B_2, \\ R = \frac{\sqrt{36 \kappa^2 + B_2 - 36 \sigma^2 - 36 v^2}}{6}. \end{array} \right\} \quad (2.67)$$

Placing values in Eqs. (2.51) and (2.32), yields the following solution

$$w_{5.2}(\xi) = \frac{1}{9} \frac{B_2 (-4 \cosh(\xi) \sinh(\xi) + 5 (\cosh(\xi))^2 - 1)}{-4 \cosh(\xi) \sinh(\xi) + 5 (\cosh(\xi))^2 - 4}. \quad (2.68)$$

Then we get the following solution of Eq. (1.6):

$$L_{2_{5.2}}(x, y, z, t) = \frac{1}{2} \ln \left( \frac{B_2}{9} \frac{-4 \cosh(\xi) \sinh(\xi) + 5 (\cosh(\xi))^2 - 1}{-4 \cosh(\xi) \sinh(\xi) + 5 (\cosh(\xi))^2 - 4} \right). \quad (2.69)$$

where  $\xi = \sigma x + \nu y + Rz - \frac{\kappa t^\beta}{\beta}$ .

Using the values in Group 6 and (2.39) for Eq. (2.11), we have

**Set 6.1:**

$$\left\{ \begin{array}{l} A_0 = \frac{9}{4} A_2, A_1 = -3 A_2, B_1 = 0, \\ B_2 = 0, Q = \frac{1}{4} i A_2, \\ R = \frac{\sqrt{A_2 - 16 \sigma^2 + 16 \kappa^2 - 16 \nu^2}}{4}. \end{array} \right\} \quad (2.70)$$

Placing values in Eqs. (2.51) and (2.39), yields the following solution

$$w_{6.1}(\xi) = \frac{1}{4} \frac{A_2 (\sinh(\xi))^2}{(\cosh(\xi))^2}. \quad (2.71)$$

Then we get the following solution of Eq. (1.6):

$$L_{2_{6.1}}(x, y, z, t) = \frac{1}{2} \ln \left( \frac{1}{4} A_2 \frac{\sinh \left( \sigma x + \nu y + Rz - \frac{\kappa t^\beta}{\beta} \right)^2}{\cosh \left( \sigma x + \nu y + Rz - \frac{\kappa t^\beta}{\beta} \right)^2} \right). \quad (2.72)$$

Using the values in Group 7 and (2.43) for Eq. (2.11), we have

**Set 7.1:**

$$\left\{ \begin{array}{l} A_0 = -\kappa^2 + \nu^2 + \sigma^2 + R^2, \\ A_1 = 4 \sigma^2 - 4 \kappa^2 + 4 \nu^2 + 4 R^2, \\ A_2 = 4 \sigma^2 - 4 \kappa^2 + 4 \nu^2 + 4 R^2, \\ B_1 = 0, B_2 = 0, \\ Q = i(-\kappa^2 + \nu^2 + \sigma^2 + R^2). \end{array} \right\} \quad (2.73)$$

### 3. Results and Discussion

#### 3.1 Graphical Illustrations

In this section, we show two-dimensional and three-dimensional drawings for some solutions obtained by assigning appropriate values to the parameters, to help clarify the solutions we presented. In Figure 1, 3D plots of the solution  $L_{1_{1.1}}$  (2.16) with the parameters  $A_2 = 0.4, R = 0.2, \nu = 0.1, \kappa = 0.2, \sigma = 0.3, \beta = 0.5, y = 1$  for different times, namely  $t = 1, 15, 25$ , is given. If the 3D graph is examined, the movement of the wave over time can be observed. Figure 2 shows that the density plot of  $L_{1_{1.1}}$  (2.16) with  $A_2 = 0.4, R = 0.2, \nu = 0.1, \kappa = 0.2, \sigma = 0.3, \beta = 0.5, y = 1$  for  $t = 1$ . In Figure 3, 2D

Placing values in Eqs. (2.51) and (2.43), yields the following solution

$$w_{7.1}(\xi) = \frac{(\cosh(\xi)-1)(-\kappa^2 + \nu^2 + \sigma^2 + R^2)}{1 + \cosh(\xi)}. \quad (2.74)$$

Then we get the following solution of Eq. (1.6):

$$L_{2_{7.1}}(x, y, z, t) = \ln \left( \frac{(-\kappa^2 + \nu^2 + \sigma^2 + R^2) (\cosh \left( \sigma x + \nu y + Rz - \frac{\kappa t^\beta}{\beta} \right) - 1)}{1 + \cosh \left( \sigma x + \nu y + Rz - \frac{\kappa t^\beta}{\beta} \right)} \right). \quad (2.75)$$

Using the values in Group 8 and (2.47) for Eq. (2.11), we have

**Set 8.1:**

$$\left\{ \begin{array}{l} A_0 = \frac{9}{16} B_2, A_1 = 0, A_2 = 0, \\ B_1 = \frac{3}{2} B_2, B_2 = B_2, Q = \frac{1}{16} i B_2, \\ R = \frac{\sqrt{-16 \sigma^2 + B_2 - 16 \nu^2 + 16 \kappa^2}}{4}. \end{array} \right\} \quad (2.76)$$

Placing values in Eqs. (2.51) and (2.47), yields the following solution

$$w_{8.1}(\xi) = 1/16 \frac{B_2 (-3 \sinh(\xi) - 4 + 5 \cosh(\xi))}{-3 \sinh(\xi) + 5 \cosh(\xi) + 4}. \quad (2.77)$$

Then we get the following solution of Eq. (1.6):

$$L_{2_{8.1}}(x, y, z, t) = \ln \left( \frac{B_2 (-3 \sinh(\xi) - 4 + 5 \cosh(\xi))}{16 (-3 \sinh(\xi) + 5 \cosh(\xi) + 4)} \right). \quad (2.78)$$

where  $\xi = \sigma x + \nu y + Rz - \frac{\kappa t^\beta}{\beta}$ .

plot of the solution  $L_{1_{1.1}}$  (2.16) at  $A_2 = 0.4, R = 0.2, \nu = 0.1, \kappa = 0.2, \sigma = 0.3, t = 1, y = 1, x = 1$ . While drawing this 2D graph, different values of the  $\beta$  which is the conformable derivative's order were taken into account. In Figure 4, 3D and density plots of  $L_{1_{5.1}}$  (2.35) with  $A_2 = 0.2, R = 0.15, \nu = 0.2, \kappa = 0.3, \sigma = 0.5, t = 1, y = 1$  for  $\beta = 0.15$  are given, respectively. Figure 5 demonstrate that 2D plot of  $L_{1_{5.1}}$  (2.35) with  $A_2 = 0.2, R = 0.15, \nu = 0.2, \kappa = 0.3, \sigma = 0.5, t = 1, y = 1, x = 1$  for different values of  $\beta$ .

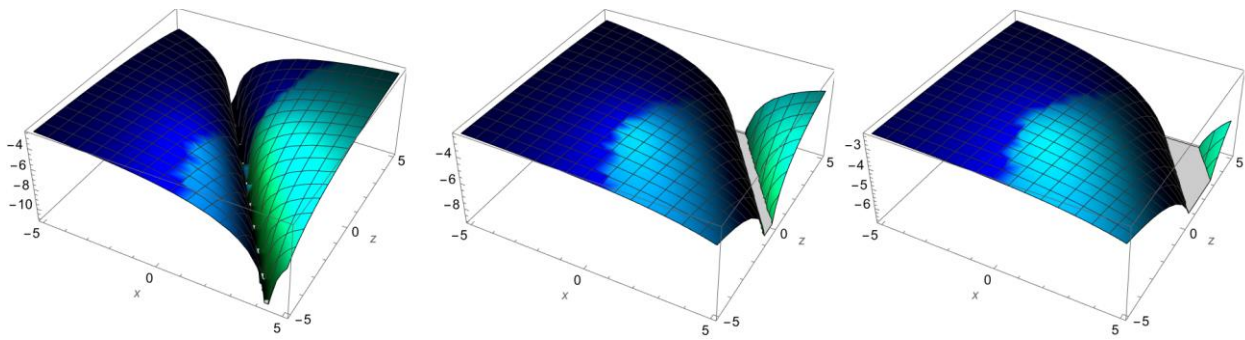


**Figure 1.** 3D plots of  $L_{1,1,1}$  (2.16) with  $A_2 = 0.4, R = 0.2, v = 0.1, \kappa = 0.2, \sigma = 0.3, \beta = 0.5, y = 1$  for  $t = 1, 15, 25$ , respectively.

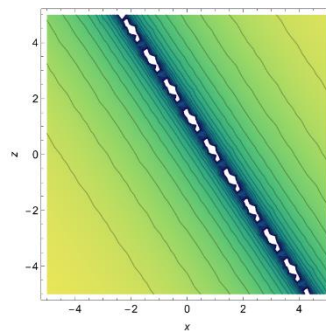


**Figure 2.** Density plot of  $L_{1,1,1}$  (2.16) with  $A_2 = 0.4, R = 0.2, v = 0.1, \kappa = 0.2, \sigma = 0.3, \beta = 0.5, y = 1$  for  $t = 1$ .

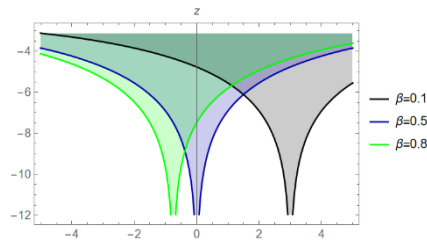


**Figure 3.** 2D plot of  $L_{1,1,1}$  (2.16) with  $A_2 = 0.4, R = 0.2, v = 0.1, \kappa = 0.2, \sigma = 0.3, t = 1, y = 1, x = 1$  for  $\beta = 0.1, 0.5, 0.8$ .

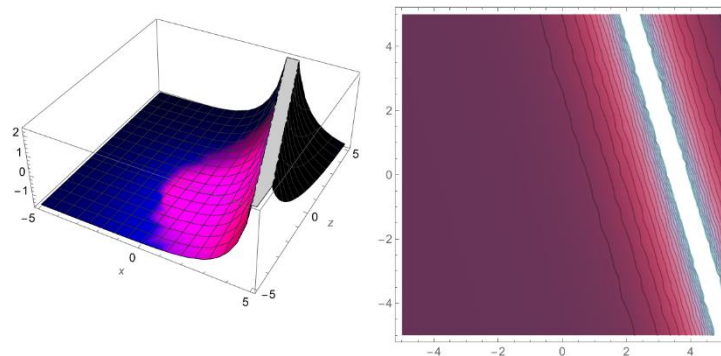


**Figure 4.** 3D and density plots of  $L_{1,5,1}$  (2.35) with  $A_2 = 0.2, R = 0.15, v = 0.2, \kappa = 0.3, \sigma = 0.5, t = 1, y = 1$  for  $\beta = 0.15$ , respectively.

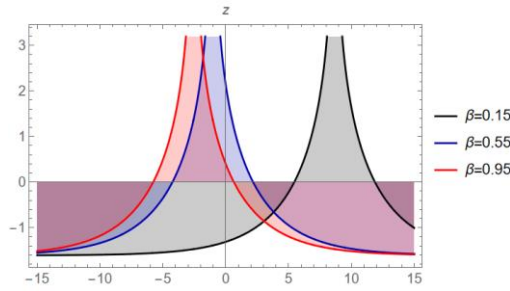


**Figure 5.** 2D plot of  $L_{1,5,1}$  (2.35) with  $A_2 = 0.2, R = 0.15, v = 0.2, \kappa = 0.3, \sigma = 0.5, t = 1, y = 1, x = 1$  for  $\beta = 0.15, 0.55, 0.95$ , respectively.

### 3.2 Comparison

In this section, we compare our performed solutions with Ali et al. [25], results for Eq. (2.6) for case one. Wherein Ali et al. [25] considered the (3 + 1)

conformal time derivative generalized q-deformed Sinh-Gordon equation by using  $G'/G$  expansion method. The comparison is ascertained as follows

**Table 1.** Comparison of solutions

Ali et al. [25]	Our solution
For $H_0 = -\frac{\sqrt{q}\sigma^2}{\sqrt{(\sigma^2-4v)^2}}, H_1 = -\frac{4\sqrt{q}\sigma}{\sqrt{(\sigma^2-4v)^2}},$ $H_2 = -\frac{4\sqrt{q}}{\sqrt{(\sigma^2-4v)^2}}, Y = \pm \sqrt{\kappa^2 - \frac{\sqrt{q}}{\sqrt{(\sigma^2-4v)^2}} - v^2 - \rho^2},$ $M_1 = \frac{\sqrt{q}(\sigma^2-4v)}{\sqrt{(\sigma^2-4v)^2}}$ and $\sigma^2 - 4v > 0$ the solution is	For $A_0 = \sqrt{Q}, A_1 = -2\sqrt{Q}, A_2 = \sqrt{Q}, B_1 = B_2 = 0,$ $M_1 = -\sqrt{Q}, R = \frac{\sqrt{\sqrt{Q}+4} \kappa^2 - 4 \sigma^2 - 4 v^2}{2}$ the solution is
$L_{1,2}(x, y, z, \tau) = \ln(H_0 + H_1 \left( \frac{-\sigma}{2} + \frac{1}{2} \sqrt{\sigma^2 - 4v} \frac{g_1 \sinh \frac{1}{2} \sqrt{\sigma^2 - 4v} \zeta + g_2 \cosh \frac{1}{2} \sqrt{\sigma^2 - 4v} \zeta}{g_1 \cosh \frac{1}{2} \sqrt{\sigma^2 - 4v} \zeta + g_2 \sinh \frac{1}{2} \sqrt{\sigma^2 - 4v} \zeta} \right) + H_2 \left( \frac{-\sigma}{2} + \frac{1}{2} \sqrt{\sigma^2 - 4v} \frac{g_1 \sinh \frac{1}{2} \sqrt{\sigma^2 - 4v} \zeta + g_2 \cosh \frac{1}{2} \sqrt{\sigma^2 - 4v} \zeta}{g_1 \cosh \frac{1}{2} \sqrt{\sigma^2 - 4v} \zeta + g_2 \sinh \frac{1}{2} \sqrt{\sigma^2 - 4v} \zeta} \right)^2$	$L_{1,2,1}(x, y, z, t) = \ln \left( \frac{\sqrt{Q} \left( \frac{\sinh \left( \sigma x + vy + Rz - \frac{\kappa t^\beta}{\beta} \right)}{\cosh \left( \sigma x + vy + Rz - \frac{\kappa t^\beta}{\beta} \right)} \right)^2}{\left( \cosh \left( \sigma x + vy + Rz - \frac{\kappa t^\beta}{\beta} \right) \right)^2} \right)$

When the solution obtained in [25] and the solution obtained in this study are compared, it is seen that the solutions are structurally similar if the parameters are

selected appropriately. When other solutions are compared, it is seen that different solutions are obtained thanks to the method applied in this study.

### 4. Conclusions

In this paper, soliton solutions of the (3 + 1) conformal time derivative generalized q-deformed Sinh-Gordon equation are constructed using the generalized exponential rational function approach. The equation containing both the conformal time derivative and the generalized q-deformation was first converted to an ordinary differential equation. The GERFM, whose effectiveness and power has been proven by many studies, has been applied to the obtained ordinary differential equation and solutions have been found. Thus, the solutions of the original equation were obtained.

These solutions are soliton solutions that have the extraordinary property of maintaining their uniformity in interaction with others. 3D and 2D drawings are given for some analytical solutions to show more features for the proposed model. The analytical solutions allow graphing soliton solutions of type dark and bright. In addition, the effectiveness of the applied method was emphasized with the Comparison section. We hope that the results obtained will be a guide for future research.

## Author's Contributions

**Yeşim Sağlam Özkan:** Drafted and wrote the manuscript, performed the experiment and result analysis.

## Ethics

There are no ethical issues after the publication of this manuscript.

## References

- [1]. Kurt, A. 2020. New analytical and numerical results for fractional Bogoyavlensky-Konopelchenko equation arising in fluid dynamics. *Applied Mathematics-A Journal of Chinese Universities*; 35, 101-112.
- [2]. Wei, CC, Tian B, Yang, DY, Liu, SH. 2023. Jacobian-elliptic-function and rogue-periodic-wave solutions of a high-order nonlinear Schrödinger equation in an inhomogeneous optical fiber. *Chin. J. Phys.*; 81, 354-361.
- [3]. Poonia, M, Singh, K. 2023. Exact solutions of nonlinear dynamics of microtubules equation using the methods of first integral and (G'/G) expansion. *Asian-Eur. J. Math.*; 16(01), 2350007.
- [4]. Younas, U, Baber, MZ, Yasin, MW, Sulaiman, TA, Ren, J. 2022. The generalized higher-order nonlinear Schrödinger equation: optical solitons and other solutions in fiber optics. *Int. J. Mod. Phys. B*; 2350174.
- [5]. Tarla, S, Ali, KK, Yilmazer, R, Osman, MS. 2022. On dynamical behavior for optical solitons sustained by the perturbed Chen-Lee-Liu model. *Communications in Theoretical Physics*; 74(7), 075005.
- [6]. Iqbal, MS, Seadawy, AR, Baber, MZ, Qasim, M. 2022. Application of modified exponential rational function method to Jaulent-Miodek system leading to exact classical solutions. *Chaos, Solitons & Fractals*; 164, 112600.
- [7]. Taghizadeh, N, Akbari, M, Esmaelnejhad, P. 2017. Application of Bernoulli sub-ODE method for finding travelling wave solutions of Schrodinger equation power law nonlinearity. *Applications and Applied Mathematics: An International Journal (AAM)*; 12(1), 38.
- [8]. Li, L, Yu, F, Duan, C. 2020. A generalized nonlocal Gross-Pitaevskii (NGP) equation with an arbitrary time-dependent linear potential. *Applied Mathematics Letters*; 110, 106584.
- [9]. Younas, U, Sulaiman, TA, Ren, J. 2022. Dynamics of optical pulses in fiber optics with stimulated Raman scattering effect. *International Journal of Modern Physics B*; 2350080.
- [10]. Salas, AH, Gomez S, CA. 2010. Application of the Cole-Hopf transformation for finding exact solutions to several forms of the seventh-order KdV equation. *Mathematical Problems in Engineering*; 2010.
- [11]. San, S, Seadawy, AR, Yasar, E. 2022. Optical soliton solution analysis for the (2+ 1) dimensional Kundu-Mukherjee-Naskar model with local fractional derivatives. *Optical and Quantum Electronics*; 54(7), 442.
- [12]. Hosseini, K, Mirzazadeh, M, Akinyemi, L, Baleanu, D, Salahshour, S. 2022. Optical solitons to the Ginzburg-Landau equation including the parabolic nonlinearity. *Optical and Quantum Electronics*; 54(10), 631.
- [13]. Hosseini, K, Mirzazadeh, M, Baleanu, D, Raza, N, Park, C, Ahmadian, A, Salahshour, S. 2021. The generalized complex Ginzburgâ “Landau model and its dark and bright soliton solutions. *The European Physical Journal Plus*; 136(7), 1-12.
- [14]. Wang, KJ, Si, J. (2023). Diverse optical solitons to the complex Ginzburgâ “Landau equation with Kerr law nonlinearity in the nonlinear optical fiber. *The European Physical Journal Plus*; 138(3), 187.
- [15]. Bullough, RK, Pilling, DJ, Timonen, J. 1986. Quantum and classical statistical mechanics of the sinh-Gordon equation. *Journal of Physics A: Mathematical and General*; 19(16), L955.
- [16]. Wazwaz, AM. 2012. One and two soliton solutions for the sinhâ “Gordon equation in (1+ 1),(2+ 1) and (3+ 1) dimensions. *Applied Mathematics Letters*; 25(12), 2354-2358.
- [17]. Wazwaz, AM. 2005. The tanh method: exact solutions of the sine-Gordon and the sinh-Gordon equations. *Applied Mathematics and Computation*; 167(2): 1196-1210.
- [18]. Malomed, BA, Mihalache, D. 2019. Nonlinear waves in optical and matter-wave media: a topical survey of recent theoretical and experimental results. *Rom. J. Phys.*; 64, 106.
- [19]. Eleuch, H. 2018. Some analytical solitary wave solutions for the generalized q-deformed Sinh-Gordon equation. *Advances in Mathematical Physics*; 2018.
- [20]. Victor, K, Pokman, C. 2002. Quantum calculus.
- [21]. Arai, A. 1991. Exactly solvable supersymmetric quantum mechanics. *Journal of Mathematical Analysis and Applications*; 158(1), 63-79.
- [22]. Kibble, TWB. 2006. Topological Defects and Their Homotopy Classification.
- [23]. Alrebdi, HI, Raza, N, Arshed, S, Butt, AR, Abdel-Aty, AH, Cesarano, C, Eleuch, H. 2022. A variety of new explicit analytical soliton solutions of q-deformed sinh-gordon in (2+ 1) dimensions. *Symmetry*; 14(11), 2425.
- [24]. Khalil, R, Al Horani, M, Yousef, A, Sababheh, M. 2014. A new definition of fractional derivative. *Journal of computational and applied mathematics*; 264, 65-70.
- [25]. Ali, KK, Al-Harbi, N, Abdel-Aty, AH. 2023. Traveling wave solutions to (3+ 1) conformal time derivative generalized q-deformed Sinh-Gordon equation. *Alexandria Engineering Journal*; 65, 233-243.
- [26]. Ghanbari, B, Inc, M. 2018. A new generalized exponential rational function method to find exact special solutions for the resonance nonlinear Schrodinger equation. *The European Physical Journal Plus*; 133(4): 142.
- [27]. Tarla, S, Ali, KK, Yilmazer, R, Osman, MS. 2022. Propagation of solitons for the Hamiltonian amplitude equation via an analytical technique. *Modern Physics Letters B*; 36(23): 2250120.
- [28]. Ali, KK, Yilmazer, R, Bulut, H, Akturk, T, Osman, MS. 2021. Abundant exact solutions to the strain wave equation in micro-structured solids. *Modern Physics Letters B*; 35(26): 2150439.
- [29]. Ghanbari, B, Liu, JG. 2020. Exact solitary wave solutions to the (2+ 1)-dimensional generalised Camassa-Holm-Kadomtsev-Petviashvili equation. *Pramana*; 94(1): 21.
- [30]. Ghanbari, B, Inc, M, Yusuf, A, Bayram, M. 2019. Exact optical solitons of Radhakrishnanâ “Kunduâ “Lakshmanan equation with Kerr law nonlinearity. *Modern Physics Letters B*; 33(06): 1950061.
- [31]. Saglam Ozkan, Y. 2021. The generalized exponential rational function and Elzaki-Adomian decomposition method for the



Heisenberg ferromagnetic spin chain equation. *Modern Physics Letters B*; 35(12): 2150200.

[32]. Kuo, CK, Gunay, B, Juan, CJ. 2023. The applications of symbolic computation to exact wave solutions of two HSI-like equations in  $(2+1)$ -dimensional. *Frontiers in Physics*; 11, 26.

[33]. Ghanbari, B, Osman, MS, Baleanu, D. 2019. Generalized exponential rational function method for extended Zakharov-Kuznetsov equation with conformable derivative. *Modern Physics Letters A*; 34(20): 1950155.

[34]. Ghanbari, B, Akgul, A. 2020. Abundant new analytical and approximate solutions to the generalized Schamel equation. *Physica Scripta*; 95(7): 075201.

## LC-MS/MS Analysis and Biological Activities of Methanol Extract from *Sagina apetala* Ard.

Rabia Nur Ün<sup>1</sup> 

<sup>1</sup> Department of Chemistry, Ege University, Bornova, İzmir, Türkiye

\*[rabia.nur.un@ege.edu.tr](mailto:rabia.nur.un@ege.edu.tr)

\*Orcid No: 0000-0001-7903-9167

Received: 15 March 2023

Accepted: 28 September 2023

DOI: 10.18466/cbayarfbe.1264511

### Abstract

This is the first study on the investigating phenolic compounds of methanol extract (ME) of *Sagina apetala* and examining its cell-based antioxidant and antibacterial activity against *Staphylococcus aureus* and *Pseudomonas aeruginosa*. The determination of phenolic compounds of ME was performed by LC-MS/MS and 25 main compounds were identified. For the cell-based antioxidant activity of ME, Vero cell line (Cercopithecus aethiops kidney epithelial, Monolayer) was used as the model cell line and ME was showed 61.22% cell viability. ME, also showed insignificant antibacterial activity against both gram-positive and gram-negative bacteria. In conclusion, this study in the species provides the basic data for future studies for the species.

**Keywords:** Antibacterial activity, Antioxidant activity, Phenolic compounds, *Sagina apetala* Ard.

### 1. Introduction

Caryophyllaceae is a family containing about 90 genera traditionally used for treatment of many diseases in different ethnic communities. Especially, it is widely used in Chinese traditional medicine to treat a wide variety of ailments [1]. Caryophyllaceae family members are rich source of natural products- triterpenes, phenolics and alkaloids are the main metabolites of this family- and these compounds are known to be pharmacologically active [2].

Among the most highly studied metabolites of the Caryophyllaceae family are flavonoids, which are classified as polyphenolic compounds and show a wide variety of biological and pharmacological activities such as antioxidant, anti-oedemic, anti-inflammatory, antimicrobial, and immunomodulatory effects [3].

*Sagina* L., affiliated with the family Caryophyllaceae, consists of about 35 species and 4 of them are represented in flora of Turkey. The diversity center of this genus is Europe, and it is found on almost all continents except Antarctica [4-6].

In the literature, there are a few number of studies on *Sagina* species and most of them are on the *S. japonica* [7, 8]. In one of this study, antitumor activity of the petroleum ether extract obtained from *S. japonica* was analyzed on three human cancer cell lines (K562, Hela and MCF-7) by MTT and SRB methods. Moreover, in this study, phytochemical investigation was performed, and twenty-five components were identified by GC-MS [9]. In another study, the antitumor activity of flavones, saponins and essential oils from *S. japonica* was tested on mice with tumor cell lines U14 and S-180 [10]. The study on *S. merinori* species was focused on antioxidant activity, investigation of total phenolic contents of *S. merinori* and uses of *S. merinori* for the skin care [11]. However, there is no study on the identification of phytochemical content and examination of the biological activities of *S. apetala*.

The aims of this study were to determine the phenolic contents by LC-MS/MS of ME from *Sagina apetala* Ard. and determined the antimicrobial and cell-based antioxidant activity of that extract.

## 2. Materials and Methods

### 2.1 Chemicals

Chemicals, solvents, and all materials required for LC-MS/MS analyzes and *Pseudomonas aeruginosa* ATCC 27853 (gram-negative) and *Staphylococcus aureus* ATCC 25923 (gram-positive) for antibacterial activity analyzes were obtained from Sigma Aldrich, USA. DMEM- high glucose (E0500-180) and 10% Fetal Bovine Serum (FBS, A0500-3010) for Cell-based Antioxidant Activity analyzes were obtained from Cegrogen Biotech, Germany, 0,5% DMSO (APA3672.0250), 1% Sodium Pyruvate (L0473), 1.0% Penisilin-Streptomisin (A2213) were obtained from Applichem, USA, Merck, Germany, Biochrom, Germany, respectively.

### 2.2. Plant Material

*Sagina apetala* Ard. (whole plants) were collected from Bozdağ, İzmir, Turkey, identified and a voucher specimen has been deposited in Ege University Herbarium (EGE- HERB 28494) (Figure 1).



**Figure 1.** *Sagina apetala* Ard.

### 2.3. Preparation of the Extract

The air-dried and powdered plant material (50.00 g) was extracted with methanol ( $3 \times 100$  mL) at room temperature. After carrying out filtration and evaporation procedures, 0.71 grams of methanol extract (ME) were obtained.

### 2.4. LC-MS/MS Analysis

LC-MS/MS analyzes of ME of *S. apetala* were carried out in Manisa Celal Bayar University Scientific Technical Application and Research Center (DEFAM) by LC-MS/MS Agilent Technologies 1260 Infinity liquid chromatography system hyphenated to a 6420 Triple Quad mass spectrometer. The column used for chromatographic analysis was Poroshell 120 EC-C18 (100 mm  $\times$  4.6 mm I.D., 2.7  $\mu$ m) and formic acid, water, methanol, ammonium acetate, acetonitrile and acetic acid

was applied gradiently. Gradient program with 0.1% formic acid/methanol, 5 mM ammonium acetate/acetonitrile with 0.1% acetic acid and, 10 mM ammonium formate with 0.1% formic acid/acetonitrile with 0.1% formic acid, respectively. The 2,0  $\mu$ L of the sample was applied into the column that fixed at 25 °C with the 0.4 mL/min flow rate of mobile phase.

### 2.5. Cell-Based Antioxidant Activity

Cell based antioxidant activities of ME was carried out by Ege University Central Research Test and Analysis Laboratory Application and Research Center (MATAL). Vero cell line (Cercopithecus aethiops kidney epithelial, Monolayer) were maintained in control medium consisting of DMEM- high glucose with 10% FBS and 1.0% P-S. The cell ( $1 \times 10^5$  cell/mL) was cultivated in medium and incubated in a 96-well plate for 24 h (37 °C and 5% CO<sub>2</sub>, 95.0 % humidified environment), Afterwards, the cell was exposed to 2  $\mu$ M H<sub>2</sub>O<sub>2</sub> (diluted with DMEM) for 3 h in order to stimulate oxidative stress. At the end of the incubation time, the cell viability was determined using MTT test (570 nm). Cell based antioxidant capacity of the extract was determined comparing to the cell viability of the control [13, 14]. Each assay in this experiment was repeated three times.

### 2.6. Determination of Antibacterial Activity

The antibacterial activity of ME was analyzed with the agar well diffusion test method [15]. This analyzes were carried out by Ege University Central Research Test and Analysis Laboratory Application and Research Center (MATAL). The antimicrobial activities of the ME were determined against two microorganisms: *Pseudomonas aeruginosa* ATCC 27853 (gram-negative) and *Staphylococcus aureus* ATCC 25923 (gram-positive). Bacteria were stored at -20 °C in media containing 16% glycerol. They were incubated in Muller-Hinton Broth (MHB) at 37 °C for 16-24 hours until a turbidity of 0.5 McFarland was reached. The ME was diluted to 50% with MHB medium and a 20  $\mu$ L of a microorganism culture solution was added to microplate [16]. After the extract was placed in the petri dish, it was waited for another 15 minutes and incubated for 24 hours at 37 °C. Standard antibiotic disc of ofloxacin (OFX, 5.0  $\mu$ g/disc) was used positive control. Each assay in this experiment was repeated three times [17].

## 3. Results and Discussion

### 3.1. LC-MS/MS Analysis

The phenolic compounds of ME from *S. apetala* were identified by LC-MS/MS and the obtained chromatogram was given in Figure 2. The results showed that *S. apetala* is very rich in phenolic compounds. 25 phenolic compounds were detected in the extract screened over 30 standards (Table 1).

The most abundant phenolics in the ME are as follows: Rosmarinic acid (392.23 mg/kg extract), protocatechuic acid (141.98 mg/kg extract), apigenin 7-glucoside (121.50 mg/kg extract), 4-Hydroxybenzoic acid (115.48 mg/kg extract), *p*-coumaric acid (73.92mg/g extract). Besides these major compounds, pyrocatechol, (+)-catechin, taxifolin, 2-hydroxycinnamic acid and eriodictyol were not observed in the ME.

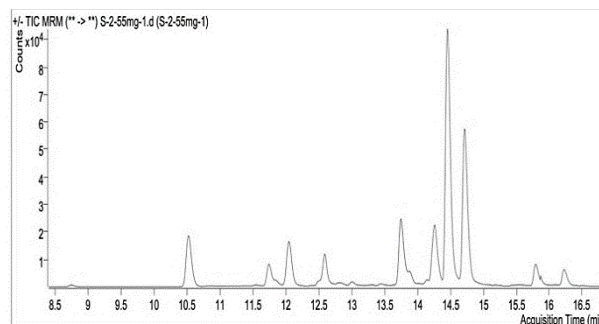


Figure 2. LC-MS/MS Chromatogram of *S. apetala* ME.

Table 1. Phenolic Compounds of *S. apetala* ME

Analytes	Transition	Retention Time	Quantification (mg analyte/kg extract)
Gallic acid	168.9 -> 125.0	8.7	4.47
Protocatechuic acid	152.9 -> 108.9	10.5	141.98
3,4-Dihydroxyphenylacetic acid	167.0 -> 123.0	10.8	1
Pyrocatechol	109.0 -> 52.9	10.9	ND
(+)-Catechin	289.0 -> 245.0	11.0	ND
Chlorogenic acid	355.0 -> 163.0	11.8	33.42
2,5-Dihydroxybenzoic acid	152.9 -> 109.0	11.9	0.99
4-Hydroxybenzoic acid	136.9 -> 93.1	12.1	115.48
(-)-Epicatechin	291.0 -> 139.1	12.3	0.12
Caffeic acid	179.0 -> 135.0	12.6	30.37
Syringic acid	196.9 -> 181.9	12.7	31.92
3-Hydroxybenzoic acid	137.0 -> 93.0	12.8	5.58
Vanillin	151.0 -> 136.0	13.0	28.73
Verbascoside	623.0 -> 160.8	13.4	2.85
Taxifolin	303.0 -> 285.1	13.7	ND
<i>p</i> -Coumaric acid	162.9 -> 119.0	13.8	73.92
Sinapic acid	222.9 -> 207.9	13.8	0.96
Ferulic acid	193.0 -> 134.0	13.9	35.79
Luteolin 7-glucoside	447.1 -> 285.0	14.2	13.26
Hesperidin	611.1 -> 303.0	14.3	5.13
Rosmarinic acid	359.0 -> 160.9	14.5	392.23
Hyperoside	465.1 -> 303.1	14.5	12.64
Apigenin 7-glucoside	433.1 -> 271.0	14.7	121.5
2-Hydroxycinnamic acid	162.9 -> 119.1	14.8	ND
Pinoresinol	357.0 -> 151.0	14.9	3.73
Eriodictyol	287.0 -> 151.0	15.1	ND
Quercetin	301.0 -> 151.0	15.6	0.53
Kaempferol	285.0 -> 229.1	15.8	2.52
Luteolin	287.0 -> 153.1	15.8	24.5
Apigenin	271.0 -> 153.0	16.2	16.65

Phenolic compounds play an important role in living organisms and establish the high majority of compounds contained in medicinal plants. For instance, in this study, rosmarinic acid, which the most abundant phenolic compound in the ME, showed biological activities such as antimicrobial, antiviral, antioxidant, anti-inflammatory, anti-angiogenic, anti-depressant, antihyperglycemic, anti-allergic, antithrombotic, anticarcinogenic, and anti-aging [18]. Protocatechuic acid is known to exhibit anticancer, antiproliferative, antioxidant, and antiadipogenesis activities [19, 20]. Apigenin, which is important flavonoid, has been reported to exhibit potential anticancer activity [21], as well as antifungal [22], antibacterial [23] and antiparasitic [24] properties. 4-hydroxy benzoic acid has biological activities such as antimicrobial and antioxidant [25]. Finally *p*-Coumaric acid has been researched for antioxidant, anti-cancer, antimicrobial, antiviral, anti-inflammatory, anti-diabetic and anti-hyperlipaemia [26].

### 3.2. Cell-based Antioxidant Activity

The antioxidant activity of the Me was examined cell based antioxidant activity test. The ME, which is rich in phenolic compounds and flavonoids, was expected to show high antioxidant activity. Antioxidant activity is often associated with phenolic compounds and flavonoids [27]. The protective effect of extract against the oxidative stress was determined by observing the cell viability of H<sub>2</sub>O<sub>2</sub>-damaged Vero cell, which was pre-treated with the extract. After the treatments with H<sub>2</sub>O<sub>2</sub> (2 µM) for 24 hours, the cell viability of Vero cell pre-treated with the extract was determined as 61.22%, as given in Figure 3.

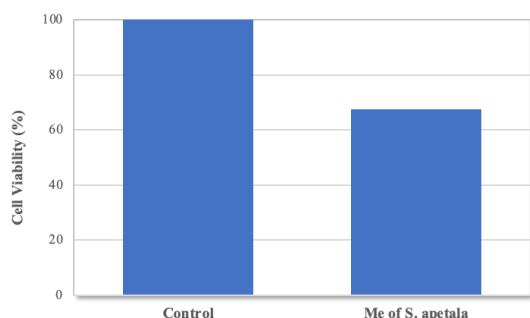


**Figure 3.** Antioxidant activity of *S. apetala* ME.

### 3.3. Antibacterial activity of *S. apetala* ME

In this study, two different bacterial strains were used to determine the antimicrobial activity. The results of the antibacterial activities of the standard antibiotics and the ME against the tested microorganisms as given in Figure 4. At a concentration of 50 µg, the ME showed any activity against Gram-negative *Pseudomonas aeruginosa* ATCC 27853 and gram-positive *Staphylococcus aureus* ATCC 25923 bacteria in this study.

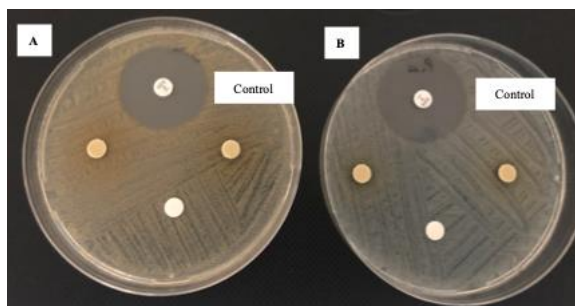


**Figure 4.** Antibacterial activity of *S. apetala* ME against *S. aureus* (A) and *P. aeruginosa* (B).

### 4. Conclusion

In this study, the chemical composition, antibacterial and antioxidant activity of *S. apetala* were reported for the first time. While medium cell based antioxidant activity was observed in ME, insignificant antibacterial activity was observed. This result may be related to the high phenolic compounds of ME. As a result, investigation of the phenolic compounds, antibacterial and antioxidant activities of the ME obtained from *S. apetala* may contribute to the biological activity tests. This study also sheds light on future studies on other species belonging to the Caryophyllaceae family.

### Author's Contributions

**Rabia Nur Ün:** Drafted and wrote the manuscript, performed the experiment and result analysis.

### Ethics

There are no ethical issues after the publication of this manuscript

### References

- [1]. Chandra, S, Rawat, DS. 2015. Medicinal plants of the family Caryophyllaceae; a review of ethno-medicinal uses and pharmacological properties. *Integrative Medicine Research*; 4: 123-131.
- [2]. Wink M. Biochemistry of plant secondary metabolism, 2nd edn; Wiley-Blackwell, Chichester, 2010; pp 464.
- [3]. Jakimiuk, K, Wink, M, Tomczyk, M. 2022. Flavonoids of the Caryophyllaceae, *Phytochemistry Reviews*; 21:179-218.
- [4]. Bittrich, V. Caryophyllaceae. In: Kubitzki, K, Rohwer, JG, Bittrich, V (ed) The families and genera of vascular plants II. Flowering plants: dicotyledons: magnoliid, hamamelid and caryophyllid families, Springer, Berlin, 1993, pp. 206-236.
- [5]. Alban, DM, Biersma, EM, Kadereit, JW, Dillenberger, MS. 2022. Colonization of the southern hemisphere by *Sagina* and *Colobanthus* (Caryophyllaceae). *Plant Systematics and Evolution*; 308(1): 1.
- [6]. Bizim Bitkiler. <https://bizimbitkiler.org.tr/yeni/demos/technical/> (accessed at 10 April 2021).

- [7]. Fu, Q, Tang, W, Cheng, Y, He, R, Liang, B. 2021. Induction of differentiation of K652 leukemia cells by Herba Saginae Japonicae. *Aibian, Jibian, Tubian*; 33(1): 37-41.
- [8]. Tang, W, Fu, Q, Cheng, Y, Luo, S, Liang, B. 2021. Induction of differentiation of human acute promyelocytic leukemia cells by an ethanol extract from Herba Saginae Japonicae, Aibian, Jibian, Tubian; 33(1): 42-47.
- [9]. Zhang, SY, He L. 2010. Analysis of chemical constituents of petroleum ether extract from Sagina japonica (Sw.) Ohwi and screening of its anti-tumor activity. *Medicinal Plant*; 1(8): 89-91.
- [10]. Huang, HP, Cheng, CF, Ren, GY, Lin, WQ. 1980. Antitumor activity and preclinical pharmacologic study of the flavone of Sagina japonica. *Yaoxue Tongbao*; 15(11): 1-2.
- [11]. Martinez, A, Estevez, JC, Silva-Pando, FJ. 2012. Antioxidant activity, total phenolic content and skin care properties of 35 selected plants from Galicia (NW Spain). *Frontiers in Life Science*; 6(3-4): 77-86.
- [12]. Cittan, M, Çelik, A. 2018. Development and validation of an analytical methodology based on liquid chromatography–electrospray tandem mass spectrometry for the simultaneous determination of phenolic compounds in olive leaf extract. *Journal of Chromatographic Science*; 56 (4): 336-343.
- [13]. Ün, RN, Barlas, FB, Yavuz, M, Seleci, DA, Seleci, M, Gumus, ZP, Guler, E, Demir, B, Can, M, Coskunol, H, Timur S. 2015. Phytosomes: In Vitro Assessment of the novel nanovesicles containing marigold extract. *International Journal of Polymeric Materials and Polymeric Biomaterials*; 64(17): 927-937.
- [14]. Guler, Emine; Barlas, FB, Yavuz, M, Demir, B, Gumus, ZP, Baspinar, Y, Coskunol, H, Timur, S. 2014. Bio-active nanoemulsions enriched with gold nanoparticle, marigold extracts and lipoic acid: In vitro investigations. *Colloids and Surfaces, B: Biointerfaces*; 121: 299-306.
- [15]. Rios, JL, Recio, MC, Villar, A. 1988. Screening methods for natural products with antimicrobial activity: a review of the literature. *Journal of Ethnopharmacology*; 23(2-3):127-149.
- [16]. Wiegand, I, Hilpert, K, Hancock, REW. 2008. Agar and broth dilution methods to determine the minimal inhibitory concentration (MIC) of antimicrobial substances. *Nature Protocols*; 3(2): 163-175.
- [17]. Yildirim, H, Guler, E, Yavuz, M, Ozturk, N, Kose Yaman, P.; Subasi, E, Sahin, E, Timur, S. 2014. Ruthenium(II) complexes of thiosemicarbazone: Synthesis, biosensor applications and evaluation as antimicrobial agents. *Materials Science & Engineering, C: Materials for Biological Applications*; 44: 1-8.
- [18]. Chao, CY, Mong, MC, Chan, KC, Yin, MC. 2010. Antigliycative and anti-inflammatory effects of caffeic acid and ellagic acid in kidney of diabetic mice. *Molecular Nutrition & Food Research*; 54: 388-395.
- [19]. Anantharaju, PG, Reddy, DB, Padukudru, MA, Chitturi, CMK, Vimalambike, MG, Madhunapantula, SV. 2017. Induction of colon and cervical cancer cell death by cinnamic acid derivatives is mediated through the inhibition of Histone Deacetylases (HDAC). *Plos One*; 12(11): e0186208.
- [20]. Byun, JW, Hwang, S, Kang, CW, Kim, JH, Chae, MK, Yoon, JS, Lee, EJ. 2016. Therapeutic effect of protocatechuic aldehyde in an in vitro model of Graves' orbitopathy. *Investigative Ophthalmology & Visual Science*; 57(10): 4055-4062.
- [21]. Shendge, AK, Chaudhuri, D, Basu, T, Mandal, NA. 2021. Natural flavonoid, apigenin isolated from *Clerodendrum viscosum* leaves, induces G2/M phase cell cycle arrest and apoptosis in MCF-7 cells through the regulation of p53 and caspase-cascade pathway. *Clinical and Translational Oncology*; 23: 718-730.
- [22]. Lee, H, Woo, ER, Lee, DG. 2018. Apigenin induces cell shrinkage in *Candida albicans* by membrane perturbation. *FEMS Yeast Research*; 18: 3.
- [23]. Kim, S, Woo, ER, Lee, DG. 2020. Apigenin promotes antibacterial activity via regulation of nitric oxide and superoxide anion production. *Journal of Basic Microbiology*; 60: 862-872.
- [24]. Wang, M, Firman, J, Liu, L, Yam, K. 2019. A review on flavonoid apigenin: dietary intake, ADME, antimicrobial effects, and interactions with human gut microbiota. *BioMed Research International*; 2019: 18.
- [25]. Wei, Q, Wang, X, Cheng, JH, Zeng, G, Sun, DW. 2018. Synthesis and antimicrobial activities of novel sorbic and benzoic acid amide derivatives. *Food Chemistry*; 268: 220-232.
- [26]. Pei, K, Ou, J, Huang, J, Ou, S. 2016. p-Coumaric acid and its conjugates: dietary sources, pharmacokinetic properties and biological activities. *Journal of the Science of Food and Agriculture*; 96 (9): 2952-2962.
- [27]. Li, W, Gao, Y, Zhao, I, Wang, Q. 2007. Phenolic, flavonoid, and lutein ester content and antioxidant activity of 11 cultivars of chinese marigold. *Journal of Agricultural and Food Chemistry*; 55: 8478.

## Preparation of ECH-PCCB for the Pre-concentration and Determination of Cadmium (II) Ions Prior to FAAS by FIA

Vedia Nüket Tirtom<sup>1\*</sup> , Fatma Özkafalı<sup>1</sup> 

<sup>1</sup> Manisa Celal Bayar University, Faculty of Science and Arts, Chemistry Department, Manisa, Türkiye

\*[nuket.tirtom@cbu.edu.tr](mailto:nuket.tirtom@cbu.edu.tr)

\*Orcid No:0000-0002-2490-2741

Received: 10 April 2023

Accepted: 15 June 2023

DOI: 10.18466/cbayarfbe.1280291

### Abstract

In this study, epichlorohydrin pumice-chitosan composite beads structures were used for the first time as mini-column filling material in a flow injection analyses added to the atomic absorption spectroscopy for the pre-concentration of cadmium ions. This method is simple, accurate and highly selective for pre-concentration of Cd(II) in water samples. Surface analysis of epichlorohydrin pumice-chitosan composite was performed by scanning electron microscopy. Elution of Cd(II) ions from the column was achieved with 0.1 mol L<sup>-1</sup> EDTA. Some parameters affecting the pre-concentration of Cd(II) ions, such as sample loading time, sample flow rate, eluent type and concentration, pH, and interference ions were investigated. Under the optimized parameters, the enrichment factor was 23 and the detection limit of the method was 16 µg L<sup>-1</sup> as a result of pre-concentration studies with epichlorohydrin pumice-chitosan composite.

**Keywords:** Cd (II), Flow injection analyses, Pumice-chitosan composite beads, Online pre-concentration.

### 1. Introduction

Due to the highly toxic effect of cadmium ions even at trace levels, pre-concentration and determination studies have gained increasing importance worldwide. The WHO and EPA limit for cadmium ions in drinking water is 0.003 mgL<sup>-1</sup>-0.005 mg L<sup>-1</sup> [1], as a result, detection of low amounts of cadmium ions is very important. Rapid progress in industry, irregular urbanization, and traffic cause water pollution with heavy and toxic metals.

Cadmium and its compounds are pollutants that cause diseases such as kidney dysfunction, lung cancer, hypertension, and prostate cancer. [2-5]. Detection of metal ions in water is very difficult without preconcentration due to low concentrations and matrix interactions. It is advantageous to use a pre-concentration step to detect low cadmium levels in water samples. The pre-concentration technique is fast, reproducible, can be worked in small volumes, and since it is a closed system, it is a method without contamination from external factors [6-8].

Connecting the flow injection system (FIA) to the flame atomic absorption spectroscopy (FAAS) online is an important technique for the pre-concentration of cadmium ions in water. Thus, while the specification

limits are improved, the interference from the matrix is also reduced. The analytical efficiency of the method increases [9]. FIA online pre-concentration techniques have some advantages for trace determination of Cd(II) ions, such as low substance consumption, high efficiency, convenience, no contamination [10-12]. Therefore, prepared new adsorbent in (flow injection) FI pre-concentration techniques are very important.

The limit of detection can be lowered using simple pre-concentration FAAS such as Pumice-chitosan composite beads (PCCB). Applications of chitosan (CTS) composites for the removal of heavy metal ions aqueous solutions were reviewed [13-18]. However, no pre-concentration study of Cd (II) PCCB has been reported in the literature so far. PCCB as a novel and great adsorbent in on-line pre-concentration technique.

Chitosan (CTS) is a natural polysaccharide containing high levels of amino and hydroxyl groups and is formed by deacetylation of chitin. CTS is a suitable adsorbent in wastewater treatment due to its low toxicity, biocompatibility, and biodegradability.

Pumice is a volcanic material that has a rough surface and a porous structure, providing multiple bonding sites with metal ions. Therefore, it has a good efficiency for the removal of cadmium ions. Pumice stone is a porous

igneous volcanic rock, with significant accessibility, which it is abundantly found in nature and considered as an inexpensive adsorbent [19-20].

In this paper, epichlorohydrin pumice-chitosan composite beads (ECH-PCCB) was prepared and tested as column packing for FAAS determination of cadmium ions in water samples by pre-concentration method. All analytical features such as sample loading time, pH, eluent type, concentration of eluent, sample, and eluent flow rates, and the effect of matrix components were studied and are described.

## 2. Materials and Methods

### 2.1. Instrumentation

A Varian Spectra FAAS containing a deuterium background correction system was used for cadmium determination. Heidolph brand peristaltic pump (four-channel) and Tygon tubes were used for the flow of solutions. Rheodyne six-way rotary injection valve was used in the FIA. Hanna P211 model pH-meter with combined glass electrode was used for pH measurements. Philips (FEI) XL30-SFEG scanning electron microscope (SEM) was used in the surface characterization studies of ECH-PCCB.

### 2.2. Reagents and Chemicals

All reagents used in the experiments were of analytical purity. (Sigma and Merck). Double deionized water used in the whole study was purified with 18 MΩ cm Millipore brand distilled water device. Stock solutions of Cd (II) was prepared by dissolving of Cd(NO<sub>3</sub>)<sub>2</sub>·4H<sub>2</sub>O (Merck) into deionized water. All solutions were prepared by dilution daily from stock solutions. Buffer solutions of 0.1 M HCl, CH<sub>3</sub>COOH/NaCH<sub>3</sub>COO, and NaH<sub>2</sub>PO<sub>4</sub>/Na<sub>2</sub>HPO<sub>4</sub> were used to adjust the pH to acidic, weakly acidic and neutral, respectively. EDTA (ex. Merck) HCl and HNO<sub>3</sub> (ex. Merck) were used as eluting solutions.

### 2.3. FIA System Descriptions

The FIA system consisted of four-line peristaltic pump. Mini-column packed with an ECH-PCCB and injection valve (six-way) were employed. A mini-column with a length of 5 cm and a diameter of 3 mm and connecting hoses with a diameter of 1.5 mm were used. Figure 1a shows the peristaltic pump, six-way valve, mini-column, and sample transport to the FAAS system.

#### Preparation of ECH-PCCB

CTS powder (2g) was dissolved in CH<sub>3</sub>COOH (100 mL) (2% v/v) solution. This mixture was stirred for 2 hours until homogeneous. Pumice stone was crushed to fine size in agate mortar. It was sieved to 100 mesh size. 20 g of pumice stone was soaked overnight in 30 mL of distilled water. The pumice chitosan mixture was

dropped into Tri-Polyphosphate (TPP) with a pH adjusted to 8.2 using a syringe needle. The beads were mixed for 4 hours to harden. The filtered and washed beads were dried at 40°C for 12 hours and placed in a desiccator. 50 mL 2.0 M NaOH, 0.266 g NaBH<sub>4</sub> and 5 mL of ECH were added and the beads were crosslinked for 15 hours at 37°C. After the cross-linking process was completed, the PCCB, washed and filtered, were dried in an oven set at 50 degrees. The ECH-PCCB particle size were 100-150 μm.

### 2.4. Preparation of ECH-PCCB Column

The pre-concentration mini-column for retaining cadmium was prepared by polytetrafluoroethylene (PTFE) with ECH-PCCB. A tygon tube with a radius of 5.0 mm and a size of 6.0 cm was used. Before placing the pumice CTS adsorbent into the tube, glass wool was placed at the bottom, and glass wool was placed on the top to prevent spillage after the ECH-PCCB was placed. The amount of ECH-PCCB in the tube was 0.020 grams.

#### Pre-concentration Methods:

FIA pre-concentration consists of three steps: enrichment step, washing step and elution step. First step (Pre-concentration): 50 μg of L<sup>-1</sup> cadmium solution or sample solution was carried out the system for 2 minutes. Second step (Washing): Pure water was passed through the system for 30 seconds for washing. (Figure 1 a). Since this stage is the loading stage to the column, the solution passing through the mini-column goes to waste. Meanwhile, the FAAS signal was not measured.

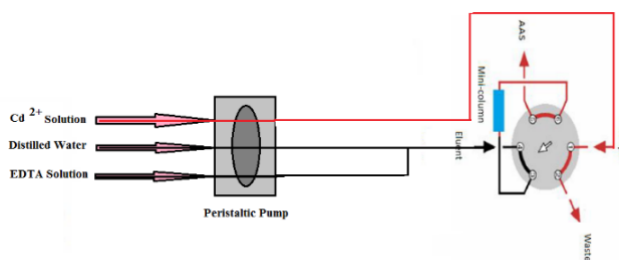


Figure 1. a. Sample Load Position

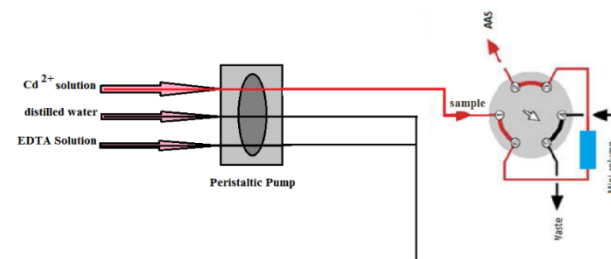


Figure 1. b. Eluting Position

Third step (Elution): starts after 2.5 minute of pre-concentration. The valve was moved to the third position and the eluent was directed to the mini-column.

At this stage, the solutions carry to the FAAS system, and the signal was read. After measuring, the valves were returned to their starting position so that the next sample could be enriched (Figure 1 b).

### 3. Results and Discussion

#### 3.1. Characterization of ECH-PCCB

In the studies, ECH-PCCB synthesized to be used as mini-column filling material were taken under scanning electron microscope. In Figure 2 a show the SEM image of natural pumice stone [20], b) ECH-PCCB(x1000) c) ECH-PCCB(x250) d) ECH-PCCB(x100). While the surface of the natural pumice stone appears flat in figure 2 a, the surface of the ECH-PCCB is recessed and porous as shown in figure 2 b. Increasing the pore size of the surface also increases the adsorption ability of pumice and enables the evaluation of pumice material, which is abundant and cheap in nature.

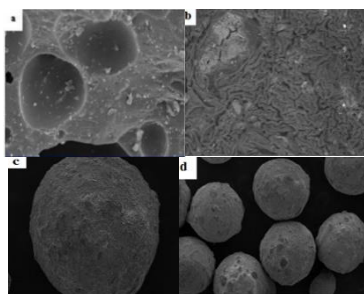


**Figure 2.** a. SEM image of natural pumice stone [20] b) ECH-PCCB (x1000) c) ECH-PCCB (x250) d) ECH-PCCB (x100).

#### 3.2. Batch Studies

##### 3.2.1. Adsorption and Desorption Studies

In batch experiments, 25 mL of 20 mg L<sup>-1</sup> Cd (II) solution was transferred into a 50 mL beaker and 0.1 ± 0.0002 g of natural pumice powder, chitosan beads and ECH-PCCB were added. ECH-PCCB and Cd (II) solution was shaken for 10 minutes to ensure the adsorption of metal ions to the sorbent. It was filtered by decantation. The filtrate was measured at FAAS. Adsorbed natural pumice powder, CTS beads and ECH-PCCB were washed with distilled water. Since the most used desorbents in our previous studies and literature are EDTA, HNO<sub>3</sub> and HCl, the performance of these three solutions as elution solutions has been investigated. The washed adsorbents were added to the beaker containing 25 mL of 0.1 M EDTA and 0.1 M HNO<sub>3</sub> and stirred in a magnetic stirrer for 10 minutes. Decanted filtrate was measured at FAAS. For adsorption and desorption processes, two parallel beads were studied from each bead species. % Adsorption and % Desorption values for the best adsorbent selected in the preliminary experiments the calculations were carried out with the following equations;

$$\% A = \frac{C_i - C_e}{C_i} \times 100 \quad (3.1)$$

where C<sub>i</sub> and C<sub>e</sub> are the initial and equilibrium concentrations of Cd (II) ion, respectively.

$$\% D = \frac{\text{amount of desorbed metal ion}}{\text{amount of adsorbed metal ion}} \times 100 \quad (3.2)$$

The results were given in Table 1. As a result, adsorbent was chosen to be used as mini-column filler material in flow injection analysis for the best results ECH-PCCB. Since it can be desorbed 90% of Cd (II) ions, EDTA has been chosen as eluent in FIA.

**Table 1.** Comparison of adsorption and desorption % of column fillers.

Epichlorohydrin cross linked pumice-chitosan composite beads	Adsorption (%)	Desorption (%)
		EDTA
1	89.40	90.00
2	89.36	88.95
3	89.30	88.93
4	89.30	88.89

To measure the repeatability of the adsorbent, the best adsorbent was determined by repeating the adsorption and desorption processes and the results were given in Table 2.

**Table 2.** Reusability of adsorbent

	Adsorption (%)	Desorption (%)	Desorption (%)
		HNO <sub>3</sub>	EDTA
Natural pumice stone powder	48.6	50.0	51.1
Chitosan beads	60.6	70.6	63.0
Epichlorohydrin cross linked pumice-chitosan composite beads	89.4	87.6	90.0

#### 3.3. FIA Studies:

##### 3.3.1. Optimizing Sample and Eluent Flow Rate

The effect of Cd (II) ions on the pre-concentration of the column was investigated by experiments with sample and eluent flow rates set to 1.5, 3.0, 4.0 and 6.0 mL min<sup>-1</sup>. Recovery values for ECH-PCCB decreased after 1.5 mL min<sup>-1</sup> (Figure 3). 1.5 ml min<sup>-1</sup> was chosen as the sample and eluent flow rate, since the highest recovery value.

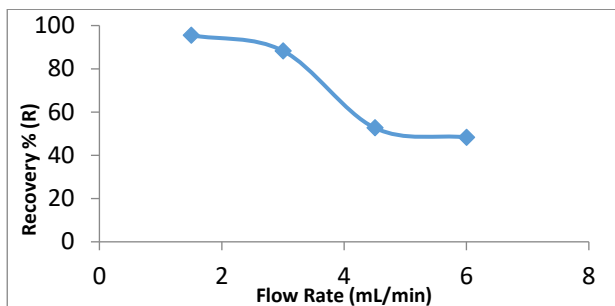


Figure 3. Effect of Sample and Eluent Flow Rate.

### 3.3.2. Optimizing Sample Load Time

In the studies carried out for ECH-PCCB filled mini-column, the system was first passed through distilled water for 30 seconds. Then  $50 \mu\text{g L}^{-1}$  Cd (II) solution was sent to the system for 0.5-1-2-3 minutes and passed through the mini-column. Then, the eluent was passed and the FAAS signals were read. Experimental results for optimization of sample loading time are given in Figure 4. The optimum time for loading ECH-PCCB filled mini-column for Cd (II) was determined as 2 minutes.

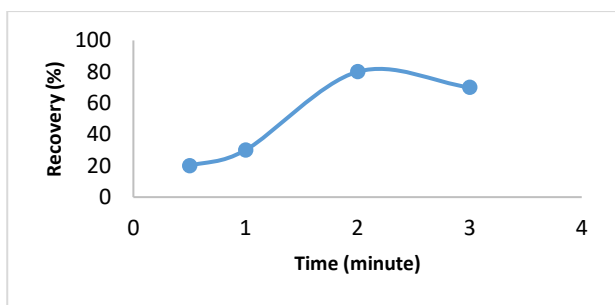


Figure 4. Effect of Sample Loading Time.

### 3.3.3. Determining of Eluent Type

The Cd (II) solution prepared at the appropriate concentration was carried out the column at the determined optimum minute (2 minutes).

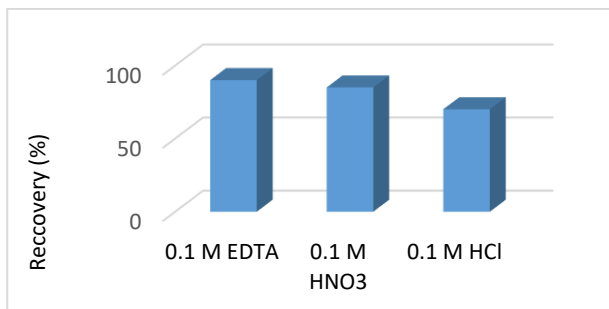


Figure 5. Effect of Eluent Type.

Then, 0.1M EDTA, 0.1M HNO<sub>3</sub> and 0.1 M HCl solutions were passed through the mini-column to select the appropriate eluent and the signal value at FAAS was read. Results obtained from the studies to determine the eluent type are given in Figure 5.

90% recovery was found by using EDTA for eluting. For cadmium (II), EDTA was chosen as the most suitable eluent for loading into ECH-PCCB filled mini-column.

### 3.3.4. Optimizing of Solution pH

The effect of pH on recovery value were investigated. Buffer solutions in the range of pH 3.0 to pH 8.0 were prepared. Signals were determined by FAAS for each pH. The results are given in Figure 6. At pH <6 the free ion Cd<sup>2+</sup> is the predominating species. The main species at pH 9.5 are Cd(OH)<sup>+</sup> and at pH =8.0 Cd(OH)<sub>2</sub> thus the removal of Cd<sup>2+</sup> is possibly accomplished by simultaneous precipitation of Cd(OH)<sub>2</sub> and sorption of Cd(OH)<sub>2</sub>. For cadmium (II), the optimum pH for loading into ECH-PCCB filled column was determined as 5.0. At this pH value the adsorption of Cd (II) ions was not masked by precipitation.

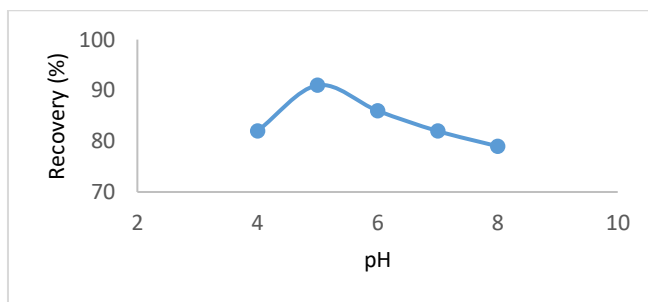


Figure 6. Effect of pH.

### 3.3.5. Effect of Interfering Ions

The effect of trace metals such as Na<sup>+</sup>, Ca<sup>2+</sup>, Mn<sup>2+</sup>, Pb<sup>2+</sup>, NH<sub>4</sub><sup>+</sup>, Al<sup>3+</sup>, Zn<sup>2+</sup>, which are thought to interfere in the pre-concentration of Cd (II) ions, was investigated. These species were added to the Cd (II) solutions in a 100-fold excess and the pH was adjusted to 5.0. The results are given in Table 3.

$$LOD = \frac{3xS_{blank}}{m} \quad (3.3)$$

$$LOQ = \frac{10xS_{blank}}{m} \quad (3.4)$$

LOD: Limit of Detection

LOQ: Limit of Quantification

The LOD of the analyte determined was calculated. The LOD of Cd (II) ion was found to be  $16 \mu\text{g L}^{-1}$  and the LOQ measurement was  $31 \mu\text{g L}^{-1}$ .

**Table 3.** Effect of Interfering Ions.

Ions	Concentration ( $\mu\text{g/L}$ )	Recovery (%)
		$\text{Cd}^{2+}$
$\text{Na}^+$	200.0	$35 \pm 1$
$\text{Ca}^{2+}$	200.0	$45 \pm 1$
$\text{Mn}^{2+}$	200.0	$65 \pm 1$
$\text{Pb}^{2+}$	200.0	$21 \pm 1$
$\text{NH}_4^+$	200.0	$35 \pm 1$
$\text{Al}^{3+}$	200.0	$41 \pm 1$
$\text{Zn}^{2+}$	200.0	$64 \pm 1$

The equation of the obtained calibration curve was found as  $y = 0,0396x + 0.0104$ .  $R^2$  was found as 0.9109. The RSD was found 3% for five replicate separate mini-column measurements. Table 4 shows general performance values for reported literatures for Cd (II) ion analysis.

### 3.3.6. Determination of Cadmium, in Water Samples

The application of this method developed for the pre-concentration of cadmium ions has been tested in tap water samples. The recovery results obtained were given in Table 5. According to the results repeated 3 times, the recovery was in the range of 96.8–99.4% as shown in Table 5. It demonstrated the suitability of the ECH-PCCB for the pre-concentration of Cd (II) from water samples prior to FAAS analysis.

**Table 4.** Analytical Performance Values for online Pre-concentration Analysis for Cd (II).

Adsorbent	Working range	Limit of detection	Pre-concentration factor	Ref.
Sulphoxine Chitosan	$5\text{--}25 \mu\text{g L}^{-1}$	$0.2 \mu\text{g L}^{-1}$	13.9	[21]
Chitosan with complexing agent 8-hydroxyquinoline:	$10\text{--}40 \mu\text{g L}^{-1}$	$0.1 \mu\text{g L}^{-1}$		[22]
Functionalization of chitosan with 2-aminopyridine-3-carboxylic acid		$0.021 \mu\text{g L}^{-1}$		[16]
XAD-4-2,6-dihydroxy phenyldiazoaminoazobenzene	$0.3\text{--}100 \mu\text{g L}^{-1}$	$0.1 \mu\text{g L}^{-1}$	42	[10]
Modified silica gel-chitosan	$0.45 \text{ mg L}^{-1}$ to $2.5 \text{ mg L}^{-1}$	$20 \text{ ngL}^{-1}$	166.7	[17]
Cross-linked chitosan functionalized with 2-amino-5-hydroxy benzoic acid moiety (CCTS-AHBA resin)	0.01–5 ppb	0.006 ppb	21.6	[23]
Epichlorohydrin cross linked pumic stone	$50\text{--}250 \mu\text{g L}^{-1}$	$16 \mu\text{g L}^{-1}$	23	This Study

**Table 5.** Recovery of Cd(II) in water samples.

Sample Water	Cd (II) added ( $\mu\text{g L}^{-1}$ )	Cd (II) found ( $\mu\text{g L}^{-1}$ )	Recovery (%)
Tap Water	50.00	$49.68 \pm 0.14$	99.36
Tap Water	70.00	$67.75 \pm 0.20$	96.78

## Conclusion

The newly synthesized ECH-PCCB were found to be effective for the adsorption of Cd (II) ions prior to its atomic absorption spectrophotometric determination. The ECH-PCCB were characterized using SEM images. The developed method provided good accuracy to determine Cd (II) in samples of tap water, according to the results of recovery tests. The LOD was found to be  $16 \mu\text{g L}^{-1}$ . This method is recommended as an inexpensive analytical pre-concentration technique for the determination of trace Cd (II) ions in water samples.

## Author's Contributions

**Vedia Nüket Tirtom:** She did the planning, analytical evaluation and interpretation of the trials and ensured that the results were reported.

**Fatma Özkafah:** Performed the experiment and result analysis.

## Ethics

There are no ethical issues after the publication of this manuscript

## References

- [1] M. Stratford. "Welcome to Mendeley: Quick Start Guide". 2018
- [2] Baláz, M, Bujňáková, Z, Baláz, P, Zorkovská, A, Danková, Z, Briančin. J. 2015. Adsorption of cadmium (II) on waste biomaterial. *J. Colloid Interface Science*; 454: 121-133.
- [3] Chen, T, Zhou, Z, Han, R, Meng, R, Wang, H, Lu, W. 2015. Adsorption of cadmium by biochar derived from municipal sewage sludge: Impact factors and adsorption mechanism. *Chemosphere*; 134: 286–293.
- [4] Soylak, M, Narin, I. 2005. On-Line Pre-concentration System for Cadmium Determination in Environmental Samples by Flame Atomic Absorption Spectrometry. *Chem. Anal. (Warsaw)*; 50:705-715
- [5] Gouda, A.A, Zordok, W.A, 2018. Solid-phase extraction method for pre-concentration of cadmium and lead in environmental samples using multiwalled carbon nanotubes. *Turkish Journal of Chemistry*; 42(4): 1018–1031.
- [6] Marguí, E, Van Grieken, R, Fonta's, C, Hidalgo, M, Queralt, I. 2010. Pre-concentration Methods for the Analysis of Liquid Samples by X-Ray Fluorescence Techniques. *Applied Spectroscopy Reviews*; 45(3): 179–205.
- [7] Mizuike, A, Pre-concentration techniques for inorganic trace analysis. 1986. *Fresenius' Zeitschrift für Analytische Chemie*; 324(7): 672–677.
- [8] D. Chen, B, Hu, C, Huang, 2009. Chitosan modified ordered mesoporous silica as micro-column packing materials for on-line flow injection-inductively coupled plasma optical emission spectrometry determination of trace heavy metals in environmental water samples. *Talanta*; 78(2): 491–497
- [9] Wuilloud, RG, González, AH, Marchevsky, EJ, Olsina, RA, Martinez, LD. 2001. On-line complexation/pre-concentration system for the determination of lead in wine by inductively coupled plasma-atomic emission spectrometry with ultrasonic nebulization. *Journal of AOAC International*; 84(5): 1555–1560.
- [10] Liu, Y, Guo, Y, Meng, S, Chang, X. 2007. Online separation and pre-concentration of trace heavy metals with 2,6-dihydroxyphenyl-diazoaminoazobenzene impregnated amberlite XAD-4. *Microchimica Acta*; 158(3–4): 239–245
- [11] Abdelhamid, HN, Lin, YC, Wu, HF, 2017. Thymine chitosan nanomagnets for specific pre-concentration of mercury (II) prior to analysis using SELDI-MS. *Microchimica Acta*; 184(5): 1517–1527
- [12] Di Nezio, MS, Palomeque, ME, Fernández B, BS. 2006. A Multi-Element Flow Injection System for Heavy Metals Determination. *Analytical Letters*; 39(6): 1211–1228.
- [13] Yari, M, Moghimi, A, Fakhari, S. 2016. Preparation of Modified Magnetic Nano-Fe<sub>3</sub>O<sub>4</sub> Chitosan/Graphene Oxide for the Pre-concentration and Determination of Copper (II) ions in Biological and Environmental Water Samples. *Oriental Journal of Chemistry*; 32(3): 1659–1669
- [14] Shinde, RN, Pandey, AK, Acharya, R, Guin, R, Das, SK, Rajurkar, NS, 2013. Chitosan-transition metal ions complexes for selective arsenic(V) pre-concentration. *Water Research*; 47(10): 3497–3506.
- [15] Yadaei, H, Beyki, MH, Shemirani, F, Nouroozi, S. 2018. Ferrofluid mediated chitosan@ mesoporous carbon nanohybrid for green adsorption/pre-concentration of toxic Cd (II): modeling, kinetic and isotherm study. *Reactive and Functional Polymers*; 122: 85–97.
- [16] Suneetha, Y, Kumar, BN, Harinath, Y, Reddy, DHK, 2012. Seshaiiah, K. Functionalization of Cross Linked Chitosan with 2-Aminopyridine-3-carboxylic Acid for Solid Phase Extraction of Cadmium and Zinc Ions and Their Determination by Atomic Absorption Spectrometry. *Microchimica Acta*; 176(1–2): 169–176.
- [17] He, JC, Zhou, FQ, Mao, YF, Tang, ZN, Li, CY, 2013. Pre-concentration of Trace Cadmium (II) and Copper (II) in Environmental Water Using a Column Packed with Modified Silica Gel-Chitosan Prior to Flame Atomic Absorption Spectrometry Determination. *Analytical Letters*; 46(9): 1430–1441.
- [18] Al-Saidi, HM. 2016. Biosorption using chitosan thiourea polymer as an extraction and pre-concentration technique for copper prior to its determination in environmental and food samples by flame atomic absorption spectrometry: Synthesis, characterization and analytical applications. *International Journal of Biological Macromolecules*; 93: 390–40.
- [19] Akbal, F. 2005. Adsorption of basic dyes from aqueous solution onto pumice powder. *Journal of Colloid and Interface Science*; 286(2): 455–458.
- [20] Shokoohi, R, Torkshavand, Z, Bajalan, S, Zolghadnasab, H, Khodayari, Z. 2019. Cadmium removal by using pumice modified with iron nanoparticles. *Global Nest Journal*; 21(2): 91–97.
- [21] Martins, AO, Da Silva, EL, Carasek, E, Laranjeira, MCM, De Fávère, VT. 2004. Sulphoxine immobilized onto chitosan microspheres by spray drying: Application for metal ions pre-concentration by flow injection analysis. *Talanta*; 63(2): 397–403.
- [22] Martins, AO, Da Silva, EL, Carasek, E, Gonçalves, NS, Laranjeira, MCM, De Fávère, VT. 2004. Chelating resin from functionalization of chitosan with complexing agent 8-hydroxyquinoline: Application for metal ions online pre-concentration system. *Analytica Chimica Acta*; 521(2): 157–162
- [23] Sabarudin, A, Lenghor, N, Oshima, M, Hakim, L, Takayanagi, T, Gao, Y.H, Talanta. Elsevier, 2007. Sequential-injection on-line pre-concentration using chitosan resin functionalized with 2-amino-5-hydroxy benzoic acid for the determination of trace elements in environmental water samples by inductively coupled plasma-atomic emission spectrometry. *Talanta*; 72(5): 1609–1617.

## Evaluation of Various Flexibility Resources in Power Systems

Emir Kaan Tutuş<sup>1\*</sup> , Nevzat Onat<sup>1</sup> 

<sup>1</sup>Manisa Celal Bayar University, Faculty of Engineering, Department of Electrical and Electronics Engineering,  
Yunusemre, Manisa, Türkiye

\*[emir.tutus@cbu.edu.tr](mailto:emir.tutus@cbu.edu.tr)

\*Orcid No: 0000-0001-5119-8174

Received: 10 April 2023

Accepted: 27 September 2023

DOI: 10.18466/cbayarfbe.1280545

### Abstract

Variable Renewable Energy Resources (VRES), especially wind and solar power, are known for their intermittent, uncertain, and low-energy-density nature. The increasing adoption of these stochastic sources presents irregularity in the net load in the power system network; therefore, it poses a challenge to the reliable operation of power systems. Consequently, there's an increasing need for power system flexibility to cope with VRES-related challenges. Flexibility planning will therefore be a crucial aspect for power system management, particularly as the penetration of VRES continues to rise. To reach this objective, the diversification of flexibility options emerges as a promising solution. Various strategies are prominent in the literature for enhancing power system flexibility to adapt to VRES variability. These include the utilization of flexible generators, adjusting load profiles through demand-side management, integrating energy storage systems and electric vehicle batteries, developing grid infrastructure, using surplus energy for various daily applications (e.g., heating), and the implementing of curtailment practices. Demand-side management and energy storage, for example, offer valuable flexibility by allowing consumers to adjust their consumption patterns to electricity supply and demand fluctuations. Additionally, flexible generation technologies like gas turbines and combined heat and power systems provide rapid responses, aiding grid balance during high VRES output variability periods. Overall, this paper provides an overview of power system flexibility, exploring the various flexibility resources available to VRES-related challenges. Finally, this paper emphasizes the importance of continued innovation in developing new flexibility solutions to meet the growing demand for sustainable and reliable power systems.

**Keywords:** Power system flexibility, assessment of flexibility, variable renewable energy resources, demand-side management, electric vehicle.

### List of Abbreviations

Variable Renewable Energy Resources  
Renewable Energy Resources  
Microgrids  
Variable Renewable Generation  
Energy Storage System  
Demand Response  
European Union  
United States  
Demand-Side Management  
Electric Vehicles  
Vehicle-to-Home  
Vehicle-to-Vehicle  
Vehicle-to-Building  
Vehicle-to-Grid  
National Renewable Energy Laboratory

VRES  
RES  
MG  
VRG  
ESS  
DR  
EU  
US  
DSM  
EV  
V2H  
V2V  
V2B  
V2G  
NREL

### 1. Introduction

The Earth is experiencing a noticeable change due to the global warming. It has been changing significantly in recent years, and temperatures are rising at an unprecedented rate. This is largely due to human activities such as the burning of fossil fuels, deforestation, and industrial processes that release greenhouse gases into the atmosphere and trap heat from the sun. On the other hand, the increasing energy demand is causing a parallel increase in installed power that will lead to the installation of new power plants. The installation of new facilities constantly does not make economic sense. Hence, such environmental and economic issues pushed into societies to adopt new practices and technologies, leading among them is the increasing use of Renewable Energy Resources (RES).

This offers new opportunities for power systems and one of the opportunities that RES is taking in place of emission-emitting sources. Thus, the governments have implemented policies and incentives to encourage the use of renewable energy, and as technology has progressed, the cost of these sources has decreased year by year [1], making them increasingly viable. Also, thanks to natural disasters, which are defined as high-impact low-probability events, network outages can occur, leaving sufferers without power for extended periods of time. However, Microgrids (MG) equipped with RES are capable of operating in island mode, ensuring that critical facilities and infrastructure can continue to operate independently from the main grid. As a result, the penetration of RES has increased substantially in most parts of the world [2, 3].

These types of sources, mainly solar and wind, are considered as clean and sustainable energy sources contribute to decarbonization and reduction of greenhouse gases, however, they are also known as VRES [4] due to the *inherent variability and unpredictability of their generation profiles*, which depend on meteorological conditions. Their characteristics pose a significant challenge to the reliable and stable operation of the power system, as they can make difficult to maintain a stable supply-demand balance, especially when their penetration levels are high, which can lead to blackouts and other issues [5]. To address this challenge, maintaining the flexibility of the power system is essential [6, 7]. *Flexibility is the ability to deploy system resources in a way that responds to changes in net load. Here the net load is called as remaining system load that cannot be met by variable renewable generation (VRG) (e.g., solar and wind) as seen in eq. (1.1) [8].*

$$Net\ Load = Load - VRG \quad (1.1)$$

As flexibility could be provided through power plants with constant voltage/frequency output in the past, (i.e., dispatchable power plants) there were no problems with the concept of flexibility. Moreover, in conventional power plants, the reserve capacities of generation plants were also considered system flexibility [5, 6]. However, as the VRG installed capacity increases, existing power system flexibility is insufficient. Therefore, it is required to re-model the system's flexibility or create new flexibility options (i.e., *diversification in the flexibility resources*). Flexibility might be achieved through several means such as Energy Storage Systems (ESS), Demand Response (DR), and flexible generation. These flexible resources can cope with the inherent variability and unpredictability of VRES and ensure the continuity of power system stability.

In this paper, a comprehensive review of resources contributing to the flexible framework of power systems

is carried out, accompanied by evaluation of their present merits and drawbacks. The main contribution of the study is a detailed review and evaluation of the options that can be integrated into the system to ensure power system flexibility by coping with the challenges posed by the increasing penetration of VRES.

This paper is organized as follows. Section 2 gives what flexibility is. In Section 3, sources of flexibility in each part of the power system are reviewed. A brief of power system flexibility assessment and assessment indices are presented in Section 4. And lastly, the conclusion is outlined in section 5.

## 2. Power System Flexibility

The increasing spread of greenhouse gases resulting from the burning of fossil fuels, particularly in the electricity and transportation sectors, has led to environmental pollution and contributed to global warming, leading to climate change. To meet the emission reduction targets established by the European Commission and the White House, the European Union (EU) and United States (US) power sectors are required to cut CO<sub>2</sub> emissions from 2005 levels by 58% and 42% by 2030, with the potential for reductions of up to 79% and 83% by 2050 respectively [9]. On the other hand, to ensure that the world remains habitable, it is essential to limit the increase in global temperatures and reduce the risks and effects of climate change. As a response, the Paris Agreement was signed in 2015 to reduce carbon emissions by increasing the decarbonization policies of the states and limiting the average global temperature rise to below 2 degrees [10]. To achieve this goal, the penetration of RES into the power system network has increased. RES such as solar and wind are called VRES, due to their intermittent nature, their output is dependent on meteorological conditions, resulting in fluctuations in supply and demand that cause a mismatch between of two. The imbalance can compromise the operational reliability of the power system, making flexibility an inevitable concept for the secure and reliable operation of power systems with a high share of VRES penetration. To fulfill the flexibility requirements, three different types of flexibility have been identified:

- 1) Short-Term Flexibility: It is based on estimated fluctuations in the balance of supply and demand, short-term is in the form of hour-to-hour.
- 2) Mid-Term Flexibility: It depends on the number of thermal power plants that must remain connected and operate in the system. Mid-term is in the form of hour-to-day.
- 3) Long-Term Flexibility: This type of flexibility is based on the annual and seasonal availability of VRG and electricity demand. Long-term is in the form of days, weeks, months, and years.

### 3. Sources of Power System Flexibility

Conventional generation in power systems is gradually being replaced by power systems based on VRG. It is not enough to provide the flexibility of such a system with a single source of flexibility multiple options are required [6, 8, 10]. In order to be able to say that a power system is flexible, it must always be able to ensure supply-demand balance, be able to cover changes in the amount of production caused by variable renewable energy sources, and reconfigure quickly in case of possible outages [12]. For this purpose, the resources given in the list below are defined as a source of flexibility and depicted in Figure 1.

- 1) Flexible Generators
- 2) Demand-Side Management (DSM)
- 3) Energy Storage Systems (ESSs)
- 4) Grid Infrastructure
- 5) Operational Procedures
- 6) Convert Excessive Electricity into Thermal Energy
- 7) Electric Vehicles (EVs)
- 8) Curtailment of Surplus Renewable Generation

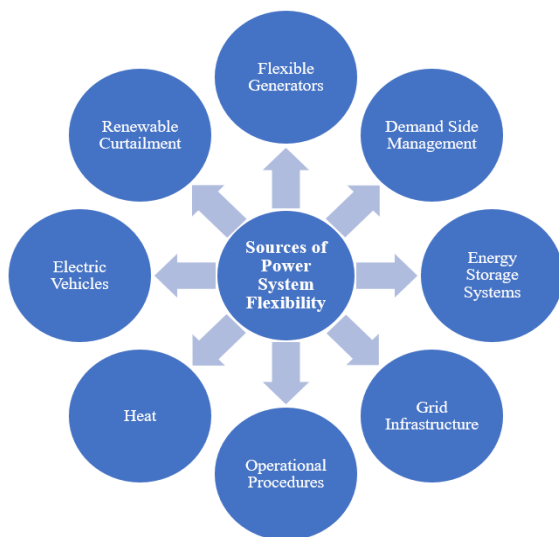


Figure 1. Sources of power system flexibility.

#### 3.1 Flexible Generators

Flexible generators are one of the key resources of power system flexibility that can respond reliably and quickly to changes in supply and demand. These types of generators have the ability to ramp up and down their output quickly, making it convenient to balance the intermittent output of VRES [8]. Flexible generation resources can include gas-fired power plants and some types of renewable energy sources that have controllable output such as hydropower [13]. Generation plants are divided into three different groups according to their economic and technical attributes as follows:

- 1) Base Load Power Plants: These power plants are operated at the rated power level. Due to their characteristics, they are used to supply the base load and continuously operated plants (e.g., hydropower plants, and nuclear power plants). These plants have a slow start-up time which reaches an hour to one day.
- 2) Intermediate (Load Following/Mid-Merit) Power Plants: In these plants, the generation of electricity is adjusted according to fluctuation in demand. They are located between peak and base load power plants to factors such as efficiency, cost, capacity, etc.
- 3) Peak Load Power Plants: These plants such as solar power plants, are used at high-demand times. They are fast start-up power plants with the ability to reach full capacity within a few minutes after a cold start. These plants are crucial for the system's reliability since they ensure reserve generation.

#### 3.2 Demand-Side Management (DSM)

This term, known as load management before, was first used by Clark Gellings in 1984 [14], is an initiative by electrical services to encourage consumers to change their load patterns through different techniques -either horizontal axis (time) or vertical axis (magnitude)- for the benefit of the grid. It has a key place in terms of flexibility by trying to provide a balance between supply and demand both on the consumer side and on the grid side.

DSM aims to extend the consumption of peak hours throughout the day, to reduce technical losses in networks, provide energy efficiency, and benefit both sides of the grid by reducing the bills of end-users [15]. Since the majority of global consumption occurs in the residential sector [16], DSM techniques, including peak clipping, valley filling, strategic protection, strategic load growth, load shifting, and flexible load shape, involve optimizing the operation of household appliances to match the existing generation value to demand. Scheduling operations of washing machines and dishwashers during off-peak hours instead of peak hours can be said as an example [17]. The six techniques defined below, are shown in Figure 2 respectively from a) to f).

- 1) Peak Clipping: It refers to the reduction of demand on-peak period.
- 2) Valley Filling: Related to its incentives for energy consumption during off-peak hours, when the cost of generation is lower than during on-peak hours.
- 3) Load Shifting: This technique identifies shifting some part of a demand from the on-peak period to the off-peak period. In load shifting, total energy consumption does not change i.e., the average power is the same but peak power is reduced. This is why, the load factor which is a ratio of average power over peak power will increase in this method, and the efficiency of energy use will increase as well. Moreover, it is possible to say that load

shifting is a combination of peak clipping and valley filling.

4) Strategic Conservation: Directs at reducing energy consumption by reducing energy waste to improve energy consumption efficiency.

5) Strategic Load Growth: Refers to an increase in electrical energy.

6) Flexible Load Shape: The last technique of DSM describes limiting energy use of the consumer at certain times thanks to load-limiting devices. This technique does not affect the security conditions.

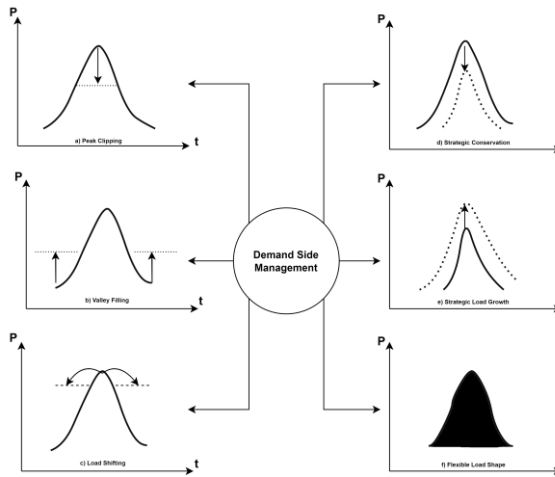


**Figure 2.** Demand-side management techniques (x-axis represents time, y-axis represents load.).

### 3.3 Energy Storage Systems (ESSs)

Energy storage systems (ESSs) have a vital role in increasing the flexibility of the power system when there is a high share of VRES penetration. ESSs are charged during hours of low demand, while base load power plants can operate at high efficiency. Also, when VRG has excess power generation, they store the surplus energy. The stored energy can be used instead of peak load power plants during high demand-insufficient generation periods which can help supply-demand balance and stabilize the power system.

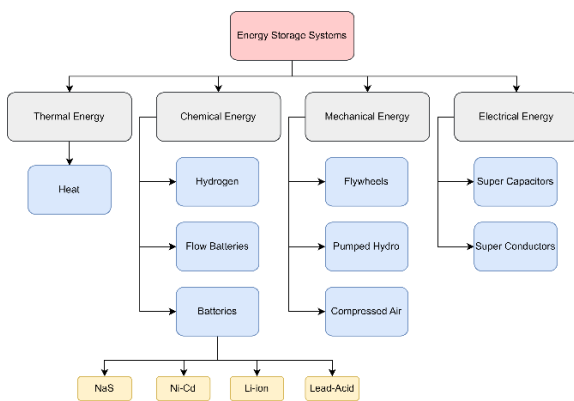


**Figure 3.** Types of energy storage systems [11].

Additionally, ESSs can provide backup power in case of power outages due to catastrophic events like earthquakes or malfunction of equipment. It can be therefore said as a flexible source and contributes to power system flexibility and reliable operation.

ESSs can be used as three different support services: load shifting service, short-term balancing service, and quick-acting instantaneous service [18]. According to their energy types, ESSs are classified into four types that are thermal, chemical, mechanical, and electrical. ESSs types are given in Figure 3.

### 3.4 Grid Infrastructure

Grid infrastructure involves all transmission lines, distribution lines, communication tools, and control equipment. Since the large-scale integration of VRES

into the power system and high-level supply security is required, more flexibility is needed [19]. Grid flexibility acts as a hyperlink between supply and demand side flexibilities. It is essential for the power system that the line capacities are sufficient [20]. If there is sufficient infrastructure, then supply can always reach demand everywhere in the power system with minimum cost [21].

### 3.5 Operational Procedures

It relies on how elements of the system are operated. The reason those operational procedures are considered a source of flexibility, they include methods for regulating the output of generating units to maintain the stability in the grid. The operational flexibility of the system refers to the ability to modify its generation or consumption regarding variability [22]. A large share of VRG in the power systems means that the energy generated from these sources will be excessive. This indicates that the operation of power systems will also become more difficult. Therefore, the flexibility requirements must be greater than before. Herein, choosing the proper operational procedure assists in providing reliable electricity to the customer at the lowest cost as much as possible. System operator needs accurate information which is related to balancing supply and demand because of changes in variable renewable generation from hour to hour.

Due to the high cost of ESSs, lower-cost flexibility options such as accurate forecasting also need to be identified [23]. Accurate forecasting of VRG output is important to manage its variability and thanks to forecasting, dispatchable generation output can be adjusted precisely. Therefore, advanced forecasting techniques must be used. On the other hand, it is especially important to balance changes on the demand side. At the same time, one of the important factors is to have coordination with neighboring regions for the import and export of electricity [11].

### 3.6 Convert Excessive Electricity into Thermal Energy

Surplus generation of renewables converted into thermal energy adds a flexibility option to the power system because of the fact that it is easier to store thermal energy than electrical energy [11]. It is both economical and efficient to convert the surplus amount of renewable energy into thermal energy to use for heating and cooling objectives [24]. Besides, this contributes to reducing carbon emissions from heating power plants by replacing fossil fuels with electricity.

### 3.7 Electric Vehicles (EVs)

The development of electric vehicle technologies is considered a solution for the energy and environmental crisis today and especially in the future. In terms of energy, EVs, are emerging as a promising technology for providing mobile power source during contingencies [25]. EVs can serve as a reliable backup power source to ensure energy availability for critical demands such as hospitals, communication networks, etc. during power outages caused by natural disasters or other unforeseen events.

Additionally, EVs just as the ESSs, equipped with bidirectional chargers, can provide energy storage to balance grid fluctuations, and reduce the impact of intermittency of VRES. In terms of flexibility option, EVs have some modes such as Vehicle-to-Home (V2H), Vehicle-to-Vehicle (V2V), Vehicle-to-Building (V2B), and Vehicle-to-Grid (V2G) through bidirectional inverters. V2G mode, shown in Figure 4, is called the situation in which the EV discharges the energy stored from the grid as a result of optimizations depending on the conditions in which it is located. When EV is charged, energy flows grid to the vehicle. When demand is high at on-peak hours, EV is discharged and energy flows from vehicle to grid through a unit that has bidirectional converter like the battery energy storage systems.



**Figure 4.** V2G technology flow diagram.

The bidirectional V2G (and the other technologies too) offers the option of flexibility to enhance the power system operations such as supporting the network, power factor control, load balancing, voltage regulation, etc. [26]. Furthermore, EVs can effectively support grid services such as DR, peak clipping, and contributing to a more sustainable and resilient power system.

By providing this flexibility to the power system, EVs can also help to improve the reliability and resiliency of the power system during normal and emergency conditions. Five EV types are defined in terms of technologies [27].

- 1) EV: This type of EV's called a pure electric vehicle. They include electric motors, supercapacitors, and batteries.
- 2) Hybrid EV: It is comprised of supercapacitors, batteries, and an electric motor, and they also have a combustion engine. To move the wheels of the car, both an electric motor and a combustion engine are used.
- 3) Plug-in Hybrid EV: Plug-in hybrid EV involves supercapacitors, batteries, an electric motor, and a combustion engine the same as Hybrid EVs. But unlike them, the battery must be charged for using the electric motor. Also, they have bigger electric motors and larger capacity batteries than Hybrid EVs.
- 4) Range Extended EV: They are just like the Hybrid EV and Plug-in hybrid EV, i.e., comprise of a combustion engine. But this combustion engine is not provided power to the vehicle but is used as a generator when the batteries run out of charge.
- 5) Fuel Cell EV: Fuel cell EV includes electric motors and fuel cells. Fuel cells provide energy to the motor not batteries. It cannot be pluggable.

However, it should also be taken into account that EVs can have a negative impact on the power system as of now. One of the most significant challenges is that as the number of EVs on the network increases, particularly during peak charging periods [28], it can result in grid congestion and necessitate significant and costly grid upgrades. This not only entails considerable costs but also potential disruptions and delays in implementation.

### 3.8 Curtailment of Surplus Renewable Generation

One of the main challenges of VRG is, in some cases it is not feasible to store or use it. Therefore, it must be curtailed. If we are looking at curtailment on the side of generation, in this situation we need to use existing RES as a primary priority and curtail the generation of emission emitting sources. According to the report published by National Renewable Energy Laboratory (NREL), it is more valid for system operators to curtail generation from wind and solar power plants when minimum generation levels are reached at some fossil fuel plants. Because these plants take a long time to be started up and shut down. Thus, they may be more costly compared to curtailing short-term renewable generation [29]. Although this situation is helpful on the one hand because the supply-demand balance is maintained, nevertheless, since there is a curtailment on RES, we cannot benefit from them i.e., this is called loss technically. This disadvantage can be coped with by using storage systems [30].

In Figure 5, the curtailment event in California on 13 May 2018 is given. As seen in the figure, solar system had been online at nearly 6 a.m. From here, some flexible generators have been shut down to make room for the generated solar energy. However, as some of the non-variable renewable generations (dispatchable generation) ensure reliability of the power system cannot be ramped up or shut down for temporarily. Hence, supply exceeded the system load, and the condition called **overgeneration** occurred. In order to maintain the supply-demand balance, the system curtailed by approximately 12 GWh of solar output [31]. It is also seen in Figure 5, drawn in red.

VRG is curtailed when the following situations occur [10, 29].

- Limited transmission line capacity,
- Over supply of VRG when demand is low,
- Absence of neighboring areas or even if there is, they have sufficient generation,
- In cases such as high share of base load power plants which are inflexible in the power system.

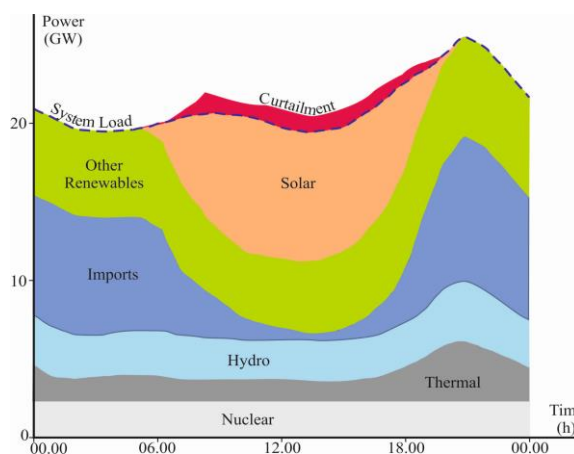


**Figure 5.** PV curtailment event in California on 13 May 2018 [31].

Table 1 provides a comprehensive overview of the various publications that address the aforementioned sources of flexibility. The objectives of the studies, the use of flexibility options and the research objectives aimed to achieve can be found in this table.

#### 4. Assessment of Power System Flexibility

The existing flexibility of the system must be assessed and determined which part of the system will be improved before optimization. After the optimization process is completed, flexibility of the system is re-evaluated. Following then, the optimization process is repeated if requires. As a result, this is a cycling process. Appropriate indices are needed to evaluate the flexibility. Today experts are determined three different index categories which are device-level flexibility quantitative

index, network-level flexibility quantitative index, and system-level flexibility quantitative index [33].

- 1) Device-level flexibility quantitative index: This index relates to flexibility of power supplies, energy storage systems and more devices. Today in most literatures for this index ramp rate, operational limits etc. are considered.
- 2) Network-level flexibility quantitative index: Topology of the network and capacity of each branch affect capacity of transmission lines of the network. Also, economic limitations should be considered.
- 3) System-level flexibility quantitative index: By considering time scale, economic cost, and response amplitude this index is used to measure the flexibility regulation ability of the entire system.

#### 5. Conclusion

With the developing technology, both sources and producers (e.g., share of VRES increases in the power system), which are different from traditional network structures, have diversified undoubtedly. In this structure, the flexibility advantages provided by the large powerful units, the base load power plant, which have a good ability to respond to disruptive effects, are gradually decreasing. To continue in reliable operating conditions in power systems, the development of flexibility requirements is one of the key options. Due to the stochastic nature of these sources (i.e., the energy they give to the system can be varied from hour-to-hour.) and diversified loads, flexibility gap that will occur in the system should be covered by other options/sources of flexibility.

The scientific aim of the review study is to provide an overview and assessment of power system flexibility and sources of flexibility that can be on the generation side, on the end-user side, etc. in many parts of the network. The options to enhance power system flexibility are examined in Section 3. These are:

- Flexible generators,
- Rearrangement of the load curve with DSM on the end-user side without affecting user's comfort,
- Storing a surplus of VRG with ESSs or EVs to use during on-peak hours,
- The status of grid infrastructure,
- Converting this surplus VRG into thermal energy so that it can be used for heating and cooling purposes,
- The inflexible power plants cannot be taken off the system, so to prevent overgeneration and maintain supply-demand balance, curtailment of surplus VRG is necessary (This situation is being worked to reduce.).

With the help of the resources mentioned above, problems can be avoided by having a more flexible

structure of the power system against the intermittent situation of VRES, whose installed capacity will increase even more in the future. Therefore, this research will be helped to the studies by contributing to the formation of ideas about how measures can be taken already before such a problem occurs in the future.

### Acknowledgement

No particular funding grant was received by this research from agencies in the public, commercial, or not-for-profit sectors.

### Author's Contributions

**Emir Kaan TUTUS:** Conceptualization, investigation-literature survey, visualization, writing-original draft  
**Nevzat ONAT:** Supervision-the researching process, helped in manuscript preparation, visualization, writing-review&editing.

### Ethics

There are no ethical issues after the publication of this manuscript.

**Table 1.** Highlights of the studies oriented on flexibility in the power systems.

Ref. No.	Aim of the paper	Results	Which flexibility options were used
[34]	Reviewing on the flexibility quantification methods, which are divided into 2 as deterministic and probabilistic approaches. The formulas and shortcomings of several of them are examined.	As a result of the research, deterministic flexibility quantification approaches yield inaccurate results in the high renewable energy penetration and the integration of demand-side resources into the system. Hence, a probabilistic approach is the preferred method for addressing intermittent net load changes within operational timeframes.	-
[17]	Optimizing the operation of household appliances in a smart home setting using renewable energy sources. The study seeks to achieve this by utilizing power forecasts and electricity tariffs to ensure the most economic operation of appliances while maintaining a desired level of comfort in the home. The ultimate goal is to ensure that the smart home can run on renewable energy sources for the longest possible time while minimizing costs and maintaining the expected level of comfort.	The reduction of electricity cost for selected two months and the year are 4.23% 2.93% respectively,  In addition to cost reduction, shifting operations are decreased 32.65% and 52.99% for dishwasher and washing machine respectively. This demonstrates that comfort level is increased.	DSM
[25]	The study aims to develop a smart home energy management system that ensures uninterrupted energy supply in post-disaster by utilizing renewable energy sources and electric vehicles. The proposed algorithm prioritizing critical appliances and ensuring their operation during power outages, while optimizing the use of available energy sources.	The simulation studies showed that the proposed algorithm resulted in a 25% to 471% increase in energy supply time compared to the conventional algorithm in the worst and best scenarios, respectively. Based on these results, the remaining energy values of the electric vehicle battery (EVB) ranged from 5.08 kWh to 2.67 kWh with the proposed algorithm, while the conventional algorithm consumed all the EVB energy. Therefore, it can be concluded that the proposed algorithm prevented the battery from running out.	DSM, EVs

- [35] Minimization of generation and investment cost. In comparison with the base case, integration both wind and DSM reduced generation and investment cost about 20%. DSM
- [36] Investigation of the effects of DSM, which is seen as a source of flexibility in power systems, on the angular stability of the system under different conditions. It is seen that the effect of DSM on angular stability depends on the operating conditions of the power system, The location and capacity of the DSM applied also play a role in angular stability. DSM
- [37] Investigation of the potential impact of demand-side flexibility (provided by DR) on the market performance of a European-wide daily electricity market under the high share of RES by 2030. It is seen that the DR reduced the cost by 8-9% for cost minimization, also the total curtailment in Europe decreased by more than 90% thanks to the DR, Another result is, increasing demand-side flexibility in integrated electricity markets with high level of VRES does not have to improve the load factor, even reduce it, it has been seen in the simulation results. Demand-side flexibility (with DR)
- [38] Planning the long-term energy transition of electric power systems from fossil fuel to the of high share of renewable energy (75%, even 90%). Depending on penetration of RESs in Chilean power system (minimum 75% in 2050), CO<sub>2</sub> emission will only reduce 40% in pessimistic scenario. However, this ratio will be almost 94% in optimistic scenario according to data obtained in 2016 (36MtCO<sub>2</sub>). BESS, transmission lines, and curtailment
- [39] Mixing existing and new generating plants (with a high level of RES) with the lowest cost to meet South Africa's predicted annual energy of 382 TWh for 2050. If prices fall as much as the determined values, solar and wind energy are installed 50% and 20% more, respectively. Also, 17 GW/48 GWh batteries will be able to be deployed by 2050 in these circumstances. This indicates that the battery will account for 35% of the flexibility resources. Pumped storage, peaking open cycle gas turbines, BESS with Li-Ion
- [40] Ensuring the generation of more renewable energy (with wind) in an isolated energy system by 2030, also ensuring the regulations with Vehicle-to-Grid and heat pumps instead of thermal generators. Compared to the reference case, the heat pump and V2G technology with different battery capacities (4-10-16 MW) is used in the other cases. As a result, a wind energy penetration of 25-30-36 MW was achieved, respectively, EV based ESS
- [41] Analyzing the role of electrolyzer in increasing power system flexibility by This study shows that, despite the impact of restrictions caused by the Electrolyzers

considering hydrogen injection connection to the gas network, the constraints. conversion of excess renewable energy into hydrogen with electrolyzers and ensuring its use in the gas network can be an important potential for increasing power system flexibility.

[42] Investigating the link between smart grids, network flexibility, and optimization models, considering short and long-term flexibility with a focus on renewable energy. It's relevant for entities planning renewable integration to enhance energy stability and reduce costs.

The addition of wind turbines, even with forecast errors, reduces the need for power plants as fossil fuel generators are replaced by wind turbines.

Some scenarios are inducted, and it is seen that in order to achieve greater flexibility, more power plants are needed in scenarios where wind energy with fluctuation is demonstrated.

Flexible generators and wind turbines

## References

- [1]. M. T. Irena, *Renewable Power Generation Costs in 2022*. 2022.
- [2]. Sancar, S, Erenoğlu, AK, Şengör, İ, Erdinç, O. 2020. Güneş Kollektörlü ve Elektrikli Şofbenli Bir Akıllı Evin Talep Cevabı Programı Kapsamında Enerji Yönetimi. *Avrupa Bilim ve Teknoloji Dergisi*; (19): 92–104.
- [3]. Papyiannis, I, Asprou, M, Tziouvani, L, Kyriakides, E. Enhancement of power system flexibility and operating cost reduction using a BESS, IEEE PES Innovative Smart Grid Technologies Conference Europe, Delft, Netherlands, 2020, pp 784–788.
- [4]. IRENA (2018). 2018. Power System Flexibility for the Energy Transition, Part 1: Overview for policy makers. *International Renewable Energy Agency*; 1-48.
- [5]. Akrami, A, Doostizadeh, M, Aminifar, F. 2019. Power system flexibility: an overview of emergence to evolution. *Journal of Modern Power Systems and Clean Energy*; 7(5): 987–1007.
- [6]. Babatunde, O M, Munda, JL, Hamam, Y. 2020. Power system flexibility: A review. *Energy Reports*; 6: 101–106.
- [7]. Saygin, D, Tör, O B, Cebeci, ME, Teimourzadeh, S, Godron, P. 2021. Increasing Turkey's power system flexibility for grid integration of 50% renewable energy share. *Energy Strategy Reviews*; 34: 100625.
- [8]. Jakhar, A. A comprehensive review of power system flexibility, IEEE International Conference on Power, Control, Signals and Instrumentation Engineering, ICPCSI 2017, Chennai, India, 2018, pp. 1747–1752
- [9]. Brouwer, A. S., Van Den Broek, M., Seebregts, A., Faaij, A., 2014. Impacts of large-scale Intermittent Renewable Energy Sources on electricity systems, and how these can be modeled, *Renewable Sustainable Energy Reviews*; 33: 443–466.
- [10]. Horowitz, C. A. 2016. Paris Agreement. *International Legal Materials*; 55(4): 740–755.
- [11]. Eltohamy, MS, Moteleb, MSA, Talaat, H, Mekhemer, SF, Omran, W. Overview of Power System Flexibility Options with Increasing Variable Renewable Generations, ACCS/PEIT 2019 - 2019 6th International Conference on Advanced Control Circuits and Systems and 2019 5th International Conference on New Paradigms in Electronics and Information Technology, Hurgada, Egypt, 2019, pp 280–292.
- [12]. Langevin, J., Harris, C. B., Satre-Meloy, A., Chandra-Putra, H., Speake, A., Present, E., Adhikari, R., Wilson, E.J.H., Satchwell, A. J. 2021. US building energy efficiency and flexibility as an electric grid resource. *Joule*; 5(8): 2102–2128.
- [13]. Gjorgievski, V. Z., Markovska, N., Abazi, A., Duić N. 2021. The potential of power-to-heat demand response to improve the flexibility of the energy system: An empirical review, *Renewable Sustainable Energy Reviews*; 138: 110489.
- [14]. P. Warren, "A review of demand-side management policy in the UK," *Renew. Sustain. Energy Rev.*, vol. 29, pp. 941–951, 2014, doi: 10.1016/j.rser.2013.09.009.
- [15]. Gaur, G, Mehta, N, Khanna, R, Kaur, S. Demand side management in smart grid environment, 2017 IEEE International Conference on Smart Grid and Smart Cities Demand, Singapore, 2017, pp 227–231.
- [16]. Taşçıkaraoğlu, A, Erdinç, O. 2019. Paylaşımlı Elektrik Enerjisi Depolama Sisteminin Kullanımına Dayanan Bir Enerji Yönetimi Yaklaşımı. *European Journal of Science and Technology*; 16: 589–604.
- [17]. Tascikaraoglu, A, Boynuegri, AR, Uzunoglu, M. 2014. A demand side management strategy based on forecasting of residential renewable sources: A smart home system in Turkey. *Energy and Buildings*; 80: 309–320.
- [18]. Flexibility Requirements and Potential Metrics for Variable Generation: Implications for System Planning Studies. *North American Electric Reliability Cooperation*; 1-55, 2010.
- [19]. Lund, PD, Lindgren, J, Mikkola J, Salpakari J. 2015. Review of energy system flexibility measures to enable high levels of variable renewable electricity. *Renewable Sustainable Energy Reviews*; 45: 785–807.

- [20]. Haidl, P, Buchroithner, A, Schweighofer, B, Bader, M, Wegleiter, H. 2019. Lifetime analysis of energy storage systems for sustainable transportation. *Sustainability*; 11(23): 1–21.
- [21]. Schreiner, L, Madlener, R. 2022. Investing in power grid infrastructure as a flexibility option: A DSGE assessment for Germany. *Energy Economics*; 107: 105843.
- [22]. Vargas-Ferrer, P, Álvarez-Miranda, E, Tenreiro, C, Jalil-Vega, F. 2022. Assessing flexibility for integrating renewable energies into carbon neutral multi-regional systems: The case of the Chilean power system. *Energy for Sustainable Development*; 70: 442–455.
- [23]. Denholm, P, Margolis, R. 2016. Energy Storage Requirements for Achieving 50 % Solar Photovoltaic Energy Penetration in California. *National Renewable Energy Laboratory*; 1-37, <https://www.nrel.gov/docs/fy16osti/66595.pdf>. (accessed at 10.08.2022).
- [24]. Mathiesen, BV, Lund, H. 2009. Comparative analyses of seven technologies to facilitate the integration of fluctuating renewable energy sources. *IET Renewable Power Generation*; 3(2): 190–204.
- [25]. Candan, AK, Boynuegri, AR, Onat N. 2023. Home energy management system for enhancing grid resiliency in post-disaster recovery period using Electric Vehicle. *Sustainable Energy, Grids and Networks*; 34: 101015, 2023.
- [26]. Sami, I, Ullah, Z, Salman, K, Hussain, I, Ali, SM, Khan, B, Mehmood C A, Farid, U. A bidirectional interactive electric vehicles operation modes: Vehicle-to-grid (V2G) and grid-to-vehicle (G2V) variations within smart grid, 2019 International Conference on Engineering and Emerging Technologies, ICEET 2019, Lahore, Pakistan, 2019, pp 1-6.
- [27]. Ricardo, M, Contreras, F, Alexander, B, Beltran, V, Armando, D, Ramirez, G. 2021. Electric Vehicles within the Distributed Generation. *International Journal of Engineering Research and Technology*; 14(9): 887–894.
- [28]. Zhang, B., Kezunovic, M., 2016. Impact on Power System Flexibility by Electric Vehicle Participation in Ramp Market. *IEEE Transaction on Smart Grid*; 7(3): 1285–1294.
- [29]. Bird, L, Cochran, J, Wang, X. 2014. Wind and Solar Energy Curtailment: Experience and Practices in the United States. *National Renewable Energy Laboratory*; 1-58, <http://www.osti.gov/servlets/purl/1126842/>. (accessed at 15.09.2022).
- [30]. Riaz, S, Chapman, AC, Verbic, G. Comparing utility and residential battery storage for increasing flexibility of power systems, 2015 Australasian Universities Power Engineering Conference: Challenges for Future Grids, AUPEC 2015, North Wollongong, Australia, 2015, pp 1-6.
- [31]. O’Shaughnessy, E, Cruce, JR, Xu, K. 2020. Too much of a good thing? Global trends in the curtailment of solar PV. *Solar Energy*; 208: 1068–1077.
- [32]. Fink, S, Mudd, C, Porter, K, Morgenstern, B. 2009. Wind Energy Curtailment Case Studies. *National Renewable Energy Laboratory*; 1-48, <http://www.nrel.gov/docs/fy10osti/48737.pdf>. (accessed at 26.12.2022).
- [33]. Xing, T, Caijuan, Q, Liang, Z, Pengjiang, G, Jianfeng, G, Panlong, J. A comprehensive flexibility optimization strategy on power system with high-percentage renewable energy, 2017 2nd International Conference on Power and Renewable Energy, ICPRE 2017, Chengdu, China, 2018, pp 553–558
- [34]. Jain, AP, Yamujala S, Bhakar R. Quantification of Power System Flexibility: A Review, 2022 OPJU Int. Technol. Conf. Emerg. Technol. Sustain. Dev. OTCON 2022, Raigarh, Chhattisgarh, India, pp. 1–6, 2023
- [35]. Rosso, A, Ma, J, Kirschen, DS, Ochoa, LF. Assessing the contribution of demand side management to power system flexibility, Proceedings of the IEEE Conference on Decision and Control, Orlando, Florida, USA, 2011, pp 4361–4365
- [36]. Wang, M, Milanovic, JV. Contribution of Advanced Demand Side Management to Angular Stability of Interconnected Transmission Networks, Proceedings of 2019 IEEE PES Innovative Smart Grid Technologies Europe, ISGT-Europe 2019, Bucharest, Romania, 2019, pp 1–5.
- [37]. Zalzar, S, Bompard, EF. Assessing the Impacts of Demand-Side Flexibility on the Performance of the Europe-Wide Integrated Day-Ahead Electricity Market, SEST 2019 - 2nd International Conference on Smart Energy Systems and Technologies, Porto, Portugal, 2019, pp 1-6.
- [38]. Seshu Kumar, R, Phani Raghav, L, Koteswara Raju, D, Singh, AR. 2021. Impact of multiple demand side management programs on the optimal operation of gridconnected microgrids. *Applied Energy*; 301: 117466.
- [39]. Klein, P, Carter-Brown, C, Wright, JG, Calitz, JR. 2019. Supply and demand side flexibility options for high renewable energy penetration levels in south africa. *SAIEE Africa Research Journal*; 110(3): 111–124.
- [40]. Pillai, JR, Heussen, K, Østergaard, PA. 2011. Comparative analysis of hourly and dynamic power balancing models for validating future energy scenarios. *Energy*; 36(5): 3233–3243.
- [41]. De Corato, AM, Riaz, S, Mancarella, P. Assessing the Flexibility of Electricity-Gas-Hydrogen Distribution Systems with P2G Units, 2021 IEEE PES Innovative Smart Grid Technologies - Asia, ISGT Asia 2021, Brisbane, Australia, 2021, pp 1–4.
- [42]. Coban, H. H., Lewicki, W., 2023. Flexibility in Power Systems of Integrating Variable Renewable Energy Sources *Journal of Advanced Research in Natural and Applied Sciences*; 9(1): 190–204.

# Enhanced Microfluidics Mixing Performance in a Grooved Serpentine Microchannel at Different Flow Rates

Faruk Aksoy<sup>1,2</sup> , Gurkan Yesiloz<sup>1,2\*</sup> 

<sup>1</sup>National Nanotechnology Research Center (UNAM) - Bilkent University, Çankaya-Ankara, Türkiye

<sup>2</sup>Institute of Material Science and Nanotechnology, Bilkent University, Çankaya-Ankara, Türkiye

\*[gurkan@unam.bilkent.edu.tr](mailto:gurkan@unam.bilkent.edu.tr)

\*Orcid No: 0000-0002-1769-8201

Received: 06 May 2023

Accepted: 04 September 2023

DOI: 10.18466/cbayarfbe.1293522

## Abstract

Reliable and efficient mixing in microfluidic systems is crucial for various applications such as molecular diagnostics, DNA hybridization, microreactors and nanoparticle synthesis. However, achieving adequate mixing at the microscale is challenging due to the fact that flow regime in microfluidics is laminar that is characterized by low Reynolds numbers. In an attempt to tackle this challenge, active and passive strategies have been utilized to enhance mixing. Passive techniques mainly rely on the interaction between fluid and channel geometry in order to extend the interface between the components of the fluid by inducing transversal flows. Passive methods have shown their simplicity over the active methods in microfluidics by simply controlling the channel geometry and flow configurations without involving any complex external forces and components. Based on this, our work presents a passive micromixer design with trapezoidal grooves placed at the bottom of the serpentine channels. The grooves induce periodic pressure drops along the channel which create staggered transversal vortices in orthogonal directions which disturbs the symmetries in the flow that results in stirring. These combined effects result in an enhanced mixing performance especially at higher flow rates. The results suggest that the design could be integrated into lab-on-a-chip systems to achieve enhanced mixing of biological or chemical components with reduced footprint, complexity and cost.

**Keywords:** Microfluidics; passive micromixers; grooved serpentine channels; mixing index; enhanced microfluidic mixing; computational fluid dynamics

## 1. Introduction

Lab-on-a-chip systems and microfluidic devices are extensively used in biological and chemical sciences [1,2] for various applications spanning from the synthesis of colloidal systems and nanoparticles (NPs) [3,4] to cell biology [5] and molecular diagnostics [6,7], owing to their ability to spatially control liquid composition with cellular resolution [8], reduced consumption of reactants [9], and the better control over reaction variables such as the reactant concentration and temperature [10]. Ideally, the utilization of these devices in biological assays/bioengineering and chemical analysis requires them to be capable of efficiently mixing predictably two or more biological or chemical components [11]. Thus, mixing element is one of the most critical and a fundamental building block in the development of microfluidic systems. However, it is also one of the

difficult functionalities to achieve because the length scales involved in microfluidics force a laminar flow regime that is characterized by low Reynolds numbers.

A number of research activities on this subject is continued to be carried out in order to achieve efficient mixing at the microscale. The employed methods, reported in the literature, to enhance mixing in laminar flow, diffusion-dominated, microscale regimes, are classified as either active or passive. Active techniques incorporate external actuators with the micromixer design in order to add an external force on the fluids in an effort to enhance mass transport within the micromixer and mix the unmixed inhomogeneous fluid solution [12]. Even though these strategies have proven to have good mixing capabilities, it comes at the price of more complex designs that are harder to integrate into analysis systems, and expensive scale-up.

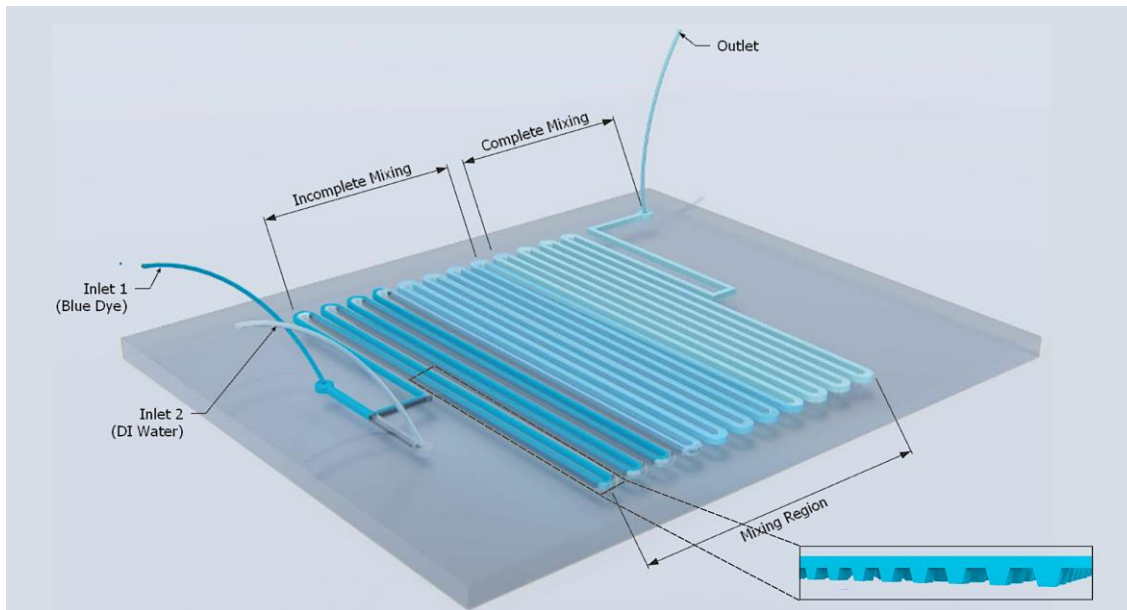


**Figure 1.** Schematic of the developed grooved serpentine microchannels for enhanced mixing.

Passive strategies, on the other hand, rely on the interactions between fluid and channel geometry. Such enhanced interactions induce transversal flows that stretch the interface between the fluids components to be mixed, and cause advection and/or breaking the symmetries in the flow [13].

In literature, numerous studies have been reported about enhancing mixing using passive techniques. The reported methods mainly rely on either chaotic and lamination advection-based designs [14-19], or utilized geometric manipulations to induce chaotic advection [20-27]. However, such passive designs that integrate obstacles/microstructure to disrupt fluid and increase mass transport, can impose very high localized strains which is capable of damaging biomolecules due to generated high shear stresses. Serpentine-based mixers have proven to prevent this damage because chaotic advection, due to high local strains, does not occur in these channels [28]. The centrifugal forces exerted by the curvy edges of the serpentine on the fluid, i.e., Dean flow, are accountable for this privilege. However, simple serpentine channels require longer footprint to achieve complete and homogeneous mixing, and usually causing inefficient mixing at higher flow rates.

Based on this, the proposed design investigated in this work involves a comparison in mixing performance between a simple serpentine micromixer and a grooved serpentine micromixer composed of 3D-trapezoidal grooves aligned to the bottom side of the microchannel. The current study takes the advantage of the fact that grooves induce staggered transversal vortices that are vertical for the grooves and horizontal for the main serpentine channel making two flows in orthogonal directions coupled with the Dean flow induced streamlines due to the serpentine itself.

Thus, an amplified transport of mass between the fluids which results in an enhanced mixing efficiency.

## 2. Materials and Methods

### 2.1. Experimental Setup and Fabrication

The experimental setup consists of two microfluidic chips integrated with a fluid pumping unit (Syringe pumps, Rotalab NE-4000), and an inverted microscope (Zeiss, Axio Observer 7) equipped with a CCD camera. The schematic of the developed microfluidic mixer unit is demonstrated in Figure 1.

#### 2.1.1. Chip Fabrication

Soft lithography and 3D printing techniques are used to fabricate the proposed microfluidic chip. Briefly, after the master fabrication, 10:1 ratio of polydimethylsiloxane (PDMS) to curing agent is prepared, mixed and poured onto two masters; one containing the simple serpentine and other containing the grooves design separately. After curing the PDMS at 65° C on hot plate for 2 hrs PDMS is peeled off followed by the bonding of the simple serpentine with the grooves with fine alignment under microscope after oxygen plasma treatment. The final design is then bonded into a glass slide after oxygen plasma treatment. Fabrication is finished by a post baking of the chip at 45° C for 2 hrs.

#### 2.1.2. PDMS Surface Treatment

After chip fabrication, a PDMS surface treatment is done to remove any possibility of air bubbles. For this, the microchannel is flushed with a chemical composition containing 1:2 of TEOS to ethanol (v/v). The solution is left for 5 minutes for incubation. Later, the chip is washed with Deionized water.

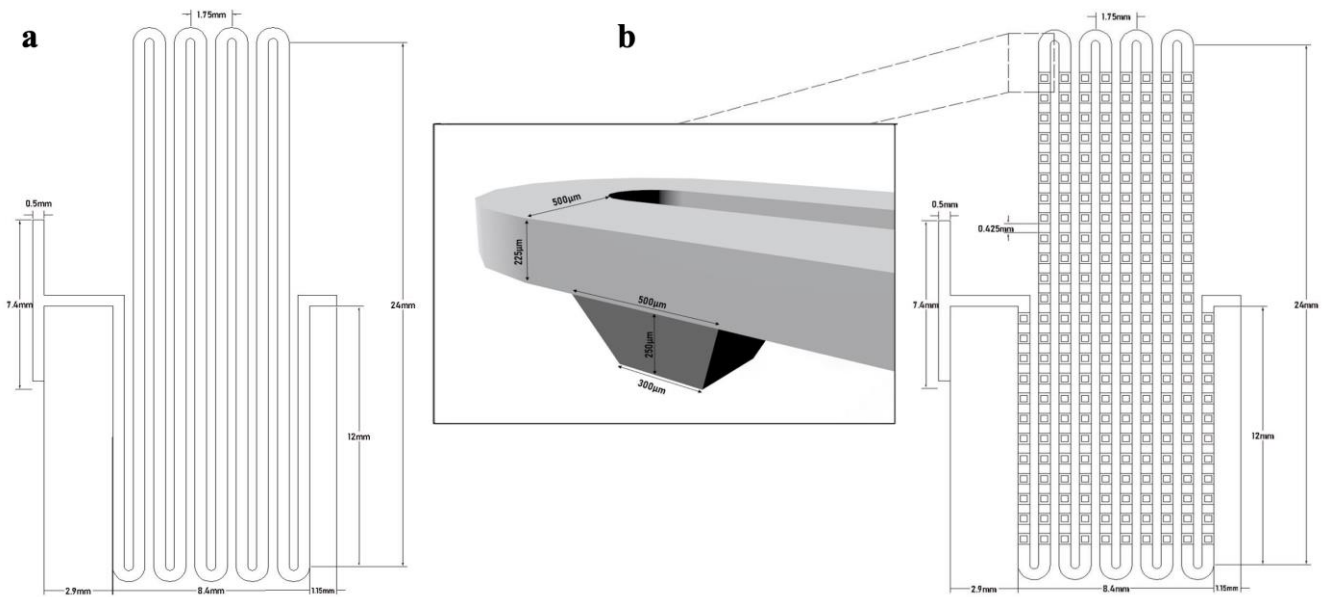


**Figure 2.** Micromixers dimensions and the channel configurations. a: Simple serpentine and b: Grooved serpentine microfluidic chips.

## 2.2. Numerical Modeling

To acquire the velocity profile inside the microchannel, the Navier-Stokes equations (conservation of momentum and continuity equations 2.1 and 2.2) are solved numerically. It is assumed that the fluids (DI water and blue dye) are Newtonian and incompressible under a steady-state pressure driven flow as follows,

$$\rho \left( \frac{\partial \mathbf{u}}{\partial t} + (\mathbf{u} \cdot \nabla) \mathbf{u} \right) = -\nabla p + \mu \nabla^2 \mathbf{u} \quad (2.1)$$

$$\nabla \cdot \mathbf{u} = 0 \quad (2.2)$$

where  $\rho$  is the fluid density ( $\text{kg/m}^3$ ),  $\mathbf{u}$  is the velocity vector ( $\text{m/s}$ ),  $t$  is the time ( $\text{s}$ ),  $p$  is the pressure ( $\text{Pa}$ ), and  $\mu$  is the fluid viscosity ( $\text{Pa}\cdot\text{s}$ ). The values for the viscosity and density are set to those for water at room temperature, i.e.,  $\mu = 1 \text{ mPa}\cdot\text{s}$  and  $\rho = 1000 \text{ kg/m}^3$ . No-slip boundary conditions are assigned for the walls of the micromixers. A free tetrahedral mesh, with all mesh elements not greater than  $\sim 10 \mu\text{m}^3$  in volume, is applied for the entire microchannel. Aftermath, the flow fields obtained are utilized in the concentration–diffusion equation to evaluate the distribution of the concentration,  $c$ , through the mixer:

$$\frac{\partial c}{\partial t} = D \nabla^2 c - \mathbf{u} \cdot \nabla c \quad (2.3)$$

where  $D$  is the diffusion constant. The diffusion constant is set to  $2.9 \times 10^{-9} \text{ m}^2/\text{s}$ , corresponding to the typical diffusivity range of most ions in aqueous solutions [29].

The molar concentration  $C$  is chosen to be  $1 \text{ (mol/m}^3\text{)}$  at one of the inlets and  $0 \text{ (mol/m}^3\text{)}$  at the opposite inlet. The computational package COMSOL Multiphysics 5.4 and its Laminar Flow/Transport of Diluted Species modules is used to solve this multi-physics problem.

## 2.3. Mixing Analysis

In order to quantitatively investigate the effect of the flow rate and grooves on mixing, mixing index (MI) is calculated based on the following equation [30]:

$$MI = 1 - \frac{\sqrt{\frac{1}{n} \sum (I_i - I_{avg})^2}}{I_{avg}} \quad (2.4)$$

where  $n$  is the total number of the pixels,  $I_i$  is the dye intensity of each point, and  $I_{av}$  is the average intensity.

## 2.4. Geometrical Design of the Micromixer

The dimensions of the serpentine micromixers used in this study are shown in Figure 2. The fluids to be mixed are pumped into the mixer through a T-shaped inlet structure. Both inlets have a square shape of the same size of  $500 \times 225 \mu\text{m}^2$ . The height of the main channels is  $H = 225 \mu\text{m}$ , while its width is  $W = 500 \mu\text{m}$  for both the simple and grooved serpentes investigated. In the grooved serpentine micromixer, the grooves are of a trapezoidal shape where each column is composed of 25 grooves placed at the bottom with spacing of  $425 \mu\text{m}$  with dimensions shown in Figure 2b.

## 2.5. Experimental Implementation

Deionized (DI) water and a dilute blue dye solution are considered as the working fluids, each with a density of  $1000 \text{ kg/m}^3$  and a dynamic viscosity of  $1 \text{ mPa}\cdot\text{s}$ . The diffusion coefficient of  $2.9 \times 10^{-9} \text{ m}^2/\text{s}$  is taken for the dye solution in water. The fluids were pumped into the channels, via the two inlets, using a syringe pump simultaneously through  $1.2 \text{ mm}$  Teflon tubing. Since the aim of this work is to investigate the effect of the grooved-serpentine on mixing efficiency at different flow rates, total flow rates of  $1000, 2000, 4000$  and  $5000 \text{ }\mu\text{l/hr}$  are selected. An inverted microscope integrated with a CCD camera are used to monitor the fluid flow and mixing inside the micromixers.

## 3. Results and Discussion

The present study aims to investigate the relationship between the mixing index, flow rate, and Reynolds number in simple and grooved serpentine models. Furthermore, an in-depth analysis of the fluid dynamics in both models is conducted, and the pressure drop relation with Reynolds number along with numerical tools is analyzed and discussed.

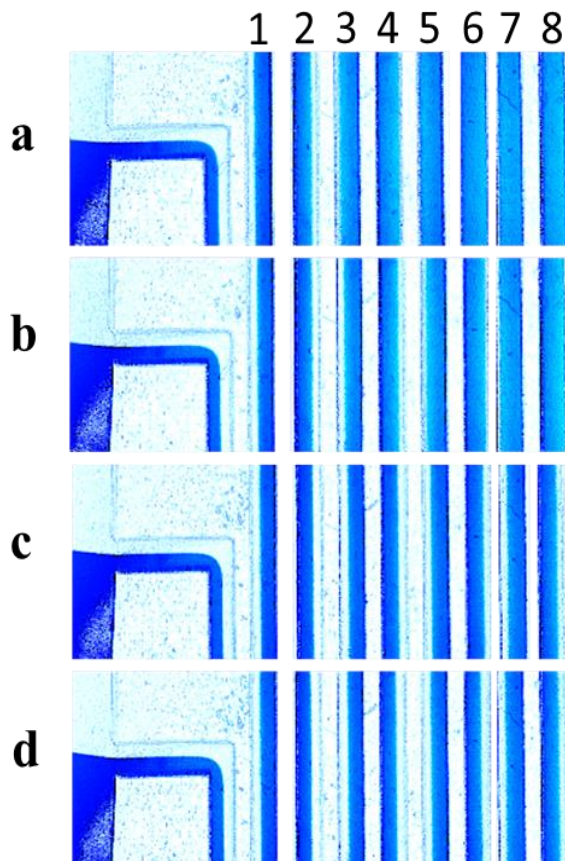


**Figure 3.** Experimental results of mixing performance at different locations in the simple serpentine channels under a:  $1000$ , b:  $2000$ , c:  $4000$ , and d:  $5000 \text{ }\mu\text{l/hr}$ .

## 3.1. Mixing Index vs Flow Rate

In the scope of this study, the effect of different flow rates on mixing efficiency is studied for two different serpentine models; simple serpentine and grooved serpentine. Total flow rates of  $1000, 2000, 4000$  and  $5000 \text{ }\mu\text{l/hr}$  are chosen to cover lower and higher flow rates. Figure 3 shows the experimental results of mixing along the middle region of the simple serpentine channel under four different flow rates.

From Figure 3, it is seen that the flow rate affects the mixing performance within the channel. As the flow rate increases, mixing efficiency of the blue dye and water is reduced. This is attributed to the phenomenon of strong flow symmetry in two streams (lacking disturbances in the flow to cause efficient mixing) and high shear force between them that is not enabling enough diffusion and mass transport of molecules [31]. At low flow rates, such as  $1000 \text{ }\mu\text{l/hr}$ , diffusion dominates the transport process and it plays a significant role in mixing, as the blue dye molecules are given enough time to diffuse across the channel and mix with the other stream of water. At such low flow rates, the fluid flows in smooth and parallel streamlines. However, as the flow rate increases ( $2000, 4000$  and  $5000 \text{ }\mu\text{l/hr}$ ), advection predominates over the molecular diffusion and controls the mass transport between the two fluids, which is a process by which substances/particles move from a high concentration region to a low concentration region until an equilibrium state is achieved [32]. This process carries the blue dye molecules along with the fluid stream without giving them enough time to diffuse across the channel and mix with the water. Thus, the fluids mix less efficiently and need high mixing length to observe efficient mixing.

Figure 4 shows the mixing index, calculated using Eq. (2.4), for the chosen four different flow rates at the exit of each column.

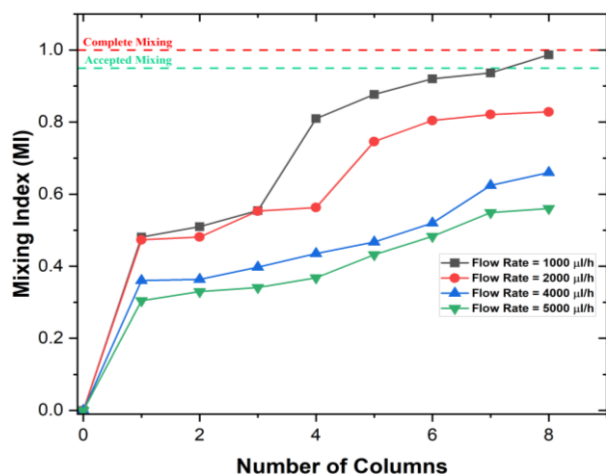


**Figure 4.** Mixing index along the simple serpentine channel for different flow rates.

In this study, a mixing index of 0.95 is taken a reference for an accepted mixing where a mixing index of 1.00 represents complete mixing and a mixing index of 0 represents no mixing at all. It is seen that for the case of 1000  $\mu\text{l/hr}$  flow rate only and after 8 turns, a mixing index of 0.98 is observed which is above the accepted mixing reference. However, for the other three flow rates, 2000, 4000 and 5000  $\mu\text{l/hr}$ , the mixing index was observed to be much below the accepted mixing reference.

Next, experiments are carried out to investigate the effect of adding trapezoidal grooves to the bottom of the serpentine channel, named grooved serpentine, on the mixing performance at different flow rates. Figure 5 shows the experimental results of mixing along the middle of the grooved serpentine channel under four different flow rates. It is observed that mixing is achieved faster in the grooved serpentine as compared to the simple serpentine. Complete mixing is observed after the 3<sup>rd</sup> column (75 grooves) for the 1000  $\mu\text{l/hr}$  flow rate, whereas complete mixing is observed after the 8<sup>th</sup> column for the same flow rate in the simple serpentine model. Moreover, at higher flow rates (2000, 4000 and 5000  $\mu\text{l/hr}$ ), unlike in the simple serpentine case, complete mixing could be achieved within the same footprint. Thus, adding the grooves contributed to faster and enhanced mixing of the blue dye and DI water.

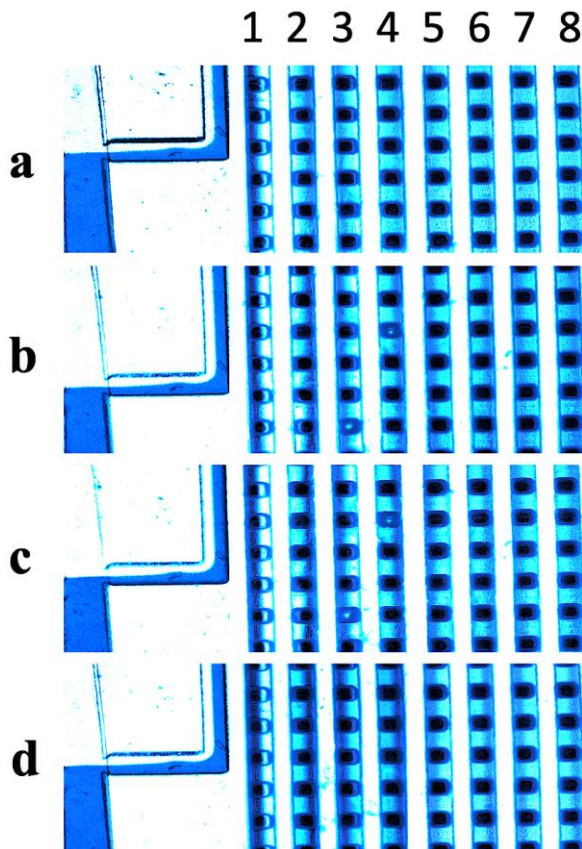


**Figure 5.** Experimental results of mixing performance at different locations in the grooved serpentine channels under a: 1000, b: 2000, c: 4000, and d: 5000  $\mu\text{l/hr}$ .

To better understand the effect of adding the grooves on the mixing performance and efficiency, the mixing index at every column's exit for the four flow rates is calculated using Eq. (2.4) and shown in Figure 6.

It is seen that after 6 columns (150 grooves), complete mixing was observed for all the four flow rates. The trapezoidal grooves placed at the bottom of the serpentine channel cause repetitive, localized and periodic increase in the surface area of the channel that is available for mixing. In other words, the grooves disrupt the laminar flow regime as they act as a chain of baffles. The induced localized and periodic increase in the surface area within the channel significantly reduced the velocity stream in these regions due to localized pressure drops generated in those regions and break the symmetries in the flow and cause stirring effect.

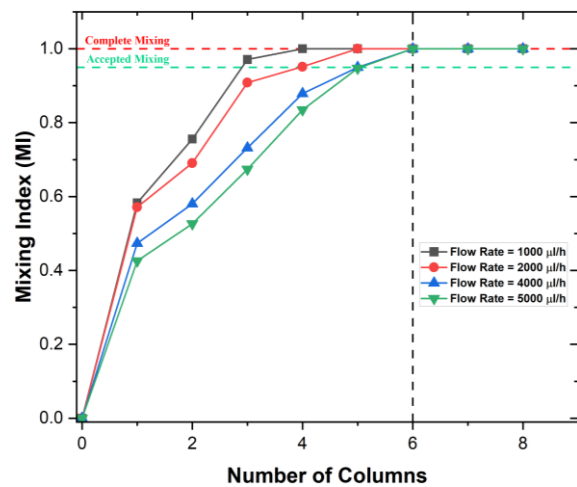


**Figure 6.** Mixing index along the grooved serpentine channel for different flow rates.

Figure 7 shows the velocity profile in both designs. The grooves enhanced convective transport of the fluid components along different parts of the microchannel due to the induced flow disruptions causing the fluids to be mixed more efficiently. Additionally, the trapezoidal grooves break-up the fluid flow into smaller segments by acting as micro-mixers cascaded through the grooved serpentine amplifying the mixing by each stage. Furthermore, the grooves cause the fluid to flow in a sinusoidal pattern, increasing the fluid-wall interaction as shown in Figure 8.

### 3.2. Mixing Index vs Reynolds Number

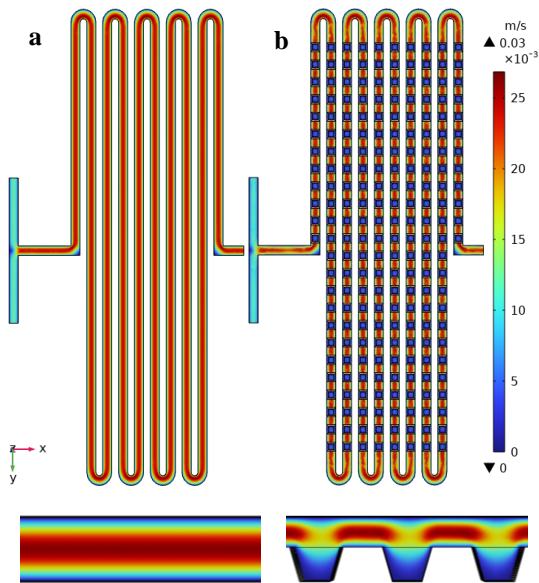
For the chosen flow rates, Reynolds number is calculated using:

$$Re = \frac{\rho u D_h}{\mu} \quad (3.1)$$

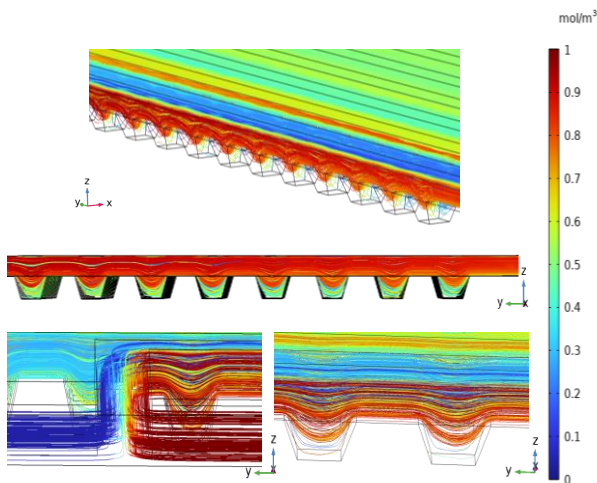
where  $Re$  is the Reynolds number,  $\rho$  is the fluid density ( $\text{kg/m}^3$ ),  $u$  is the fluid velocity ( $\text{m/s}$ ),  $D_h$  is the hydraulic diameter/characteristic length ( $\text{m}$ ), and  $\mu$  is the dynamic viscosity ( $\text{Pa}\cdot\text{s}$ ) of the fluid.

Figure 9 shows the mixing index versus Reynolds number calculated at the inlet, mid-channel and outlet for the simple and grooved serpentine. The graph shows that at the outlet of the grooved serpentine, regardless of the Reynolds number value, the mixing index is 1 which represents complete mixing. However, at the outlet of the simple serpentine, as the Reynolds number increases, mixing index decreases which means that at higher Reynolds numbers and flow rates, the simple serpentine is not efficiently achieving acceptable mixing.

At low Reynolds numbers, molecules have enough interaction time to diffuse/move across the channel and mix with the other stream. This scenario is characterized by the predominance of diffusion in the transport process in which it plays a significant role in mixing [33]. At a Reynolds number higher than 1.2, the mixing index sharply decreases because the residence time decreases with increasing velocity and is insufficient for diffusion for the simple serpentine case. However, for the grooved serpentine case, staggered transversal vortices coupled with induced dean vortices, due to the centrifugal force exerted by the curvy structures of the serpentine, are fully effective in enhancing the mixing of fluids at such Reynolds number.



**Figure 7.** Velocity profile for 5000 µl/hr flow rate. a: Simple serpentine, b: Grooved serpentine channels.



**Figure 8.** Concentration profile in the grooved serpentine channels.

The mixing index is high at Reynolds number of 1.2 despite strictly laminar flow and the absence of streamlines crossing because, at low flow rate, a long residence time of fluids in the channel allows more time for diffusion to occur, which is the dominant factor that causes mixing in this case.

### 3.3. Pressure Drop vs Reynolds Number

Reporting the pressure drop is an important factor to show the effect of the increasing the surface area within the channel due to the presence of grooves. Given that the pressure drop ( $\Delta p = P_{in} - P_{out}$ ) is the pumping pressure needed at the inlet to drive the fluids through the channel. Figure 10 shows the pressure drop versus Reynolds number in both the simple and grooved serpentine.

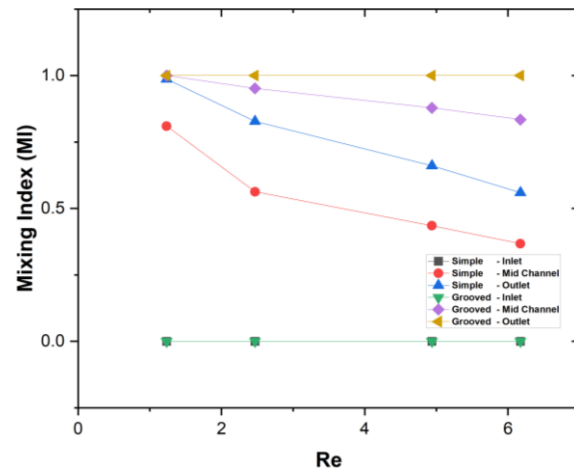


**Figure 9.** Mixing index vs Reynolds number.

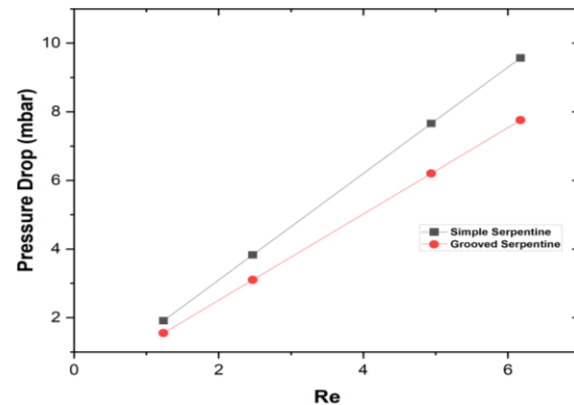


**Figure 10.** Pressure drop variation with the Reynolds number.

As seen in Figure 10, the grooved serpentine showed a lower relative pressure required to pump the fluids into the microchannel. By adding trapezoidal grooves to the bottom of the microfluidic channel, the effective surface area of the channel is increased, as the grooves provide additional surfaces for fluid-wall interactions; thus, forming localized pressure drops within the channel. For the same number of column and size of grooved serpentine and simple serpentine, mixing efficiency was greatly improved. Such design can be integrated in lab-on-a-chip systems with reduced footprint but with high mixing efficiency as simple serpentine would require much more serpentine channels to achieve acceptable mixing. By the use of the proposed grooved serpentine model, high mixing index for higher flow rates with low footprint and reduced complexity can be attained.

#### 4. Conclusions

Numerical and experimental investigations were carried out to compare the mixing performance and efficiency of aqueous solutions of blue dye and water within a simple serpentine and grooved serpentine channel models. Results elucidated that the grooved serpentine microfluidic channels, consisting of trapezoidal-shaped structures aligned at the base of the main channel, showcased superlative mixing efficiencies, particularly at higher flow rates, as compared to the simple serpentine channels. The proposed grooved serpentine design enabled complete mixing of fluids, even at high flow rates, due to several factors: (1) localized increase of surface area at each groove, (2) localized pressure drops, (3) elongated fluid routes and thus longer fluid-fluid interaction time, (4) intensified fluid-wall interaction, and (5) coupled transversal and asymmetrical-induced flows which disrupted the laminar regime and velocity streamlines. This design holds a significant enhancement for microfluidic mixing systems due to its compact footprint and persistent high mixing efficiency. Future research could utilize such design to study mixing of higher viscous fluids.

#### Acknowledgement

Dr. Gurkan Yesiloz gratefully acknowledges the support from the Scientific and Technological Research Council of Türkiye (TUBITAK) (2232-Grant No: 118C263) and (1001-Grant No: 221M575). However, the entire responsibility of the publication/article belongs to the owner of the publication/article. The financial support received from TUBITAK does not mean that the content of the publication is approved in a scientific sense by TUBITAK.

#### Author's Contributions

**Faruk Aksoy:** Performed the experiments and analyzed the results.

**Gurkan Yesiloz:** Fabricated the chip, supervised the experimental progress, analyzed the structure of the work and the results. Both authors drafted and wrote the manuscript.

#### Ethics

There are no ethical issues after the publication of this manuscript.

#### References

- [1]. Sackmann, E.K.; Fulton, A.L.; Beebe, D.J. The present and future role of microfluidics in biomedical research. *Nature* 2014, 507, 181–189.
- [2]. Chiu, D.T.; deMello, A.J.; Di Carlo, D.; Doyle, P.S.; Hansen, C.; Maceiczky, R.M.; Wootton, R.C.R. Small but perfectly formed? Successes, challenges, and opportunities for microfluidics in the chemical and biological sciences. *Chem* 2017, 2, 201–223.
- [3]. Capretto, L.; Carugo, D.; Mazzitelli, S.; Nastruzzi, C.; Xunli, Z. Microfluidic and lab-on-a-chip preparation routes for organic nanoparticles and vesicular systems for nanomedicine applications. *Adv. Drug Deliv. Rev.* 2013, 65, 1496–1543.
- [4]. Khan, S.A.; Günther, A.; Schmidt, M.A.; Jensen, K.F. Microfluidic synthesis of colloidal silica. *Langmuir* 2004, 20, 8604–8611.
- [5]. Bamford, R.A.; Smith, A.; Metz, J.; Glover, G.; Titball, R.W.; Pagliara, S. Investigating the physiology of viable but non-culturable bacteria by microfluidics and time-lapse microscopy. *BMC Biol.* 2017, 15, 121.
- [6]. Jayamohan, H.; Sant, H.J.; Gale, B.K. Applications of microfluidics for molecular diagnostics. *Methods Mol. Biol.* 2013, 949, 305–334.
- [7]. Marasso, S.L.; Mombello, D.; Cocuzza, M.; Casalena, D.; Ferrante, I.; Nesca, A.; Poiklik, P.; Rekker, K.; Aaspollu, A.; Ferrero, S.; et al. A polymer lab-on-a-chip for genetic analysis using the arrayed primer extension on microarray chips. *Biomed. Microdevices* 2014, 16, 661–670.
- [8]. Zilionis, R.; Nainys, J.; Veres, A.; Savova, V.; Zemmour, D.; Klein, A.M.; Mazutis, L. Single-cell barcoding and sequencing using droplet microfluidics. *Nat. Protoc.* 2017, 12, 44–73.
- [9]. Makgwane, P.R.; Ray, S.S. Synthesis of nanomaterials by continuous-flow microfluidics: A review. *J Nanosci. Nanotech.* 2014, 14, 1338–1363.
- [10]. Lee, C.-Y.; Chang, C.-L.; Wang, Y.-N.; Fu, L.-M. Microfluidic mixing: a review. *Int. J. Mol. Sci.* 2011, 12, 3262–3287.
- [11]. Nguyen, N.-T. *Micromixers: Fundamentals, Design and Fabrication*, 2nd ed.; Elsevier: Oxford, UK, 2012; ISBN 978-1-4377-3520-8.
- [12]. Ward, K. and Fan, Z.H., 2015. Mixing in microfluidic devices and enhancement methods. *Journal of Micromechanics and Microengineering*, 25(9), p.094001.
- [13]. Wiggins, S.; Ottino, J.M. Foundations of chaotic mixing. *Philos. Trans. R. Soc. London Ser. A.* 2004, 362, 937–970.
- [14]. Lee, C.Y.; Wang, W.T.; Liu, C.C.; Fu, L.M. Passive mixers in microfluidic systems: A review. *Chem. Eng. J.* 2016, 288, 146–160.
- [15]. Buchegger, W.; Wagner, C.; Lendl, B.; Kraft, M.; Vellekoop, M.J. A highly uniform lamination micromixer with wedge shaped inlet channels for time resolved infrared spectroscopy. *Microfluid. Nanofluid.* 2011, 10, 889–897.
- [16]. Nimafar, M.; Viktorov, V.; Martinelli, M. Experimental comparative mixing performance of passive micromixers with H-shaped sub-channels. *Chem. Eng. Sci.* 2012, 76, 37–44.



- [17]. Lim, T.W.; Son, Y.; Jeong, Y.J.; Yang, D.-Y.; Kong, H.-J.; Lee, K.-S.; Kim, D.-P. Three-dimensionally crossing manifold micro-mixer for fast mixing in a short channel length. *Lab Chip* 2011, 11, 100–103.
- [18]. SadAbadi, H.; Packirisamy, M.; Wüthrich, R. High performance cascaded PDMS micromixer based on split-and-recombination flows for lab-on-a-chip applications. *RSC Adv.* 2013, 3, 7296.
- [19]. Kim, D.S.; Lee, S.H.; Kwon, T.H.; Ahn, C.H. A serpentine laminating micromixer combining splitting/recombination and advection. *Lab Chip* 2005, 5, 739–747.
- [20]. Rhoades, T., Kothapalli, C.R. and Fodor, P.S., 2020. Mixing optimization in grooved serpentine microchannels. *Micromachines*, 11(1), p.61.
- [21]. Javaid, M.U., Cheema, T.A. and Park, C.W., 2017. Analysis of passive mixing in a serpentine microchannel with sinusoidal side walls. *Micromachines*, 9(1), p.8.
- [22]. Mengeaud, V.; Josserand, J.; Girault, H.H. Mixing processes in a zigzag microchannel: Finite element simulations and optical study. *Anal. Chem.* 2002, 74, 4279–4286.
- [23]. Hossain, S.; Ansari, M.A.; Kim, K.Y. Evaluation of the mixing performance of three passive micromixers. *Chem. Eng. J.* 2009, 150, 492–501.
- [24]. Parsa, M.K.; Hormozi, F. Experimental and CFD modeling of fluid mixing in sinusoidal microchannels with different phase shift between side walls. *J. Micromech. Microeng.* 2014, 24, 65018.
- [25]. Parsa, M.K.; Hormozi, F.; Jafari, D. Mixing enhancement in a passive micromixer with convergent-divergent sinusoidal microchannels and different ratio of amplitude to wave length. *Comput. Fluids* 2014, 105, 82–90.
- [26]. Afzal, A.; Kim, K.Y. Convergent-divergent micromixer coupled with pulsatile flow. *Sens. Actuator B-Chem.* 2015, 211, 198–205.
- [27]. Akgönül, S.; Özbey, A.; Karimzadehkhoei, M.; Gozuacik, D.; Koşar, A. The effect of asymmetry on micromixing in curvilinear microchannels. *Microfluid. Nanofluid.* 2017, 21, 1–15.
- [28]. Liu, R.H.; Stremler, M.A.; Sharp, K.V.; Olsen, M.G.; Santiago, J.G.; Adrian, R.J.; Aref, H.; Beebe, D.J. Passive mixing in a three-dimensional serpentine microchannel. *J. Microelectromech. Syst.* 2000, 9, 190–197.
- [29]. Holz, M., Heil, S.R. and Sacco, A., 2000. Temperature-dependent self-diffusion coefficients of water and six selected molecular liquids for calibration in accurate 1H NMR PFG measurements. *Physical Chemistry Chemical Physics*, 2(20), pp.4740-4742.
- [30]. Yesiloz, G., Boybay, M.S. and Ren, C.L., 2017. Effective thermo-capillary mixing in droplet microfluidics integrated with a microwave heater. *Analytical Chemistry*, 89(3), pp.1978-1984.
- [31]. Stremler, M.A., Haselton, F.R. and Aref, H., 2004. Designing for chaos: applications of chaotic advection at the microscale. *Philosophical Transactions of the Royal Society of London. Series A: Mathematical, Physical and Engineering Sciences*, 362(1818), pp.1019-1036.
- [32]. Bordbar, A., Taassob, A. and Kamali, R., 2018. Diffusion and convection mixing of non-Newtonian liquids in an optimized micromixer. *The Canadian Journal of Chemical Engineering*, 96(8), pp.1829-1836.
- [33]. Cho, C.C., 2008. A combined active/passive scheme for enhancing the mixing efficiency of microfluidic devices. *Chemical Engineering Science*, 63(12), pp.3081-3087.

# Use of Pyrolysed Almond and Walnut Shells (PAS and PWS) for the Adsorption of Cationic Dye: Reusing Agro-Waste for Sustainable Development

Gül Kaykioğlu<sup>1</sup> , Nesli Aydın<sup>1,2\*</sup> 

<sup>1</sup> Tekirdağ Namık Kemal University, Faculty of Engineering, Department of Environmental Engineering, Çorlu, Tekirdağ, Türkiye

<sup>2</sup> Karabük University, Faculty of Engineering, Department of Environmental Engineering, Karabük, Türkiye

\*[nesli.ciplak.aydin@gmail.com](mailto:nesli.ciplak.aydin@gmail.com)

\* Orcid No: 0000-0002-7561-4280

Received: 06 June 2023

Accepted: 10 September 2023

DOI: 10.18466/cbayarfbe.1310461

## Abstract

Agro-wastes are recognised as a carbon-rich source, which can be converted into value-added products in sustainable development. In this study, the effect of pH, contact time, initial concentration, and ionic strength were evaluated in Methylene Blue (MB) adsorption by using an activated carbon obtained from pyrolysed almond (PAS) and walnut shells (PWS). The characterisation of PAS and PWS was conducted by SEM-EDX, FT-IR and BET analysis. The removal efficiency of 6 mg/L initial MB concentration improved from 10.6% to 50.42% for PAS, when the adsorbent dose was increased from 0.5 g to 3.5 g/L in 1 L dye solution. It also improved from 14.8% to 48.7% for PWS, when the adsorbent dose was increased from 0.5 g to 3.5 g. The adsorption fits well with the Freundlich isotherm model and the second-order kinetic model is more favourable. In the adsorption experiments using PWS, 48% removal efficiency was obtained in the absence of NaCl. Depending on the increasing NaCl concentration, the removal efficiencies showed a decrease. 36% removal efficiency was obtained for PWS when 2500 mg/L NaCl was used. In the adsorption experiments using PAS, 40% removal efficiency was obtained in the absence of NaCl. When 500 mg/L NaCl was used, the maximum removal efficiency improved to 48%. However, with the increase in ionic strength, removal efficiencies decreased to approximately 39%. This study revealed that PAS and PWS could be used effectively instead of commercial activated carbon, which also provides an advantageous option from an economic point of view.

**Keywords:** Adsorption, Agro- Waste, Methylene Blue, Removal Efficiency, Sustainable Development

## 1. Introduction

Agro-waste has recently created new opportunities for the production of eco-friendly and sustainable materials in environmental engineering. As it is cheap and available in large amounts, employing this resource by the direct use or developing, functioning, and/or preparing adsorbents in the adsorption process has been a focus of adsorption studies. Some researchers investigated the use of agro-wastes, such as rice husk, olive stones, fruit stones and nutshells and revealed their high adsorption capacity [1-3]. The performance of H<sub>2</sub>SO<sub>4</sub>-activated rice husk ash was also studied for the removal of MB and it was determined that the highest adsorption capacity was 44.25 mg/g by reporting that the dye uptake occurred rapidly and the adsorption was improved with longer contact time in all experiments [1]. There have also been further studies examining how

pre-treatment, such as the implementation of pyrolysis, influences the capacity of adsorption. For instance, it was found that pyrolysis temperature affected MB adsorption capacity for activated carbons produced from hazelnut and walnut shells [3]. It was reported in the same study that the release of volatiles during pyrolysis leads removal of non-carbon particles and the enhancement of activated carbon.

When the publications regarding the adsorption process are examined in the literature, it is seen that various studies are focusing on the use of agro-wastes as an adsorbent material for colour removal. However, there is no study particularly concerned with the use of pyrolysed almond (PAS) and walnut shells (PWS), which are produced in large quantities worldwide as walnut and almond easily adapt to different climates. So far, various shells have been analysed to reveal their

reusability for different purposes. For example, the production of bio-oil, which was generated from the pyrolysis of coconut shells, was evaluated under different conditions [4]. Physico-chemical properties of almond shells were characterised to determine appropriate applications to reuse them [5]. Therefore, this study aims to investigate the potential of pyrolysed almond and walnut shells as an adsorbent material in the adsorption process comparatively by evaluating the effect of pH, contact time, initial concentration, and ionic strength. Adsorption kinetics and isotherm models were examined and the characterisation of the adsorbents was conducted by SEM-EDX, FT-IR and BET analyses to explore their morphologic features.

## 2. Materials and Methods

### 2.1. Preparation of PAS and PWS

In this study, pyrolysis was applied to almond and walnut shells. The size of the shells was reduced to 2-3 cm in diameter and then subjected to pyrolysis with nitrogen gas at 550°C for 60 minutes. The pyrolysis process was carried out in a downstream fixed bed and throatless type pyrolysis unit. The diameter of the pyrolysis reactor is 170 mm and the length is 750 mm, and the effective height of the reactor is 700 mm. The pyrolysis unit was operated at a speed of 200 kg/m<sup>2</sup>h [6]. After thinning the pyrolysis product in a porcelain mortar, it was separated according to the pore size by using 2 mm and 1 mm sieves. In this study, adsorbents with pore diameters less than 1 mm were used.

### 2.2 Analyses

In this study, pH measurements were performed with the WTW pH 315i pH meter. The colour measurement in the supernatants obtained as a result of adsorption studies was carried out in a spectrophotometer (Thermo Spectronic Hellios Aquamate), taking into account the maximum absorbance value of MB ( $\lambda_{max}$ , 670 nm). Absorbance values obtained at different wavelengths were recorded and RES values were calculated [Equation (1)] [7].

$$RES(\lambda) = (A/d).f \quad (1)$$

In Equation 1, “A” ( $\lambda$ ) represents absorbance in the water sample at wavelength. “d” (mm) shows the thickness of the tub. While f (f=1000) is a factor to obtain the spectral absorbance in m<sup>-1</sup>, RES ( $\lambda$ ) indicates wavelength chromaticity number in m<sup>-1</sup>.

The surface properties and chemical characterisation of PAS and PWS were performed by using SEM, FT-IR and BET analyses. SEM (FEI, Quanta FEG 250) and FT-IR (Bruker, Vertex 70 ATR) analyses were run in Tekirdağ Namik Kemal University Central Research Laboratory (Nabiltem). BET (Quantachrome Autosorb 6B) analysis was performed in the MERLAB (Middle East Technical University Central Laboratory).

### 2.3 Dye Adsorption

MB, which is a cationic dye with strong water-adhesive properties, is used in different industrial areas. In this study, MB (Merck) was used as an adsorbate. The chemical properties of MB are given in Table 1. A 50 mg/L solution was prepared and used for adsorption studies by making dilutions (2-10 mg/L). Adsorption studies were carried out from synthetic solution prepared with MB at different concentrations (2, 4, 6, 8 and 10 mg/L) at different pH conditions (4, 5.8, 7, 9 and 11).

The variation of the colour removal efficiency depending on the ionic strength was evaluated in the solution to which 500, 1000, 1500, 2000 and 2500 mg/L NaCl were added. The adsorption study was carried out in an orbital shaker and sampling was done at 0, 1, 5, 15, 30, 60, 90 and 120 minutes. Collected samples were centrifuged at 4000 rpm for 5 minutes, and then colour measurement was performed.

**Table 1.** Chemical properties of MB.

Classification number	52015
Solubility in water	%3.55
Solubility in alcohol	%1.48
$\lambda_{max}$	665 nm
Molecular weight	319.9 g/mole
Paint group	Thiazine
Ionisation	Acidic

### 2.4 Adsorption Kinetics

One of the important factors in evaluating the efficiency of adsorption is the determination of the sorption rate. A pseudo-first-order kinetic model and pseudo-second-order kinetic model were applied to analyse the kinetics of MB adsorption.

The Lagergren equation, which is based on a method used to determine the adsorption rate in liquid phase systems, was used in this study to determine the adsorption kinetics [8]. It is one of the most widely used equations in the pseudo-first-order kinetic model. The line drawn on the graph of  $t$  versus  $\log(qe-qt)$  shows the application of the first-order kinetic equation for the system. The values of  $qe$  and  $k_1$  could be determined from the slope of the graph and the cut-off point. “ $qe$ ” is the adsorbed amounts (mg/g) at equilibrium, at time  $qt$ ,  $t$ . The straight line drawn to the slope of the  $t$  versus  $t/qt$  graph in the adsorption kinetic rate equation in the second-order kinetic model shows the application of the second-order kinetic model equation for the system.  $qe$  and  $k_2$  could be determined from the slope of the graph and the cut-off point.

## 2.5 Adsorption Isotherms

The adsorption capacity at equilibrium was calculated. Langmuir and Freundlich isotherms were applied in this study.

Adsorption continues until equilibrium is established between the adsorbed pollutant concentration and the pollutant concentration remaining in the solution. The adsorption capacity at equilibrium was calculated using Equation 2 [9].

$$qe=(C_0-C_e)V/m \quad (2)$$

In Equation 2,  $q_e$  represents the amount of MB (mg/g) adsorbed by each unit of adsorbent at equilibrium. While  $C_0$  shows MB concentration in solution before adsorption (mg/L),  $C_e$  indicates MB concentration remaining in solution at equilibrium after adsorption (mg/L).  $V$  is a volume of solution (L) and  $m$  is an adsorbent dose (g). The equilibrium state could be explained by various isotherm models such as Freundlich and Langmuir which were also used in this study [10].

The Langmuir isotherm is applied to describe monolayer homogeneous adsorption and provides estimation for the highest adsorption capacity. In Langmuir isotherm ( $C_e/q_e$ ),  $K_L$  (L/g), which is the equilibrium constant, and  $q_{max}$  (mg/g), which shows the maximum adsorption capacity for monolayer formation are used. To explain the basic characteristics of the Langmuir model, the dimensionless separation factor  $R_L$  was used (Equation 3). An  $R_L$  value between 0 and 1 indicates favourable adsorption.

$$R_L = \frac{1}{1+K_L \cdot C_0} \quad (3)$$

Freundlich model is also based on an empirical equation used to determine the adsorption density which could occur on the adsorbent surface [11]. In the model,  $K_F$  (L/g) is the experimentally calculated adsorption capacity and  $1/n_F$  is an adsorption density. The line in the graph which is drawn using  $\ln q_e$  vs.  $\ln C_e$  values shows compliance with the Freundlich model. The  $n_F$  value represents the compatibility of adsorbent and adsorbate.  $1/n_F$  and  $K_F$  values are calculated from the slope of the obtained line.

## 3. Results and Discussion

### 3.1 Characteristics of PAS and PWS

The results of SEM EDX (Energy-Dispersive X-Ray) and FT-IR analyses of PAS and PWS are given in Figure 1. According to the SEM EDX analysis results, there are three elements (C, O, and K) in the surface elemental composition of both adsorbents. The percentage of carbon element, which plays an active role in the removal of pollutants in the adsorption process, was determined as 88.91% for PAS and 92.02% for PWS.

SEM analyses were used to determine the morphological properties of the adsorbent. Surface porosity for PAS and PWS seems suitable for adsorption. A more uniform porosity distribution is observed for PAS, while relatively irregular porosity and rock-like structures are determined for PWS. As temperature increases with high heating rates, various volatile compounds are released. De-volatilization causes morphological changes in biochar followed by the formation of highly porous surface structures of biochar samples [12]. The result of a BET surface area measurement shows that the surface area for PAS is 3.38 m<sup>2</sup>/g and for PWS is 51.54 m<sup>2</sup>/g. The SEM images in Figure 1 also support the surface area results.

The FT-IR spectrum was used to determine the frequency deviations of the functional groups in PAS and PWS. As is seen in Figure 1, the spectrum takes place between 400 and 4000 cm<sup>-1</sup>. Peak points represent broad adsorption bands; 1553, 1409, 1045, 869, 820, 749, 704, 568 cm<sup>-1</sup> for PAS and 1554, 1425, 1110, 1050, 869, 804, 751, 446 cm<sup>-1</sup> for PWS. It is estimated that this is correlated to the hemicellulosic and cellulosic breakdown reactions and the elimination of O<sub>2</sub>, including compounds leading to the release of CO<sub>2</sub>. It is also related to H<sub>2</sub>O removal reactions, resulting in the generation of amorphous carbon with various degrees of hydrogenation [13]. The bands observed between 1554 and 1409 cm<sup>-1</sup> indicate C—C bonds attributed to the conjugated alkene and (or) C—C stretching in the aromatic ring [14]. Bands in the range of 1110 to 1045 cm<sup>-1</sup> represent C—C and C—O stretching vibration [6]. The peaks seen at 869-749 cm<sup>-1</sup> are indicative of the presence of CO<sub>3</sub> in biochar [15]. The band at 568-446 cm<sup>-1</sup> could correspond to the SiO—H vibration.

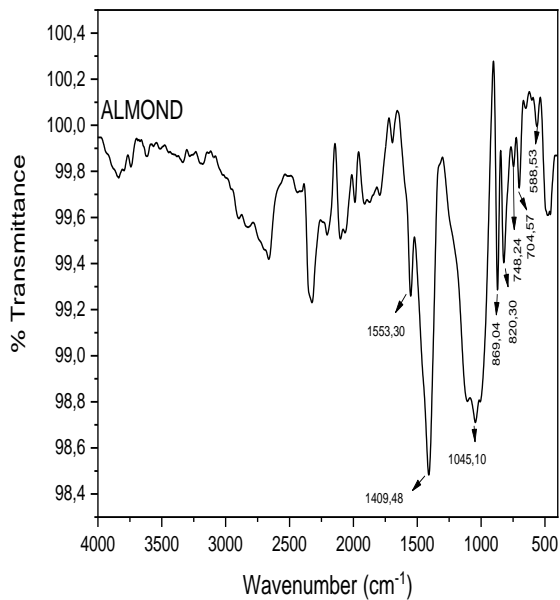
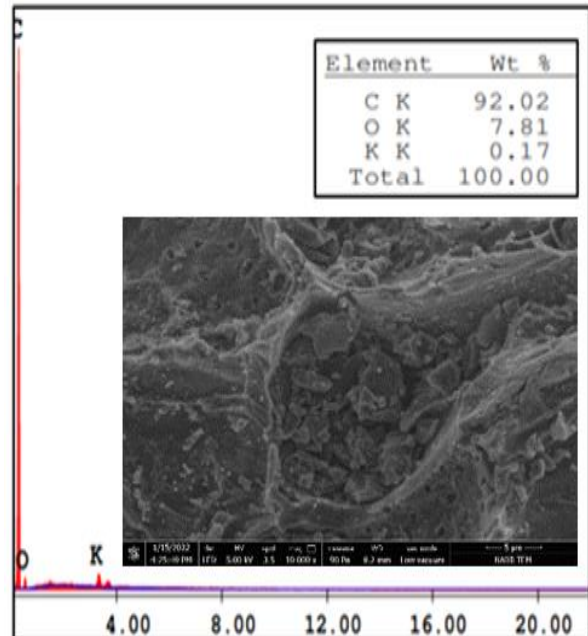
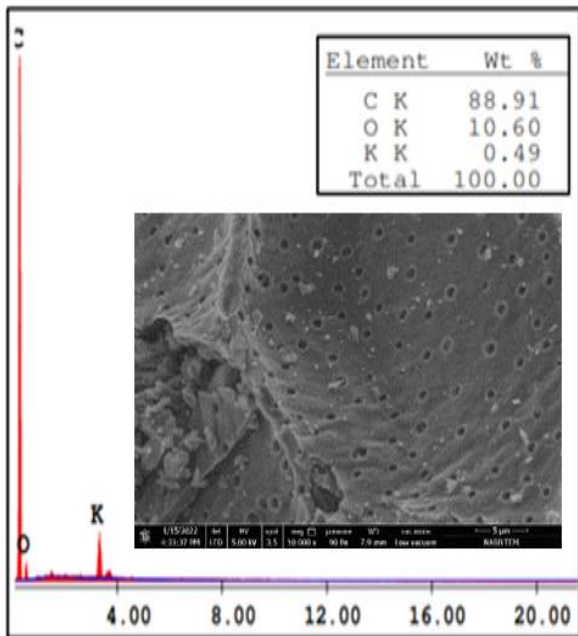
### 3.2 Effect of pH on MB Adsorption with PAS and PWS

The pH value of the solution is important in determining the adsorption mechanism. This is due to the change in the surface charge and thus the adsorption capacity of the adsorbents [16]. Adsorption capacities depending on pH for PAS and PWS are shown in Fig. 2 (a). The effect of pH [4, 5.8 (original pH), 7, 9, 11] was evaluated at  $C_0 = 6$  mg/L concentration with PAS and PWS. With the increase in the pH of the solution, the  $q_e$  values decreased for both adsorbents. The best  $q_e$  value for PAS was obtained as 2.93 mg/g at the original pH (5.8), while the highest  $q_e$  for PWS was found as 3.19 mg/g at the original pH (5.8).

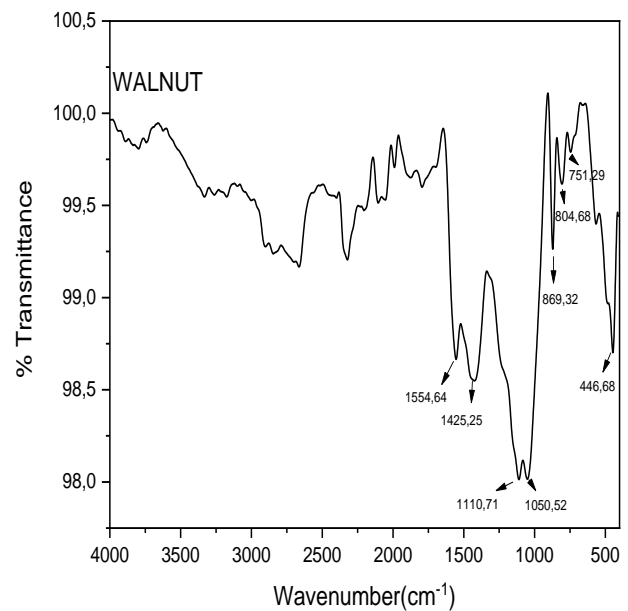
The surface charge of an adsorbent is related to the  $pH_{pzc}$  value. If the  $pH_{pzc}$  value is greater than the pH value of the solution, the adsorbent has a positive surface charge, and if the  $pH_{pzc}$  value is less than the pH value of the solution, it has a negative surface charge. It is known that the surface charge of the adsorbent will

increase the adsorption efficiency due to the cationic nature of the MB dyestuff. This is due to the repulsions between the cationic dye molecules and the H<sup>+</sup> ions in the solution. The PH<sub>pzc</sub> values obtained for pyrolysed almond shells and walnut shells were determined as 5.6 and 5.1, respectively. In this case, if the pH value is

below 5, the adsorption efficiency is expected to be low. For this reason, it is possible to explain the adsorption mechanism with electrostatic attraction. In this study, maximum q<sub>e</sub> values were obtained at pH 5.8 (original pH), and therefore the original pH was used in subsequent evaluations.



a) PAS



b) PSW

**Figure 1.** SEM EDX and FT-IR analysis.

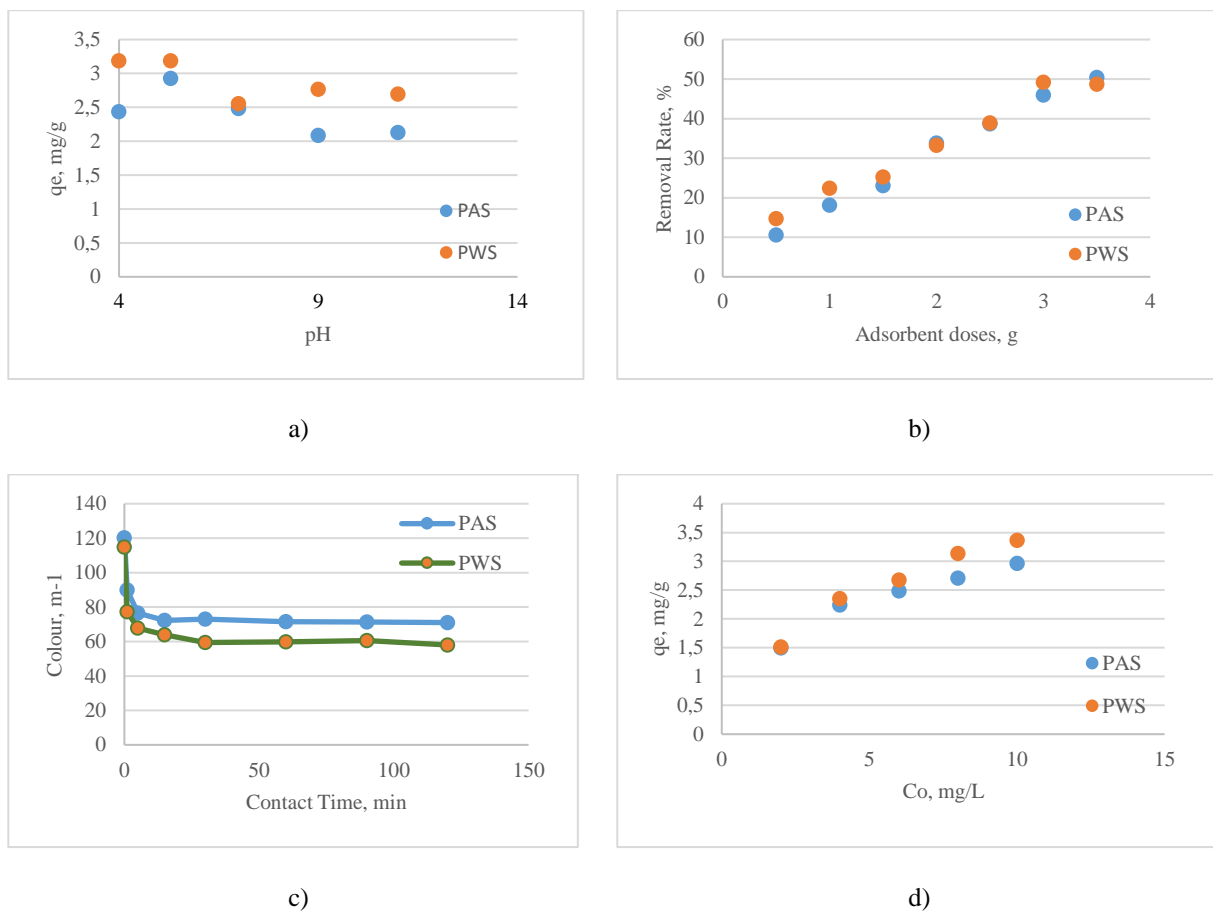


**Figure 2.** The effect of a) pH, b) adsorbent doses (m), c) contact time ( $C_o=6$  mg/L, pH=5.8,  $m=2.5$  g/L), d) initial dye concentration (pH=5.8,  $m=2.5$  g/L) on dye adsorption with PAS and PWS.

### 3.3 Effect of PAS and PWS Dose on MB Adsorption

As a result of the MB adsorption study performed with 6 mg/L initial dye concentration and under constant pH conditions, the varying removal efficiencies within 60 minutes of contact time are shown in Figure 2 (b). Accordingly, for both adsorbents, increasing adsorbent doses allowed removal efficiencies to improve. It was determined that approximately 50% colour removal efficiency was obtained in the case of 3.5 g adsorbent application.

### 3.4 Effect of Contact Time on MB Adsorption by PAS and PWS

The effect of contact time was evaluated for 120 minutes in the case of 6 mg/L initial concentration, original pH (5.8) and 2.5 g/L adsorbent application in 200 mL dye solution. Results are given in Figure 2 (c). According to Figure 2, it is seen that the adsorption takes place rapidly. Depending on the increase in the contact time, the MB concentration in the solution decreases and reaches the equilibrium state at the end of the 60-minute contact period.

### 3.5 Effect of Initial Dye Concentration on MB Adsorption by PAS and PWS

The effect of initial dye concentration on MB removal with PWS and PAS is shown in Figure 2 (d). An increase in  $q_e$  values was observed due to increasing concentrations in adsorption experiments using initial concentrations ranging from 2 mg/L to 10 mg/L, pH 5.8 and fixed adsorbent dose (2.5 g). As it is seen in Figure 2 (d), when  $C_o$  is 2mg/L,  $q_e$  for both adsorbents was determined as approximately 1.2 mg/g. When  $C_o$  was increased to 10 mg/L, the  $q_e$  values were determined as 3.36 mg/g and 2.96 mg/g for PWS and PAS, respectively.

### 3.6 Adsorption Kinetics

In adsorption studies, the time required for the adsorption to reach equilibrium or the rate of adsorption is important to explain the adsorption mechanism. In order to determine the adsorption rate, MB adsorption in PWS and PAS was evaluated using the first-order and second-order kinetic models. The results of the study carried out to explain the adsorption kinetic model are given in Table 2.

When the  $R^2$  values were examined, it was determined that the adsorbents were compatible with both the first-order and the second-order kinetic models. Since the correlation coefficients determined for the second-order kinetic model were higher, it was determined that it was more favourable for the second-order kinetic model. It is seen that the equilibrium adsorption capacities ( $q_{e,cal}$ ) calculated for the second-order kinetic model of both adsorbents are quite compatible with the experimental adsorption capacities ( $q_{e,exp}$ ). The  $q_{e,exp}$  and  $q_{e,cal}$  values were found as 2.89 mg/g and 3.11 mg/g for PAS, 3.02 mg/g and 3.08 mg/g for PWS, respectively. The rate constants ( $k_2$ ) determined according to the second-order reaction kinetics were measured as 0.069 and 0.166 m/mg.min for PAS and PWS, respectively. This shows that MB adsorption takes place at a higher rate of PWS compared to PAS.

**Table 2.** Kinetic parameters for the adsorption of MB by using PAS and PWS ( $C_0=6$  mg/L,  $m= 2.5$  g/L,  $pH=5.8$ ).

Pseudo-first order					
	$C_0$	$q_{e, exp}$ (mg/g)	$q_{e, cal}$ (mg/g)	$k_1$ ( $min^{-1}$ )	$R^2$
PAS	6	2.89	1.22	0.007	0.9896
PWS	mg/L	3.02	1.04	0.0099	0.989
Pseudo-second order					
	$C_0$	$q_{e, exp}$ (mg/g)	$q_{e, cal}$ (mg/g)	$k_2$ (g/mg min)	$R^2$
PAS	6	2.89	3.11	0.069	0.9958
PWS	mg/L	3.02	3.08	0.166	0.9975

The  $q_{max}$  values obtained in previous studies on MB adsorption are also summarised in Table 3. The MB adsorption capacities of PWS and PAS were determined to be lower than the adsorption capacities of similar adsorbents used in other studies. For instance, a 4-fold difference between the  $q_{max}$  values (12.21 mg/g) was obtained in MB adsorption of granular activated carbon and the  $q_{max}$  values of PWS and PAS [1]. This shows that approximately 4 times more adsorbent should be used to obtain the same removal efficiency. The fact that the adsorbents (PWS and PAS) to be used instead of commercial activated carbon are waste materials makes the application advantageous from an economic point of view.

**Table 3.**  $q_{max}$  values obtained in studies on MB adsorption.

Adsorbent	$q_{max}$ (mg/g)	Source
Activated Carbon	263.49	[16]
Granular activated carbon	12.21	[1]
Lemon peel	29.0	[17]
Olive stones	22.10	[2]
Nutshell	8.82	[3]
Sunflower seed husk (Helianthus annuus)	23.20	[18]
Spent rice	8.13	[19]
Orange waste	30.3	[20]
PAS	3.02	This study
PWS	3.50	This study

### 3.7 Adsorption Isotherms

Langmuir and Freundlich isotherms were evaluated by using the data obtained as a result of MB adsorption experiments with PWS and PAS. Isotherm coefficients and correlation coefficients ( $R^2$ ) are given in Table 4. Langmuir and Freundlich isotherm curves are shown in Figure 3. Considering the  $R^2$  values given in Table 4, the Freundlich model was more favourable for adsorption than the Langmuir model.

In the Freundlich isotherm, the KF value represents the adsorption capacity and the  $1/n$  shows the adsorption density or heterogeneity factor [3, 21]. As the heterogeneity of the adsorbent surface increases, the  $1/n$  value approaches zero [21]. This indicates the favourability of MB removal.

As is seen in Table 4, the  $1/n$  values of MB adsorption for PWS and PAS were determined as 0.20 and 0.17, respectively. This shows that both adsorbents are favourable for MB adsorption [21]. If the adsorption process between an adsorbent and a pollutant is physical,  $n > 1$ ; if it is chemical, then  $n < 1$ , and if it is linear,  $n = 1$  [21]. All  $n$  values obtained in this study are greater than 1. For this reason, it can be stated that the adsorption process for both adsorbents is physical adsorption.

**Table 4.** Isotherm constants for Langmuir and Freundlich isotherms.

	Langmuir			Freundlich			
	$Q_{max}$ (mg/g)	$K_L$	$R^2$	$K_F$	$1/n$	$n$	$R^2$
<b>PAS</b>	3.02	2.23	0.992	2.05	0.17	5.88	0.9937
<b>PWS</b>	3.50	1.84	0.9867	2.22	0.20	5	0.9904

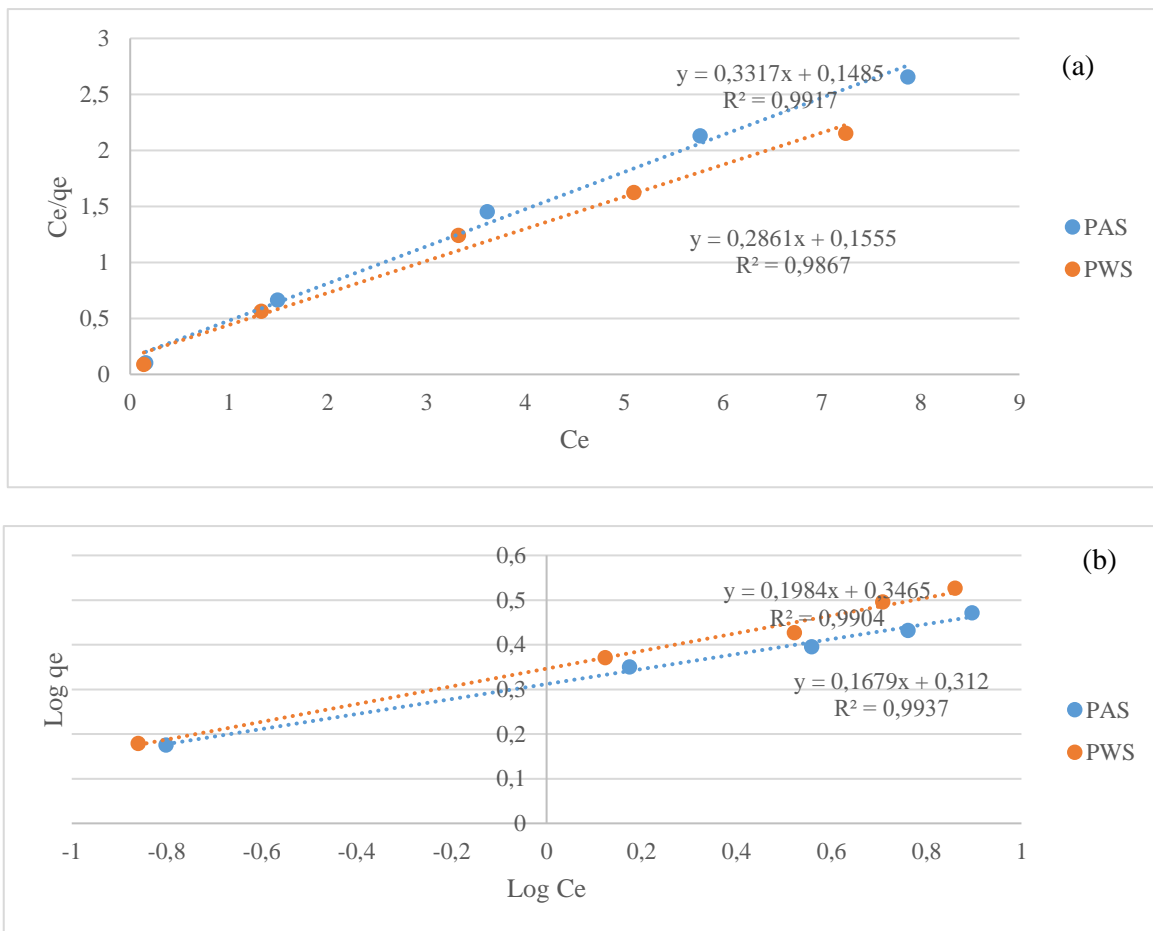


**Figure 3.** Isotherm Curves a) Langmuir, b) Freundlich (pH = 5.8, t = 60 min,  $C_o = 2, 4, 6, 8$  and  $10$  mg/L,  $m = 2.5$  g/L)

### 3.8 Effect of Ionic Strength on MB Adsorption by PAS and PWS

The effect of ionic strength on MB adsorption with PAS and PWS was examined by adding 500, 1000, 1500, 2000 and 2500 mg/L NaCl into the solution. The removal efficiencies obtained are shown in Figure 4. In the adsorption experiments with PWS, 48% removal efficiency was obtained in the absence of NaCl in the

solution. However, removal efficiencies decreased with increasing NaCl concentration. 36% removal efficiency was obtained with 2500 mg/L NaCl. Increasing the ionic strength in the solution could prevent the electrostatic interaction between the adsorbent surface and the pollutant. It is possible for electrolyte ions to affect potential interfaces on the adsorption surface and to compete for electrolyte ions and adsorbed ions for sorption sites.

In the adsorption experiments made with PAS, an increase in MB removal efficiency was determined in the case of using 500 mg/L NaCl in the solution compared to the case of not using NaCl. This can be explained by the fact that NaCl contributes to the dissociation of the dyestuff into protons and thus positively affects the adsorption. The dyestuff dissociates and becomes more easily adsorbed. Similar results were obtained in some studies [21]. In the

absence of NaCl, 40% removal efficiency was obtained for PAS, while in the case of 500 mg/L NaCl, the removal efficiency improved to 48%. However, with the increase in ionic strength in solution (1000-2000 NaCl mg/L) removal efficiencies were approximately 39%. NaCl concentration was increased up to 2500 mg/L but no significant decrease in removal efficiency was detected.

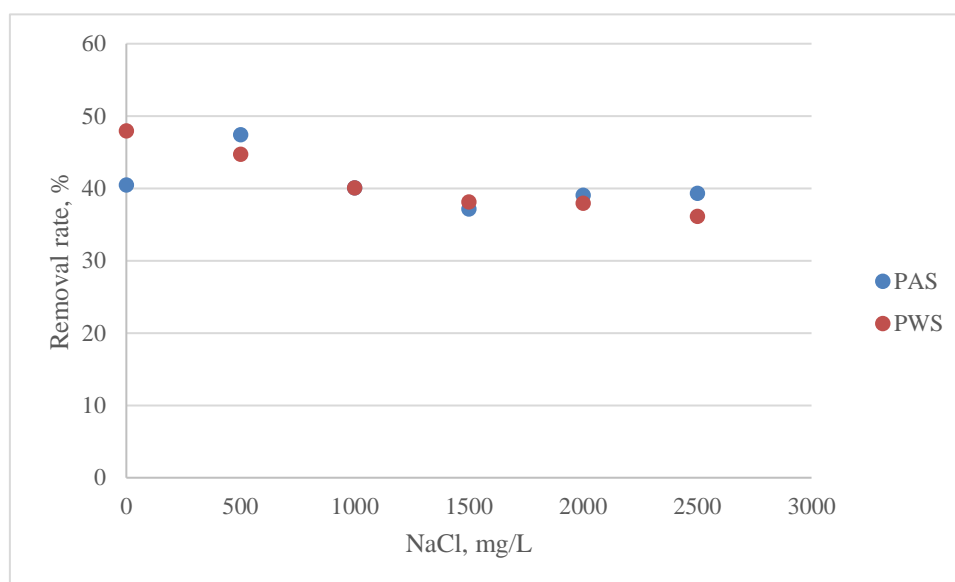


**Figure 4.** The effect of ionic strength on the adsorption of MB using PAS and PWS ( $C_0=6$  mg/L,  $m= 2.5$  g/L,  $pH=5.8$ ,  $t=60$  min)

#### 4. Conclusion

In this study, the effect of pH, contact time, initial concentration, and ionic strength in MB adsorption were evaluated by using adsorption agents obtained from the pyrolysis of almond and walnut shells. The results of the study are summarised below;

- According to the SEM-EDX results of PAS and PWS used as an adsorbent in the study, the C content was determined as 88.91% and 92.02%, respectively. In addition, according to SEM images, PWS has irregular porosity and rock-like structures, although PAS has a more uniform pore distribution. The result of a BET surface area measurement shows that the surface area for PAS is 3.38 m<sup>2</sup>/g and for PWS, it is 51.54 m<sup>2</sup>/g.
- The adsorption efficiency was affected by the initial MB concentration and the adsorbent dose for both adsorbents. The removal efficiency of 6 mg/L initial MB concentration improved from 10.6% to 50.42% for PAS, when the adsorbent dose was increased from 0.5 g to 3.5 g. It also improved from 14.8% to 48.7% for PWS, when the adsorbent dose was increased from 0.5 g to 3.5 g.
- The best  $q_e$  value for PAS was obtained as 2.93 mg/g at the original pH (5.8), while the highest  $q_e$  for PWS was found as 3.19 mg/g at the original pH (5.8). Depending on the increase in the contact time, the MB concentration in the solution decreases and reaches the equilibrium state at the end of the 60-minute contact period.
- Freundlich isotherm model  $R^2$  values for PWS and PAS used in MB adsorption were found as 0.9904 and 0.9937, respectively. The adsorption process for both adsorbents could be expressed as physical adsorption. It was found that the second-order kinetic model is more favourable to the MB adsorption with PAS and PWS. It was also determined that PWS adsorption took place at a higher rate than PAS.
- A decrease in removal efficiency with PWS was determined due to increasing ionic strength. However, in the case of 500 mg/L NaCl in the solution with PAS, the removal efficiency increased compared to the case of no NaCl. This can be explained by the fact that the salt in the solution dissociates the dyestuffs and facilitates adsorption.

In conclusion, the use of pyrolysed almond and walnut shells in the removal of MB by the adsorption method, which is used in a wide range of industrial activities, was evaluated in this study. It was determined that it is possible to use this adsorbent as an alternative to activated carbon in colour removal. However, due to the low  $q_{max}$  values of PAS and PWS compared to activated carbon, a high amount of adsorbent (PAS and PWS) could be required. The  $q_{max}$  values can be increased with various chemical activation methods that can be applied to PAS and PWS, and further studies are required on this subject.

### Acknowledgement

This research did not receive any specific grant from funding agencies.

### Author's Contributions

**Nesli Aydın:** Drafted and wrote the original manuscript, organised experimental analysis and results.

**Gül Kaykioğlu:** Supervised experimental work and helped to improve results and discussion.

### Ethics

There are no ethical issues after the publication of this manuscript.

### Statements and Declarations

This study did not receive any funding. There is no competing interest to declare.

### Compliance with ethics guidelines

Ethical approval was not required for the study

### References

- [1]. Kaykioğlu, G, Güneş, E. 2016. Kinetic and equilibrium study of methylene blue adsorption using H<sub>2</sub>SO<sub>4</sub>-activated rice husk ash. *Desalination and Water Treatment*; 57: 7085–7097
- [2]. Alaya, M, Hourieh, M, Youssef, A, El-Sejarah, F. 1999. Adsorption properties of activated carbons prepared from olive stones by chemical and physical activation. *Adsorption Science and Technology*; 18: 27–42
- [3]. Aygun, A., Yenisoy-Karakas, S., Duman, I. 2003. Production of granular activated carbon from fruit stones and nutshells and evaluation of their physical, chemical and adsorption properties. *Microporous Mesoporous Mater.*; 66: 189–195
- [4]. Fardhyanti, DS, Damayanti, A. 2017. Analysis of bio-oil produced by pyrolysis of coconut shell. *International Journal of Chemical and Molecular Engineering*; 11(9).
- [5]. Boulrika, H, El Hajam, M, Hajji Nabih, M, Idrissi Kandri, N, Zerouale, A. 2022. Physico-chemical proprieties of almond residues (shells & hulls) collected from the northern region of Morocco (Fez-Meknes). *Research Square*. <https://doi.org/10.21203/rs.3.rs-1676689/v1>
- [6]. Aktaş, T, Dalmış, S, Tuğ, S, Dalmış, F, Kayışoğlu, B. 2017. Development and testing of a laboratory type gasifier for gasification of paddy straw, *Journal of Tekirdag Agricultural Faculty*; 14(2).
- [7]. Polat, MP. 2018. Atıksularda renk ölçüm metotlarının karşılaştırılması, Master Theses, Hasan Kalyoncu University, Gaziantep, Turkey
- [8]. Garg, VK, Gupta, R, Yadav, AB, Kumar, R. 2003. Dye removal from aqueous solution by adsorption on treated sawdust. *Bioresource Technology*. [https://doi.org/10.1016/S0960-8524\(03\)00058-0](https://doi.org/10.1016/S0960-8524(03)00058-0)
- [9]. Aldemir, A, Kul, AR. 2020. Comparison of Acid Blue 25 adsorption performance on natural and acid-thermal co-modified bentonite: Isotherm, kinetics and thermodynamics studies. *Pamukkale University Journal of Engineering Sciences*; 26: 1335-1342.
- [10]. Kaykioğlu, G, Güneş, E. 2016. Comparison of Acid Red 114 dye adsorption by Fe<sub>3</sub>O<sub>4</sub> and Fe<sub>3</sub>O<sub>4</sub> impregnated rice husk ash. *Journal of Nanomaterials*; 6304096. <https://doi.org/10.1155/2016/6304096>
- [11]. El-Halwany, MM. 2010. Study of adsorption isotherms and kinetic models for Methylene Blue adsorption on activated carbon developed from Egyptian rice hull (Part II), *Desalination*, <https://doi.org/10.1016/j.desal.2008.07.030>
- [12]. Alfattani, R, Shah, MA, Siddiqui, MIH, Ali, MA, Alnaser, IA. 2022. Bio-Char characterization produced from walnut shell biomass through slow pyrolysis: Sustainable for soil amendment and an alternate bio-fuel, *Energies*. doi: <https://doi.org/10.3390/en15010001>
- [13]. Genieva, S, Gonsalvesh, L, Georgieva, V, Tavlieva, M, Vlaev, L. 2021. Kinetic analysis and pyrolysis mechanism of raw and impregnated almond shells. *Thermochimica Acta*; 698, 178877
- [14]. Farges, R, Gharzouni, A, Ravier, B, Jeulin, P, Rossignol, S. 2018. Insulating foams and dense geopolymers from biochar by-products. *Journal of Ceramic Science and Technology*; 2(9): 193-200. 10.4416/JCST2017-00098
- [15]. Shofiyani, A, Gusrizal. 2006. Determination of pH effect and capacity of heavy metals adsorption by water hyacinth (*Eichhornia Crassipes*) biomass, *Indonesian Journal of Chemistry*; 6(1): 56-60.
- [16]. Li, Y, Du, Q, Liu, T, Peng, X, Wang, J, Sun, J, Wang, Y, Wu, S, Wang, Z, Xia, Y, Xia, L. 2013. comparative study of methylene blue dye adsorption onto activated carbon, graphene oxide, and carbon nanotubes. *Chemical Engineering Research and Design*; 91: 361–368
- [17]. Kumar, KV, Porkodi, K. 2006. Relation between some two- and three-parameter isotherm models for the sorption of Methylene Blue onto lemon peel. *Journal of Hazardous Materials*; 138: 633–635
- [18]. Ong, ST, Keng, PS, Lee, SL, Leong, MH, Hung, YT. 2010. Equilibrium studies for the removal of basic dye by sunflower seed husk (*Helianthus annuus*). *International Journal of the Physical Sciences*; 5, 1270.
- [19]. Rehman, MSU, Kim, I, Han, JI. 2012. Adsorption of methylene blue dye from aqueous solution by sugar extracted spent rice biomass. *Carbohydrate Polymers*; 90: 1314-1322
- [20]. Irem, S, Khan, QM, Islam, E, Hashmat, AJ, ul Haq, MA, Afzal, M, Mustafa, T. 2013. Enhanced removal of reactive navy blue dye using powdered orange waste. *Ecological Engineering*. 58: 399-405
- [21]. Wu, Z, Zhong, H, Yuan, X, Wang, H, Wang, L, Chen, X, Zeng, G, Wu, Y. 2014. Adsorptive removal of methylene blue by rhamnolipid-functionalized graphene oxide from Wastewater. *Water Research*; 67: 330-344



## Experimental and DFT-Based Investigation of Structural, Spectroscopic, and Electronic Features of 6-Chloroquinoline

Etem Köse<sup>1\*</sup> , Fehmi Bardak<sup>1</sup> 

<sup>1</sup>Department of Physics, Faculty of Art and Sciences, Manisa Celal Bayar University, Manisa, Türkiye

\*[etemmm43@gmail.com](mailto:etemmm43@gmail.com)

\*Orcid No: 0000-0001-5791-8873

Received: 12 June 2023

Accepted: 02 September 2023

DOI: 10.18466/cbayarfbe.1313229

### Abstract

This study, spectroscopic, molecular structure, and electronic features of 6-chloroquinoline were studied via experimental techniques of FT-IR, UV-Vis, <sup>1</sup>H and <sup>13</sup>C NMR and electronic structure with DFT/B3LYP method and 6-311++G(d,p) basis set combination. The modes of vibrational were assigned according to the potential energy distributions through the VEDA program. The gauge-invariant atomic orbital method was utilized to obtain nuclear magnetic resonance properties and chemical shifts and provided in comparison to the experimental data. Frontier molecular orbital properties and electronic absorption spectral properties, hence UV-Vis spectrum, were obtained by TD-DFT modeling. The compound of chemical reactivity was explored according to frontier molecular orbital properties, electrostatic potential surface characteristics, and analysis of atomic charge. It has been achieved that the chlorine substitution significantly alters the reactive nature of quinoline moiety.

**Keywords:** 6-chloroquinoline; DFT; IR; NMR

### 1. Introduction

Quinoline is heterocyclic compound with chemical formula C<sub>9</sub>H<sub>7</sub>N and consisting of phenyl fused with a pyridine at two adjacent carbon atoms. Applications of quinoline and its derivatives span a wide range of fields, including pharmaceuticals, agrochemicals, dyes, and organic synthesis. Biological [1–3], antifilarial [4], antibacterial [5], [6], antimalarial [7–9], cardiovascular [10], and antineoplastic [11] activities of its derivatives have been investigated widely. For instance, a quinoline derivative aminoquinoline has been tested for inhibitory potential for human immunodeficiency virus (HIV) [12]. Some of quinoline derivative has also been investigated [13–18] by using quantum chemical calculations and the spectroscopic features were presented due to their significance.

It has been revealed that the substitution in quinoline derivatives affects chemical and physical properties, such as solubility, reactivity, and biological activity. The chlorine substitution in quinoline has promising potential to alter these properties considerably because of the high electronegativity of chlorine atoms. The aforementioned points provide a general overview, but detailed studies and experimental evidence are necessary to fully understand the consequences of chlorine substitution in a particular quinoline derivative.

Therefore, this study investigated the structural characteristics, spectroscopic features, orbital interactions, electronic transitions, and nuclear magnetic resonance properties of 6-chloroquinoline (6CQ) molecules from both experimental and theoretical perspectives.

The experimental techniques utilized to reveal structural and spectroscopic features of the 6CQ are FT-IR, UV-Vis, and NMR. The electronic structure calculation performed to support experimental data by simulation the related spectra theoretically and reveal further details about the reactivity and interaction profile of the title molecules is based on DFT and Time-Dependent DFT. By examining the electronic structure and studying the theoretical spectra, this approach allowed for a more comprehensive understanding of the compound's properties and behavior. This study contributes to the existing knowledge by investigating the structural and spectroscopic characteristics of 6CQ, shedding light on its properties and potential applications. Besides, it provides a further understanding of the influence of chlorine substitution on physical and chemical properties in quinoline derivatives.

## 2. Materials and Methods

### 2.1 Quantum Chemical Calculations and Spectral Data

The DFT and TD-DFT method preferred for electronic structure calculations by the Gaussian 16 program [19]. The firstly the 6CQ was fully optimized to have stable molecular geometry in the gas phase at the B3LYP method 6-311++G(d,p) basis set [20–22]. The other spectroscopic calculations were obtained with their optimized structure. The scaled factors were used to 0.983 greater than  $1700\text{ cm}^{-1}$  and 0.958 for up to  $1700\text{ cm}^{-1}$  respectively, for vibrational wavenumbers, to correct overestimations [23] because of systematic errors [24]. The fundamental modes were determined in accordance with their PED (potential energy distribution) by using the VEDA program [25] and the GaussView interface [26] to have visual animation and for the verification of these modes. The GIAO method is the most prevalent approach for calculating shielding tensors and is necessary for reliable studies. So,  $^1\text{H}$  and  $^{13}\text{C}$  NMR isotropic shielding of the 6CQ were investigated by using the GIAO method [27], [28] at the same level of theory. The frontier orbitals including the highest occupied and lowest unoccupied molecules orbitals and their energies, electronic transitions, oscillator strengths, and absorbance spectrum were obtained by Time-Dependent DFT (TD-DFT) method.

The infrared spectrum of the studied molecule was used in the databank Standard Reference Data of the National Institute of Standards and Technology, NIST [30]. The  $^1\text{H}$  NMR spectrum data was used in the experimental data of Spectral Database for Organic Compounds, SDBS [31].

## 3. Results and Discussion

### 3.1 Geometrical Structure

Because there is not any revealed x-ray crystallography data of 6CQ, the geometric parameters were compared with that of 2-dichloroquinoline (2DCQ), and quinoline [32], [33] to ensure the validity of electronic structure model chemistry applied in this study. **Figure 1** shows the optimized structure of 6CQ with atom numbering, and the related geometrical parameters were collated in **Table 1**.

The theoretical C–C bond lengths in the phenyl group are in the range of 1.371-1.429 Å for the B3LYP method 6-311G++(d,p) basis set. They are in good agreement with their experimental values reported between 1.358 and 1.4152 Å for quinoline [33] and 1.367 and 1.4175 Å for 2DCQ [32].

Also the bond lengths of C–C in the pyridine range from 1.372 to 1.429 Å for B3LYP with 6-311G++(d,p) basis set which is in good agreement with experimental values [32], [33]. The average deviation of bond lengths from experimental values is nearly 0.086 and 0.072 Å already for quinoline and 2DCQ molecules, respectively. Bond angle calculations also well correlated with experimental results with only averages of 0.8° and 1.9° deviations, for quinoline and 2DCQ molecules, respectively. The maximum variation, 3.4°, is observed in the  $\text{C}_{10}\text{-C}_4\text{-H}_{13}$  bond angle indicating that the N atom located as para position in this state, plays an important role in the distortion of the benzene ring despite creating no effect on bond lengths. The C-H bond lengths are in good agreement with its experimental values [32], [33]. For example, the calculated average of C-H bond lengths, 1.084 Å is in good consistent with their experimental reports of 0.984 Å and 0.95 Å for quinoline and 2DCQ molecules, respectively.

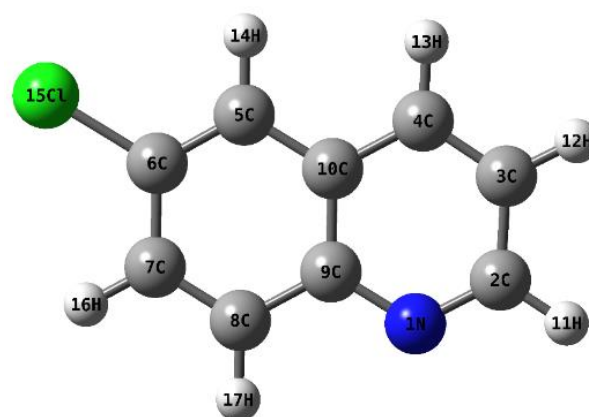


**Figure 1:** The optimized geometrical structure of 6CQ.

The variation, due to the substitution of the Cl atom to phenyl, in the bond length of the  $\text{C}_5\text{-C}_6$  and  $\text{C}_9\text{-C}_{10}$  bond is 0.044 and 0.071 Å, respectively, while expecting deviations from the quinoline molecule. The deviation of bond lengths from experimental values is nearly insignificant as expected because this difference does not belong to the molecule. Bond angle calculations also well correlated with experimental results with only an average of 0.8° and 1.8° deviations for quinoline and 2DCQ molecules, respectively. Lastly, dihedral angles show clearly that the molecule is perfectly planar.

**Table 1.** The experimental and optimized bond lengths (Å) and angles (°) for 2-dichloroquinoline, quinoline, and 6-chloroquinoline (6CQ) molecules B3LYP/6-311++G(d,p).

Parameters	Exp.			Theory			
Bond Lengths	2DCQ <sup>a</sup>	Quinoline <sup>b</sup>	6CQ	Bond Angles	2DCQ <sup>a</sup>	Quinoline <sup>b</sup>	6CQ
N <sub>1</sub> -C <sub>2</sub>	1.2959 (17)	1.319 (2)	1.315	C <sub>6</sub> -C <sub>5</sub> -C <sub>10</sub>	120.06 (13)	120.80(14)	119.4
N <sub>1</sub> -C <sub>9</sub>	1.3738 (17)	1.3742 (17)	1.363	C <sub>6</sub> -C <sub>5</sub> -C <sub>14</sub>	120.0	121.5(10)	120.7
C <sub>2</sub> -C <sub>3</sub>	1.4096 (18)	1.400 (3)	1.417	C <sub>10</sub> -C <sub>5</sub> -H <sub>14</sub>	120.0	117.7(10)	119.9
C <sub>2</sub> -H <sub>11</sub>	1.7475 (13)	1.01 (2)	1.087	C <sub>5</sub> -C <sub>6</sub> -C <sub>7</sub>	120.67 (13)	120.28(15)	121.7
C <sub>3</sub> -C <sub>4</sub>	1.3589 (19)	1.350 (3)	1.372	C <sub>5</sub> -C <sub>6</sub> -Cl <sub>15</sub> (H)	119.7	122.1(11)	119.8
C <sub>3</sub> -H <sub>12</sub>	0.95	0.98 (2)	1.084	C <sub>7</sub> -C <sub>6</sub> -Cl <sub>15</sub> (H)	119.7	117.6(11)	118.5
C <sub>4</sub> -C <sub>10</sub>	1.4225 (18)	1.414 (2)	1.417	C <sub>6</sub> -C <sub>7</sub> -C <sub>8</sub>	120.38 (13)	120.47(15)	119.6
C <sub>4</sub> -H <sub>13</sub>		0.97 (2)	1.085	C <sub>6</sub> -C <sub>7</sub> -H <sub>16</sub>	119.8	119.5(10)	119.4
C <sub>5</sub> -C <sub>6</sub>	1.371 (2)	1.4152 (18)	1.371	C <sub>8</sub> -C <sub>7</sub> -H <sub>16</sub>	119.8	120.0(10)	121.0
C <sub>5</sub> -C <sub>10</sub>	1.4175 (19)	1.416 (2)	1.418	C <sub>7</sub> -C <sub>8</sub> -C <sub>9</sub>	120.63 (13)	120.44(14)	120.9
C <sub>5</sub> -H <sub>14</sub>	0.95	0.95 (2)	1.083	C <sub>7</sub> -C <sub>8</sub> -H <sub>17</sub>	119.7	122.0(10)	121.2
C <sub>6</sub> -C <sub>7</sub>	1.408 (2)	1.412 (2)	1.414	C <sub>9</sub> -C <sub>8</sub> -H <sub>17</sub>	119.7	117.6(10)	117.9
C <sub>6</sub> -Cl <sub>15</sub> (H)	0.95	0.97 (2)	1.758	N <sub>1</sub> -C <sub>9</sub> -C <sub>8</sub>	118.04 (12)	118.42(12)	118.6
C <sub>7</sub> -C <sub>8</sub>	1.367 (2)	1.365 (2)	1.373	N <sub>1</sub> -C <sub>9</sub> -C <sub>10</sub>	122.89 (12)	122.40(12)	122.6
C <sub>7</sub> -H <sub>16</sub>	0.95	0.98(2)	1.083	C <sub>8</sub> -C <sub>9</sub> -C <sub>10</sub>	119.07 (12)	119.17(13)	118.8
C <sub>8</sub> -C <sub>9</sub>	1.4114 (19)	1.410(2)	1.419	C <sub>4</sub> -C <sub>10</sub> -C <sub>5</sub>	124.81 (12)	122.1(11)	122.9
C <sub>8</sub> -H <sub>17</sub>	0.95	1.03(2)	1.083	C <sub>4</sub> -C <sub>10</sub> -C <sub>9</sub>	116.01 (12)	117.32(13)	117.5
C <sub>9</sub> -C <sub>10</sub>	1.4217 (19)	1.358(2)	1.429	C <sub>5</sub> -C <sub>10</sub> -C <sub>9</sub>	119.18 (12)	118.83(13)	119.6
Bond Angles (°)				Selected Dihedral Angles (°)			
C <sub>2</sub> -N <sub>1</sub> -C <sub>9</sub>	116.14 (13)	116.71 (11)	117.9	C <sub>9</sub> -N <sub>1</sub> -C <sub>2</sub> -C <sub>3</sub>	-	-	0
N <sub>1</sub> -C <sub>2</sub> -C <sub>3</sub>	126.50 (12)	124.48(16)	124.1	C <sub>9</sub> -N <sub>1</sub> -C <sub>2</sub> -H <sub>11</sub>	-	-	180
N <sub>1</sub> -C <sub>2</sub> -H <sub>11</sub>	116.73 (10)	116.6(11)	116.3	C <sub>2</sub> -N <sub>1</sub> -C <sub>9</sub> -C <sub>8</sub>	-	-	180
C <sub>3</sub> -C <sub>2</sub> -H <sub>11</sub>	116.77 (10)	118.9(11)	119.6	C <sub>2</sub> -N <sub>1</sub> -C <sub>9</sub> -C <sub>10</sub>	-	-	0
C <sub>2</sub> -C <sub>3</sub> -C <sub>4</sub>	116.60 (12)	118.95(16)	118.9	N <sub>1</sub> -C <sub>2</sub> -C <sub>3</sub> -C <sub>4</sub>	-	-	0
C <sub>2</sub> -C <sub>3</sub> -H <sub>12</sub>	121.7	119.4(10)	119.8	N <sub>1</sub> -C <sub>2</sub> -C <sub>3</sub> -H <sub>12</sub>	-	-	180
C <sub>4</sub> -C <sub>3</sub> -H <sub>12</sub>	121.7	121.7(10)	121.4	C <sub>10</sub> -C <sub>5</sub> -C <sub>6</sub> -Cl <sub>15</sub>	-	-	180
C <sub>3</sub> -C <sub>4</sub> -C <sub>10</sub>	121.26 (12)	119.83(15)	119.2	H <sub>14</sub> -C <sub>5</sub> -C <sub>6</sub> -Cl <sub>15</sub>	-	-	0
C <sub>3</sub> -C <sub>4</sub> -H <sub>13</sub>	-	124.0(10)	121.2	C <sub>3</sub> -C <sub>4</sub> -C <sub>10</sub> -C <sub>5</sub>	-	-	180
C <sub>10</sub> -C <sub>4</sub> -H <sub>13</sub>	-	116.2(10)	119.6	C <sub>6</sub> -C <sub>5</sub> -C <sub>10</sub> -C <sub>9</sub>	-	-	0

<sup>a</sup> The X-Ray data from ref [32]

<sup>b</sup> The X-Ray data from ref [33]

### 3.2 Vibrational Spectral Analysis

The vibrational analysis was prepared as theoretical by using DFT/B3LYP/6-311G++(d,p) model chemistry and compared the experimental data belonging to the 6CQ and the similar structural molecules. The title molecule has C<sub>s</sub> symmetry and has 45 fundamental vibrational modes that can be distributed as 31A' + 14A'' in which A'' and A' represent the out-of-plane and in-plane modes, respectively. The experimental and theoretical IR spectra of 6CQ are given in **Figure 2** and the proposed vibrational assignments generated through PED calculation and visual examination via the GaussView6 program are gathered in **Table 2**. Last column presents a description of detailed fundamental modes. The results of the theory obtained by the B3LYP method and 6-311++G (d,p) basis set. The frequencies of vibrational spectra obtained through electronic structure

single molecule either in vacuum or in polarizable continuum model (PCM) whereas the experiments conducted in solid phase. Besides, the theoretical calculations are obtained at the lowest energy equilibrium geometry and the anharmonic behaviors are omitted to avoid the calculational expense.

The C–H stretching modes of organic molecules are generally observed as multiple peaks in the region of 3000–3100 cm<sup>-1</sup> [34]. In this study, we observed (ν<sub>1</sub>–ν<sub>6</sub>) in the range of 3006–3070 cm<sup>-1</sup> and calculated in the range of 3010–3072 cm<sup>-1</sup> as pure modes by B3LYP functional of DFT as seen PED column in **Table 2**. The C-H symmetric vibrations modes have higher wavelengths than asymmetric ones in rings.

calculations are generally higher than that from experimental results because the calculations are based on

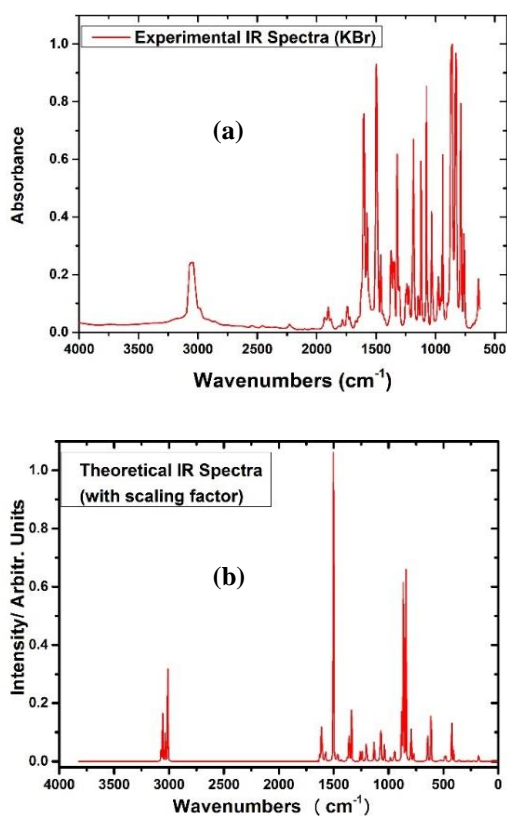


**Figure 2.** The experimental (a) and theoretical (b) IR spectra of 6CQ.

The in-plane and out-of-plane bending modes of C–H are generally observed in aromatic compounds in the range of 1000–1300  $\text{cm}^{-1}$  and 750–1000  $\text{cm}^{-1}$ , respectively [35]. The experimental C–H in-plane bending modes of the studied molecule are in the range of 1032–1497  $\text{cm}^{-1}$  and generally mixed with C–C and C–N stretching modes according to their PED results. The C–H out-of-plane bending vibrations were found at 873, 946–976  $\text{cm}^{-1}$  region.

The stretching vibrations modes of C–N are generally very difficult to determine due to the mixing of other modes. Silverstein et al. [36] defined the C–N stretching modes in the region of 1386–1266  $\text{cm}^{-1}$  for aromatic amines. The modes are very broadband and mixed with the C–C modes, the biggest contribution of C–N vibrations comes from mode  $\nu_{15}$  according to the PED analysis. The scaled wavenumbers of C–N are well correlating with experimental observations. The results have also good similarity for similar quinoline derivatives [13], [37], [38].

Two or three bands were recorded in the region 1600–1200  $\text{cm}^{-1}$  named skeletal vibrations modes.

The most conurbations generally at about 1500  $\text{cm}^{-1}$  for six-membered aromatic rings like phenyl and pyridine. Varsányi [39] also recorded five bands at 1625–1590, 1590–1575, 1540–1470, 1465–1430, and 1380–1280  $\text{cm}^{-1}$  and implied that these bands are of variable intensity. In this study, C–C stretching vibrations modes were dedicated in the region 1032–1621, 941, 859, 766, 607, 516, 417, and 218  $\text{cm}^{-1}$  and overlapped the other stretching modes. The highest percentages of PED were obtained as 61%, and 64%, for  $\nu_7$  and  $\nu_{22}$  modes, respectively. The results of the C–C stretching modes are in good correlation with the experimental vibrational results. C–C stretching modes are also well correlated for similar structural molecules in the literature [37], [40], [41].

The stretching vibrations of C–Cl are recorded generally as broad bands region at 760–505  $\text{cm}^{-1}$  [42]. The C–Cl stretching modes of the 1-chloroisoquinoline molecule were identified at 675  $\text{cm}^{-1}$  and at 674  $\text{cm}^{-1}$ , FT-Raman and FT-IR bands respectively [43]. Also, the C–Cl stretching modes of 8CQ were recorded as a very strong band at 659 and 651  $\text{cm}^{-1}$  in IR and Raman, respectively [13]. The C–Cl stretching vibrations that appeared at 355 and 589  $\text{cm}^{-1}$  show a deviation due to nitrogen atoms with electro-negative properties [37]. In the present work, the C–Cl stretching modes of the 6CQ molecule were observed at 351, 607, and 637  $\text{cm}^{-1}$  and showed a good correlation with the experimental results, and literature. The experimental and theoretical correlation of vibrational frequencies can be seen from **Figure 3**.

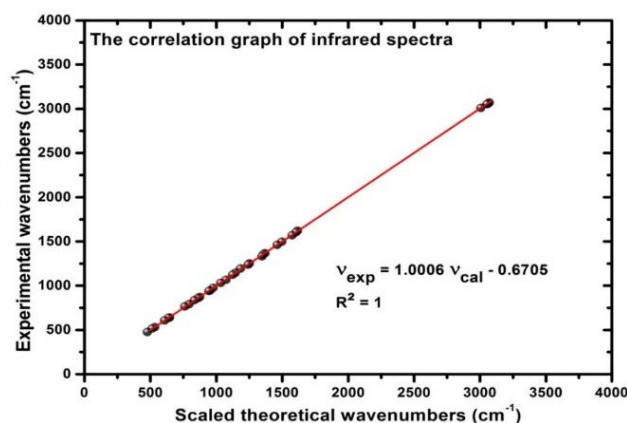


**Figure 3.** The correlation of the of 6CQ molecule for IR spectra.

**Table 2.** The calculated and experimental (FT-IR) wavenumbers ( $\text{cm}^{-1}$ ) using B3LYP method 6-311++G(d,p) basis set of 6CQ molecule.

Modes No	Sym.	Theoretical		Experimental		PED <sup>b</sup> ( $\geq 10\%$ )
		Unscaled freq.	Scaled freq. <sup>a</sup>	FT-IR <sub>nujol</sub>	FT-IR <sub>KBR</sub>	
v1	A'	3206	3072	3070		$\nu\text{CH}_{\text{sym.}}$ (100)
v2	A'	3192	3058	3059		$\nu\text{CH}_{\text{sym.}}$ (99)
v3	A'	3191	3057	3056		$\nu\text{CH}_{\text{asym.}}$ (100)
v4	A'	3188	3054		3052	$\nu\text{CH}_{\text{asym.}}$ (99)
v5	A'	3166	3033			$\nu\text{CH}_{\text{asym.}}$ (100)
v6	A'	3142	3010	3006		$\nu\text{CH}_{\text{asym.}}$ (100)
v7	A'	1649	1621	1616		$\nu\text{CC}$ (61), $\delta\text{CCCH}$ (21), $\delta\text{CCC}$ (13)
v8	A'	1632	1604	1595	1604	$\nu\text{CC}$ (46), $\nu\text{CN}$ (19), $\delta\text{CCCH}$ (16), $\delta\text{CCC}$ (10)
v9	A'	1598	1571	1566	1574	$\nu\text{CC}$ (39), $\nu\text{CN}$ (16), $\delta\text{CCC}$ (31)
v10	A'	1523	1497	1491	1496	$\nu\text{CC}$ (29), $\nu\text{CN}$ (10), $\delta\text{CCCH}$ (41), $\delta\text{CCN}$ (13)
v11	A'	1487	1461	1454	1461	$\nu\text{CC}$ (27), $\delta\text{CCCH}$ (44), $\delta\text{CCN}$ (10), $\delta\text{CCC}$ (10)
v12	A'	1451	1427			$\nu\text{CC}$ (22), $\delta\text{CCCH}$ (65)
v13	A'	1392	1368	1369	1372	$\nu\text{CC}$ (48), $\nu\text{CN}$ (11), $\delta\text{CCC}$ (26), $\delta\text{CCCH}$ (12)
v14	A'	1377	1354	1355	1356	$\nu\text{CC}$ (47), $\nu\text{CN}$ (18), $\delta\text{CCCH}$ (31)
v15	A'	1356	1333	1347	1346	$\nu\text{CC}$ (15), $\nu\text{CN}$ (28), $\delta\text{CCCH}$ (36), $\delta\text{CCC}$ (14)
v16	A'	1274	1252	1250	1251	$\nu\text{CC}$ (18), $\delta\text{CCCH}$ (57), $\delta\text{CCC}$ (14)
v17	A'	1260	1239	1241	1240	$\nu\text{CC}$ (21), $\nu\text{CN}$ (13), $\delta\text{CCCH}$ (46), $\delta\text{CCC}$ (10)
v18	A'	1215	1195	1184	1183	$\nu\text{CC}$ (18), $\delta\text{CCCH}$ (72)
v19	A'	1166	1146	1145	1144	$\nu\text{CC}$ (29), $\delta\text{CCCH}$ (66)
v20	A'	1144	1125	1120	1123	$\nu\text{CC}$ (31), $\delta\text{CCCH}$ (38), $\delta\text{CCC}$ (16), $\delta\text{CCN}$ (10),
v21	A'	1085	1067	1074	1073	$\nu\text{CC}$ (40), $\nu\text{CN}$ (13), $\delta\text{CCCH}$ (22), $\delta\text{CCC}$ (14)
v22	A'	1050	1032	1033	1032	$\nu\text{CC}$ (64), $\delta\text{CCCH}$ (26)
v23	A''	993	976	980	975	$\gamma\text{CH}$ [ $\tau\text{CCCH}$ (78), $\tau\text{CCCN}$ (18)]
v24	A''	983	967	959		$\gamma\text{CH}$ [ $\tau\text{CCCH}$ (73), $\tau\text{CCCN}$ (24)]
v25	A''	963	946		952	$\gamma\text{CH}$ [ $\tau\text{CCCH}$ (70), $\tau\text{CCCN}$ (21)]
v26	A'	957	941	943	940	$\nu\text{CC}$ (11), $\delta\text{CCCH}$ (14), $\delta\text{CCC}$ (54), $\delta\text{CCN}$ (10)
v27	A''	888	873	874		$\gamma\text{CH}$ [ $\tau\text{CCCH}$ (89), $\tau\text{CCCN}$ (10)]
v28	A'	874	859	854	860	$\nu\text{CC}$ (11), $\delta\text{CCC}$ (52), $\delta\text{CCN}$ (21)
v29	A''	850	836	832	828	$\gamma\text{CH}$ [ $\tau\text{CCCH}$ (90)]
v30	A''	804	790	792	787	$\gamma\text{CH}$ [ $\tau\text{CCCH}$ (25), $\tau\text{CCCN}$ (61), $\tau\text{CCCC}$ (12)]
v31	A''	779	766	766		$\nu\text{CC}$ (19), $\nu\text{CN}$ (13), $\delta\text{CCN}$ (30), $\delta\text{CCCH}$ (11), $\delta\text{CCC}$ (23)
v32	A'	779	765		760	$\gamma\text{CH}$ [ $\tau\text{CCCH}$ (78), $\tau\text{CCCN}$ (12)]
v33	A'	651	640	645		$\gamma\text{CH}$ [ $\tau\text{CCCH}$ (21), $\tau\text{CCCN}$ (38), $\tau\text{CCCC}$ (15)], $\tau\text{CNCCI}$ (25)
v34	A''	648	637		637	$\nu\text{CC}$ (22), $\nu\text{CCI}$ (10), $\delta\text{CCN}$ (25), $\delta\text{CCCH}$ (14), $\delta\text{CCC}$ (24)
v35	A'	618	607	607		$\nu\text{CC}$ (14), $\nu\text{CCI}$ (19), $\delta\text{CCN}$ (11), $\delta\text{CCC}$ (45)
v36	A'	540	531	532		$\gamma\text{CH}$ [ $\tau\text{CCCH}$ (21), $\tau\text{CCCN}$ (38), $\tau\text{CCCC}$ (18)], $\tau\text{CNCCI}$ (21)
v37	A''	525	516	512		$\nu\text{CC}$ (23), $\delta\text{CCN}$ (16), $\delta\text{CCCH}$ (21), $\delta\text{CCC}$ (36)
v38	A''	485	477	476		$\gamma\text{CH}$ [ $\tau\text{CCCH}$ (14), $\tau\text{CCCN}$ (67), $\tau\text{CCCC}$ (14)]
v39	A'	425	417			$\nu\text{CC}$ (19), $\delta\text{CNCl}$ (22), $\delta\text{CCC}$ (45)
v40	A''	408	401			$\gamma\text{CH}$ [ $\tau\text{CCCH}$ (14), $\tau\text{CCCN}$ (73), $\tau\text{CCCC}$ (11)]
v41	A'	357	351			$\nu\text{CN}$ (10), $\nu\text{CCI}$ (49), $\delta\text{CCCH}$ (10), $\delta\text{CCC}$ (15)
v42	A''	274	269			$\tau\text{CCCN}$ (60), $\tau\text{CNCCI}$ (25), $\tau\text{CCCC}$ (11)
v43	A'	221	218			$\nu\text{CC}$ (12), $\delta\text{CNCl}$ (61), $\delta\text{CCC}$ (16)
v44	A''	174	171			$\tau\text{CCCN}$ (95)
v45	A''	101	99			$\tau\text{CCCN}$ (67), $\tau\text{CNCCI}$ (16)

<sup>a</sup> The scale factor used to 0.958 and 0.983 ranges from 4000 to 1700  $\text{cm}^{-1}$  and lower than 1700  $\text{cm}^{-1}$ , respectively.

<sup>b</sup> Potential Energy Distribution; PED,  $\nu$ ; stretching,  $\gamma$ ; out-of plane bending,  $\delta$ ; in-plane-bending,  $\tau$ ; torsion,  $\rho$ ; scissoring,  $\omega$ ; wagging,  $\phi$ ; twisting,  $\rho$ ; rocking.

### 3.3 Nuclear Magnetic Resonance Spectra

NMR spectra is a principal method for studying of organic molecules. The NMR spectroscopic results, recorded with computer simulation methods, help to have more information about the structure of biomolecules as a strong method [27], [28]. The Gauge-including atomic orbital (GIAO) [27], [28] method at B3LYP method 6-

311G++(d,p) level theory is used to obtain  $^1\text{H}$  and  $^{13}\text{C}$  NMR spectra of 6CQ molecule after full optimization of its geometry. The theoretical (gas phase and in  $\text{CDCl}_3$ ) and experimental data (in  $\text{CDCl}_3$ ) [31] of  $^1\text{H}$  and  $^{13}\text{C}$  NMR spectra were gathered in **Table 3**. **Figure 4a-4b** present the taken experimental spectra [31] of  $^1\text{H}$  and  $^{13}\text{C}$  NMR of the studied molecule.

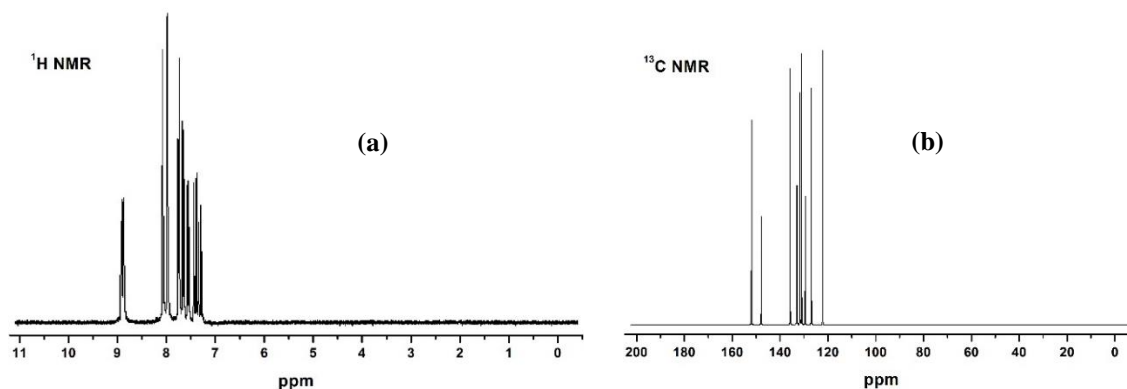


**Figure 4.** (a) The experimental  $^1\text{H}$  and (b)  $^{13}\text{C}$  NMR spectra of 6CQ

**Table 3.** Theoretical and experimental  $^1\text{H}$  and  $^{13}\text{C}$  NMR chemical shifts of 6CQ molecule B3LYP method 6-311++ G(d,p) basis set.

Atoms	Exp. ( $\text{CDCl}_3$ )	Teo. $\text{CDCl}_3$	Teo. Gas
C <sub>2</sub>	150.51	156.07	155.08
C <sub>3</sub>	121.79	126.39	125.35
C <sub>4</sub>	134.93	140.53	138.80
C <sub>5</sub>	126.32	131.33	130.47
C <sub>6</sub>	132.18	146.26	147.15
C <sub>7</sub>	130.26	134.94	134.69
C <sub>8</sub>	131.06	137.17	137.63
C <sub>9</sub>	146.57	153.27	153.56
C <sub>10</sub>	128.71	134.13	133.84
H <sub>11</sub>	8.89	9.11	9.07
H <sub>12</sub>	7.39	7.58	7.36
H <sub>13</sub>	8.03	8.29	8.04
H <sub>14</sub>	7.76	8.00	7.82
H <sub>16</sub>	7.63	7.90	7.80
H <sub>17</sub>	8.03	8.25	8.24

It can be assumed that the quinoline ring contains a phenyl and a pyridine ring. The signal of protons in the phenyl ring is often observed in the range of 7–8.5 ppm. Electron withdrawing atoms or groups of atoms can reduce shielding and move the resonance to a higher frequency, while in electron donating systems it drops to a lower frequency. [44]. The H<sub>12</sub> atom has appeared to have the lowest chemical shifts ( $\delta = 7.39$  ppm) and the H<sub>11</sub> atom is at the highest chemical shifts ( $\delta = 8.89$  ppm) due to shielding by electronegative nitrogen atom [31].

Theoretical calculations obtained under PCM give slightly higher chemical shifts in comparison to both gas phase calculations and the experimental data. However, the correlation between experimental data and PCM modeling is better than the accordance between gas phase calculations and the measured ones.

The chemical shifts of carbons especially show resonance and overlap in the region at 100-150 ppm [45], [46] and also seen same region for quinoline in the literature [47], [48]. The shifts for carbons C<sub>2</sub>, and C<sub>9</sub> are higher than the others which can be due to the neighboring nitrogen atom. The difference of the carbon NMR value of C<sub>2</sub> atom is reasonable as 150.51 ppm (exp.) and 156.07 ppm (calc.), similar correlations are seen the other carbons. A general correlation evaluation between the theoretical and experimental chemical shifts is given in **Figure 5**.

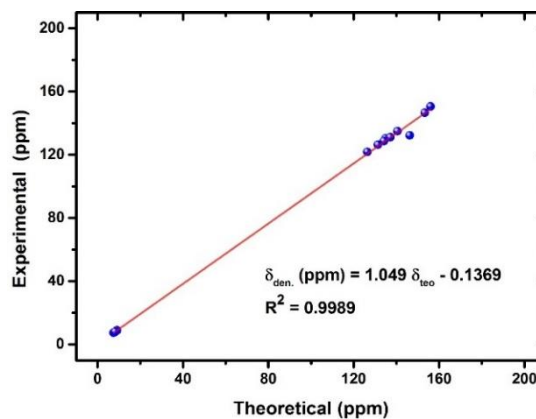


**Figure 5.** The correlation graphic of NMR spectra for 6CQ molecule.

### 3.4 UV-Vis Spectra and Frontier Molecular Orbital Analysis

UV-Vis spectra were presented in gas phase, water and ethanol solvents as a theoretically to understand electronic transitions and predict the UV-Vis spectrum of 6CQ. TD-DFT method was utilized confidently because of its computational plausibility and validity for medium size molecules [49–51]. The absence of experimental data quantum chemical calculations can be useful to shed light on the literature and contribute to future studies. Theoretical electronic absorption properties were obtained using the TD-DFT method B3LYP/6-311++G(d,p) basis set. The results of UV-Vis (electronic absorption) spectra of the 6CQ molecule were graphed in **Figure 6**. The excitation energies ( $E$ ), calculated absorption ( $\lambda$ ), oscillator strength ( $f$ ), and major contributions, obtained via GaussSum 2.2 [29] program, for the 6CQ, are given in **Table 4** for the gas phase, ethanol, and water solvents. The maximum wavelengths were obtained at about 290 nm for all solvents. The excitation properties chemical reactivity behavior, spectroscopic features, and the ability of electron transport were obtained by using the frontier molecular orbital (MO) determination [52]. The electron donating and accepting form of molecule can be described by highest occupied molecular orbital (HOMO) and lowest unoccupied molecular orbital (LUMO), respectively. The frontier molecular orbitals isosurface, energy gaps, and orbital transitions were listed in **Table 5** and pictured in **Figure 7**. The MO diagrams were given in **Figure 8**, to see energy levels.

The energy gaps for the gas phase, water, and solvents were obtained as 4.74, 4.77, and 4.77 eV, respectively. The red and green nodes in **Figure 7** are positive and negative values of frontier molecular orbitals. The orbital distribution of HOMO localized all regions except some hydrogen atoms. The orbital distribution of LUMO is changed on all atoms on the molecule. The other important energy gaps rather than HOMO, LUMO such as  $H-1 \rightarrow L$ ,  $H \rightarrow L+1$ ,  $H-1 \rightarrow L+1$ , and  $H \rightarrow L+2$  (also the others) can be critical parameters in determining molecular electrical transport properties (see **Table 5** and **Figure 7**).

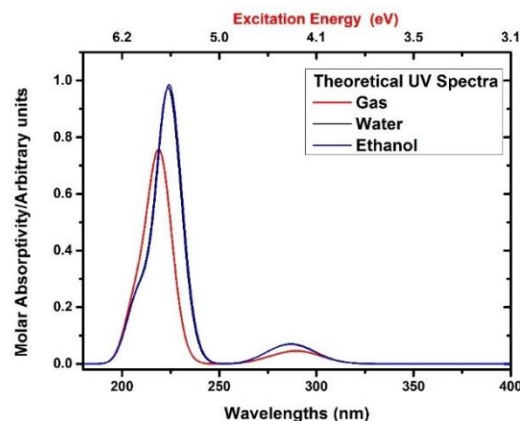


**Figure 6.** The theoretical UV-Vis spectra of 6CQ molecule gas phase, in ethanol and water.

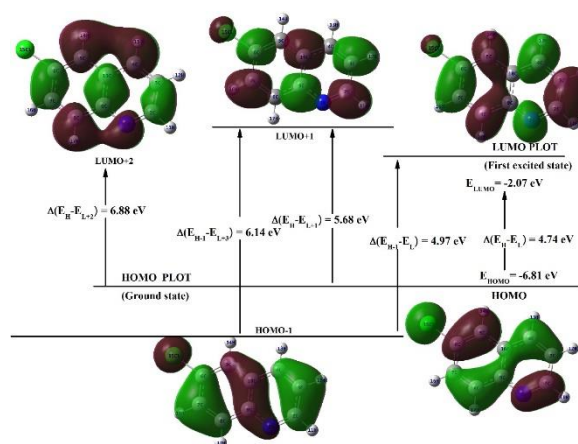


**Figure 7.** The remarkable FMOs of 6CQ molecule with energy gaps.

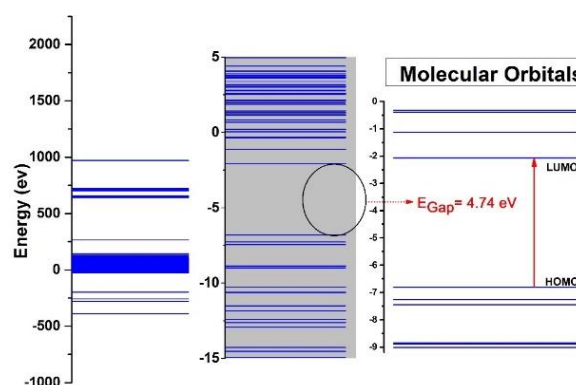


**Figure 8.** The MO energy levels of the 6CQ molecule.

**Table 4.** Experimental and calculated wavelengths  $\lambda$  (nm), excitation energies (eV), oscillator strengths ( $f$ ) of 6CQ for gas phase, in ethanol and water solutions.

TD-DFT				
	$f$	Major contributes	E (eV)	$\lambda$ (nm)
Gas	0.0479	H→L (79%)	4.2421	292.31
	0.4897	H-1→L (13%), H-1→L+1 (16%), H→L+1 (38%), H→L+2 (21%)	5.6480	219.55
	0.2252	H-5→L (11%), H-1→L+1 (56%), H→L+2 (21%)	5.9421	208.68
Water	0.0641	H→L (81%)	4.2679	290.54
	1.2232	H-1→L (29%), H→L+1 (64%)	5.5413	223.77
	0.2591	H-1→L+1 (62%), H→L+2 (25%)	5.9114	209.76
Ethanol	0.0658	H→L (81%)	4.2646	290.77
	1.2389	H-1→L (29%), H→L+1 (64%)	5.5306	224.21
	0.2618	H-1→L+1 (62%), H→L+2 (25%)	5.9068	209.93

H: HOMO, L: LUMO

**Table 5.** The calculated energy values of 6CQ molecule using B3LYP 6-311++G(d,p) basis set.

TD-DFT/B3LYP/6-311++G(d,p)	Gas	Ethanol	Water
$E_{\text{total}}$ (Hartree)	-861.49846	-900.83420	-861.50292
$E_{\text{HOMO-5}}$ (eV)	-9.02	-9.08	-9.09
$E_{\text{HOMO-1}}$ (eV)	-7.27	-7.26	-7.26
$E_{\text{HOMO}}$ (eV)	-6.81	-6.83	-6.83
$E_{\text{LUMO}}$ (eV)	-2.07	-2.06	-2.06
$E_{\text{LUMO+1}}$ (eV)	-1.13	-1.12	-1.12
$E_{\text{LUMO+2}}$ (eV)	-0.39	-0.37	-0.38
$E_{\text{LUMO+3}}$ (eV)	-0.32	-0.16	-0.16
$E_{\text{HOMO-1-LUMO gap}}$ (eV)	5.20	5.20	5.20
$E_{\text{HOMO-1-LUMO+1 gap}}$ (eV)	6.14	6.14	6.14
$E_{\text{HOMO-1-LUMO+2 gap}}$ (eV)	6.88	6.89	6.88
$E_{\text{HOMO-1-LUMO+3 gap}}$ (eV)	6.95	7.10	7.10
$E_{\text{HOMO-LUMO gap}}$ (eV)	4.74	4.77	4.77
$E_{\text{HOMO-LUMO+1 gap}}$ (eV)	5.68	5.71	5.71
$E_{\text{HOMO-LUMO+2 gap}}$ (eV)	6.42	6.46	6.45
$E_{\text{HOMO-LUMO+3 gap}}$ (eV)	6.49	6.67	6.67
Chemical hardness ( $\eta$ )	-2.37	-2.39	-2.39
Electronegativity ( $\chi$ )	4.44	4.45	4.45
Chemical potential ( $\mu$ )	-4.44	-4.45	-4.45
Electrophilicity index ( $\omega$ )	-4.16	-4.14	-4.14

The chemical potential ( $\mu$ ), and hardness ( $\eta$ ) by  $\mu = -(I-H)/2$ , and  $\eta = (I-H)/2$  in these equations I and H are ionization potential and electron affinity, were determined by Parr and Pearson [53]. Also, global electrophilicity index ( $\omega$ ), expressed,  $\omega = \mu^2/2\eta$ , in terms of  $\mu$  and  $\eta$  [54]. The chemical hardness of molecules indicates that a hard or soft molecule according to the

energy gaps, has large or small, respectively. Also, the soft molecules have more polarizable than the hard molecules because they can be excited through small excitation energies. The chemical reactivity values for 6CQ are nearly the same for gas phase and solvents indicating that the solvent does not significantly alters the chemical reactivity of the compound.

### 3.5 Molecular Electrostatic Potential Surface

The molecular electrostatic potential surfaces (MEPs) of molecules generally provide more information about the reactive behavior of a compound because it is related to their electron density describing nucleophilic and electrophilic regions, as negative and positive, respectively [55], [56]. The counter map and three-dimensional electrostatic potential mapped electron density surface (MEP) of the studied molecule were given in **Figure 9**. The values on MEP surfaces increase from red to blue color and line up between  $-4.046e^{-2}$  to  $4.046e^{-2}$  (a.u.). The MEPs picture indicates that while regions with negative potential are over the electronegative nitrogen and chloride atoms, the positive ones are over the hydrogen atoms, especially H<sub>12</sub> and H<sub>13</sub>. The lowest negative value and highest positive potential indicate electron-rich and deficient surfaces, respectively. The MEP surface also indicates the steric center of phenyl and pyridine rings. The MEP surface is a qualitative representation of the charge distribution of the atoms in a molecule.

### 3.6 The Mulliken Atomic Charges

The quantum mechanical calculations of the molecular systems can generate a quantitative assignment of partial atomic charges through several types of population analysis techniques in which the most used is Mulliken population analysis. [57]. The Mulliken atomic charges of quinoline and 6CQ molecules were predicted at DFT/B3LYP method 6-31G(d) level rather than with a 6-311++G(d,p) basis set to have more reliable results. It has been observed that the large basis sets with diffusive character create an increased overlap of electron densities and causes some systematical error [37], [58]. The Mulliken atomic charges of 6CQ are given in **Figure 10** in comparison to that of Quinoline. The chloride atom creates a significant change in the charge distribution and nearby atoms due to its strong electronegative character. The charge redistribution mostly takes place among the chloride atom and the carbon atoms, and the charge of hydrogen atoms in Quinoline and 6CQ have almost the same. The hydrogen atoms are partially positive in both cases and act as electrophilic sites of the molecules.

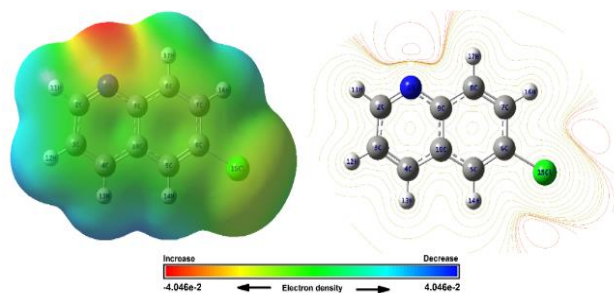


**Figure 9.** The molecular electrostatic potential (MEPs) surface graph for 6CQ molecule.

Significant changes occur in the partial charges of the carbon atoms in which the sign of charges of C<sub>2</sub>, C<sub>9</sub>, and C<sub>10</sub> atoms changed from negative to positive and that of C<sub>5</sub> and C<sub>6</sub> atoms shows a change from positive to negative. This alteration is most likely caused by the strong electronegative substitution.

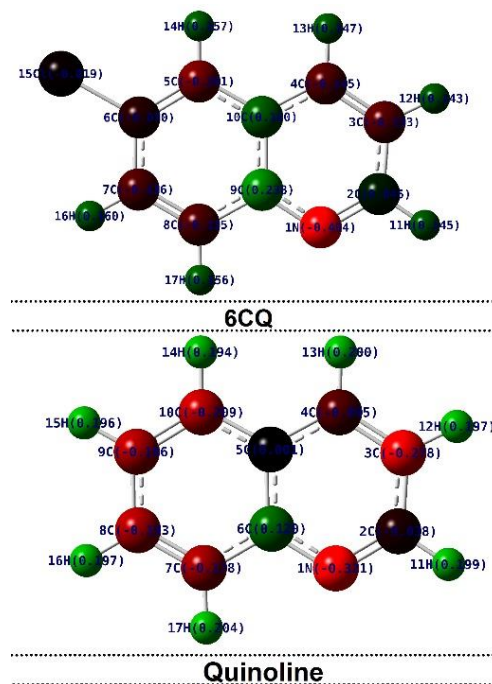


**Figure 10.** The Mulliken charge distribution for Quinoline and 6CQ molecules obtained through DFT/B3LYP method 6-31G(d) level model chemistry.

### 4. Conclusion

In conclusion, our study shows that the electronic structure and spectroscopic properties of 6-chloroquinoline have been successfully simulated using the DFT/B3LYP method and 6-311++G(d,p) basic set model chemistry. The high accuracy achieved in the theoretical simulation is supported by the perfect match with the experimental FT-IR and NMR spectroscopic data. Analysis of frontier molecular orbitals and reactivity parameters provides valuable information about the observed spectral peaks found to originate from various orbital transitions with similar probabilities. The addition of a chlorine substituent significantly affects the vibrational and chemical shielding properties of neighboring atoms within two bond distances. Moreover, the strong correlation between the simulated and observed spectra highlights the reliability and accuracy of our computational approach. In this study, it is seen that the effect of the chlorine atom is effective on both the spectroscopic and electronic properties when viewed easily in terms of the quinol molecule. The binding of halogens such as chlorine and/or fluorine attached to the quinol molecule may produce similar results.

In addition, it can be predicted that both chlorine and other halogens may be effective in spectroscopic and electronic studies for different quinol derivatives. These findings contribute to a comprehensive understanding of the electronic and spectroscopic properties of 6-chloroquinoline and pave the way for future research in this area.

## References

- [1] R. Gupta, A. K. Gupta, S. Paul, and P. L. Kachroo, "Synthesis and biological activities of some 2-chloro-6/8-substituted-3-(3-alkyl aryl-5, 6-dihydro-s-triazolo-[3, 4-h][1, 3, 4] thiadiazol-6-yl) quinolines," *Indian J. Chem.*, vol. 37B, pp. 1211–1213, 1998.
- [2] R. Gupta, A. K. Gupta, S. Paul, and P. Somal, "Microwave-assisted synthesis and biological activities of some 7/9-substituted-4-(3-alkyl/aryl-5, 6-dihydro-s-triazolo [3, 4-b][1, 3, 4] thiadiazol-6-yl) tetrazolo [1, 5-a] quinolines," *Indian J. Chem.*, vol. 39B, pp. 847–852, 2000.
- [3] D. Dubé *et al.*, "Quinolines as potent 5-lipoxygenase inhibitors: Synthesis and biological profile of L-746,530," *Bioorganic Med. Chem. Lett.*, vol. 8, no. 10, pp. 1255–1260, 1998, doi: 10.1016/S0960-894X(98)00201-7.
- [4] S. Tewari, P. M. S. Chauhan, A. P. Bhaduri, N. Fatima, and R. K. Chatterjee, "Syntheses and antifilarial profile of 7-chloro-4(substituted amino) quinolines: A new class of antifilarial agents," *Bioorganic Med. Chem. Lett.*, vol. 10, no. 13, pp. 1409–1412, 2000, doi: 10.1016/S0960-894X(00)00255-9.
- [5] M. Fujita, K. Chiba, Y. Tominaga, and K. Hino, "7-(2-Aminomethyl-1-azetidiny)-4-oxoquinoline-3-carboxylic Acids as Potent Antibacterial Agents: Design, Synthesis, and Antibacterial Activity," *Chem. Pharm. Bull.*, vol. 46, no. 5, pp. 787–796, 1998, doi: 10.1248/cpb.46.787.
- [6] M. Kidwai, K. R. Bhushan, P. Sapra, R. K. Saxena, and R. Gupta, "Alumina-supported synthesis of antibacterial quinolines using microwaves," *Bioorganic Med. Chem.*, vol. 8, no. 1, 2000, doi: 10.1016/S0968-0896(99)00256-4.
- [7] J. Ziegler, R. Linck, and D. W. Wright, "Heme aggregation inhibitors: Antimalarial drugs targeting an essential biomineralization process," *Stud. Nat. Prod. Chem.*, vol. 25, pp. 327–366, 2001, doi: 10.1016/S1572-5995(01)80011-9.
- [8] F. M. D. Ismail, M. J. Dascombe, P. Carr, S. A. M. Mérette, and P. Rouault, "Novel aryl-bis-quinolines with antimalarial activity in vivo," *J. Pharm. Pharmacol.*, vol. 50, no. 5, pp. 483–492, 1998, doi: 10.1111/j.2042-7158.1998.tb06189.x.
- [9] O. Famin, M. Krugliak, and H. Ginsburg, "Kinetics of inhibition of glutathione-mediated degradation of ferriprotoporphyrin IX by antimalarial drugs," *Biochem. Pharmacol.*, vol. 58, no. 1, pp. 59–68, 1999, doi: 10.1016/S0006-2952(99)00059-3.
- [10] K. M. Khan *et al.*, "Syntheses and cytotoxic, antimicrobial, antifungal and cardiovascular activity of new quinoline derivatives," *Arzneimittelforschung*, vol. 50, no. 10, pp. 915–924, 2000, doi: 10.1055/s-0031-1300313.
- [11] L. W. Deady, J. Desneves, A. Kaye, G. Finlay, B. Baguley, and W. Denny, "Positioning of the carboxamide side chain in 11-oxo-11H-indeno[1,2-b]quinolinecarboxamide anticancer agents: Effects on cytotoxicity," *Bioorganic Med. Chem.*, vol. 9, no. 2, pp. 445–452, 2001, doi: 10.1016/S0968-0896(00)00264-9.
- [12] L. Strekowski *et al.*, "Synthesis and Quantitative Structure-Activity Relationship Analysis of 2-(Aryl or Heteroaryl)quinolin-4-amines, a New Class of Anti-HIV-1 Agents," *J. Med. Chem.*, vol. 34, no. 5, pp. 1739–1746, 1991, doi: 10.1021/jm00109a031.
- [13] V. Arjunan, P. Ravindran, T. Rani, and S. Mohan, "FTIR, FT-Raman, FT-NMR, ab initio and DFT electronic structure investigation on 8-chloroquinoline and 8-nitroquinoline," *J. Mol. Struct.*, vol. 988, no. 1, pp. 91–101, 2011, doi: 10.1016/j.molstruc.2010.12.032.
- [14] V. Arjunan, I. Saravanan, P. Ravindran, and S. Mohan, "Ab initio, density functional theory and structural studies of 4-amino-2-methylquinoline," *Spectrochim. Acta. A. Mol. Biomol. Spectrosc.*, vol. 74, no. 2, pp. 375–84, Oct. 2009, doi: 10.1016/j.saa.2009.06.028.
- [15] S. Sivaprakash, S. Prakash, S. Mohan, and S. P. Jose, "Molecular structure, vibrational analysis (IR and Raman) and quantum chemical investigations of 1-aminoisoquinoline," *J. Mol. Struct.*, vol. 1149, pp. 835–845, 2017, doi: 10.1016/j.molstruc.2017.08.060.
- [16] G. Oanca, J. Stare, A. G. Todirascu, D. Creanga, and D. O. Dorohoi, "Substituent influence on the spectra of some benzo[f]quinoline derivatives," *J. Mol. Struct.*, vol. 1126, pp. 158–164, Dec. 2016, doi: 10.1016/J.MOLSTRUC.2016.03.072.
- [17] M. Kumru, A. Altun, M. Kocademir, V. Küçük, T. Bardakçı, and B. Şaşmaz, "Combined experimental and quantum chemical studies on spectroscopic (FT-IR, FT-Raman, UV–Vis, and NMR) and structural characteristics of quinoline-5-carboxaldehyde," *J. Mol. Struct.*, vol. 1125, pp. 302–309, 2016, doi: 10.1016/j.molstruc.2016.06.066.
- [18] V. Arjunan, S. Mohan, P. S. Balamourougane, and P. Ravindran, "Quantum chemical and spectroscopic investigations of 5-aminoquinoline," *Spectrochim. Acta Part A Mol. Biomol. Spectrosc.*, vol. 74, no. 5, pp. 1215–1223, 2009, doi: 10.1016/j.saa.2009.09.039.
- [19] M. J. Frisch *et al.*, "Gaussian 16 Revision A.03." Gaussian, Inc., Wallingford, CT, 2016.
- [20] J. P. Perdew and Y. Wang, "Accurate and simple analytic representation of the electron-gas correlation energy," *Phys. Rev. B*, vol. 45, no. 23, pp. 13244–13249, Jun. 1992, [Online]. Available: <http://link.aps.org/doi/10.1103/PhysRevB.45.13244>.
- [21] C. Lee, W. Yang, and R. G. Parr, "Development of the Colle-Salvetti correlation-energy formula into a functional of the electron density," *Phys. Rev. B*, vol. 37, no. 2, pp. 785–789, Jan. 1988, [Online]. Available: <http://link.aps.org/doi/10.1103/PhysRevB.37.785>.
- [22] A. D. Becke, "Density-functional thermochemistry. III. The role of exact exchange," *J. Chem. Phys.*, vol. 98, no. 7, pp. 5648–5652, 1993, doi: 10.1063/1.464913.
- [23] N. Sundaraganesan, S. Ilakiamani, H. Saleem, P. M. Wojciechowski, and D. Michalska, "FT-Raman and FT-IR spectra, vibrational assignments and density functional studies of 5-bromo-2-nitropyridine," *Spectrochim. Acta Part A Mol. Biomol. Spectrosc.*, vol. 61, no. 13–14, pp. 2995–3001, Oct. 2005, doi: 10.1016/j.saa.2004.11.016.
- [24] J. B. Foresman and A. Frisch, "Exploring chemistry with electronic structure methods, 1996," *Gaussian Inc, Pittsburgh, PA*, pp. 98–99, 1996.
- [25] M. H. Jamróz, "Vibrational energy distribution analysis (VEDA): scopes and limitations," *Spectrochim. Acta Part A Mol. Biomol. Spectrosc.*, vol. 114, pp. 220–230, Oct. 2013, doi: 10.1016/j.saa.2013.05.096.
- [26] R. Dennington, T. Keith, and J. Millam, *GaussView, Version 5*. 2009.
- [27] R. Ditchfield, "Molecular Orbital Theory of Magnetic Shielding and Magnetic Susceptibility," *J. Chem. Phys.*, vol. 56, no. 11, pp. 5688–5691, 1972, doi: 10.1063/1.1677088.



- [28] K. Wolinski, J. F. Hinton, and P. Pulay, "Efficient implementation of the gauge-independent atomic orbital method for NMR chemical shift calculations," *J. Am. Chem. Soc.*, vol. 112, no. 23, pp. 8251–8260, Nov. 1990, doi: 10.1021/ja00179a005.
- [29] N. M. O'Boyle, A. L. Tenderholt, and K. M. Langner, "Software News and Updates cclib: A Library for Package-Independent Computational Chemistry Algorithms," *J. Comput. Chem.*, vol. 29, no. 5, pp. 839–845, 2008, doi: 10.1002/jcc.20823.
- [30] NIST Web: <http://cccbdb.nist.gov/vibscalejust.asp>, "http://cccbdb.nist.gov/vibscalejust.asp," 2018. .
- [31] SDBS Web: <http://sdb.srioddb.aist.go.jp> (National Institute of Advanced Industrial Science and Technology), "SDBS Web: <http://sdb.srioddb.aist.go.jp> (National Institute of Advanced Industrial Science and Technology)," 2018. [http://sdb.srioddb.aist.go.jp/sdb/cgi-bin/direct\\_frame\\_top.cgi](http://sdb.srioddb.aist.go.jp/sdb/cgi-bin/direct_frame_top.cgi).
- [32] R. Kimmel, M. Nečas, and R. Vicha, "2,4-Dichloroquinoline," *Acta Crystallogr. Sect. E Struct. Reports Online*, vol. 66, no. 6, pp. o261–o1261, 2010, doi: 10.1107/S160053681001576X.
- [33] J. E. Davies and A. D. Bond, "Quinoline," *Acta Crystallogr. Sect. E*, vol. 57, no. 10, pp. 947–949, Oct. 2001, [Online]. Available: <https://doi.org/10.1107/S1600536801014891>.
- [34] G. Socrates, *Infrared and Raman Characteristic Group Frequencies: Tables and Charts*. West Sussex, England: John Wiley & Sons Ltd., 2001.
- [35] R. M. Silverstein, F. X. Webster, and D. J. Kiemle, *Spectrometric identification of organic compounds*. John Wiley & Sons, 2005.
- [36] R. M. Silverstein, G. C. Bassler, and T. C. Morrill, *Spectrometric Identification of Organic Compounds*. New York: Wiley, 1981.
- [37] E. Kose, A. Atac, and F. Bardak, "The structural and spectroscopic investigation of 2-chloro-3-methylquinoline by DFT method and UV–Vis, NMR and vibrational spectral techniques combined with molecular docking analysis," *J. Mol. Struct.*, vol. 1163, pp. 147–160, Jul. 2018, doi: 10.1016/j.molstruc.2018.02.099.
- [38] A. E. Ozel, S. Celik, and S. Akyuz, "Vibrational spectroscopic investigation of free and coordinated 5-aminoquinoline: The IR, Raman and DFT studies," *J. Mol. Struct.*, vol. 924, pp. 523–530, 2009, doi: 10.1016/j.molstruc.2008.12.065.
- [39] G. Varsányi, *Assignments for vibrational spectra of 700 benzene derivatives*. Halsted Press, 1973.
- [40] F. Bardak *et al.*, "Conformational, electronic, and spectroscopic characterization of isophthalic acid (monomer and dimer structures) experimentally and by DFT," *Spectrochim. Acta Part A Mol. Biomol. Spectrosc.*, vol. 165, pp. 33–46, Aug. 2016, doi: 10.1016/J.SAA.2016.03.050.
- [41] V. Balachandran, M. Boobalan, M. Amaladasan, and S. Velmathi, "Synthesis and vibrational spectroscopic investigation of methyl l-prolinate hydrochloride: A computational insight," *Spectrosc. Lett.*, vol. 47, no. 9, pp. 676–689, 2014, doi: 10.1080/00387010.2013.834456.
- [42] G. Socrates, *Infrared and Raman Characteristic Group Frequencies: Tables and Charts*. West Sussex, England: John Wiley & Sons Ltd., 2001.
- [43] M. Arivazhagan and V. Krishnakumar, "Normal coordinate analysis of 1-chloroquinoline and 2-methyl-8-nitroquinoline," *Indian J. Pure Appl. Phys.*, vol. 43, no. August, pp. 573–578, 2005.
- [44] H. Friebolin, *Basic One- and Two-Dimensional NMR Spectroscopy*. Wiley, 2005.
- [45] H. O. Kalinowski, S. Berger, and S. Braun, *Carbon-13 NMR spectroscopy*. New York: Wiley, 1988.
- [46] K. Pihlaja and E. Kleinpeter, *Carbon-13 NMR Chemical Shifts in Structural and Stereochemical Analysis*. VCH, 1994.
- [47] E. Pretsch, P. Bühlmann, and C. Affolter, *Structure determination of organic compounds*, Fourth, Re., vol. 40, no. 3. Berlin, Heidelberg: Springer Berlin Heidelberg, 2009.
- [48] P. O. Fort, D. C. G. a Pinto, C. M. M. Santos, and A. M. S. Silva, *Advanced NMR techniques for structural characterization of heterocyclic structures*, vol. 661, no. 2. 2007.
- [49] D. Guillaumont and S. Nakamura, "Calculation of the absorption wavelength of dyes using time-dependent density-functional theory (TD-DFT)," *Dye. Pigment.*, vol. 46, no. 2, pp. 85–92, Aug. 2000, doi: 10.1016/S0143-7208(00)00030-9.
- [50] A. Zangwill and P. Soven, "Density-functional approach to local-field effects in finite systems: Photoabsorption in the rare gases," *Phys. Rev. A*, vol. 21, no. 5, pp. 1561–1572, May 1980, doi: 10.1103/PhysRevA.21.1561.
- [51] E. Runge and E. K. U. Gross, "Density-Functional Theory for Time-Dependent Systems," *Phys. Rev. Lett.*, vol. 52, no. 12, pp. 997–1000, Mar. 1984, Accessed: Mar. 26, 2014. [Online]. Available: [http://prl.aps.org/abstract/PRL/v52/i12/p997\\_1](http://prl.aps.org/abstract/PRL/v52/i12/p997_1).
- [52] R. Hoffmann and R. B. Woodward, "The Conservation of Orbital Symmetry," *Acc. Chem. Res.*, vol. 1, no. 1, pp. 17–22, 1968, doi: 10.1021/ar50001a003.
- [53] R. G. Parr and R. G. Pearson, "Absolute hardness: companion parameter to absolute electronegativity," *J. Am. Chem. Soc.*, vol. 105, no. 26, pp. 7512–7516, Dec. 1983, doi: 10.1021/ja00364a005.
- [54] R. G. Parr, Y. Weitao, and W. Yang, *Density-Functional Theory of Atoms and Molecules*. Oxford University Press, USA, 1989.
- [55] N. Okulik and A. H. Jubert, "Theoretical analysis of the reactive sites of non-steroidal anti-inflammatory drugs," *Internet Electron. J. Mol. Des.*, vol. 4, pp. 17–30, 2005, [Online]. Available: [http://www.biochempress.com/av04\\_0017.html](http://www.biochempress.com/av04_0017.html).
- [56] F. J. Luque, J. M. López, and M. Orozco, "Perspective on 'Electrostatic interactions of a solute with a continuum. A direct utilization of ab initio molecular potentials for the prevision of solvent effects,'" *Theor. Chem. Accounts Theory, Comput. Model. (Theoretica Chim. Acta)*, vol. 103, no. 3–4, pp. 343–345, Feb. 2000, doi: 10.1007/s002149900013.
- [57] R. S. Mulliken, "Electronic Population Analysis on LCAO-MO Molecular Wave Functions. I," *J. Chem. Phys.*, vol. 23, no. 10, pp. 1833–1840, 1955, doi: 10.1063/1.1740588.
- [58] E. Kose, F. Bardak, and A. Atac, "The investigation of fluorine substitution in difluoroanilines with focus on 2,6-difluoroaniline by spectroscopic methods, density functional theory approach, and molecular docking," *J. Mol. Struct.*, vol. 1196, pp. 201–214, 2019, doi: 10.1016/j.molstruc.2019.06.038.

# Preparation and Characterization of Polylactic Acid Based Nanofiber Loaded with Tangerine Peel (*Citrus Unshiu*) Essential Oil

Tuğba Güngör Ertuğral<sup>1\*</sup> , Sevim Akçura<sup>2</sup> 

<sup>1</sup>Department of Food Technology, Faculty of Canakkale Applied Sciences, Canakkale Onsekiz Mart University, Türkiye

<sup>2</sup>Department of Field Crops, Agriculture Faculty, Çanakkale Onsekiz Mart University, Çanakkale, Türkiye

\*[tugbagungor@comu.edu.tr](mailto:tugbagungor@comu.edu.tr)

\*Orcid No: 0000-0002-1306-3399

Received: 27 July 2023

Accepted: 22 September 2023

DOI:10.18466/cbayarfbe.1333674

## Abstract

Electrospinning method used in nanofiber production is an economical method applied with high voltage electricity. Essential oils obtained from natural sources have antioxidant, antimicrobial and antifungal properties and are preferred for production of nanomaterials by electro-spinning method. In this study, tangerine (*Citrus unshiu*) peel essential oil (TPEO) was obtained by hydro-distillation method and D-Limonene (77.45%) was one of 10 main components in Gas Chromatography Mass Spectrometry (GC-MS) analysis. The composite nanofiber was prepared with 25% TPEO and polylactic acid (PLA). Nanofibers were characterized by Scanning Electron Microscopy (SEM) and Thermogravimetric Analysis (TGA). Essential oil is composited with prominent spheroidal structures in PLA nanofiber according to SEM results, and nanofiber diameter obtained is approximately 76.8 nm. Its decomposition temperature is about 324.8°C. Nanofibers obtained from tangerine peels and their antibacterial properties, can be recommended use for food preservation and medicine fields.

**Keywords:** Tangerine peel, Hydro-distillation, Essential oil, PLA, Electrospin, Food preservation, Nanofiber.

## 1. Introduction

Due to slow degradation rate of waste plastic materials, environmental problems have increased interest in biodegradable polymers [1]. Prevention of increasing environmental pollution and necessity of foodstuffs to have a long shelf life for many reasons have made biopolymer and edible films attractive in food and packaging industry [2]. Polylactic acid (PLA), obtained from corn, beet and cane products, is a lactic acid condensation polymer with catalytic ring opening method, and it is preferred in food packaging applications for than hydrophobic and biodegradable [3,4]. Natural bioactive agents can be an alternative to synthetic products in food industry [5]. Important advantage of electrospinning technique is large surface area, nanometer fine fiber production, good mechanical properties and ease of processing [6]. Adjusting (reducing) voltage in applications can affect the targeted structures and density, and it is possible to determine some structure of nanofibers in a short time by observing the electrical current data [7]. As a protective materials and sensors nanofiber reinforced

composites, where electrospinning technique is used, are important application areas [8].

There is evidence in literature that antimicrobial additives can effective as food additives when used for food packaging materials [9].

Stable shapes are formed by electrically charging the suspended polymer solution droplets between flat plate and electric potential difference. These stable shapes are due only to electric forces balance and surface tension in non-viscous, Newtonian and viscoelastic fluids. The fluid takes a conical and known as Taylor cone [10].

Colorless, volatile, strong-smelling, natural products essential oils, called essential oils or essential oils that are obtained from leave, fruit, bark, root please of plants [11]. Antimicrobial and antioxidant properties of essential oils are used in food packaging. Antimicrobial effect of hydrosols obtained from orange grown in three different regions was investigated against both Gram (+) and Gram (-)

bacteria. Hydrosols and essential oils obtained from Dalaman, Köyceğiz and Finike oranges showed inhibitory properties against *Staphylococcus aureus* and *Escherichia coli* bacteria. [12]. Essential oils obtained from tangerine peel extract feature as a glazing material in cold preservation of fish. Essential oils obtained from *Citrus reticulata*, *Citrus bigarradia* and *Citrus sinensis* can be effective in aquaculture preservation [13]. Antioxidant extracts obtained from herbal material are important research areas [14]. In different uses of essential oils, for example, peppermint and peppermint essential oils against weeds, bio-herbicides can replace chemical herbicides [15]. Distillation methods are divided into 3 as hydro-distillation distillation (Hydrodistillation - HD), steam distillation and vacuum distillation [16]. Microwave assisted hydro-distillation method can also be used to obtain essential oil by adjusting microwave parameters [17]. Hydro-distillation method was successful in examining to components of Anatolian Sage (*Salvia fruticosa Mill.*) essential oil.[18]. hydro-distillation is a process performed with a Clevenger type apparatus and is carried out in retorts in industrial applications [16].

The basis of method; balloon Neo-Clevenger assembly is placed in heated jacket and vertical graduated glass tube is connected to glass balloon at bottom and upper part to cooler system, and pure water is filled into graduated and inclined tube and hydro-distillation is performed for approximately 2 hours after cooling system and heater are turned on. After essential oil is separated from aqueous phase, it is determined in ml and amount of essential oil in a 100 g sample is calculated as a percentage (%) according to sample amount (g) weighed [18, 19]. In this study, essential oil composition obtained from tangerine (*C. unshiu*) peels by hydro-distillation was investigated by GC-MS analysis and composite nanofibers were formed with this obtained essential oil and PLA using electrospinning method. Nanofibers formed were characterized.

## 2 Materials and Methods

### 2.1. Samples and Reagents

Poly(lactic acid) (PLA) (Mn=160000 g/mol) was purchased from Natureworks LLC (4043 D Nebraska, USA) and NN-Dimethylformamide - anhydrous, 99.8% (DMF) and n- hexane 99% were purchased from Sigma-Aldrich (Taufkirchen Germany) and deionized water. October 2022 harvest tangerines were obtained from Antalya / Turkey. Tangerine peel essential oil was obtained by hydro-distillation method. Essential oil of tangerine was achieved with Modified-Clevenger device according to water vapor distillation principle.

## 2.2. Methods

### 2.2.1. Essential Oil Extraction

Fresh tangerine peels were washed and peeled to cut into pieces of 1.5x1x1 cm in size and added directly to a transparent flask that was containing distilled water at room temperature. Obtaining essential oil was done with SH-Clevenger device according to water vapor distillation principle. 242 g of tangerine peels were taken, crushed and placed in a swollen balloon, 900 mL of deionized water was added, and distillation was carried out for 3 hours . The extracted distillate was stored in a closed glass tube and wrapped in aluminum foil [20].

### 2.2.2. GC-MS Analysis Of Tangerine Peel Essential Oil

TPEO components were determined by Shimadzu GC/MS QP-2010. Esesential oil sample was analyzed with HP-88 100m(length)-(0.20 $\mu$ m thickness, 0,25mm diameter) column. Column oven temperature is 100 °C and injection temperature was 220 °C and 30 split ratio. Carrier gas was He Prim Press. (500-900) and 232.8 kPa. Total flow was 37.2 mL/min and column flow was 1.10 mL/min. Mass Spectrometer ion source and interface temperatures were 230 °C and 250 °C. Solvent cutoff time was 10 min. [21].

### 2.2.3. Preparation of the PLA/TPEO Electrospun Nanofiber

Nanofibers were prepared according to method specified by Zhang et al. Before electrospinning, 0.4 g of PLA was added to 5 ml of DMF (v/v) and dissolved [22]. After obtaining a homogeneous mixture, 1 g of essential oil was added and mixed again for 1 hour. Solution placed in a 5 ml syringe was attached horizontally to electrospinning device and PLA/EO nanofibers were prepared at 17.2 kV with NE 100 electrospinning system (Inovenso LLC. Istanbul, Turkey). Solution progressed at 0.62 mL/h (New Era Pump Systems, Farmingdale, NY) and between of needles -collector distance was 15.5 cm and drum collecting nanofibers was covered with an aluminum foil. [23].

## 3. Characterization of PLA/TPEO Nanofiber

### 3.1. Thermogravimetric (TGA) Analysis

Thermal degradation graphs of PLA/TPEO nanofibers were determined with a thermogravimetric analyzer (SDT Q600 V20.9 Build 20) under nitrogen atmosphere at a heating rate of 10 °C min<sup>-1</sup> and between 0-700 °C [24].

### 3.2. Scanning Electron Microscopy (SEM) Analysis

Surface properties and morphology of PLA/TPEO nanofiber was observed by scanning electron microscope (SEM; Carl Zeiss 300VP). In SEM analysis, gold plating was applied and investigated with an acceleration voltage of 5 kV [25, 26].

## 4. Results and Discussion

### 4.1. GC-MS Analysis

Fatty acid composition of essential oil obtained by steam distillation in Clevenger system is examined that is high terms of oleic acid (Table 1). Among essential fatty acid components defined in Table 2, D-Limonene and  $\gamma$ -Terpinene are important compounds with antibacterial effect [27] and D-Limonene was determined to be 77.45% and  $\gamma$ -Terpinene 12.2% (Table 2).

**Table 1.** Fatty acid components identified in *C. unshiu* type tangerine peel essential oil.

Fatty acid components	(%)
Palmitic Acid (C16:0)	16.60
Stearic Acid (C18:0)	6.32
Oleic Acid (C18:1) (n-9)	67.60
Linoleic Acid (C18:2) (n-9, 12)	9.48

**Table 2.** Essential fatty acid components identified in *C. unshiu* type tangerine peel essential oil

Essential fatty acid components	(%)
$\beta$ -Myrcene	3.56
D-Limonene	77.45
$\gamma$ -Terpinene	12.2
$\alpha$ -Terpinolene	0.75
<i>p</i> -Cymene	0.44
$\Delta$ -Elemene	0.35
$\beta$ -Linalool	1.7
$\beta$ -Elemene	0.56
$\alpha$ -Farnesene	1.79
$\alpha$ -Terpineol	1.18

### 4.2. TGA analysis

According to TGA results of PLA/TPEO nanofiber is seen decomposes between approximately 145.8°C-358.4°C and degradation peak is at an average of 324.8°C (Figure 1,a) and degradation temperature of pure PLA nanofiber is about 320°C (Figure 1,b), and higher temperature degradation of PLA/TPEO nanofiber can be explained with thermal stability of PLA/TPEO nanofiber is better than PLA-containing nanofiber after addition of essential oil [28, 29].

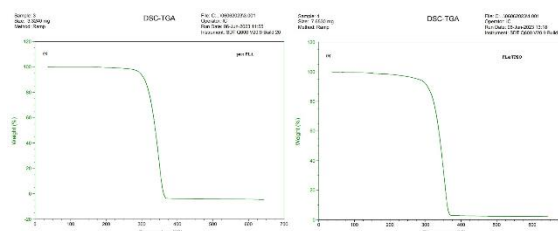


**Figure 1.** TGA curve of pure PLA nanofiber (a) and PLA/TPEO nanofiber (b).

### 4.3. SEM Analysis

According to SEM images of 25% TPEO loaded into PLA nanofiber, 47nm and 76.8 nm diameter fibers were observed (Figure 2;c,d). Spherical formations (Figure 2; e, f) and their homogeneous distribution on fiber are evident in essential oil added PLA nanofiber compared to pure PLA (Figure 2; a, b). Pure PLA nanofiber diameter can average up to 512 nm [30], but PLA/TPEO composite nanofiber diameter has decreased, which can be due to hydrogen bonding [28].

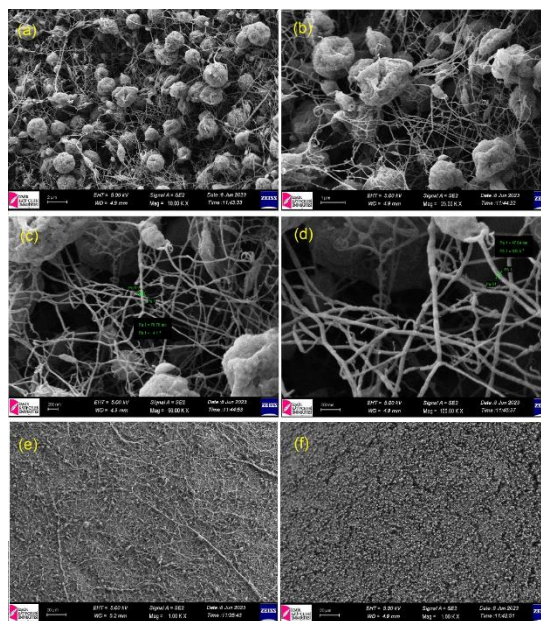


**Figure 2.** PLA/TPEO nanofiber SEM images and scales; 2  $\mu$ m (a), 1  $\mu$ m (b), 200nm 50.00 KX magnification (c) and 200nm 100 KX magnification (d), pure PLA nanofiber 20  $\mu$ m (e) and PLA/TPEO nanofiber 20 $\mu$ m (f).

## 5. Conclusion

Biodegradable polymers are often preferred over synthetic polymers in terms of environment and health. PLA/TPEO nanofibers were obtained by using electrospinning method with success. TPEO essential oil composition was investigated by GC-MS and obtained nanofiber was characterized by TGA and

SEM. It was determined that TPEO contains 77.45% high level of D-Limonene fatty acid and 12.2%  $\gamma$ -Terpinene. Degradation temperature of PLA/EO nanofiber is 324.8°C and nanofiber diameters were measured as 47nm and 76.8nm. PLA/TPEO composite nanofiber can be nominated as a candidate for food packaging industry and medical application.

### Acknowledgement

This study was supported by Çanakkale Onsekiz Mart University Scientific Research (BAP) project code FHD-2022-3969.

### Author contributions

**Tuğba Güngör Ertuğral:** Wrote draft of article, including preparation of composition and production of nanofibers by electrospinning method, and carried out characterization of nanofiber and analyzed results.  
**Sevim Akçura:** Obtained essential oil with SH-Clevenger from tangerine peel.

### Ethic

There are no ethical problems after publication of this publication.

### References

- [1]. De Azeredo, H. M. 2009. Nanocomposites for food packaging applications. *Food research international*, 42(9), 1240-1253
- [2]. Tharanathan, R. N. 2003. Biodegradable films and composite coatings: past, present and future. *Trends in food science & technology*, 14(3), 71-78.
- [3]. John, R. P., Gangadharan, D., and Nampoothiri, K. M. 2008. Genome shuffling of *Lactobacillus delbrueckii* mutant and *Bacillus amyloliquefaciens* through protoplasmic fusion for L-lactic acid production from starchy wastes. *Bioresource Technology*, 99(17), 8008-8015.
- [4]. Nampoothiri, K. M., Nair, N. R., and John, R. P. 2010. An overview of the recent developments in polylactide (PLA) research. *Bioresource technology*, 101(22), 8493-8501.
- [5]. Zhang, W., Ronca, S., and Mele, E. 2017. Electrospun nanofibres containing antimicrobial plant extracts. *Nanomaterials*, 7(2), 42
- [6]. Agarwal, S., Wendorff, J. H. and Greiner, A. 2008. Use of electrospinning technique for biomedical applications. *Polymer*, 49(26), 5603-5621.
- [7]. Yalcinkaya, F. 2015. Effect of current on polymer jet in electrospinning process. *Textile and Apparel*, 25(3), 201-206.
- [8]. Min, B. M., Lee, G., Kim, S. H., Nam, Y. S., Lee, T. S. and Park, W. H. 2004. Electrospinning of silk fibroin nanofibers and its effect on the adhesion and spreading of normal human keratinocytes and fibroblasts in vitro. *Biomaterials*, 25(7-8), 1289-1297.
- [9]. Cooksey, K. 2005. Effectiveness of antimicrobial food packaging materials. *Food additives and contaminants*, 22(10), 980-987.
- [10]. Taylor, G. I. 1964. Disintegration of water drops in an electric field. *Proceedings of the Royal Society of London. Series A. Mathematical and Physical Sciences*, 280(1382), 383-397.
- [11]. Ceylan, A. 1983. Tıbbi Bitkiler-II. *Ege Üniversitesi Ziraat Fakültesi Yayını* No:481, Bornova-İzmir
- [12]. Dikmetaş, D. N., Konuşur, G., Mutlu-İngök, A., Gülsünoğlu, Z., and Karbancıoğlu-Güler, F. 2019. Portakal (*Citrus sinensis*) kabuğundan elde edilen hidrosol/esansiyel yağların antimikrobiyal ve antioksidan özellikleri. *Düzce Üniversitesi Bilim ve Teknoloji Dergisi*, 7(1), 274-283.
- [13]. He, Q., and Xiao, K. 2016. The effects of tangerine peel (*Citrus reticulatae pericarpium*) essential oils as glazing layer on freshness preservation of bream (*Megalobrama amblycephala*) during superchilling storage. *Food Control*, 69, 339-345.
- [14]. Candan, T., and Bağdatlı, A. 2017. Use of natural antioxidants in poultry meat. *Celal Bayar University Journal of Science*, 13(2), 279-291.
- [15]. Turgut, T. and Coskun, Y. 2021. Chemical Composition of Essential Oils of Peppermint and Spearmint Dry Leaves and Their Allelopathic Effects on Wheat Species. *Journal of Essential Oil Bearing Plants*, 24(4), 772-785.
- [16]. Kılıç, A. 2008. Uçucu yağ elde etme yöntemleri. *Bartın Orman Fakültesi Dergisi*, 10(13), 37-45.
- [17]. Argui, H., Braidia, F., Ben Youchret-Zarella, O., Yalçın, C., Ben-Attia, M., Fauconnier, M. L. and Said, H. 2023. Influence of drying plant material on yield, chemical composition, antioxidant and anti-inflammatory activities of essential oil extracted from the Tunisian Cupressus sempervirens leaves. In *9th International Conference on Green Energy & Environmental Engineering (GEE-2023)*.
- [18]. Karayel, H. B. and Akçura, M. 2016. Farklı lokasyonlarda yetiştirilen Anadolu adaçayı (*Salvia fruticosa* Mill.)'in uçucu yağ bileşenlerindeki değişimlerin incelenmesi. *Gaziosmanpaşa Bilimsel Araştırma Dergisi*, (13), 13-23.
- [19]. Skoula, M., J. E. Abbes, C. B. Johnson. 2000. Genetic variation of volatil esand rosmarinic acidin populations of *Salvia fruticosa* Mill, growing in Crete. *Journal of Biochemical Systematics and Ecology*, 28:551-561.
- [20]. Akçura, S. 2023. Biplot analysis of monthly variations in essential oil concentration and chemical composition of *Pittosporum tobira* leaves in Mediterranean conditions. *Biochemical Systematics and Ecology*, 110, 104712.
- [21]. Ignjatovic-Micic, D., Vancetovic, J., Trbovic, D., Dumanovic, Z., Kostadinovic, M., & Bozinovic, S. 2015. Grain nutrient composition of maize (*Zea mays* L.) drought-tolerant populations. *Journal of agricultural and food chemistry*, 63(4), 1251-1260.
- [22]. ME, Z. Q. T. Q. H. Xiao JC Gao B. Tian C. Heng P. Jiao Y. Peng TQ Wang JY. 2018. Preparation and study of the antibacterial ability of graphene oxide-catechol hybrid polylactic acid nanofiber mats. *Colloids and Surfaces B*, 172, 496-505.
- [23]. Zhang, S., Ye, J., Sun, Y., Kang, J., Liu, J., Wang, Y., ...and Ning, G. 2020. Electrospun fibrous mat based on silver (I) metal-organic frameworks-poly(lactic acid) for bacterial killing and antibiotic-free wound dressing. *Chemical Engineering Journal*, 390, 124523.
- [24]. Argui, H., Suner, S. C., Periz, Ç. D., Ulusoy, S., Türker, G., Ben-Attia, M. and Said, H. 2021. Preparation of cypress (*Cupressus*

sempervirens L.) essential oil loaded poly (lactic acid) nanofibers. *Open Chemistry*, 19(1), 796-805.

[25]. Arik, N., Horzum, N., and Truong, Y. B. 2022. Development and characterizations of engineered electrospun bio-based polyurethane containing essential oils. *Membranes*, 12(2), 209.

[26]. Cesur, S., Oktar, F. N., Ekren, N., Kilic, O., Alkaya, D. B., Seyhan, S. A., ... and Gunduz, O. 2020. Preparation and characterization of electrospun polylactic acid/sodium alginate/orange oyster shell composite nanofiber for biomedical application. *Journal of the Australian Ceramic Society*, 56, 533-543.

[27]. Xing, C., Qin, C., Li, X., Zhang, F., Linhardt, R. J., Sun, P., and Zhang, A. 2019. Chemical composition and biological activities of essential oil isolated by HS-SPME and UAHD from fruits of bergamot. *LWT*, 104, 38-44.

[28]. Wang, D., Sun, Z., Sun, J., Liu, F., Du, L., and Wang, D. 2021. Preparation and characterization of polylactic acid nanofiber films loading Perilla essential oil for antibacterial packaging of chilled chicken. *International Journal of Biological Macromolecules*, 192, 379-388.

[29]. Özcan, İ. 2021. Sucuk baharatı karışımı uçucu yağları ile zenginleştirilen poli laktik asit esaslı nano-liflerin çözelti üfleme eğirme tekniği ile üretimi. *Master's thesis, BTÜ, Lisansüstü Eğitim Enstitüsü*.

[30]. Wang, Y., Qian, J., Liu, T., Xu, W., Zhao, N., and Suo, A. 2017. Electrospun PBLG/PLA nanofiber membrane for constructing in vitro 3D model of melanoma. *Materials Science and Engineering, C*, 76, 313-318.

## Chemical Composition and Antibacterial Activities of *Corylus avellana* L. Bioproducts Grown in Giresun-Türkiye

Mehmet Emin Şeker<sup>1\*</sup> , Ayşegül Erdoğan<sup>2</sup> , Emriye Ay<sup>3,4</sup> , Derya Efe<sup>1</sup> , Rena Hüseyinoğlu<sup>3</sup> 

<sup>1</sup>Department of Medicinal and Aromatic Plants, Giresun University, Espiye/Giresun-Türkiye

<sup>2</sup>Ege University Application and Research Center For Testing and Analysis (EGE MATAL), İzmir- Türkiye

<sup>3</sup>Şebinkarahisar School of Applied Science, Giresun University, Giresun- Türkiye

<sup>4</sup>Tobacco Technology and Chemistry, Manisa Celal Bayar University, Manisa- Türkiye

\*[mehmet.emin.seker@giresun.edu.tr](mailto:mehmet.emin.seker@giresun.edu.tr)

\* Orcid No: 0000-0003-4463-6898

Received: 19 August 2023

Accepted: 25 September 2023

DOI: 10.18466/cbayarfbe.1346393

### Abstract

Hazelnut has become an important commercial product in recent years due to its worldwide applications in the pharmaceutical industry as well as in the confectionery and food industry. In addition, hazelnut shell is a waste material obtained after hazelnut harvest and mainly used as heating sources. However, its bioproducts are essentially a very important phytochemical source. In this study, the composition of phenolic compounds, carotenoids, tocopherols and fatty acids of different bioproducts of hazelnut plant were investigated. The highest phenolic compound content (2630.84 µg/g), and lutein amount (73.05 µg/g) were determined in green leafy cover. The major fatty acids were found to be as oleic acid (81.493%), linoleic acid (7.778%) and palmitic acid (6.408%), respectively. Total tocopherol concentration of hazelnut kernel was determined as 364.1 µg/g. The antimicrobial activities of hazelnut components were tested against eight different pathogenic bacteria. The compounds showed strong antimicrobial activity against both Gram (+) and Gram (-) bacteria which might be attributed to the rich phytochemical composition of hazelnut bioproducts. This work comprehensively summarized the chemical composition of hazelnut bioproducts and their antibacterial activity potential grown in Giresun-Türkiye region which had an important place in the global market.

**Keywords:** *Corylus avellana*, hazelnut, bioproducts, chemical composition, antimicrobial activity

### 1. Introduction

The hazelnut (*Corylus avellana* L.), which belongs to the Betulaceae family, is the most widely grown tree nut in the world after almonds [1, 2]. *C. avellana* L. is cultivated in Europe and neighboring areas of Asia, including Türkiye and the Caucasus Mountains. Providing approximately 70% of the total production, Türkiye is the world's largest hazelnut producer. It is followed by Italy (~16%), the United States (~4%), and Spain (~3%) [3-5]. According to the Ministry of Agriculture and Forestry of the Republic of Türkiye, 665 thousand tons of hazelnuts were produced in 2016, with 60.5% produced in Türkiye, and 1.1 million tons of hazelnuts were produced globally in 2020 [6].

About 400 *C. avellana* cultivars have been identified and 18 of them are cultivated in Türkiye. Among them, Tombul hazelnut, which is mostly cultivated in Giresun

province, is the first class quality (Giresun quality); the other varieties are classified as second class quality (or Levant quality). For this reason, Tombul hazelnut is considered to be the most important commercial variety worldwide [3, 7].

Hazelnuts are a rich source of phytochemicals that exhibit high antioxidant and antibacterial activity. Phytochemicals are defined as non-nutritive but biologically active compounds found in plants. They generally consist of carotenoids, phenolic compounds, organosulfur compounds, nitrogen-containing compounds, and alkaloids [8, 9]. Phytochemicals are known to protect against the harmful effects of free radicals, as well as reduce the risk of developing certain types of cancer, coronary heart disease, stroke, osteoporosis, type 2 diabetes, inflammation, diabetes, insulin resistance, and sudden death [9]. It is known that most tree nuts, especially hazelnuts, contain some phenolics and carotenoids [8].

Thus, hazelnut consumption is associated with a reduced risk of cardiovascular disease events [10-12].

Hazelnut oil is another valuable component for the food industry. The oil content of the dry weight of Turkish hazelnuts differs according to the region and variety where it is cultivated, and it is around 60%. Hazelnut oil, oleic acid (73.6–82.6%), linoleic acid (9.8–16.6%), palmitic acid (4.1–6.8%), and stearic acid (1.6–6%), mainly consists of unsaturated fatty acids. For this reason, its oil has high oxidative stability and nutritional value [13-16].

Hazelnut oil has commercial importance due to its rich nutrients. It contains a significant amount of biologically active substances, such as  $\alpha$ -tocopherol and  $\beta$ -sitosterol, in addition to beneficial unsaturated fatty acids. These natural components not only provide anti-oxidation and anti-aging properties to hazelnut oil but also improve immunity with consumption, prevent arteriosclerosis and regulate cholesterol [14, 15].

Alongside the considerable body of research focusing on hazelnut kernels and oil, there has been a notable surge in interest towards exploring hazelnut by-products, encompassing elements such as skin, hard shell, green leafy covering, and tree leaves. These bio-products are the outcomes yielded subsequent to a sequence of procedural stages encompassing roasting, crushing, shelling/peeling, and the culminating act of harvesting. Among these by-products, none of them has commercial value except the hazelnut hard shell, which is used as a heat source. Also, green leafy covers are removed from hazelnuts immediately after harvest and can be used as fertilizer for hazelnut trees [17]. As a result of previous studies, especially chemical content analysis showed that these by-products are considered sources of phytochemicals with biological activity [18, 19]. Although more than 5000 plant-derived phytochemicals have been identified, a large percentage is still unknown. To understand their health benefits, their phytochemicals need to be defined. By-products of tree nuts, which are cheaper sources than their kernels, contain rich phytochemicals with multifunctional properties such as antioxidant and free radical scavenging activities and, anticarcinogenic and antimutagenic effects. Because of this it is of great interest to include them in the diet as functional food and natural antioxidant [9, 20].

In the food industry, interest in the use of natural antimicrobial compounds is increasing day by day as consumers avoid chemical preservatives. In this context, it is important to determine the antimicrobial capacity of phenolic compounds [4]. There are studies on antiradical activities and antioxidant capacities in extracts of other hazelnut by-products such as Turkish hazelnut kernel, green leafy cover, and tree leaf [1, 4, 18, 21]. Many studies have been performed on the most commercially valuable hazelnut species. Among them, tombul hazelnut

and its by-products, including its nutritional properties, chemical contents, biological activities, and agricultural cultivation play an important role.

The phenolic characterization of the kernel, kernel oil, hard shell, and green leafy cover of this commercially valuable hazelnut species, as well as the total carotenoid content, particularly  $\beta$ -carotene, lutein, and zeaxanthin content, of the cold-pressed oil, were determined in this study. Finally, the antibacterial activity of the methanol extract of hazelnut kernel, oil, and by-products (hard shell, green leafy cover) against Gram-positive and Gram-negative bacteria was evaluated. Although studies on hazelnut and its bio-products have been done before, one of the most important aspects of this research is that hazelnuts and bio-products collected in the same harvest period are subjected to chemical analysis to determine many components in the same study.

## 2. Materials and Methods

### 2.1. Plant materials

Hazelnut kernels, hazelnut hard shells, and hazelnut green leafy covers belonging to *C. avellana* species were obtained from Giresun center. Kernel oil is obtained by squeezing the kernel with cold press. Hazelnuts were crushed and the shells were ground by the knife mill for rapid size reduction (4000 rpm, for 2.0 minutes).

### 2.2. Chemicals / Reagents

All analytical grade phenolic standards used in the analysis were obtained from Sigma- Aldrich (St. Louis, MO, USA). All the reagents were purchased from Sigma-Aldrich and they were either chromatographic or analytical grade. FAME mix (Supelco FAME 37 Mix.lot: LC-07964) was used as a standard for the determination of the retention time of fatty acids.

For the determination of  $\alpha$ -tocopherol, Merck standard was used. In addition, carotenoid standards (all-trans lutein and all-trans  $\beta$ -carotene),  $\text{CaCO}_3$ , pyrogallol, KOH,  $\text{CaCl}_2$ , and  $\text{Na}_2\text{SO}_4$  were provided from Sigma Aldrich. All the solvents used in this study were Merck LC-grade (LiChrosolv® solvents).

### 2.3. LC-MS/MS analysis of phenolic compounds

The bioproducts of the nut (kernel, green leafy cover, and shell) were separated, cleaned, and dried in a 40°C, 48-hour hot-air oven. Methanol was utilized as the extraction solvent during the Soxhlet procedure. For Soxhlet extraction, 10 g samples (kernel, green leafy cover, and shell) of various nut bioproducts were ground in a blender and placed in a Soxhlet cartridge, 250 mL methanol was added to the device, and the system was activated. After this, the solvent mixture was filtered, and the solvent was then extracted using a rotary evaporator at 175 mbar and 40°C. The samples were finally diluted

in methanol for LC-MS/MS analysis. In LC-MS/MS analysis, the ODS Hypersil (4.6 250 mm, 5 µm) column was utilized. Water with 0.1% formic acid and B methanol were employed as mobile phases. Using the previously known approach, analyses were conducted. Each sample was extracted three times and examined in conjunction with three parallel samples [22].

#### 2.4. FAME analysis by GC-FID

The hazelnuts were cold pressed, no solvent was used to determine the oil composition and the temperature was kept below 40°C during this process as reported in the literature [23]. A cold press machine has been used with a capacity of 1kg/hour. Cold-pressed oil was stored in stainless steel tanks for one day and allowed to settle for sediments. Then, the oil was filtered using filter paper with 1 µm-filter paper. In the last step, cold-pressed oils were filled into 50 mL amber-coloured glass bottles and stored at 25°C until analysis.

The reference standard mixture was analyzed for the identification of fatty acids based on their retention times. Analysis was performed in duplicate, and the relative amount of each fatty acid was calculated over the total fatty acid content. FAME analysis was performed with an Agilent 7890 Series GC/FID. An Agilent J&W CP-Sil 88 column (100 m x 0.25 mm ID x 0.2 µm) and a 1:100 split ratio was used. The inlet and detector temperatures were 250°C and 260°C, respectively. The oven temperature was held at 140°C for 1 minute and then increased to 240°C at a rate of 4°C/min and held for 5 minutes.

#### 2.5. Tocopherol Analysis

For the determination of tocopherol amounts hazelnut oil was obtained from hazelnut kernels by cold pressing method. The hazelnut oil sample was kept in the incubator at 35°C for 1 hour to ensure its viscous fluidity. Then, the oil sample was shaken vigorously for 30 seconds and diluted 1:3 with 2-propanol according to the previously developed method [24]. Finally, by vortexing for 30 seconds, 20 µL of this solution was injected into the chromatographic system for analysis. For HPLC analysis, an Agilent 1260 Series high-performance liquid chromatography instrument, analytical column (Zorbax Rx, 3 µm, 150 × 4.6 mm, Agilent Technologies) with a C<sub>18</sub> guard column was utilized at a constant temperature of 40°C. Acetonitrile and methanol, (60:40, v:v) mobile phase mixture were used as an isocratic system [25].

#### 2.6. Carotenoid analysis

A modified procedure was used to extract carotenoids from hazelnut kernel, shell, and green leafy cover samples based on previously used methods [26]. Briefly, 1.0 g of each sample was weighed, followed by the addition of 1.0 g of CaCO<sub>3</sub>. The mixture was extracted in

an ultrasonic bath (Elmasonic S80H) for 10 minutes at 30 °C using 20 mL of THF: DCM (1:1 v/v tetrahydrofuran: dichloromethane) containing 0.01% pyrogallol. The solution was then centrifuged at 5000 rpm for two minutes. The supernatant was saved, and the residue was re-extracted with new ethanol until the biomass lost its color. The mixed solutions were further filtered by vacuum filtration using 47 mm of 0.20 µm nylon filter paper (Sartorius). These were kept at -20°C as unsaponified extracts until the LC-MS/MS analysis.

The method was repeated on the identical samples, and then the filtered extracts were saponified with 10% methanolic KOH for two hours in the dark. To prevent the degradation of carotenoids, N<sub>2</sub> gas was used to flush the samples. To halt the saponification process, 10.0 mL of a 10% (w/v) Na<sub>2</sub>SO<sub>4</sub> solution was added. Then, 10.0 mL of diethyl ether was added to the extracts to pool the carotenoid fraction. The collection of the top phase was performed three times. CaCl<sub>2</sub> was then added to the mixture to eliminate any remaining water. Next, the carotenoid extract was again filtered using nylon filter paper, and the solution was rotary-evaporated at 40 °C and 400 mbar (Stuart RE 400). Before LC-MS/MS analysis, the residue was dissolved in 5.0 mL of methanol and stored at -20°C. Each experiment was conducted in triplicate.

Liquid Chromatography-Tandem Mass Spectrometry (LC-MS/MS) fitted with an Atmospheric Pressure Chemical Ionization probe was used to evaluate carotenoids in this investigation (APCI). At a vaporization temperature of 350°C, the mass spectrometer (Thermo Scientific/TSQ Quantum Access Max) was run in full scan mode from m/z 50 to 900. Carotenoids were separated using gradient elution utilizing a YMC, C<sub>30</sub> column (4.6 x 250 mm, 5 µm). 70% methanol, 5% water (containing 0.1% formic acid), and 25% methyl-tert-butyl ether constituted the first mobile phase. It was adjusted to 60% methanol and 35% methyl-tert-butyl ether after 5 minutes. At the 10-minute mark, 45% methanol and 55% methyl-tert-butyl ether were used. 15 minutes later, methanol was reduced to 25% and Methyl-tert-butyl ether was dropped to 75%. The overall time for analysis was 15 minutes. Analytical standards were used to identify and determine the retention periods of lutein and β-carotene. Positive ion mode analysis was conducted and optimized using commercial lutein and β-carotene standards. SIM mode employed m/z values of 569, 551, and 459 for lutein and 537, 445, and 431 for β-carotene.

#### 2.7. Antibacterial activity assay

In this study, four Gram-negative (*Enterobacter aerogenes* ATCC 3048, *Escherichia coli* ATCC 36218, *Pseudomonas aeruginosa* ATCC 9027, *Klebsiella pneumoniae* ATCC 13883) and four Gram-positive (*Bacillus cereus* ATCC 10876, *Bacillus megaterium*

ATCC14581, *Staphylococcus epidermis* ATCC 12228, *Methicillin-resistant Staphylococcus aureus* (MRSA) ATCC 6710 bacteria were used to test antibacterial activity of methanol extracts obtained from different parts of *C. avellana* L. The bacteria were supplied from the Culture Collection of Erzurum Technical University (Erzurum, Türkiye). Tryptic soy agar (TSA) and tryptic soy broth (TSB) supplied from Merck (Darmstadt, Germany) were used to culture bacteria.

The antibacterial activity was performed by the disc diffusion method. The studied samples and their concentrations were given as followed; hazelnut hard shell (22 mg/μL, 11 mg/μL, 7.3 mg/μL, 5.5 mg/μL), hazelnut kernels (33 mg/μL, 16.5 mg/μL, 11 mg/μL, 8.25 mg/μL), hazelnut green leafy covers (21 mg/μL, 10.5 mg/μL, 7 mg/μL, 5.25 mg/μL). As the concentration of the studies samples were prepared according to the obtained extracts from the extraction process, they exhibited some differences. Netilmicin (NET30) (30 μg/disc) and ofloxacin sulbactam (OFX) (10 μg/disc) were used as the positive control and methanol was used as the negative control. The cell suspension concentrations of tested bacteria were adjusted to a 0.5 McFarland standard. 100 μL of the bacterial culture was spread on TSA. Then sterilized paper discs (Whatman no.5, 6 mm dia) impregnated with 10 μL of each methanol extract at different concentrations were placed on the bacteria and incubated at 37 °C for 24 hours. The clear zones of the paper discs were measured and recorded. The microdilution method was used to determine the minimum inhibitory concentrations (MIC). Maxipime (Bristol-Myers Squibb) in concentrations between 500 and 7.81 μg/μL was used as a positive

reference for microdilution assay [22]. The experiments were repeated three times.

### 3. Results and Discussion

The results of phenolic components and LC-MS/MS parameters are given in Table 1 and Table 2 respectively. Among the results we obtained, protocatechuic acid in the green leafy cover, vanillin and gallic acid in the hazelnut shell, protocatechuic acid, gallic acid, and ferulic acid in the hazelnut kernel is higher than the other phenolic compounds. It is noteworthy here that protocatechuic acid is very high in the bark.

The most detailed studies on the bioproducts of *C. avellana* L. species grown in Giresun were carried out by Alasalvar et al. [3, 8, 9, 18]. In one of these studies, Alasalvar et al. [18] investigated the free and esterified amounts of some phenolic acids (gallic, caffeic, p-coumaric, ferulic and sinapic acid) in the green leafy cover. For this purpose, two different types of extraction solvents, ethanol, and acetone were tried. In the extractions, free caffeic, ferulic and sinapic acids were not found in the samples. Gallic acid and p-coumaric acid amounts in ethanol extractions were found to be 253 and 38 μg/g extract, respectively. Although the results we found are slightly higher, the amounts are close to each other. However, according to our results, 18.71 μg/g caffeic acid and 137.36 μg/g ferulic acid per extract were found in the green leafy cover. Apart from these, a high amount of (2630.84 μg/g per extract) protocatechuic acid was detected in the green leafy cover. The amount of ellagic acid (191.80 μg/g extract) was also found to be relatively high compared to other phenolics.

**Table 1.** Phenolic compounds quantified in hazelnut (*Corylus avellana* L.) sample (μg/g).

Phenolic Compound	Green leafy cover	Shell	Kernel
Gallic Acid	419.46	913.20	44.94
Protocatechuic acid	2630.84	655.25	41.35
Protocatechuic aldehyde	8.03	238.54	8.05
Catechin	13.49	169.23	ND
Epicatechin	ND	ND	ND
Caffeic Acid	18.71	ND	ND
Vannilin	25.22	1364.69	16.22
Taxifolin	21.47	51.16	5.99
p-Cumaric Acid	41.47	95.39	14.16
Ferulic Acid	137.36	ND	29.95
4-OH-Benzoic Acid	8.93	16.10	6.73
Salisilic Acid	8.17	17.37	7.34
Rosmarinic Acid	ND	ND	ND
Oleuropein	ND	ND	ND
Rutin	ND	3.13	2.09
Resveratrol	ND	0.41	ND
Ellagic Acid	191.80	ND	5.53
Syringic Acid	ND	ND	ND

ND: Not detected

\*The values are mean of three replicate analyses and RSD values are < 3%.

In another study by Shahidi et al. [1], the amounts of the same phenolic acids (gallic, caffeic, p-coumaric, ferulic, and sinapic acid) in green leafy cover, kernel, and hazelnut shell were given as the sum of their free and esterified forms. In this study, total gallic, caffeic, p-coumaric, and ferulic acid amounts in hazelnut shells were found to be 3261, 212, 757, and 333 µg/g, respectively. In our study, the free gallic acid and p-coumaric acid amounts of the same phenolic acids were found to be 913.20 and 95.39 µg/g, respectively. Caffeic and ferulic acid could not be detected. In the same study, Shahidi et al. [1] analyzed the hazelnut kernel with its skin and found the total gallic, caffeic, p-coumaric, and ferulic acid amounts as 127, 81, 208, and 105 µg/g extract, respectively. In our results, caffeic acid, one of these phenolic compounds, could not be detected in free form. The amounts of free gallic, p-coumaric, and ferulic acid in the kernel were found to be 44.94, 14.16, and 29.95 µg/g extract, respectively.

When compared to the studies of Gültekin et al. [27] with hazelnut kernel, the amounts of gallic acid and protocatechuic acid found were close to each other. In our study, ferulic acid was found to be quite higher than the results they found, while the amount of rutin found by them seems to be much higher than we found. In the four hazelnut extracts they studied, gallic acid amounts were found to be 40.03 µg/g (min 24.83-max 65.92) on average, while the average of protocatechuic acid amounts was 57.07 µg/g (min 48.45-max 64.50). The average amount of ferulic acid is 2.47 µg/g (min 1.72-max 3.65), while the average amount of rutin is 11.4 µg/g (min 8.72-max 15.18). These amounts are in the same order as us; 44.94, 41.35, 29.95, and 2.09 µg/g. While p-coumaric acid was found to be 14.16 µg/g in our study, the average result of four hazelnuts in their study was 4.87 µg/g (min 2.23-max 7.50). While Gültekin et al. [27] detected catechin amounts between 12.00-20.08 µg/g and epicatechin between 1.53-5.81 µg/g, we could not detect catechin and epicatechin in our sample.

**Table 2.** LC-MS/MS parameters for phenolic compound standards

Phenolic compounds	R <sub>t</sub> (min.)	MS [m/z]	MS/MS [m/z]	LOD (mg/L)	LOQ (mg/L)	Polarity
Gallic acid	8.92	169.7	80.50	0.061	0.203	-
			126.20			-
Protocatechuic acid	12.13	153.8	110.40	0.049	0.162	-
			92.50			-
Protocatechuic aldehyde	13.16	136.9	92.25	0.026	0.087	-
			108.20			-
Catechin	10.92	289.2	203.90	0.068	0.227	-
			245.70			-
Epicatechin	11.26	291.5	123.30	0.045	0.151	+
			139.30			+
Caffeic acid	15.27	179.7	135.20	0.047	0.157	-
			136.20			-
Vanillin	15.87	150.91	92.30	0.023	0.076	-
			136.10			-
Taxifolin	16.68	303.0	126.20	0.058	0.194	-
			285.50			-
p-coumaric acid	17.00	163.9	94.30	0.116	0.387	-
			120.20			-
Ferulic acid	17.19	193.35	134.10	0.061	0.204	-
			178.00			-
4-OH-benzoic acid	18.12	137.90	66.60	0.031	0.104	-
			94.60			-
Salicylic acid	18.13	137.14	65.51	0.030	0.099	-
			93.26			-
Rosmarinic acid	17.82	359.18	134.30	0.029	0.095	-
			162.20			-
Oleuropein	18.00	539.10	275.80	0.050	0.167	-
			377.50			-
Rutin	18.26	609.37	300.60	0.007	0.024	-
			301.70			-
Rezveratrol	18.45	228.98	107.20	0.030	0.099	+
			135.10			+
Ellagic acid	19.47	300.90	229.10	0.087	0.289	-
			229.10			-
Syringic Acid	15.45	183.07	123.2	0.192	0.643	-
			77.3			-

In another study by Pelvan et al. [28], gallic acid 1.09, proto-catechuic acid 0.07, salicylic acid 0.06, 4-Hydroxybenzoic acid 0.07, ferulic acid 0.03 µg/g were found in hazelnut kernels, while these values were found 2.20, 2.02, 0.36, 0.33 and 1.63 µg/g respectively in our samples.

In a study conducted with *C. avellana* in Poland, per µg/g kernel; gallic acid 4.1 µg/g and 11.1 µg/g, proto-catechuic acid 1.1 µg/g, catechin 0.5 µg/g and 1.0 µg/g, epicatechin 0.1 µg/g, while taxifolin and p-coumaric acid could not be detected [29]. The amounts of taxifolin and p-coumaric acid were determined as 0.29 µg/g and 0.69 µg/g samples, respectively. Ceylan et al. [30] also analyzed some free phenolics in hazelnut shells in the same study. Among the results they found, to be given as µg/g per sample; while gallic acid was 0.8 µg/g and 2.7 µg/g, catechin was 0.3 µg/g and 0.8 µg/g, proto-catechuic acid, epicatechin, taxifolin, and p-coumaric acid could not be determined. These phenolic compounds in our extracts in the same order as µg/g per sample; 20.13 µg/g, 3.73 µg/g, 14.45 µg/g, n.d., 1.13 µg/g, 2.10 µg/g. There are serious differences between these results.

In another study with hazelnut shells, gallic acid was 62.17 µg/g, proto-catechuic acid 22.13 µg/g, catechin 176.41 µg/g, epicatechin 17.11 µg/g per sample, while taxifolin and p-coumaric acid could not be detected. The amounts found for these phenolic compounds are many times higher than the amounts of catechin and epicatechin found in our study [31].

As can be seen from the comparison of the results, there are serious differences between the results given per µg/g extract or per µg/g sample. The reason for these differences may be due to the differences in the regions where the hazelnuts are collected, and the extract contents may change from year to year.

The predominant fatty acid was found to be oleic acid (81.49%) followed by linoleic acid (7.78%), palmitic acid (6.41%), and stearic acid (3.14%) as shown in Table 3. Tüfekçi and Karataş reported the fatty acid profiles (%) of hazelnut samples from different regions in the Black Sea [32]. In that study, it was apparent that the results did not significantly differ according to the regions. According to Taş and Gokmen [7], Giresun round hazelnuts had 80.1% oleic acid, 10.9% linoleic acid, 5.7% palmitic acid, and 2.4% stearic acid. In addition, Bacchetta et al. [33] determined that the predominant fatty acid in European hazelnuts was oleic acid (80.63 percent), followed by linoleic acid (10.57 percent), palmitic acid (5.95 percent), and stearic acid (2.48 percent). Parcerisa et al. [34] reported that the fatty acid profiles of American hazelnut varieties were as follows: oleic acid ranged between 77.08 and 80.76 percent, linoleic acid ranged between 10.46 and 15.55 percent, palmitic acid ranged between 4.72 and 5.77 percent, and stearic acid ranged between 1.38 and 3.34 percent. These findings were moderately consistent with our own, with the variations perhaps attributable to harvesting season, growth circumstances, and geographical location.

**Table 3.** Fatty acid profiles (%) of hazelnut kernel (*Corylus avellana* L.) sample.

Fatty Acids	Area %
Lauric A.(C12:0)	0.00923
Myristic A. (C14:0)	0.0386
Pentadecanoic A.(C15:0)	0.00945
Palmitic A.(C16:0)	6.408
Palmitoleic A.(C16:1)	0.190
Heptadecanoic A. (C17:0)	0.0478
cis-10-heptadecanoic A. (C17:1)	0.0686
Stearic A. (C18:0)	3.141
Oleic A.(C18:1 cis)	81.493
Linolelaidic A.(C18:2 trans)	0.00912
Linoleic A.(C18:2 cis)	7.778
Arachidic A.(C20:0)	0.168
Linolenic A.(C18:3n3)	0.311
cis-11-eicosenoic A.(C20:1)	0.161
Heneicosanoic A.(C21:0)	0.0118
Behenic A.(C22:0)	0.0346
Arachidonic A.(C20:4)	0.0373
cis-5,8,11,14,17-eicosapentaenoic A.(C20:5)	0.0119
cis-4,7,10,13,16,19-docosahexaenoic A.(C22:6)	0.0128

\*The values are mean of three replicate analyses and RSD values are < 5%.

In the literature, there are not many studies on carotenoids in hazelnut kernels, hazelnut shells, and green leafy cover. When the data on carotenoids in the hazelnut itself was examined, Alasalvar and Bolling [8] reported that carotenoids were not found in their studies on the fat-soluble parts of the hazelnut. In another study conducted by Kornsteiner et al. [35], in which they investigated tocopherol types and carotenoids in many

dried nut cultivars,  $\beta$ -carotene and lutein were not detected in hazelnut. In the study of Durmaz and Gokmen [14], they found lutein (0.19  $\mu\text{g/g}$ ), and zeaxanthin (0.88  $\mu\text{g/g}$ ) in hazelnut oil. In the studies of Stuetz et al. [36] on raw and fried nuts, the total lutein-zeaxanthin was found to be 1.69  $\mu\text{g/g}$  in raw hazelnuts, while  $\beta$ -carotene was found to be 0.26  $\mu\text{g/g}$ .

**Table 4.** Effect of saponification on the amount of carotenoids in hazelnut (*C. avellena* L.) samples.

Hazelnut samples	Green Leafy Cover		Shell		Kernel	
	Before saponification	After saponification	Before saponification	After saponification	Before saponification	After saponification
Carotenoids						
*Lutein ( $\mu\text{g/g}$ )	73.05	13.77	ND	2.57	ND	2.67
$\beta$ -carotene ( $\mu\text{g/g}$ )	ND	ND	ND	ND	ND	ND

ND: Not detected

\*The values are mean of three replicate analyses and RSD values are < 2%.

As can be seen, although hazelnut is an oily food source, it is not rich in carotenoids. There are mostly tocopherol types in this oil. Apart from these, no study has been found on carotenoids in green leafy cover or hazelnut shells. In our study, carotenoids could not be detected in the kernel and shell. However, when saponification was applied, 2.67  $\mu\text{g/g}$  lutein was detected in the hazelnut kernel and 2.57  $\mu\text{g/g}$  in the shell. The amounts found after saponification is higher than the values in the literature, but this shows that lutein is found in hazelnut in ester form, not in free form. On the other hand, 73.05  $\mu\text{g/g}$  of lutein was determined without saponification, and 13.77  $\mu\text{g/g}$  after saponification. The results were summarized in Table 4. The amount of lutein found in the free form of green leafy cover is very high compared to the amounts found in studies with hazelnuts in the literature. This means that hundreds of tons of chocolate chips left over from the hazelnut traded every year can be evaluated in terms of lutein.

The results we found in our study; were 284.8 $\pm$ 22.8  $\mu\text{g/g}$  for  $\alpha$ -tocopherol, 2.1 $\pm$ 0.4  $\mu\text{g/g}$  for  $\gamma$ -tocopherol, 77.2  $\mu\text{g/g}$  for  $\beta$ + $\Delta$ - tocopherols and 364.1 as total tocopherol. It is seen that  $\alpha$ -Tocopherol values are within normal limits. However, the total amount of tocopherol, excluding  $\alpha$ -tocopherol, seems to be higher than the amount of tocopherol found in other studies. This may be due to the fact that  $\alpha$ -tocopherol is more resistant to heat than other tocopherols and the cold pressing method prevents the degradation of heat-sensitive tocopherols. The results for tocopherols are given in Table 5. Since it is stated that the amount of tocopherol in the oils obtained by the cold press method is approximately 20% higher than the amounts obtained by the soxhlet extraction, the cold pressing method was used in order to determine the tocopherols in the study [37]. Among the 17 varieties of *C. avellana*, it was determined in the studies that the variety with the highest amount of tocopherol was Tombul [38]. However, it was also stated that the amount of tocopherol in hazelnuts showed significant differences from year to year.

**Table 5.** Tocopherol profiles of hazelnut kernel (*C. avellena* L.) sample ( $\mu\text{g/g}$ ).

Sample	$\alpha$ -Tocopherol	$\gamma$ -Tocopherol	B+ $\Delta$ - Tocopherol	Total Tocopherol
Tombul Hazelnut	284.8	2.1	77.2	364.1

\*The values are mean of three replicate analyses and RSD values are < 5%.

In one of the studies,  $\alpha$ - tocopherol and  $\beta$  +  $\gamma$ - Tocopherol amounts of Tombul hazelnut were found as 248.3 and 33.5  $\mu\text{g/g}$  respectively, while the total amount of tocopherol was given as 281.7  $\mu\text{g/g}$  [5, 7]. In another study, the amounts found for  $\alpha$ -Tocopherol,  $\gamma$ -Tocopherol,  $\delta$ -Tocopherol, and total tocopherol were given as 38.4, 0.61, 3.08, and 41.4  $\mu\text{g/g}$ , respectively [38].

Taş and Gökmen [7] found the amounts of  $\alpha$ -tocopherol,  $\beta$  +  $\gamma$ - tocopherol, and total tocopherols for Tombul hazelnut harvested in 2013 as 36.3, 4.90 and 41.2  $\mu\text{g/g}$  respectively. When the same study was repeated for hazelnuts harvested in 2014, these values were found to be 16.0, 6.03, and 22.0  $\mu\text{g/g}$  respectively. The study of Parcerisa [34] stated that the amount of  $\alpha$ -Tocopherol was found as 303.8 for Tombul hazelnut grown in Türkiye.

Although there are changes in tocopherol amounts according to the harvest years, it is seen that the amount of a-tocopherol varies between 160-384 µg/g, and total tocopherol amounts between 282-414 µg/g in the Tombul hazelnut variety collected from Türkiye.

### 3.1. Antibacterial activity of hazelnut bioproducts

According to the results of antibacterial results, the methanol extracts of all the hazelnut bioproducts (hazelnut hard shell, hazelnut kernels, hazelnut green leafy covers) had moderate antibacterial activity against Gram-negative and Gram-positive bacteria. The MIC values of hazelnut hard shell extract against all the bacteria were determined as 7.3 mg/µL. The MIC values of hazelnut kernels were determined as 11 mg/µL against all the bacteria except *P. aeruginosa* and *K. pneumoniae*. The concentration of 16.5 mg/µL of hazelnut nutmeat extract inhibited *P. aeruginosa* and *K. pneumoniae*. Hazelnut green leafy covers extract showed higher inhibition rates at lower concentrations compared to other extracts. The MIC values were 7 mg/µL for *E. aeruginosa*, *P. aeruginosa*, *S. epidermis*, and MRSA; 5.25 mg/µL for *E. coli*, *K. pneumoniae*, and *B. cereus*; 2.625 mg/µL for *B. megaterium*. The results of antibacterial experiments were given in Table 6.

Nowadays, there has been growing interest in natural antimicrobial compounds because of discovering the adverse health effects of synthetic food preservatives. *Corylus colurna* and its wastes such as hazelnut hard shell and hazelnut green leafy covers have been evaluated as an antimicrobial agent in previously performed studies [4, 30, 39- 41]. Oliveira et al. [4] reported the aqueous leaf extracts of different hazel (*C. avellana* L.) cultivars (Cv. M. Bollwiller, Fertille de Coutard, and Daviana) exhibited significant antimicrobial activity at

concentrations between 0.1 mg/µL and 100 mg/µL against *B. cereus*, *B. subtilis*, *S. aureus*, *P. aeruginosa*, *E. coli*, *K. pneumoniae*, *C. albicans*, and *C. Neoformans*.

In another study performed by Oliveira et al. [40], the aqueous extracts of hazelnut kernels were reported that high antimicrobial activity was only found against Gram-positive bacteria (*B. cereus*, *B. subtilis*, and *S. aureus*, MIC values of 0.1 mg/µL) and Gram-negative bacteria and fungi were found to be resistant to the extracts at all the assayed concentrations. Kirbaslar et al. [39] reported that Turkish nuts and seeds showed strong antimicrobial activity against the Gram-positive and Gram-negative bacteria and the fungi, however, they did not indicate the concentrations of the tested material. In research performed by Ceylan et al. [30], *C. colurna* extracts prepared with petroleum ether, dichloromethane, methanol, and water reported that all the extracts at the concentration of 5 mg/µL had antimicrobial activity against different bacteria. Özaslan et al. [41] reported that green leafy cover (279 mg/µL) exhibited an antibacterial effect against *E. faecalis*, *K. pneumoniae*, *L. monocytogenes*, *S. epidermidis*, *S. aureus*, and *B. subtilis* and green leaves of nut (320 mg/µL) against *K. pneumoniae* and *S. aureus*. The results obtained from this study were compatible with the literature in terms of showing antibacterial activity. However, all studies in the literature were different from each other in terms of the degrees of antibacterial activity and the concentrations, at which the studied samples exhibited activity [19]. The antibacterial activity of *C. colurna* and its derivatives can be explained by the bioactive compounds, they contain such as phenolic compounds [42, 43], cyclic diarylheptanoids, quinic acid, flavonoid, and citric acid [17, 44], carpinontriol [45] etc. The differences between the results of different research can be explained by geographical and climatical differences [19].



**Table 6.** The antibacterial activity of *C. avellana* L. bioproducts.

Bacteria		Hazelnut hard shell			Hazelnut kernels			Hazelnut green leafy covers				Positive controls	
		11 mg/µL	7.3 mg/µL	5.5 mg/µL	16.5 mg/µL	11 mg/µL	8.25 mg/µL	10.5 mg/µL	7 mg/µL	5.25 mg/µL	2.625 mg/µL	NET30	OFX
Gram -	<i>E. aerogenes</i>	8	<b>7</b>	-	9	<b>7</b>	-	10	<b>8</b>	-	-	20	20
	<i>E. coli</i>	9	<b>7</b>	-	10	<b>8</b>	-	13	10	<b>7</b>	-	19	20
	<i>P. aeruginosa</i>	8	<b>8</b>	-	<b>8</b>	-	-	11	<b>8</b>	-	-	19	19
	<i>K. pneumoniae</i>	10	<b>7</b>	-	<b>9</b>	-	-	15	12	<b>8</b>	-	20	19
Gram +	<i>B. cereus</i>	11	<b>8</b>	-	11	<b>9</b>	-	12	9	<b>7</b>	-	20	21
	<i>B. megaterium</i>	11	<b>9</b>	-	10	<b>8</b>	-	14	11	8	<b>7</b>	21	21
	<i>S. epidermis</i>	10	<b>8</b>	-	10	<b>7</b>	-	11	<b>8</b>	-	-	18	20
	MRSA	9	<b>7</b>	-	9	<b>7</b>	-	11	<b>7</b>	-	-	18	19

Netilmicin (NET30) (30 µg/disc), \* Ofloxacin sulbactam (OFX) (10 µg/disc)

Minimum inhibitory concentration (MIC) values (mm) obtained from disc dilution values were indicated in bold in the table.

#### 4. Conclusion

This study tried to investigate all components of the hazelnut, including the shell, which was considered a waste product. This study provides significant information for food processors and the industry to evaluate hazelnut bioproducts for their needs. In addition, the nutritional and technological quality of hazelnut bioproducts from nations with low production rates is comparable or even superior, making them competitive on the worldwide market. Besides, the antibacterial activity of all components of hazelnut makes them more preferable for use as a food additive. In this connection, the study provides a comprehensive investigation of the Giresun-grown hazelnut bioproducts.

#### Acknowledgements

The authors thank "Karaerler Machine" for allowing us to use the cold press oil machine to extract the hazelnut oil and Giresun University Scientific Research Projects Coordinatorship for supporting the project.

#### Author's Contributions

**Mehmet Emin Şeker.:** Designed the study, worked on phenolic, tocopherol and carotenoid extractions.

**Ayşegül Erdoğan:** Performed GC-FID analyzes of oil analyzes and carotenoid extractions.

**Emriye Ay:** Carried out phenolic extractions.

**Derya Efe:** Carried out antimicrobial analysis.

**Rena Hüseyinoğlu:** Involved in identification and collection of the *C. Avellana*. All authors contributed to the writing of the article, read and approved the final version of the article.

#### Ethics

There are no ethical issues after the publication of this manuscript.

#### Funding

The authors declare that this study was partially supported by the Scientific Research Projects Department with a project number of FEN-BAP-A-150219-15, Giresun University.

#### References

- [1]. Shahidi, F, Alasalvar, C, Liyana-Pathirana, CM. 2007. Antioxidant phytochemicals in hazelnut kernel (*Corylus avellana* L.) and hazelnut byproducts. *Journal of Agricultural and Food Chemistry*; 55(4), 1212-20.
- [2]. Shataer, D, Abdulla, R, Ma, QL, Liu, GY, Aisa, HA. 2020. Chemical Composition of Extract Of *Corylus avellana* Shells. *Chemistry of Natural Compounds*; 56, 338-340.
- [3]. Alasalvar, C, Shahidi, F, Liyanapathirana, CM, Ohshima, T. 2003. Turkish Tombul hazelnut (*Corylus avellana* L.). 1. Compositional characteristics. *Journal of Agricultural and Food Chemistry*; 51(13), 3790-3796.

- [4]. Oliveira, I, Sousa, A, Morais, JS, Ferreira, IC, Bento, A, Estevinho, L, Pereira, JA. 2008. Chemical composition, and antioxidant and antimicrobial activities of three hazelnut (*Corylus avellana* L.) cultivars. *Food Chemistry and Toxicology*; 46(5), 1801-1807.

- [5]. Taş, NG, Gökmen, V. 2015a. Bioactive compounds in different hazelnut varieties and their skins. *Journal of Food Composition and Analysis*; 43, 203-208.

- [6]. Toprak Mahsulleri Ofisi (TMO) 2020 Yılı Fındık Sektör Raporu; Ankara: TMO 2021. <https://www.tmo.gov.tr/Upload/Document/sektorraporlari/findik2020.pdf>

- [7]. Taş, NG, Gökmen, V. 2015b. Profiling triacylglycerols, fatty acids and tocopherols in hazelnut varieties grown in Turkey. *Journal of Food Composition and Analysis*; 44, 115-121.

- [8]. Alasalvar, C, Bolling, BW. 2015. Review of nut phytochemicals, fat-soluble bioactives, antioxidant components and health effects. *British Journal of Nutrition*; 113(2), S68-78.

- [9]. Alasalvar, C, Shahidi, F. 2008. Tree nuts: Composition, phytochemicals, and health effects: An overview. (pp. 15-24) CRC press.

- [10]. Brown, R, Ware, L, Tey, S. L. 2022. Effects of Hazelnut Consumption on Cardiometabolic Risk Factors and Acceptance: A Systematic Review. *International Journal of Environmental Research and Public Health*; 19(5), 2880.

- [11]. Tey, SL, Brown, RC, Chisholm, AW, Delahunty, CM, Gray, AR, Williams, SM. 2011. Effects of different forms of hazelnuts on blood lipids and alpha-tocopherol concentrations in mildly hypercholesterolemic individuals. *European Journal of Clinical Nutrition*; 65(1), 117-24.

- [12]. Schmitzer, V, Slatnar, A, Veberic, R, Stampar, F, Solar, A. 2011. Roasting affects phenolic composition and antioxidative activity of hazelnuts (*Corylus avellana* L.). *Journal of Food Science*; 76(1), S14-9.

- [13]. Balta, MF, Yarılgac, T, Askin, MA, Kucuk, M, Balta, F, Ozrenk, K. 2006. Determination of fatty acid compositions, oil contents and some quality traits of hazelnut genetic resources grown in eastern Anatolia of Turkey. *Journal of Food Composition and Analysis*; 19(6-7), 681-686.

- [14]. Durmaz, G, Gokmen, V. 2019. Effect of refining on bioactive composition and oxidative stability of hazelnut oil. *Food Research International*; 116, 586-591.

- [15]. Sun, JY, Feng, XN, Lyu, CM, Zhou, S, Liu, ZX. 2022. Effects of different processing methods on the lipid composition of hazelnut oil: a lipidomics analysis. *Food Science and Human Wellness*; 11(2), 427-435.

- [16]. Xu, YX, Hanna, MA, Josiah, SJ. 2007. Hybrid hazelnut oil characteristics and its potential oleochemical application. *Industrial Crops and Products*; 26(1), 69-76.

- [17]. Cerulli, A, Lauro, G, Masullo, M, Cantone, V, Olas, B, Kontek, B, Nazzaro, F, Bifulco, G, Piacente, S. 2017. Cyclic Diarylheptanoids from *Corylus avellana* Green Leafy Covers: Determination of Their Absolute Configurations and Evaluation of Their Antioxidant and Antimicrobial Activities. *Journal of Natural Products*; 80(6), 1703-1713.

- [18]. Alasalvar, C, Karamac, M, Amarowicz, R, Shahidi, F. 2006. Antioxidant and antiradical activities in extracts of hazelnut kernel (*Corylus avellana* L.) and hazelnut green leafy cover. *Journal of Agricultural and Food Chemistry*; 54(13), 4826-32.

- [19]. Bottone, A, Cerulli, A, D'Urso, G, Masullo, M, Montoro, P, Napolitano, A, Piacente, S. 2019. Plant Specialized Metabolites in Hazelnut (*Corylus avellana*) Kernel and Byproducts: An Update on Chemistry, Biological Activity, and Analytical Aspects. *Planta Medica*; 85(11/12), 840-855.
- [20]. Arcan, I, Yemencioğlu, A. 2009. Antioxidant activity and phenolic content of fresh and dry nuts with or without the seed coat. *Journal of Food Composition and Analysis*; 22(3), 184-188.
- [21]. Şahin, S, Tonkaz, T, Yarılgöç, T. 2022. Chemical Composition, Antioxidant Capacity And Total Phenolic Content of Hazelnuts Grown In Different Countries. *Tekirdağ Ziraat Fakültesi Dergisi*; 19(2), 262-270.
- [22]. Şeker, ME, Ay, E, Karacelik, AA, Hüseyinoğlu, R, Efe, D. 2021. First determination of some phenolic compounds and antimicrobial activities of *Geranium ibericum* subsp. *jubatum*: A plant endemic to Turkey. *Turkish Journal of Chemistry*; 45(1), 60-70.
- [23]. Celenk, VU, Gumus, ZP, Argon, ZU, Buyukheliçigil, M, Karasulu, E. 2018. Analysis of chemical compositions of 15 different cold-pressed oils produced in Turkey: a case study of tocopherol and fatty acid analysis. *Journal of the Turkish Chemical Society Section A: Chemistry*; 5(1), 1-18.
- [24]. Aksoz, E, Korkut, O, Aksit, D, Gokbulut, C. 2020. Vitamin E ( $\alpha$ -,  $\beta$ +  $\gamma$ -and  $\delta$ -tocopherol) levels in plant oils. *Flavour and Fragrance Journal*; 35(5), 504-510.
- [25]. Górnas, P, Soliven, A, Segliņa, D. 2015. Seed oils recovered from industrial fruit by-products are a rich source of tocopherols and tocotrienols: Rapid separation of  $\alpha/\beta/\gamma/\delta$  homologues by RP-HPLC/FLD. *European Journal of Lipid Science and Technology*; 117(6), 773-777.
- [26]. Erdoğan, A, Çağır, A, Dalay, MC, Eroğlu, AE. 2015. Composition of carotenoids in *Scenedesmus protuberans*: Application of chromatographic and spectroscopic methods. *Food Analytical Methods*; 8, 1970-1978.
- [27]. Gültekin-Özgülven, M, Davarcı, F, Paslı, AA., Demir, N, Özçelik, B. 2015. Determination of phenolic compounds by ultra-high liquid chromatography-tandem mass spectrometry: Applications in nuts. *LWT-Food Science and Technology*; 64(1), 42-49.
- [28]. Pelvan, E, Olgun, EO, Karadağ, A, Alasalvar, C. 2018. Phenolic profiles and antioxidant activity of Turkish Tömbül hazelnut samples (natural, roasted, and roasted hazelnut skin). *Food Chemistry*; 244, 102-108.
- [29]. Ciemnińska-Zytkiewicz, H, Verardo, V, Pasini, F, Brys, J, Koczon, P, Caboni, MF. 2015. Determination of lipid and phenolic fraction in two hazelnut (*Corylus avellana* L.) cultivars grown in Poland. *Food Chemistry*; 168, 615-22.
- [30]. Ceylan, O, Sahin, M Avaz, S. 2013. Antibacterial activity of *Corylus colurna* L.(Betulaceae) and *Prunus divaricata* Ledeb. subsp. *divaricata* (Rosaceae) from Usak, Turkey.
- [31]. Yuan, B, Lu, M, Eskridge, KM., Isom, LD, Hanna, M. A. 2018. Extraction, identification, and quantification of antioxidant phenolics from hazelnut (*Corylus avellana* L.) shells. *Food Chemistry*; 244, 7-15.
- [32]. Tüfekci, F, Karataş, Ş. 2018. Determination of geographical origin Turkish hazelnuts according to fatty acid composition. *Food Science and Nutrition*; 6(3), 557-562.
- [33]. Bacchetta, L, Aramini, M, Zini, A., Di Giammatteo, V, Spera, D, Drogoudi, P, Rovira, M, Silva, AP, Solar, A, Botta, R. 2013. Fatty acids and alpha-tocopherol composition in hazelnut (*Corylus avellana* L.): a chemometric approach to emphasize the quality of European germplasm. *Euphytica*; 191, 57-73.
- [34]. Parcerisa, J, Richardson, DG, Rafecas, M, Codony, R, Boatella, J. 1998. Fatty acid, tocopherol and sterol content of some hazelnut varieties (*Corylus avellana* L.) harvested in Oregon (USA). *Journal of Chromatography A*; 805(1-2), 259-268.
- [35]. Kornsteiner, M, Wagner, KH, Elmadfa, I. 2006. Tocopherols and total phenolics in 10 different nut types. *Food Chemistry*; 98(2), 381-387.
- [36]. Stuetz, W, Schlormann, W, Glei, M. 2017. B-vitamins, carotenoids and alpha-/gamma-tocopherol in raw and roasted nuts. *Food Chemistry*; 221, 222-227.
- [37]. Al Juhaime, F, Ozcan, MM, Ghafoor, K, Babiker, EE, Hussain, S. 2018. Comparison of cold-pressing and soxhlet extraction systems for bioactive compounds, antioxidant properties, polyphenols, fatty acids and tocopherols in eight nut oils. *Journal of Food Science and Technology*; 55, 3163-3173.
- [38]. Köksal, Aİ, Artık, N, Şimşek, A, Güneş, N. 2006. Nutrient composition of hazelnut (*Corylus avellana* L.) varieties cultivated in Turkey. *Food Chemistry*; 99(3), 509-515.
- [39]. Kirbaslar, FG, Türker, G, Özsoy-Günes, Z, Ünal, M, Dülger, B, Ertaş, E, Kizilkaya, B. 2012. Evaluation of Fatty Acid Composition, Antioxidant and Antimicrobial Activity, Mineral Composition and Calorie Values of Some Nuts and Seeds from Turkey. *Records of Natural Products*; 6(4), 339.
- [40]. Oliveira, I, Sousa, A, Valentao, P, Andrade, PB, Ferreira, ICFR, Ferreres, F, Bento, A, Seabra, R, Estevinho, L, Pereira, JA. 2007. Hazel (*Corylus avellana* L.) leaves as source of antimicrobial and antioxidative compounds. *Food Chemistry*; 105(3), 1018-1025.
- [41]. Öztaşlan, M, Oğuzkan, SB, Uğraş, S, Merve, C, Ayşe, U, Ülger, S, Üzmez, Ş, Karagül, B, Kiliç, İH, Uğraş, Hİ. 2016. Fındık (*Corylus Avellana* L.) yeşil kabuk ve yaprak ekstraktlarında biyolojik aktivite tayini. *KSÜ Doğa Bilimleri Dergisi*; 19(4), 373-378.
- [42]. Amarowicz, R, Dykes, GA, Pegg, RB. 2008. Antibacterial activity of tannin constituents from *Phaseolus vulgaris*, *Fagopyrum esculentum*, *Corylus avellana* and *Juglans nigra*. *Fitoterapia*; 79(3), 217-9.
- [43]. Proestos, C, Chorianopoulos, N, Nychas, GJ, Komaitis, M. 2005. RP-HPLC analysis of the phenolic compounds of plant extracts. investigation of their antioxidant capacity and antimicrobial activity. *Journal of Agricultural and Food Chemistry*; 53(4), 1190-5.
- [44]. Caligiani, A, Coisson, JD, Travaglia, F, Acquotti, D, Palla, G, Palla, L, Arlorio, M. 2014. Application of (1)H NMR for the characterisation and authentication of "Tonda Gentile Trilobata" hazelnuts from Piedmont (Italy). *Food Chemistry*; 148, 77-85.
- [45]. Bachmann, R, Klockmann, S, Haerdter, J, Fischer, M, Hackl, T. 2018. (1)H NMR Spectroscopy for Determination of the Geographical Origin of Hazelnuts. *Journal of Agricultural and Food Chemistry*; 66(44), 11873-11879.